Studies of Corneal Structure and Transparency

Steven John Gardner B.Phys., M.Sc.

Structural Biophysics Group,
Department of Optometry and Vision Sciences,
Cardiff University.

Thesis submitted to Cardiff University for the degree of Doctor of Philosophy

March 2015

Acknowledgements

I'd most of all like to thank my supervisor, Prof. Keith Meek, for his support, knowledge and patience. I could not imagine having completed this thesis without his supervision.

I also acknowledge the invaluable contribution of a wide array of present and former members of the school of optometry. Including Dr Carlo Knupp, for advice and knowledge of modelling methodology, Mr Nick White for advice on cell imaging methodology and for supervising the microscopy sections of this thesis, Dr Christian Pinali and Dr Rob Young for their expertise and teaching in electron microscopy methods, Dr Tina Kamma-Lorger and Dr Julie Albon for their training in cell culture protocol, Dr Sally Hayes and Mr Nick Hawksworth for securing and providing corneal tissue for study, summer intern student Ms Maeva Vallet for some enlightening discussions about the physics of latex beads, Dr Justyn Regini for fulfilling his role as pastoral advisor and more widely the whole of the structural biophysics group for providing a healthy and sociable working environment.

I also wish to thank my parents, for the many sacrifices they've made to provide me with a comprehensive education. Last but certainly not least, I'd like to thank my long-suffering partner Jane, who has provided so much moral support since the beginning of my studies, and my son Henry. I hope he's proud of his daddy.

Abstract

This thesis presents the results and conclusions of experiments designed to extend the current models for the origin of corneal transparency. The cornea is the transparent window at the front of the eye, which is responsible not only for the majority of refraction of light that enters, but also the protection against damage, infection and mechanical stress. The property of transparency is only realised by corneal and lens tissue in the human body. In the cornea, it has long been suspected to be caused by the precise arrangement of the fibrils of collagen that are contained within the central layer, the stroma, regulated by the sulphated proteoglycans (PG) that keep fibril spacing within acceptable boundaries. These models are consistent and give a complete description of the reasons for the transparency of a stroma that is entirely acellular. However, it is well known that the stroma is not acellular, and that the short-range order that is critical for transparency would necessarily be disturbed by the cells of the stroma, the keratocytes, which are at least an order of magnitude thicker than the maximum allowed range. Originally, an acellular stroma was considered to be a reasonable approximation due to the perceived sparsity of the cells, but more recent measurements have cast doubt upon this, and explanations have begun to focus on the properties of the cells themselves. One such property would be their refractive index (RI). If the cells could match their own RI to that of their surroundings then they would not scatter and hence would not cause a loss in transparency. This research attempts to measure that RI and by comparison with previously calculated values for the RI of the extra-cellular matrix, attempts to quantify the scale of the scattering that any mismatch would cause, using theoretical models based on both Mie scattering and finite-difference time-domain methods.

In addition to models of healthy corneas, this thesis also provides results and conclusions drawn from studies of pathological corneas and discussions of how the pathology, and the treatments,

can cause initial losses in transparency. The first such study concerned a cornea afflicted with keratoconus, a disorder of as yet unknown origin that causes the weakening of the corneal tissue, leading to a characteristic cone-shaped cornea, which had been treated with a full penetrating keratoplasty (PK) transplant before being donated. The study was conducted using the techniques of electron microscopy and x-ray diffraction, to both qualitatively and quantitatively analyse the properties of the fibrils and their spacing. This was done on both the original sections of diseased tissue and the donated sections, in order to investigate the idea of keratoconus recurring in previously healthy donated tissue. Any such discovery could provide evidence that keratoconus is not an entirely inherited disorder. The structural properties of the observed scar, that was present as a direct result of the PK procedure that was carried out decades before, were also investigated using the same methods. This investigation was designed to provide insights into the priorities of wound healing in the cornea, and whether any appreciable change in fibril spacing could account for the observed loss of transparency. The final study presented here is a novel tomographic reconstruction of a feature of the disease macular corneal dystrophy (MCD). MCD is a genetic disorder that affects the sulphation of the PG keratan sulphate. MCD gives rise to a multitude of abnormalities but one that has not been fully investigated is the apparent presence of areas within the stroma entirely populated by PGs, with no collagen present. This study attempts to reconstruct three-dimensional views of these lakes, as well as stromal lamellae, in order to investigate the interactions between free PGs and between PGs and collagen in MCD.

Contents

List of Figures

Chapter 1: Introduction

Chapter 2: Calculating the refractive index of corneal stromal cells

Chapter 3: Corneal transparency Modelling

List of Abbreviations

ADA	Anomalous diffraction approximation
ALDH	Aldehyde dehydrogenase
ALDH3A1	Aldehyde dehydrogenase 3A1
CCD	Charged-coupled device
CS	Chondroitin sulphate
CS/DS	Chondroitin/Dermatan sulphate
CT	Computed tomography
DMEM	Dulbecco's modified Eagle's medium
DS	Dermatan sulphate
EM	Electron microscopy
FBS	Foetal bovine serum
FDTD	Finite-difference time-domain
FGF-2	Fibroblast growth factor-2
FITC	Fluorescent isothiocyanate
GAG	Glycosaminoglycan
IGF-II	Insulin-like growth factor-II
KS	Keratan sulphate
LASIK	Laser in-situ keratomileusis
LASEK	Laser subepithelial keratectomy
MCD	Macular corneal dystrophy
MEM	Minimal essential medium
NA	Numerical Aperture
NIST	National Institute of Science and Technology (USA)
PDGF	Platelet-derived growth factor
PG	Proteoglycan

PK	Penetrating keratoplasty
PRK	Photorefractive keratectomy
PTA	Phosphotungstic acid
QPI	Quantitative phase imaging
SAXS	Small angle X-ray scattering
TEM	Transmission electron microscopy
TGF-β	Transforming growth factor-beta
TIE	Transport of Intensity Equation
UA	Uranyl acetate
WAXS	Wide angle X-ray scattering
WT	Wild type

1 Introduction

1.1 The Eye

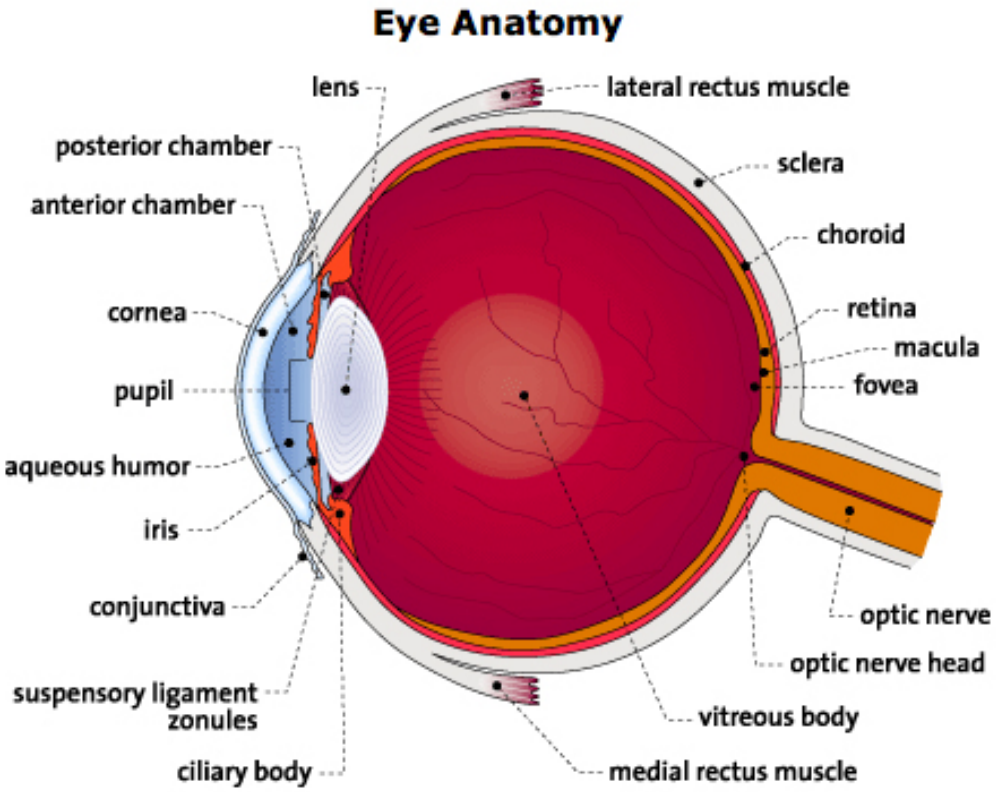

Figure 1.1: Schematic cross-section of a human eye (www.med.upenn.edu)

The eye (Figure 1.1) is the organ primarily responsible for sensing visible light. It is composed of several specialised tissues whose functions co-operate to allow both a sharp resolution of light from objects directly in the field of view and a more general resolution of objects in a wider field of view, known as the periphery. Light in the visible spectrum, defined as that of wavelength from 390nm to 700nm, passes first through the cornea, the most anterior tissue of the eye and the part most responsible for refraction. Behind the cornea is located a water based transparent gel-like substance known as the aqueous humour, which is secreted by the epithelial cells of the ciliary body. The ciliary body supports and manipulates the lens, a transparent structure that is responsible for the remaining refraction of light not covered by the cornea. The ratio of light refraction of cornea to lens is around 2:1 in land mammals, with the cornea's

optical power at around 40 diopters. The optical power of the lens is around 20 diopters, but can be modified within certain limits depending on the desired depth of focus. The shape of the lens is determined by the actions of the ciliary muscles, which form part of the ciliary body, a process which is referred to as accommodation. In aquatic animals, since the cornea's refractive index is close to that of water, the lens is almost totally responsible for the focussing of light. The lens and ciliary body are located behind the iris, which regulates the size of the pupil, the hole at the centre, to prevent damage to the posterior section of the eye from light of too great an intensity. Together, these tissues are known as the anterior chamber of the eye. Visible light that has passed through the lens then enters the vitreous humour, another water based gel that fills the posterior space behind the lens. The vitreous humour is a more viscous gel than the aqueous humour and serves to bathe the posterior tissues of the eye in water as well as forming a transparent space between the lens and the retina, which forms along the posterior interior boundary of the eye. The light sensitive cells in the retina are known as rods and cones, rods being responsible for the pitch and three types of cones to distinguish the three primary colours. These cells then pass signals on to the optic nerve, which in turn carries the signal to be interpreted to the brain within the visual cortex.

1.2 The Cornea

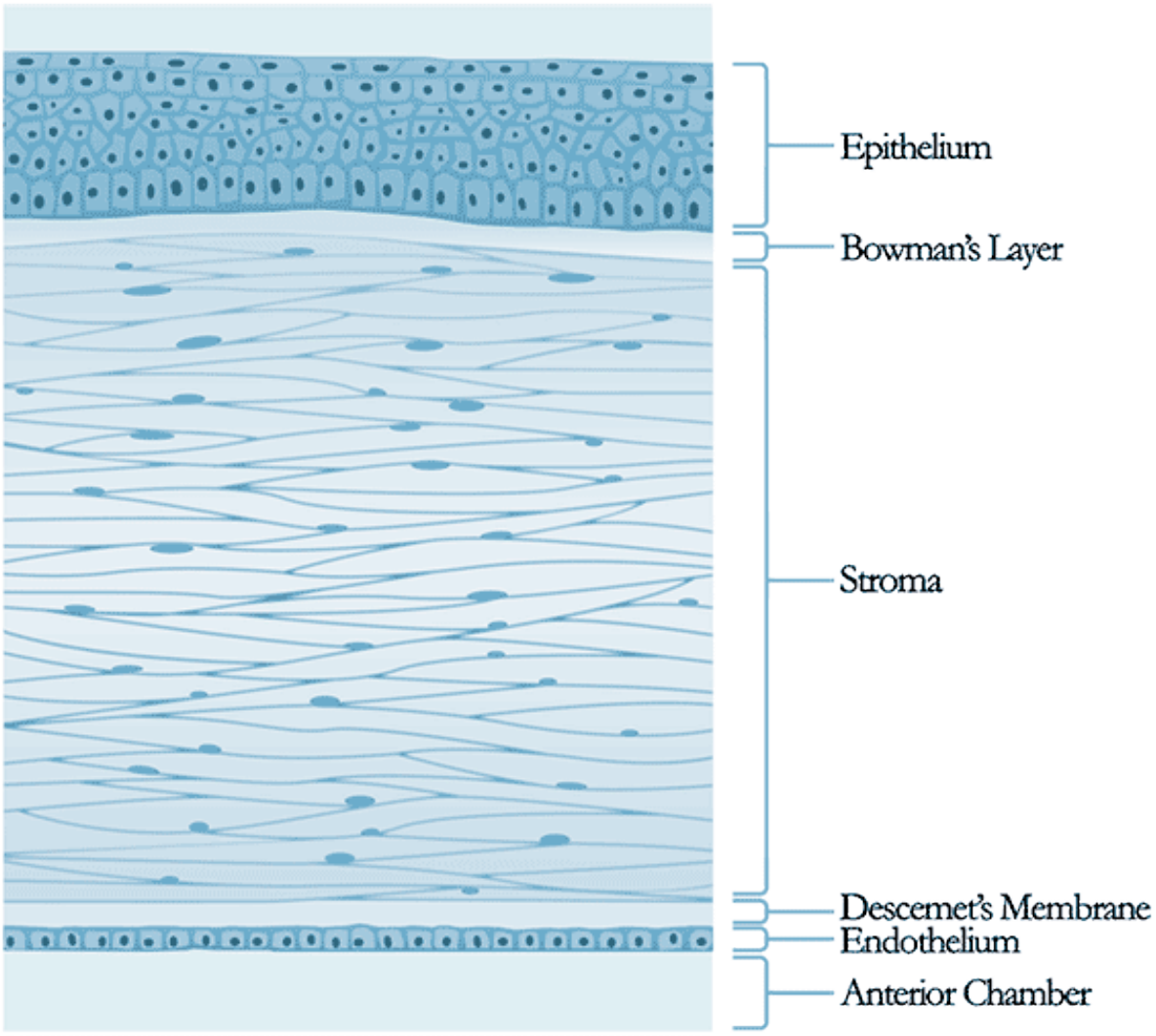

Figure 1.2: Schematic diagram of cornea cross-section (Adapted from http://webeye.ophth.uiowa.edu)

The cornea is the transparent window at the front of the eye which is responsible for around two-thirds of its refractive power. The cornea is composed of six distinct layers which are, from anterior to posterior, the epithelium, Bowman's layer, the stroma, Descemet's layer and the endothelium. Recently, a new layer has been proposed to exist between the posterior stroma and Descemet's layer (Dua et al. 2013; Dua et al. 2014), however at the time of writing, its identity as a distinct layer is still controversial (Jester et al. 2013). In mammals, the total thickness of the cornea tends to increase with the size of the organism, from 70-90µm in mice

to 325-500µm in rabbits, up to 1mm in cows and pigs. Human corneal thickness usually falls in the range 500-600µm. The thickness of the individual layers remains roughly constant, with the exception of the stroma which differs between species and accounts for the vast majority of the thickness differences (Bartholomew et al. 1997; Moller-Pedersen et al. 1998). The cornea is known to be highly innervated, but lacks a blood supply, the cells in the cornea obtain the raw materials for respiration via a combination of oxygen diffusion from the air via the tear film and glucose diffusion from the aqueous humour.

1.2.1 Epithelium and Bowman's layer

The corneal epithelium are located at the extreme anterior of the eye. In mammals, the total thickness of the epithelial layer remains approximately constant, at around 45±5µm (Moller-Pedersen et al. 1998; Cavanagh et al. 2002). The layer is composed of around six layers of cells that are shed and replaced constantly, with complete turnover around every 7-10 days (Hanna et al. 1961). The deepest layer of basal cells is anchored to Bowman's layer by a basal membrane. Corneal epithelial cells are also known to be a part of the wound healing response. When a wound is detected, they release signalling biochemicals such as transforming growth factor-beta (TGF-β), which activates the keratocytes of the stroma and causes them to proliferate and migrate to the site of the wound.

Bowman's layer is located between the cellular epithelial layer and the stroma. It is mainly comprised of a meshwork of collagen fibrils. The layer is first detectable at between 13 and 19 weeks gestation in humans (Tisdale et al. 1988). The precise function of Bowman's layer is not well understood, reports of congenital absence of the layer have been associated with several corneal abnormalities including Peter's anomaly (Stone et al. 1976) and sclerocornea (Wilson and Hong 2000), although Kasner et al (1993) have reported the cases of three patients with a total bilateral absence of Bowman's layer with no observed degradation of clarity or function.

It is also thought that it could have a role to play in the anchoring of heterotypic type I and V collagen fibrils from the stroma. Bowman's layer is thought to be comprised mainly of collagen types I, III and V (Jacobsen et al. 1984) but type XII has also been observed aligned with the stromal fibrils in Bowman's layer and may perform the anchoring function (Wessel et al. 1997).

1.2.2 Stroma and Keratocytes

The stroma comprises roughly 90% of the total thickness of the cornea; it is composed of strings of collagen, known as fibrils, arranged in parallel sheets known as lamellae. These lamellae are arranged in a stack with collagen orientated in all directions, although in some areas of the cornea certain directions are preferred over others (Aghamohammadzadeh et al. 2004; Boote et al. 2005) and this pattern mirrors in the nasal-temporal axis between the left and right eyes (Boote et al. 2006). Keratocytes are fibroblast cells located between lamellae in the corneal stroma. They are responsible for the creation and maintenance of the specific structure of the collagen that is required for transparency. Measurements of their population density vary, but what is known is that they are much more concentrated in the anterior section of the stroma (Patel et al. 2001; Popper et al. 2004; McLaren et al. 2010), presumably as this is the area more likely to sustain an injury. Measurements of the volume fraction of the entire stroma that is occupied with cells have been recorded as high as 17% (Hahnel et al. 2000) with Patel et al (2001) returning a result of 12% just under Bowman's layer, down to 5% in the posterior stroma. Recent measurements of cell volume using three-dimensional tomography have placed a figure for the volume fraction of cells in the stroma in developing chicks to be 20% (Young et al. 2014). It should be noted that these measurements are higher than was anticipated when the first models of the mechanism of corneal transparency were conceived by Maurice (1957), Hart and Farrell (1969), and Benedek (1971).

The thickness of a typical keratocyte is much larger than the maximum separation the collagen fibrils can be and still maintain transparency. As such it is thought that keratocytes must in some way be acting to minimise the amount of light they scatter. One possible mechanism for this process is theorised by Jester et al (1999), Piatigorsky (2000) and Moller-Pedersen (2004), that scattering may be reduced by increasing the concentration of crystallin proteins in the cell cytoplasm, in order to match the refractive index to their surroundings. The main candidate molecule for this process is the enzyme aldehyde dehydrogenase 3A1 (ALDH3A1), which was first discovered in bovine corneas in 1973 (Holt and Kinoshita) and first identified eight years later (Alexander et al. 1981; Silverman et al. 1981). ALDH proteins catalyse the oxidation of aldehyde molecules, which are a common intermediate stage in the breakdown of alcohols in the liver. Clearly the presence of this enzyme would serve no catalytic purpose in the cornea, making it a good candidate for the molecule that is produced by keratocytes, although ALDH3A1 has also been shown to protect cells against both ultraviolet light and oxidative apoptosis (Manzer et al. 2003; Pappa et al. 2005; Lassen et al. 2006). The optical properties of ALDH3A1 are already utilised in the lens. The crystallins reduce light scattering in the lens by forming a structural unit known as a refracton, thereby providing short range order within the cytoplasm of the lens fibres (Benedek 1971; Delaye and Tardieu 1983).

It has already been stated that part of the role of keratocytes in the stroma is that of maintenance of the extracellular matrix. When the fibrils are damaged the cells activate and begin attempting to repair the damage. Keratocytes can be isolated by excising pieces of stroma and introducing collagenase to break down the collagen lattice. This pulp can then be centrifuged to separate the cells from the protein. The cells then behave in their usual way in culture (Jester et al. 1996; Beales et al. 1999), which is perhaps surprising given the traumatic method of isolation. This shows that the method of activation is not rooted in simple physical trauma which gives more

credence to the theory that keratocytes are activated using biochemical signals (Li and Tseng 1995).

1.2.3 Proposed pre-Descemet's layer

The pre-Descemet's layer (Dua's layer) was first proposed in a paper by Harminder Singh Dua (2013). Dua used air injections of up to 1.45 bar to fracture donor corneas, and in doing so separated out an acellular layer of type 1 collagen of 10.15 ± 3.6 micron thickness, located between the posterior stroma and Descemet's membrane. The collagen bundles comprised between six and eight lamellae and showed no preferred orientation. At the time of writing there has been no independent verification of Dua's proposed layer. If it is found to exist, Dua's layer could have implications in the corneal disease of keratoconus, more specifically in the formation of fluid lakes in the stroma known as hydrops. Dua's hypothesis is that these lakes are caused by a failure of this pre-descemet's layer, which is normally impervious to fluids, allowing the aqueous humour to penetrate the cornea and cause a weakening of the stroma. Again this very recent idea has not been independently tested at the time of writing and has been the subject of much recent correspondence (Jester et al. 2013).

1.2.4 Descemet's membrane and Endothelium

Descemet's membrane, also sometimes known as the posterior elastic laminar, is a basement membrane located between the posterior boundary of the stroma or Dua's layer and the endothelium. It is predominantly made up of type IV collagen and is known to increase in thickness with age from around 2µm at the age of ten years to 10µm by the age of 80 years (Johnson et al. 1982). Descemet's membrane provides an anchoring point for the corneal endothelium and is known to be extremely elastic, presumably to prevent it from tearing under the internal pressure of the eye. Abnormalities of Descemet's membrane can lead to an overall weakening of the cornea due to swelling caused by the penetration of the aqueous humour into

the stroma, and an abnormally thick membrane is known to be a symptom of Fuch's dystrophy, a disorder thought to be caused by abnormalities of the endothelium, but which might also manifest sooner in individuals with a mutation in the gene that codes for collagen type VIII (Gottsch et al. 2005).

The corneal endothelium is a cell monolayer located at the very posterior of the cornea. In humans, corneal endothelial cells are non-mitotic. Their main function is to act as a pump to remove water from the stroma by using an ion exchange process.

1.3 Collagen

Collagen is a fibrous protein that forms a major part of connective tissue in many areas of the body. To date twenty-nine different versions of collagen have been identified (Gordon and Hahn 2010) and 40 different genes have been isolated that encode for it (Ihanamaki et al. 2004). In the developing cornea, the collagen is first synthesised by the epithelium, and organised into orthogonal layers about one or two fibrils thick (Hay and Revel 1969; Trelstad and Coulombre 1971). This matrix is the primary stroma and serves as a template for the rest of development. Collagen in the developed cornea is synthesised by the keratocytes, first as procollagen in the rough endoplasmic reticulum of the cells and then fully formed once secreted into the extra-cellular matrix. These molecules then combine to form fibrils (Hassell and Birk 2010).

1.3.1 Corneal Collagen Types and Functions

Collagen comprises around 70% of the dry weight of the cornea. Of the different types, nine have been identified within the human adult cornea, though the bulk of the stroma is type I. The other types present in the cornea (IV, V, VI, VIII, XII, XIII, XIV and XXIV) fulfil smaller and more specialised roles. In addition to these, type III has also been claimed to be synthesised by fibroblasts in chick corneas (Conrad et al. 1980). Although it is currently unknown to exist

within the healthy adult human cornea, type III collagen has also been reported in foetal corneal tissue and also in healing adult corneas (Lee and Davison 1981; Newsome et al. 1981; Newsome et al. 1982; Lee and Davison 1984). In calf corneas, type I synthesis accounts for as much as 75% of the total biosynthesis process, with type V and VI accounting for 8% and 16% respectively (Kern et al. 1991).

Stromal fibrils are heterotypic fibrils formed from a combination of both type I and type V. This process is thought to reduce the diameter of the fibril compared to using type I alone (Birk et al. 1990). This reduced diameter allows for a more compact lattice, which is vital for the transparency of the cornea (Birk 2001). Each fibril contains roughly 300 molecules (Meek and Leonard 1993) of which around 10% are type V, the rest being type I (Holmes and Kadler 2004).

Type XII collagen has been found at the boundaries between the stroma and Bowman's layer and Descemet's membrane, (Gordon et al. 1996), during corneal development in chick embryos. This might imply that type XII has a role to play in the anchoring of the stromal fibrils in these layers, although the terminus of a stromal fibril has not yet been observed. Type XII has already been observed to align with the heterotypic fibrils of the stroma in Bowman's layer (Wessel et al. 1997).

Type XIII collagen is reported to have been found in the posterior stroma (Sandberg-Lall et al. 2000), the precise role is not explicitly understood. There is also evidence from the expression in heavily scarred keratoconic corneas that type XIII may play a small role in wound healing (Maatta et al. 2006b).

The presence of type XIV collagen has been demonstrated in embryonic avian corneas and seems to be a crucial part of their healthy development. Specifically, the suggestion is that type XIV is involved with the regulation of fibrillogenesis at the embryonic stage. The lack of type

XIV leading to a cornea that has not undergone a period of compaction, a crucial requirement for transparency (Gordon et al. 1996; Young et al. 2002).

Types XV and XVIII have been found in healthy corneas but have been found to be decreased or absent in corneas afflicted by keratoconus and scarring (Maatta et al. 2006a). That these two types can be found in the limbal region of the cornea as well as the conjunctival epithelial membranes, but not in the transparent central regions suggests they have some structural focus. The decreased expression in pathologic corneas however might suggest a role in wound healing. At this point it is difficult to determine whether the decreased expression is a cause of the pathology or a symptom. Maatta et al (2006a) take the view that the absence of the molecule in scarred corneas is clear evidence that they must take an active role in wound healing. Right now that has yet to be demonstrated conclusively, and cannot be so until the genes responsible for types XV and XVIII were identified, nullified and the effects measured.

1.3.2 Stromal Collagen Fibrils

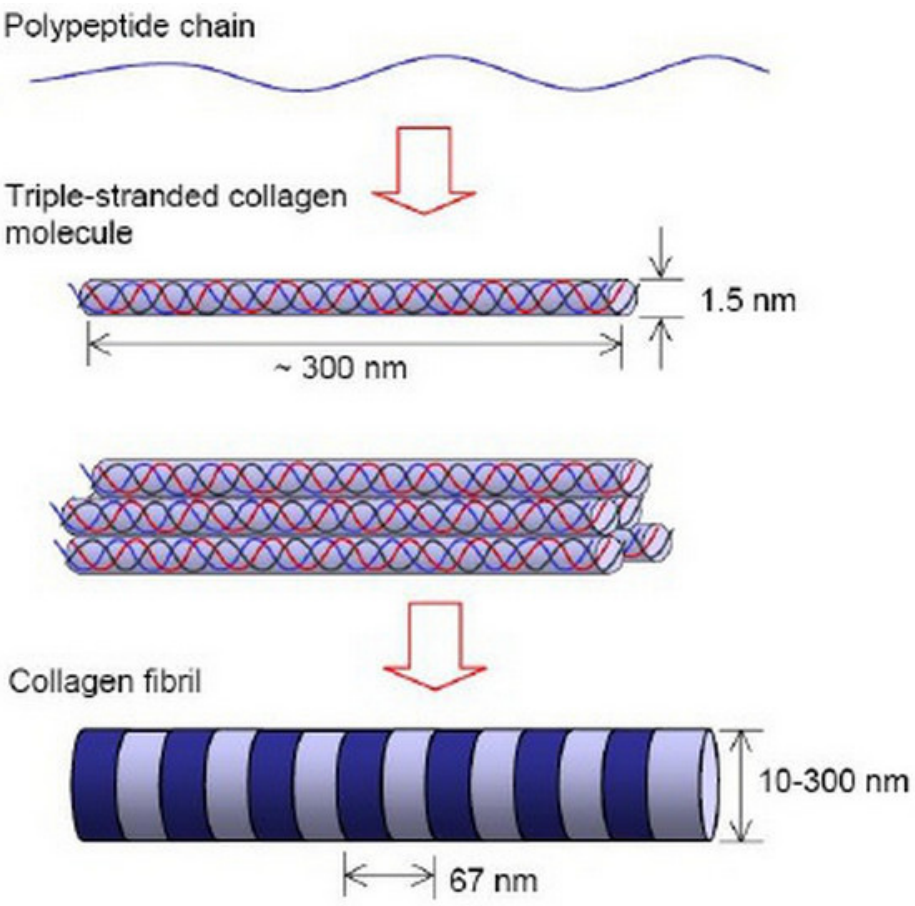

Figure 1.3: Schematic showing the different levels of fibril assembly. Polypeptide α-chains are arranged in a triple helical structure to forms collagen molecules, which then join together laterally to form a fibril (www.namrata.co)

The properties of the fibrils of the transparent stroma are well established and have been extensively studied. The microfibrils are arranged in a helical fashion to form fibrils in much the same way that strings are wound together to form rope. The advantage of the increase in tensile strength of the resulting bundles over their component parts is intuitively obvious, resulting in a measured Young's modulus of 1.0GPa (Pinsky and Datye 1991), which is comparable to that of nylon, for instance. Along the major axis the fibrils exhibit a periodicity of 65nm (Meek et al. 1981). It is thought that fibrils in the cornea have an increased hydration over those of the sclera, based on comparisons of the Bragg spacing calculated from X-ray diffraction patterns (Meek et al. 1991). The reason for this difference is to reduce the amount

of light scattering within the stroma by reducing the refractive index mismatch between the fibrils and the ground substance, a hydrated gel that fills in the space between the fibrils.

At the sub-fibrillar level, collagen molecules exhibit a triple helical structure, requiring the amino acid proline for helix formation and glycine at every third bond in order to pack the strands together. Collagen molecules also contain two unique amino acid variants, namely hydroxyproline and hydroxylysine, which are important for helix stability and glycosylation respectively (Canty and Kadler 2005).

1.3.3 Lamellae

Collagen fibrils are themselves grouped together to form sheets, known as lamellae, that run parallel to the surface of the cornea. The stroma is made up of around 200 lamellae. The fibrils in one lamella are all orientated in the same direction, but make large angles with the fibrils in adjacent lamellae. Although the lamellae can be found at all different orientations through the thickness of the cornea, the orientation is most certainly not random. It has been conclusively shown that there are preferred orientations within the central portion of the cornea and in the limbus region. In the central area of the cornea, the preferred orientations lie along the nasal-temporal and inferior-superior axes (Meek et al. 1987), while in the limbus the orientations form a ring where the preferred orientation lies perpendicular to the direction of the centre. Wide angle X-ray scatter (WAXS) studies at different area of the cornea show that the preferred directions are not symmetrical in the nasal-temporal axis within an individual cornea, although they do appear to be symmetrical between left and right eyes (Boote et al. 2006), which could have implications in the future use of donor corneas for transplants. It may be necessary for surgeons to take into account the orientation and original side of the donated tissue in order to allow the transplant the best chance of healing in a way that maintains its two primary functions, transparency and resistance to internal and external pressures. Lamellae in humans

are typically 2 microns in depth and up to 0.2mm wide (Polack 1961; Komai and Ushiki 1991). Posterior lamellae run the whole width of the cornea and lie in well defined stacked layers (Aghamohammadzadeh et al. 2004). At the anterior edge, there is more interweaving between layers (Muller et al. 1995), possibly so that many lamellae can anchor to Bowman's layer for stability (Meek and Boote 2009).

1.4 Proteoglycans

Proteoglycans (PG) are the other main component of the stroma. They are molecules secreted by keratocytes that bind to the collagen fibrils within the stromal matrix. They are widely regarded as being essential to the maintenance of the lattice and thus are essential for the transparency of the cornea as a whole (Hart and Farrell 1969; Benedek 1971; Bettelheim and Plessy 1975).

Proteoglycans consist of a core protein covalently attached to one or more sulphated polysaccharide chains, known as glycosaminoglycans (GAG) (Iozzo 1998). As with collagen, the proteoglycan protein is synthesised in the rough endoplasmic reticulum, and the side chains added within the Golgi apparatus, and then secreted as whole proteoglycans into the extra-cellular matrix (Rada et al. 1993). The negative charges on the GAG chains cause osmotic imbalances that allow the cornea to maintain hydration in a passive way (Elliott 1980). To prevent the possibility of overhydration causing swelling this process is countered by the endothelium, which actively transport sodium ions and water out of the stroma to the aqueous humour (Hodson and Miller 1976).

Proteoglycans have been implicated in the mechanism by which the fibrils achieve a uniform spacing. The proteoglycans present in the stroma, decorin (Li et al. 1992), lumican (Blochberger et al. 1992), keratocan (Corpuz et al. 1996) and mimecan (Funderburgh et al. 1997) attach to the fibril's surface. Fibril spacing collapses when the proteoglycans are

removed (Meek and Holmes 1983) and mouse corneas engineered with a lumican deficiency show evidence of fibril fusion (Chakravarti et al. 1998). In addition the core proteins of both lumican and decorin have been shown to inhibit fibril formation and reduce fibril diameter in vitro (Rada et al. 1993), and the same proteoglycans interact with and stabilise the fibril network once formed (Neame et al. 2000). These effects have been demonstrated using mice with nullified versions of the genes encoding for lumican, decorin and type V collagen (Figure 1.4) (Hassell and Birk 2010).

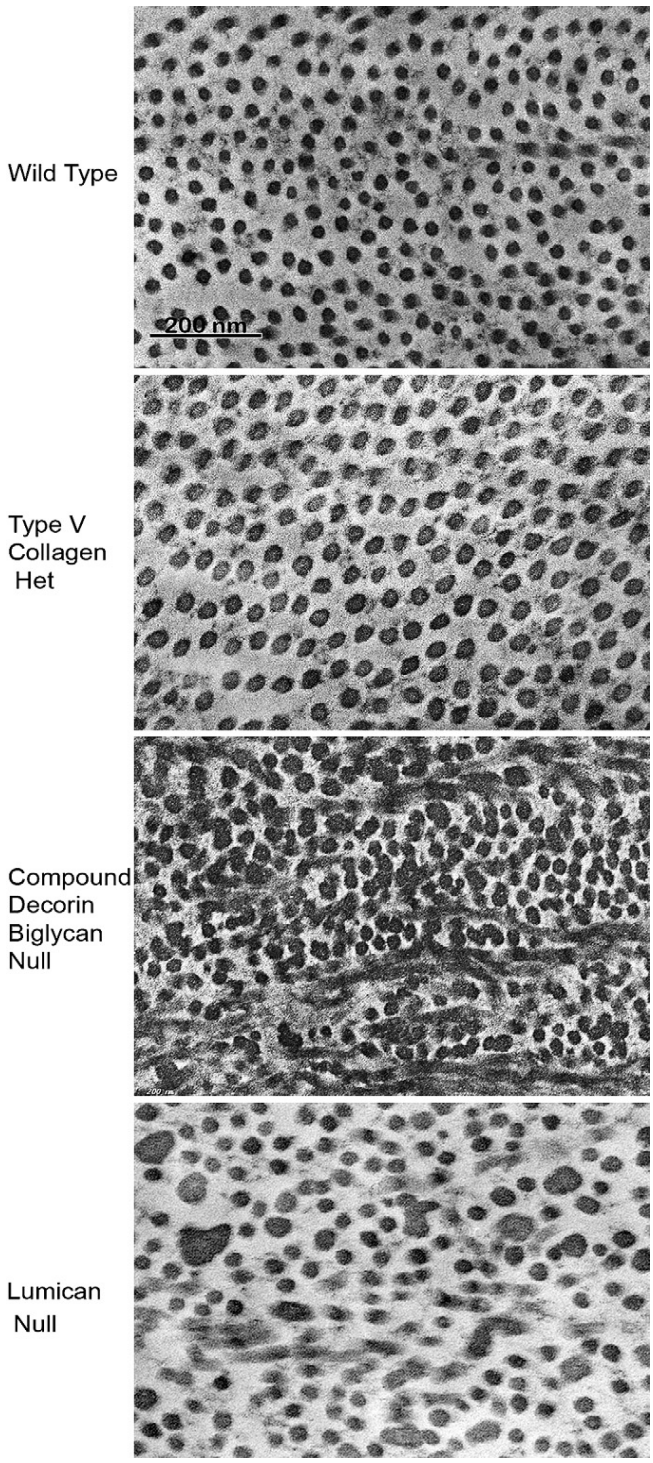

Figure 1.4: Electron micrographs of mouse corneas, with various nullified genes (Hassell and Birk 2010).

The most important structural feature of the corneal proteoglycans that allows for their interaction with collagen fibrils is located within the polypeptide chain, which contains several leucine-rich areas. When these areas coil into a tight spiral, there is one for every 360^{o} of arc, in a regular repeating pattern. Thus all of these leucine-rich areas align along one side of the spiral, and it is this section that interacts with the fibrils. The presence of leucine-rich areas is the defining feature that dictates which of the large and varied proteoglycans are present within the corneal stroma (Dunlevy et al. 1998).

Genetic disorders affecting proteoglycan synthesis have proven that they are absolutely necessary for the transparency of the cornea. Mutations in the gene KERA that codes for the core protein of keratocan is a known cause of the disorder cornea plana, where the curvature of the cornea is severely decreased leading to a loss of visual acuity (Pellegata et al. 2000). A mutation in the CHST6 gene is known to cause congenital problems affecting the production of the carbohydrate sulfotransferase enzyme, which is responsible for adding the GAG side chains to the core protein (Akama et al. 2000; Liu et al. 2000). Without the GAGs, proteoglycans are unable to bind to water and keep the stroma sufficiently hydrated. This leads to a condition known as macular corneal dystrophy (Hassell et al. 1980; Midura et al. 1990; Hayashida et al. 2006; Musselmann and Hassell 2006), a congenital degenerative pathology of the cornea which manifests as opaque spots across the cornea, usually first seen in adolescence, that grow progressively larger until the cornea become fully opaque. A further mutation of the gene encoding for decorin is thought to be responsible for congenital stromal corneal dystrophy, where the cornea become completely opaque shortly after birth (Bredrup et al. 2005; Rodahl et al. 2006). This may suggest that decorin is not involved during the initial development of the cornea in utero, but then is manufactured during the normal life span in order to maintain the transparency of the cornea.

Perhaps the most extensively studied of the GAGs present in the stroma is keratan sulphate, which binds to the collagen fibrils at specific sites (Scott and Haigh 1985). Keratan sulphate deficiency is a known symptom of macular corneal dystrophy (Hassell et al. 1980; Nakazawa et al. 1984; Midura et al. 1990), due to the failure to synthesise the carbohydrate sulfotransferase as already mentioned. The disease can be characterised into three immunophenotypes, type I, type Ia and type II, although this information is irrelevant from a clinical perspective, as all three types manifest in an identical fashion (Klintworth 2009). Immunophenotyping is carried out by testing for a reaction of both corneal tissue and serum in

the presence of the antibody 5D4 (Caterson et al. 1983). Type I patients exhibit no reaction from either tissue or serum (Klintworth et al. 1986; Thonar et al. 1986), type II patients show a reaction to both tissue and serum (Edward et al. 1988; Yang et al. 1988) and type Ia display a reaction in the tissue only (Klintworth et al. 1997). Keratan sulphate forms part of three of the four proteoglycans present in the stroma, lumican, keratocan and mimecan. These proteoglycans are notable for being shorter in length than most others, and are of a similar size to the normal fibril spacing of around 30nm. Corneas affected by macular corneal dystrophy lack these molecules which may cause the interfibrillar spacing to be reduced. This would be consistent with the results of X-ray diffraction studies of affected corneas (Meek et al. 1989; Quantock et al. 1990), which measured the average spacing through the entire thickness of the cornea. There has also been some suggestion that although the spacing is reduced across all areas, the effect is more pronounced in the deeper, more posterior lamellae (Palka et al. 2010). This is a possible indication that proteoglycans containing keratan sulphate are more prevalent in the more posterior areas of the stroma, or that their affect is more important to the structure of the collagen matrix. It is possible that keratan sulphate is used as a substitute for other GAG side chains in hypoxic conditions, which would occur more often in the posterior stroma (Scott and Haigh 1988; Scott 1991). This effect has previously been noted in larger animals with thicker corneas, this could be the first evidence of a similar phenomenon in humans.

1.5 Theory of Transparency in the Healthy Cornea

The most important aspect of the cornea is the fact that it is transparent at the visible wavelengths. Without a transparent window, all the other highly specialised parts of the eye are rendered completely useless. The cornea and lens together are the only tissues in the entire body that exhibit this transparency. Despite the obvious necessity, this transparency presented a paradox; it was known that the cornea was made, primarily, from collagen. However,

collagen itself is not inherently transparent, indeed it is present in a wide variety of tissues throughout the human body and yet the cornea is unique among them as having this property. The respective refractive indices of collagen type I and the ground substance of the stroma are measurably different at 1.47 and 1.35 (Meek et al. 2003). Such a difference in refractive index should be catastrophic, calculations by Maurice (1957) using representative values for the refractive index and volume fraction of collagen showed that 94% of the incoming light should be scattered, which would result in an opaque tissue. Maurice however, has an answer to this apparent paradox. If the collagen fibrils were arranged in a perfect hexagonal lattice, with a uniform spacing, and if they were kept sufficiently small in diameter, then the scattering from the different fibrils would destructively interfere completely in every direction but the anterior to posterior axis, the result of which would be a transparent tissue.

The problem with this theory was the assumption that the fibrils in the cornea possessed a long range order, when both electron microscopy and X-ray diffraction showed that not to be the case. The fibrils instead only possessed a short range order extending to approximately 120nm (Sayers et al. 1982; Worthington and Inouye 1985). However, investigations of Goldman and Benedek (1967) modified Maurice's perfect lattice theory to show that only a short range order with a liquid-like fibril arrangement was a requirement for destructive interference. This would also go on to explain the opacity of the cornea at particular wavelengths (Benedek 1971). The final realised condition for transparency was for the scattering element to be no greater than half the wavelength of the incident light.

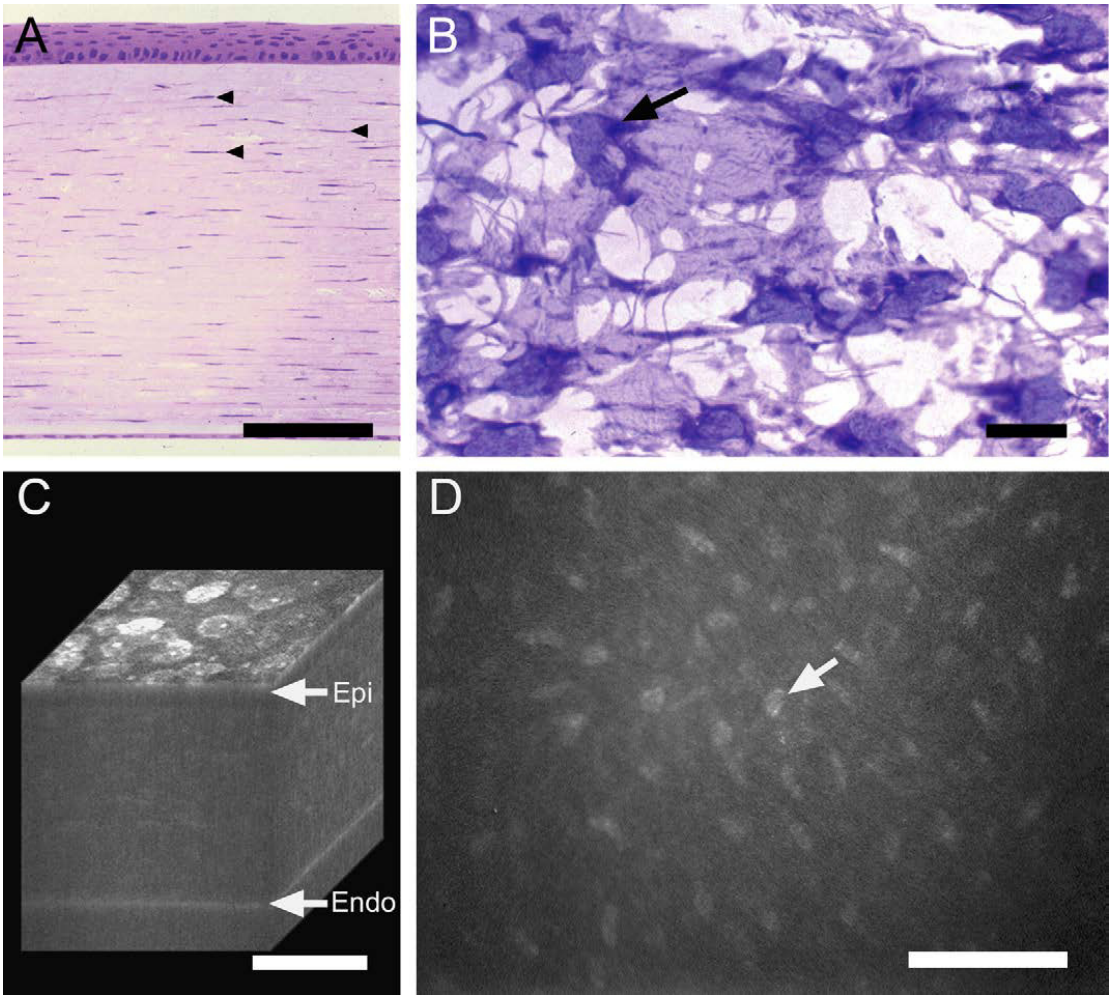

Figure 1.5: Healthy rabbit cornea shown by histology (A&B) and confocal microscopy (C&D). A) Cross section of cornea, arrowheads indicate keratocytes within the stroma. B) Coronal section of cornea stained to show cell bodies and nuclei (arrow). C) Three dimensional reconstruction of corneal tissue showing the largest areas of scattering to be the epithelium (Epi) and endothelium (Endo). D) Section of the stroma used in the reconstruction in C, showing the nuclei of the keratocytes to be the most prominent area of scattering within the stroma. Scale bar = 100 µm (Jester 2008).

The transmission of light in the visible spectrum through the human cornea is of the order of 90% (Boettner and Wolter 1962). Of the 10% that is scattered, in vivo confocal microscopy has shown that the majority occurs in the epithelium and endothelium (Jester 2008). The more interesting result of this work however, has been to show that the small amount of scattering that does occur in the stroma is mainly caused by the nuclei of the keratocytes that populate it, and not from any of the other organelles. Since the keratocyte cells are embedded between the collagen lamellae, and since the thickness of the cell body, at 500-1500nm (Doughty et al. 2001), is much larger than the maximum fibril separation that is required for transparency the

scattering should be at a maximum at the interface between the cells and the surrounding lamellae. This would appear not to be the case, providing further evidence for the crystallin theory of keratocyte transparency.

1.6 Corneal Wound Healing

An important feature of any living tissue is the ability to heal injuries. This is especially true for the cornea, given its status as surface tissue and the unique function it fulfils. The cornea is unique amongst human tissues as a transparent barrier, and therefore ideally any repair mechanism would preserve this property. However, it might be of even greater importance that the cornea remains intact structurally, as any failure to handle the pressures that the cornea has to protect against will result in a complete failure of the eye altogether. For this reason the cornea's healing process seems to prioritise structural considerations over transparency. All but the most superficial of corneal wounds leave opaque scars. Understanding the mechanisms behind this process has become increasingly important in recent years with the development of laser-assisted in-situ keratomileusis (LASIK) and photorefractive keratectomy (PRK), elective techniques designed to correct refractive defects such as myopia and hyperopia using excimer laser ablation of the stroma. These procedures wrongly assume a biologically inert cornea (Roberts 2000), and while the vast majority of patients are treated without any complications there is a possibility that abnormal biological responses could be causing the build-up of scar tissue in some patients. It is therefore of great importance to the future of these techniques that the biological mechanisms behind scar tissue formation are well understood. Additionally, there might also be applications of this knowledge that could contribute to the treatment of corneal diseases that are known to cause scarring in either their pathology or their treatment.

Superficial injuries to the epithelium layer are healed by a combination of mitosis and migration. Epithelial cells are able to migrate at a rate of 60-80μm/h (Matsuda et al. 1985) allowing most shallow wounds to be closed within hours of the original injury.

When the cornea is wounded such that Bowman's layer is penetrated as deep as the stroma the first cellular response is a programmed apoptosis of the keratocytes most proximal to the wound site (Wilson 2000). This is followed by the migration of keratocytes from further afield which activate and then begin to repair and reverse the damage done to the collagen matrix. The precise biochemical method of this activation is as yet unknown but there are several competing models. The first candidate of these was found by culturing keratocytes in vitro and adding extracts from the corneal stroma. This produced an increase in keratocyte proliferation (Musselmann et al. 2003), indicating that the biochemical responsible was located within the ground substance. Five years later insulin-like growth factor-II (IGF-II) was isolated as the critical trigger for the activation of the cells (Musselmann et al. 2008). A further suggestion has been made based on the presence of several growth factors in the tear film, namely platelet-derived growth factor (PDGF), transforming growth factor beta (TGF-β) and fibroblast growth factor-2 (FGF-2). In the event of a wound to the cornea, these molecules penetrate into the stroma and act upon the keratocytes, thereby stimulating them into action (Tuominen et al. 2001; Zhou et al. 2007). A similar suggestion originally from Hong et al (2001) and supported by many others (Brissette-Storkus et al. 2002; Chinnery et al. 2008; Stapleton et al. 2008) is that these same factors are produced by either invading macrophages or the body's own defensive neutrophils and lymphocytes. This invasion of bacteria would be an inevitable result of any wound to the cornea, and in practice would seem to be a novel way for the body to stimulate the keratocytes. The corneal epithelium itself has also been implicated as a possible source of TGF-β and FGF-2 (Stramer et al. 2003), and release the growth factors upon detection of a wound to the surface. The final method of activation suggests that TGF-β acts upon the

keratocytes in a different way. Rather than activating them directly, it causes the cells to produce FGF-2 themselves, which in turn activates a wider radius of cells and thus starting a chain reaction (Kay et al. 1998).

With so many competing models, each with their own compelling evidence it would be extremely surprising if one were to dominate over the others in the future. As with many biochemical processes, the body most probably utilises many different pathways to reach the same end goal, thereby reducing the potential damage caused by a failure to execute one specific pathway. With the only debate seemingly being the source of the stimulating factor, there is certainly the possibility that more than one or even all of them are correct. The competing models are not necessarily mutually exclusive, but testing one while trying to suppress another appears to be a great challenge at the time of writing.

Scarring in the cornea is normally seen in transmission electron microscopy studies as a disorganised arrangement of collagen fibrils, as opposed to the regular and highly ordered lamella structure of healthy transparent tissue, even after healing for many months (Connon and Meek 2004). Studies using X-ray diffraction on scarred rabbit corneas, again allowed to heal for months, showed a general increase in the interfibrillar spacing and fibril diameter (Rawe et al. 1994), which may explain the loss of transparency.

1.7 Pathological Abnormalities of the Cornea

1.7.1 Keratoconus

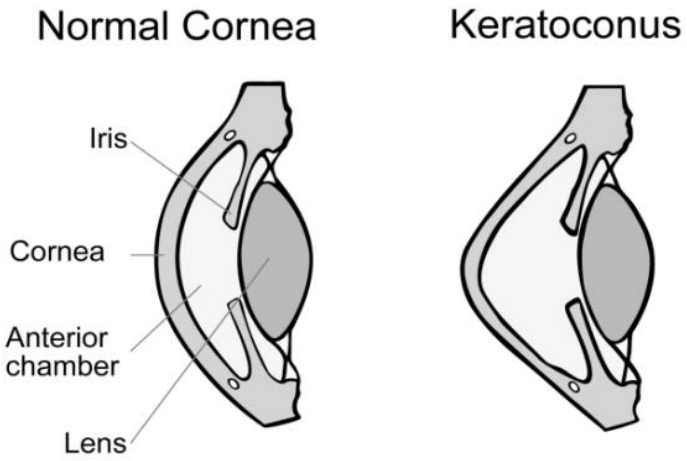

Figure 1.6: Schematic representation of a normal and keratoconic anterior section of a human eye

A normal healthy cornea has a characteristic shape which is important to be able perform its function as the principle refractive element in the eye's optics. The normal cornea has an approximately spherical curvature at the centre and a considerably flatter shape at the limbus region. Keratoconus is a pathological disorder that affects this vital shape (Figure 1.5). The corneal stroma becomes thinner, and weaker, forcing the tissue to respond to internal pressure and bulge into a more conical shape. The change in shape leads to a catastrophic loss of visual acuity, as focussing light sharply onto the retina becomes impossible. The precise underlying cause or causes of the disease is not known, but it generally presents in young adults and is thought to affect approximately 1 in 2000 members of the general population (Rabinowitz 1998). The cause of the thinning is not known absolutely, but it is sometimes attributed to the breakdown of the collagen matrix in the stroma (Critchfield et al. 1988), which has led to a large amount of research into the possible expression of collagenase enzymes as a possible cause. This expression has not been demonstrated, but it could be that only minute levels are needed to cause keratoconus, owing to the slow progression of the disease (Alexander and Werb 1989).

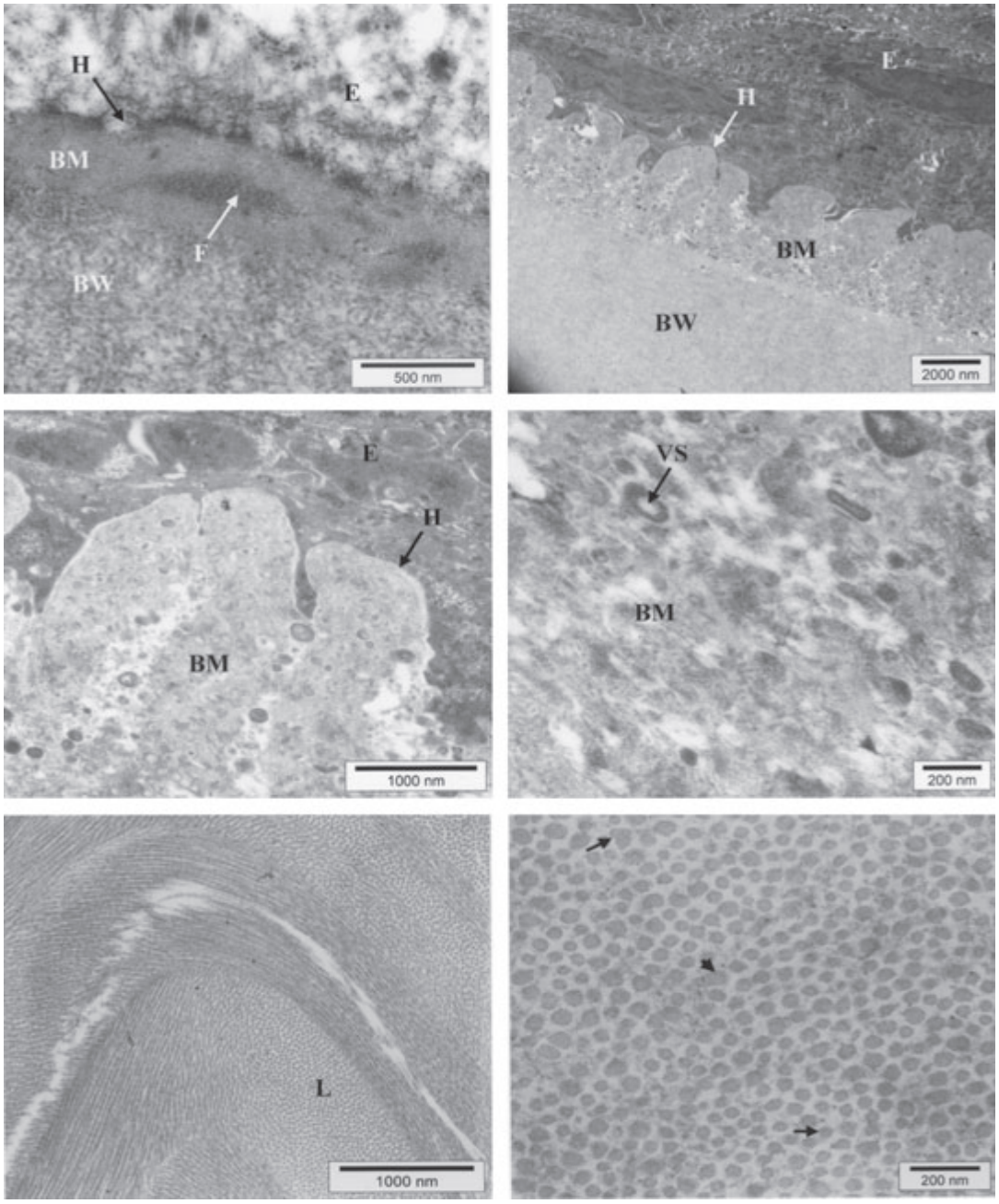

Figure 1.7: Electron micrographs of keratoconus corneal tissue. (a) Degenerate epithelium (E), degenerate hemidesmosomes (H), thickened basement membrane (BM) containing filaments and normal Bowman's layer (BW). (b, c) Thickened BM invaginates the overlying epithelial (E) plasmalemma and hemidesmosomes (H). Normal BW lies below the BM. (d) The BM contains small vesicles (VS). (e) Organization of very steep pointed lamellae (L) in the posterior stroma. (f) Collagen fibrils of small (arrow) and large (arrowhead) diameter in the stroma (Akhtar et al. 2008).

A rival attempt to explain the effects of keratoconus that has been proposed is that it is caused by a shift in the lamellae within the matrix. This shifting would cause the lamellae to slide over each other and away from the centre of the cornea, leading to localised thinning and hence a

change in topology (Meek et al. 2005; Dawson et al. 2008). Overzealous eye rubbing has also been proposed as a possible cause of thinning (Krachmer 2004), although this might be a case of different causes producing the same effect and hence similar symptoms.

X-ray scattering techniques have been utilised to show that the normal arrangement of the lamellae is disrupted in keratoconus (Daxer and Fratzl 1997; Meek et al. 2005). The precise extent of the change in structure varies between cases, but what is known to be true in the majority, from results of electron microscopy scans (Radner et al. 1998b), is that there is a lack of significant interweaving of the lamellae in the apical regions. Other typical characteristics of keratoconic tissue seen in electron microscopy studies include breaks in Bowman's layer and the epithelial basement membrane (Sawaguchi et al. 1998), abnormally thin lamellae and abnormal keratocytes (Nirankari et al. 1983; Unal et al. 2007). These changes weaken the anchoring that is necessary to counter the increased stress on the lamellae at the apical areas (Meek et al. 2005). This weakness could potentially be caused by an increased activity of protease enzymes, which would allow the lamellae to slip past each other when stressed.

Treatments for keratoconus normally include customised hard contact lenses that are designed to reshape the cornea into its correct shape. The drawback with this treatment method is that it often leads to injuries to the cornea, as the lenses must be worn for long periods of time and hard lenses tend to be more abrasive. If the cornea becomes too scarred to remain transparent, then often the only course of action to prevent blindness is a penetrating keratoplasty (PK). PK surgery has a very high rate of success, 98.9% after 46 months (Lim et al. 2000), however there have been a number of reports in the literature of failures owing to the recurrence of the keratoconus symptoms within the previously healthy grafted tissue (Abelson et al. 1980; Nirankari et al. 1983; Thalasselis and Etchepareborda 2002; Patel et al. 2005; Unal et al. 2007). The reasons for this are not well understood and suggestions have ranged from genetic predispositions (Stoiber et al. 2000) to eye rubbing as a result of irritation (Koenig 2008;

Yeniad et al. 2009). If abnormal characteristics can be found within a graft that had never been diagnosed as a failure, then it would be possible to link the failures of other grafted tissue to the abnormalities found. Any changes would likely be extremely subtle, since even in the small cases where recurrent keratoconus has been suspected the symptoms had not manifested until years after the initial PK treatment.

1.7.2 Macular Corneal Dystrophy

Figure 1.8: Clinical photograph of an eye afflicted with macular corneal dystrophy. The disease first presents as small cloudy patches that can be seen in the image, over time these patches grow until the whole cornea is opaque.

Macular corneal dystrophy (MCD) is a progressive congenital disorder that presents as small cloudy patches in the cornea, usually in early adolescence, but it has been known to present as late as a patient's fifties, and as early as infancy (Figure 1.7). These cloudy patches become gradually larger until they cover the whole cornea in the most severe cases. MCD is a genetic disorder caused by a mutation in the CHST6 gene that prevents the synthesis of keratan sulphate. The mutation does not have to be specific, with more than 125 different mutations having been identified in patients with MCD (Klintworth et al. 2006; Weiss et al. 2008). MCD can be characterised into three different types based on the amount of keratan sulphate present in the corneal ground substance, although this distinction has no clinical relevance. Any

connection of specific mutations in CHST6 to the MCD phenotype has yet to be shown, with identical mutations being known to cause all three types of MCD (Bao et al. 2001; Sultana et al. 2009). A simple correlation therefore seems unlikely. As is common with congenital conditions, the proportion of those affected varies according to the geographical location of the population, with India, Saudi Arabia and Iceland among the countries with the greatest prevalence, although MCD is found throughout the world. The condition is so common in Iceland, that only 25 years ago it was the most common reason for penetrating keratoplasty transplants (Jonasson et al. 1989). MCD is primarily a disorder of the stroma, but it is known to affect other layers of the cornea and to produce abnormal keratocytes. The stromal cells exhibit vacuoles (Klintworth 2009), inside of which can be found granular material which may be either incomplete fibrils or possibly proteoglycans that have not been secreted into the ground substance. Stromal thinning is seen in MCD, although not to the same extent as in keratoconus. This could be due to the closer packing of fibrils that is observed in electron micrographs (Quantock et al. 1990). Descemet's membrane appears heavily granulated with large vacuoles, mainly at the posterior edge.

1.8 Background to Electron Microscopy

When first introduced, light microscopy proved to be a revelation for the biological sciences. The microscopic world was opened to researchers for the first time, allowing them to probe the workings of complex systems. Light microscopy, while simple and convenient, has an unavoidable limitation that lies in its physical properties. Any wave can only provide spatial information about objects it encounters that are up to half the size of its wavelength. In the case of visible light, this gives a minimum resolvable size of around 200-300nm. While this size is acceptable for studying whole cells and even some cell processes, it is disastrously large when

attempting the study the collagen matrix of the stroma, where important features are one or two orders of magnitude smaller than that.

The obvious answer to the problem would be to simply use light of a lower wavelength, but this runs into problems. Electromagnetic radiation from the ultra-violet, x-ray and gamma ray wavelengths are difficult to manipulate, as they do not easily refract or reflect. Additionally, as the eye is not sensitive to these wavelengths some form of detector, such as a charged-coupled device array, would be necessary and would counteract the gain in resolution achieved from the lower wavelength. At the time of writing, x-ray microscopy techniques, which attempt to exploit the lower wavelength of x-ray radiation, are still in their infancy but have had some success imaging structures (Yamamoto and Shinohara 2002; McDermott et al. 2009; Larabell and Nugent 2010; Chien et al. 2013).

A more robust attempt at a solution can be found by exploiting the nature of matter, in particular the wave-particle duality of electrons. Unlike the case for electromagnetic radiation, the wavelength of a quantum particle (λ) is proportional to the inverse of its momentum (p), according to the de Broglie relation

$$\lambda = h/p \tag{1.1}$$

where h is Planck's constant. By increasing the energy of electrons that propagate within a beam, and hence increasing their momentum, the wavelength can be adjusted accordingly. In this case, the diffraction limit can be decreased as far as is necessary. In practice, the potential for damage to the specimen and the exponential rise in costs of the increase in energy provides limits to the resolving power of an electron microscope. Theoretical limits on resolving power can be calculated using the knowledge that the minimum resolvable distance of the eye is around 250µm. Given the minimum resolvable limit of visible light is around 250nm this gives a theoretical magnification limit of around x1000. In practice even the best light microscopes

fall short of this limit by around one order of magnitude. Electron microscopes are theoretically capable of magnifying object by a factor of a million times, although again practicalities limit the magnifying power of most working electron microscopes to a factor of about 250,000.

Contrast in optical images is usually achieved by the absorption of light by the specimen. Greater absorption produces darker areas that correspond to structures. Interference effects can also be used in phase contrast imaging, which is discussed in more detail in chapter 3. Light scattering within optical systems do not normally contribute to the formation of an image. In electron microscopy however, scattering is the main physical principle involved in the formation of an image. When electrons pass through a specimen, they can scatter in one of two ways; either the electron scatters from the electron cloud within an atom of the specimen, or it scatters from the nucleus of the atom. The probability of an interaction that scatters a particle through some solid angle is known as the scattering cross section. Within samples of the order of a 100nm thickness, the majority of the electrons passing through the sample are unaffected, given the small scale of the nucleus and electron orbitals when compared with the atom as a whole. Scattering events from the nucleus are known as elastic scattering. The difference in size and charge between the incident electron and the nucleus being so great that the interaction happens with no loss of energy to the particle. Elastic scattering for this reason also often occurs through large angles, with the electrons reversing direction counter to the path of the beam. This is known as backscattering, or backscatter. Scattering events from collisions of electrons within the atoms of the specimen are referred to as inelastic scattering. The total energy of the system of exiting particles is conserved as required by the first law of thermodynamics of course; the term inelastic refers specifically to the scattered electrons, which lose some of their momentum as X-rays that are sometimes referred to as bremsstrahlung, or “breaking radiation”. The absorption of electron radiation is possible in the event that a single electron undergoes several inelastic collisions during one path through the specimen. However, since several of

these events are required and each is less likely than an unscattered path, either extremely intense beams of electrons or very thick samples would be required in order to utilise absorption information to form an image. Neither of these options is ideal for biological tissue, as too much absorption will lead to degradation of the sample as it warms. It is thus the scattered electrons that allow an ultrathin sample to survive for long enough in lower intensity beams and still form a focussed image. Inelastic scattering events spread electrons from below the sample, these can then be focussed using magnetic lenses to form an image.

The main disadvantage to electron microscopy studies stems from the requirement for the electron beam to travel in a vacuum. Optical imaging is free from this requirement, as visible light travels through air with the minimum of impediment. Electrons however would not pass through air so freely, and the beam would attenuate quickly. This added absorption and scattering would interfere with that from the sample, and an image of the sample would become impossible to produce. Clearly, this requirement means there must be a process of preparation for the imaging of biological tissues, since cellular processes would soon cease in a vacuous environment. Structures could also completely lose hydration, which is vital for a representative imaging of the stroma.

As inelastic scattering events originate from the collision of electrons then it logically follows that chances increase in atoms that contain more electrons. Sadly biological tissue contains light elements, hydrogen, carbon, oxygen and nitrogen, almost exclusively. It is for this reason that during the preparation of biological samples steps are taken to dope the tissue with heavy metals. Standard methods in the preparation of corneal samples usually involve the addition of stains containing osmium, tungsten and uranium (Scott 1985).

1.9 Background to X-ray Diffraction

X-rays are a form of electromagnetic radiation that is generated from the rapid acceleration or deceleration of electrons. They form a section of the shortest wavelength radiation of the electromagnetic spectrum between ultraviolet light and gamma radiation, although there is some overlap between the wavelengths of the shortest wavelength generated X-rays and the largest wavelength gamma rays. X-rays cover a wavelength range of between 100fm to 10nm, although the majority of X-radiation falls in the range of between 0.01 and 10nm. When a wave passes through a slit of a similar width to its wavelength, the wave will undergo diffraction. This effect is often represented by waves bending and spreading beyond the original path. However, when instead a single slit is replaced by multiple slit, in the case of a diffraction grating for example, a different pattern will be produced. As light beams are made up of many photons, which all exhibit a diffraction effect, there exists a resulting interference between these photons which causes areas of constructive and destructive interference when projected onto a detector. In one dimension they form a series of bright and dark fringes in a direction perpendicular to the direction of the opening, with the size of the spaces between the fringes being related to both the wavelength of the light and the width of the slits. This classic phenomenon is known as a diffraction pattern, with the bright fringes usually referred to as reflections. Using the size and directional information of the diffraction pattern, it is possible not only to determine the width of the slits that formed it, but also the orientation of the slits as well, by making use of the Bragg equation which relates the wavelength (λ) and scattering angle (θ) to the width of the slit (d) and the diffraction order (N).

$$N\lambda = 2d \sin\theta \tag{1.2}$$

In the case that the hole through which the light is passing is of the order of the wavelength in both the x and y direction, the diffraction yields a classic pattern of concentric circles, which

can alternatively be thought of as the one dimensional pattern extended to all directions. This pattern could also be formed from an infinite series of one dimensional gaps of random orientation.

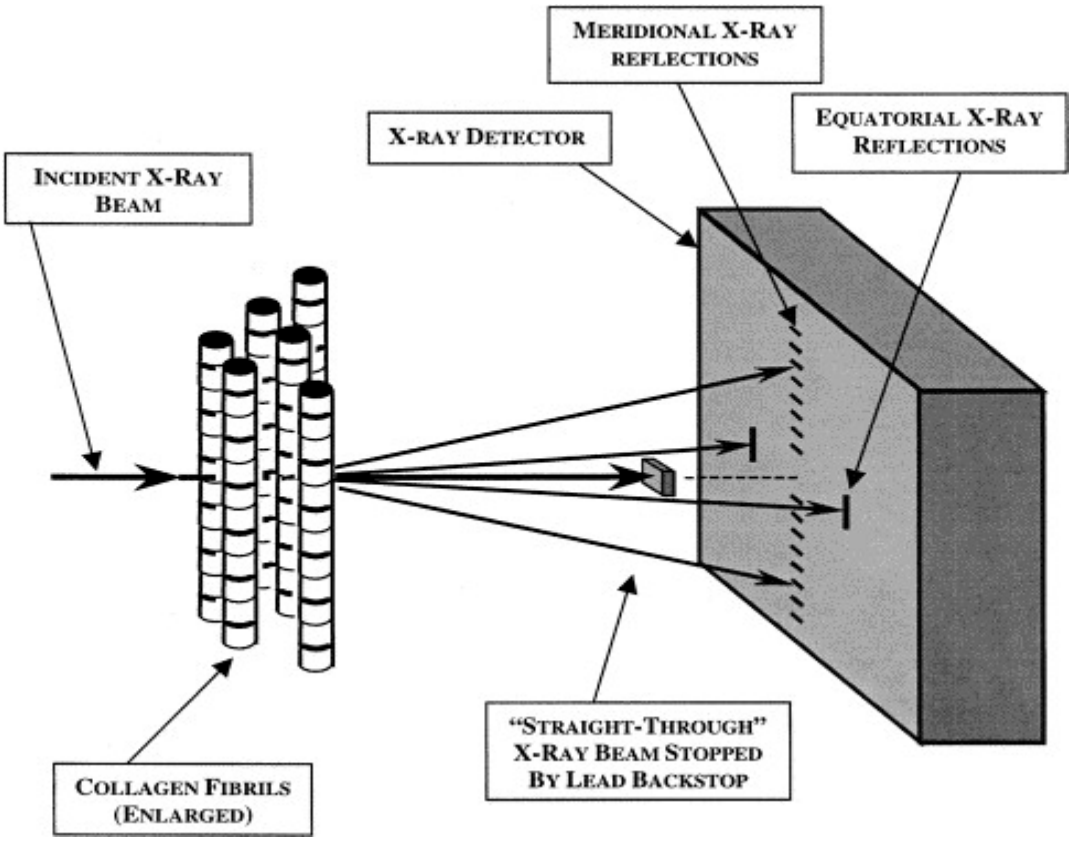

Figure 1.9: Schematic diagram showing how the orientation of collagen fibrils causes two distinct diffraction patterns at orthogonal angles (Meek and Quantock 2001).

When an x-ray beam is passed through a cornea from the anterior to posterior, diffraction events will occur from the space between the collagen molecules that make up the fibril, as well as according to the orientation of the collagen fibrils that the x-ray is passing between and the D-period of the collagen molecules. The diffraction pattern formed from the collagen molecule spacing produces a wider diffraction pattern according to the Bragg relation (Eq 1.2), as the space between the collagen molecules is smaller than the interfibrillar spacing. These two patterns are referred to as wide angle x-ray scattering (WAXS) and small angle x-ray scattering (SAXS). WAXS patterns from perfectly ordered and unidirectional collagen fibrils would produce a pattern with one order each side of the central point, known as the equatorial

reflections, located in a perpendicular direction to that of the fibrils. When the WAXS pattern from the cornea as a whole is measured the x-rays will diffract in all directions, as the fibrils run in all directions through the cornea. However, if any direction for the fibril is preferred, the intensity of the wide angle pattern at an angle perpendicular to this preferred direction will be increased. By analysing the symmetry of the wide angle pattern, it is possible to infer which, if any, direction is preferred and the degree to which that preference dominates. This method has long been used to determine the internal structure of inanimate crystals. The work of WL and WH Bragg, for which they shared the 1915 Nobel Prize in Physics, provides a full account (see for example: Bragg and Bragg 1913; Bragg 1913). The high degree of order of a crystal lattice provided accurate and easily interpreted diffraction patterns. It was realised that the emerging science of x-ray diffraction could also be used to investigate the ultrastructure of biological tissues. The cornea, with its collagen fibril structure, was a perfect fit for this technique, but early attempts to produce a useable diffraction pattern failed. The cornea scattered x-rays very weakly, and the technology of the time could not produce high enough intensity beams. The first successful small angle diffraction patterns were produced in 1978 (Goodfellow et al. 1978), and with the rise in the power and availability of synchrotrons, which produce high energy beams of bremsstrahlung radiation by accelerating electrons around a large ring, producing higher quality diffraction patterns became much easier. The first such synchrotron studies were conducted by Meek (1981), and showed that the more diffuse diffraction patterns could not be produced by the perfect lattice proposed by Maurice (1957).

With the increase in the power of synchrotrons, the exponential rise in the power of computers to control them and the invention of charged-coupled device (CCD) detectors, the time required to produce individual x-ray diffraction patterns has decreased down to fractions of seconds. With this decrease of time, the potential to produce diffraction patterns at many different places in the cornea has become more feasible. Previously, the hours required to produce a full grid

of patterns led to the sample succumbing to the effects of dehydration, even with the preventative effects of polyethylene film. The idea that the collagen in the cornea might exhibit preferred directions for strength was for a long time controversial, but the observations of Meek et al (1983) of a diffraction pattern with four maxima at 90º intervals appeared to settle the argument. When the observation was investigated again with a sample of known orientation, it was found that the central cornea exhibits a preference in both the nasal-temporal and superior-inferior axes (Meek et al. 1987). It was also noted that the outer limbal region showed a preference in only one axis. More quantitative investigations yielded results showing that in the central cornea 66% of the collagen lamellae are orientated within 22.5º of the preferred directions (Daxer and Fratzl 1997) and that the proportions are roughly equal between the two directions (Boote et al. 2005). At the limbus, investigations showed the percentage of aligned collagen rose to around 75%, and confirmed that the preferred directions of the collagen of the limbus forms an obvious ring (Newton and Meek 1998a). This leads to the question of how exactly collagen that runs in cardinal directions can join with a ring in the outer sections. Results from a further WAXS study (Newton and Meek 1998b) were combined with results from scanning electron micrographs of the limbus (Radner et al. 1998a) led to a proposed model where lamellae separate in the limbal region and join with other lamellae to form the annulus (Newton and Meek 1998b). Later proposals postulated the formation of the annulus as a product of lamellae from the scleral regions (Meek and Boote 2004), which was consistent with the observation of an increase in the number of lamellae in the limbal regions of the cornea (Hamada et al. 1972). The attention of investigation then turned to the idea of mapping the cornea. By using microfocused beams of x-ray radiation whole maps of corneal collagen could be produced (Boote et al. 2003; Aghamohammadzadeh et al. 2004; Boote et al. 2004; Boote et al. 2006; Hayes et al. 2007; Pijanka et al. 2012; Boote et al. 2013; Pijanka et al. 2013). One potential drawback of this method arises from the curved surface of the cornea. X-ray scattering

from a surface that is not normal to the path of the beam could lead to an overestimate in the amount of scattering. Effect of dehydration over time would make the cumbersome act of shifting the position for every scan undesirable. However, this limitation is not thought to greatly affect the results, with even the very steepest areas of keratoconic cones leading to an overestimate in the region of 6% (Meek et al. 2005).

These maps not only confirmed the existence of the orthogonal preferred fibril directions in the central cornea and the annulus in the periphery, but also showed the strength of alignment in the annulus was several times stronger than in the centre. Meek and Boote (2009) mapped fibril orientation across the cornea at high resolution, and noticed an incremental shift in the angle of orientation as the position moved from the centre to the periphery. These data were interpreted as showing the true nature of the transition between central and peripheral collagen lamella was a combination of previously described models. By integrating graphs of both the aligned and total scatter as a function of angle, plots for both the total and aligned collagen at any point across the cornea could be produced. When compared, these plots showed the total collagen increased from the centre outwards, in accordance with the greater peripheral thickness, but the aligned collagen did not. Plots of aligned collagen formed maps showing a clear rhombic pattern around the central area leading to the authors to propose that the integration of the lamellae may not be symmetrical in the superior-inferior plane, with the limbal collagen penetrating more deeply in the superior-nasal and inferior-temporal sectors. This effect also appears to be bilateral between left and right eyes. This might have large implications for corneal transplants, it may be necessary not only to attempt to preserve the orientation of the donor tissue but also to make sure the lateral information is preserved from donor tissue to recipient (Boote et al. 2006).

So far we have been assuming that the collagen molecules within the fibril run parallel to the fibril direction only. This is not always the case, and provides a further complication to the

interpretation of x-ray diffraction patterns. The contribution to the WAXS pattern from collagen molecules that are situated at some angle to the direction of the fibril will lead to a greater smearing out of the most intense regions of the pattern. This would lead to an underestimate of the extent of dominance of the preferred fibril orientation. This issue is not trivial to solve. Attempts have been made to experimentally derive a distribution function (Aspden and Hukins 1979; Kirby et al. 1988) by deconvolving the measured WAXS intensity distribution from the distribution from a perfectly ordered fibril system (Woodhead-Galloway et al. 1978). However some care must be taken with this approach. One might assume that the angle of the collagen molecules within a fibril to be a property of the material, but instead it appears that value might vary between different tissues, with a value of around 15º estimated in fibrils of the cornea (Marchini et al. 1986) but a value of around 4º within rat tail tendon (Fraser et al. 1983), which is composed of the same heterotypic fibrils. The direction of the stress on that collagen could be the underlying reason for this difference. Tendon tissue's primary role is to resist extension in one particular direction only, whereas the cornea and sclera must combat the force applied by the extra ocular muscles in all directions. This could lead to differences in the alignment of the collagen molecules. This discrepancy might also be the origin of the difference in the measured D-period of collagen taken from the two tissues (Meek et al. 1981; Orgel et al. 2000). Meek and Boote (2009) devised a different method of empirically determining a correction for the molecular angle, by combining results from both WAXS and SAXS patterns obtained simultaneously. Lower order SAXS reflections are obscured during wide angle data collection by a lead beam stop, designed to prevent the high intensity undeflected x-ray beam from damaging the CCD collector. However, at sufficiently high intensities, higher order reflections become visible from patterns obtained from the limbal region of the cornea. This area is specifically chosen since the high degree of preferred orientation produces a pattern that has a minimal smearing effect. Thus the meridional

reflections of the SAXS pattern do not spread as far laterally and can be resolved. This smearing effect is present in both the WAXS and SAXS data, but crucially within the SAXS dataset it is dependent only on the degree of alignment of the fibrils, whereas the WAXS dataset smearing is dependent on both the degree of alignment of the fibrils and the degree of alignment of the collagen molecule within the fibrils. By comparing the full-width half maximum of the two datasets, they found that the spread of WAXS patterns was 2.5 times that of SAXS, and used this result to produce a more accurate correction protocol.

1.10 Aims and Objectives

The aims of the experiments contained within the following chapters of this thesis are:

- To calculate values for the refractive index of live in-vitro cultured keratocytes, both activated and quiescent.
- To use the calculated values to determine what effect, if any, the scattering from stromal cells should have and to compare these theoretical values with what is observed in healthy tissue.
- To use the comparison between RI values of active and quiescent keratocytes to comment on the theory of corneal crystallins proposed by Jester et al (1999; 2008)
- To investigate the properties of tissue samples obtained from a donor originally diagnosed with keratoconus, who underwent a penetrating keratoplasty procedure some years before death. Including:
    - WAXS studies to determine fibril orientations across the original and grafted tissue, with the scarred and opaque regions being of special interest.
    - TEM studies to both qualitatively and quantitatively determine fibril spacings within the various sites of the tissue.
- To investigate the possibility that keratoconus can recur within grafted tissue not subject to the original diagnosis.
- To determine from TEM studies, whether opacity attributed to scarring can be explained by a change in the arrangement of the collagen matrix.
- To produce three-dimensional reconstructions of tissue diagnosed with MCD, and to attempt to deduce from those reconstructions what effect the lack of sulphated keratan PGs has on the collagen matrix as a whole, and whether these changes are sufficient by themselves to affect transparency.

- To produce three-dimensional reconstructions of previously observed PG filled voids that are known to populate MCD tissue.

2 Corneal Stromal Cell Refractive Index

2.1 Introduction

2.1.1 Refractive Index

The refractive index (n) of a material is defined as the ratio of the speed of light in a vacuum (c) to the speed of light through the material (v_m).

$$n = \frac{c}{v_m} \tag{2.1}$$

As a simple ratio of two velocities, the refractive index is a dimensionless quantity. Some examples of the refractive index of different materials are given in table 2.1.

Table 2.1: Representative refractive indices of common materials

Air	1.0003
Water	1.33
Ethanol	1.36
Glycerol	1.47
Benzene	1.50
Crown Glass	1.53
Diamond	2.42

In humans, the refractive index of the cornea as a whole ranges from 1.380±0.005 in the most anterior section of the stroma to 1.373±0.001 in the posterior layers (Patel et al. 1995), with a mean value of 1.375 (Maurice 1957; Sivak 1988).

Refractive index can also be defined in terms of the magnitude of the phase shift caused by the reduction of the velocity of light in the medium. The phase shift of a wave is defined as the difference in radians of the phase of the wave that has travelled through a medium of interest compared to a wave of the same frequency that has propagated in the background medium. The refractive index (n) of an object of thickness (τ) causes a phase shift $(\Delta\phi)$ of light, moving through the object from a vacuum, of a given wavelength (λ) according to the relation

$$\Delta\phi = kn\tau \tag{2.2}$$

Where $k = 2\pi/\lambda$ and assuming negligible refraction at the interface due to an angle of incidence close to 90º. When light is moving from one medium of refractive index n_1 to another of refractive index n_2 this relation becomes

$$\Delta\phi = k\tau(n_2 - n_1) \tag{2.3}$$

With the same assumption as for Eq 2.2. Refractive index therefore can be measured once the thickness of an object and the phase shift of the incident light of a known wavelength are experimentally verified. This method has previously been used in the literature to determine the refractive index of airway smooth muscle cells (Curl et al. 2005). The intent of this chapter is to apply this previously published method to the question of the refractive index of corneal stromal cells.

2.1.2 The Transport of Intensity Equation

To measure the phase shift of the light passing through the cells in vitro it is necessary to have some way of relating the intensity of the light in different planes to the phase shift of the light. With this in mind we will here derive such a formula, known as the transport of intensity equation (TIE).

Following the argument of Paganin and Nugent (1998), we start with Poynting's theorem, which relates the Poynting vector (S), which represents the direction of the energy flux, to the energy density (W):

$$\nabla . S(\vec{r}, t) + \frac{\partial}{\partial t} W(\vec{r}, t) = 0 \tag{2.4}$$

Where $\vec{r}$ is the vector representing the position within a two-dimensional plane, and t is the time dimension. We can define $S(\vec{r}, t)$ in terms of a coherent scalar electromagnetic field ($U(\vec{r}, t)$) (Green and Wolf 1953):

$$S(\vec{r}, t) = -\frac{1}{8\pi}\left(\nabla U(\vec{r}, t)\frac{\partial}{\partial t}U^*(\vec{r}, t) + \nabla U^*(\vec{r}, t)\frac{\partial}{\partial t}U(\vec{r}, t)\right) \tag{2.5}$$

Where the scalar field can be defined as:

$$U(\vec{r}, t) = \sqrt{I_{coh}} exp[i(\phi(\vec{r}) - \omega t)] \tag{2.6}$$

Where I_{coh} is the irradiance, $\phi(\vec{r})$ is the phase of the coherent field, ω is the angular frequency and $i = \sqrt{-1}$. Asterisks in Eq 2.5 denote the complex conjugate, where the function is the same except all i terms are replaced with $-i$. If we impose the condition on Eq 2.4 that the field is strictly monochromatic, then the energy density becomes time invariant. Therefore we can rewrite Eq 2.4 in terms of the coherent Poynting vector:

$$\nabla . S_{coh}(\vec{r}) = 0 \tag{2.7}$$

If we substitute Eq 2.6 into Eq 2.5 (see Appendix A) we can obtain an expression for the coherent Poynting vector:

$$S_{coh}(\vec{r}) = \frac{\omega}{4\pi} I_{coh} \nabla\phi(\vec{r}) \tag{2.8}$$

So then Eq 2.7 can be rewritten as:

$$\nabla.[I_{coh} \nabla\phi(\vec{r})] = 0 \tag{2.9}$$

Which is the coherent form of transport of intensity equation (Green and Wolf 1953; Teague 1983). However, if we wish to use calculate phase images from bright field images, this condition must be generalised to partially coherent fields. Again following the argument of Paganin and Nugent (1998), for a partially coherent field the Poynting vector is averaged, as it varies over time. An analogous relationship between the mean Poynting vector $\left(S_{av}(\vec{r})\right)$ and the mean irradiance (I_{av}) to Eq 2.8 can be shown such that

$$S_{av}(\vec{r}) = \frac{\bar{\omega}}{4\pi} I_{av} \nabla\phi(\vec{r}) \tag{2.10}$$

where $\bar{\omega}$ is the mean angular frequency. It is now possible to make a paraxial approximation for Poynting's theorem (Eq 2.4). The paraxial approximation is made on the basis that for bright field images the direction of propagation of light will not deviate appreciably from the z-axis, where the plane of the image is the xy-plane. The errors associated with this small angle approximation $(\sin\theta \approx \theta)$ remain below 1% so long as the incident light is less than 14° from the vertical axis. The incident angle would be expected to be much less than this so long as Köhler illumination conditions are met. By substituting Eq 2.10 into Poynting's theorem and making the paraxial approximation, the equation becomes

$$-\bar{k}\frac{\partial I(\vec{r})}{\partial z} = \nabla_{\perp}.[I(\vec{r})\nabla_{\perp}\phi(\vec{r})] \tag{2.11}$$

where $\bar{k}$ is the average wavenumber and the subscripted symbol $\perp$ refers to the two-dimensional xy-plane of the image, such that $\nabla_{\perp}$ is now the two-dimensional differential operator acting within the plane $\vec{r}$, and $\frac{\partial}{\partial z}$ represents the first partial derivative with respect to z, the direction perpendicular to the plane of the image. This is the form of the TIE that is used for the formation of phase images.

2.1.3 Calculation of Phase Images

The phase shift caused by stromal cells in vitro can be measured by solving the transport of intensity equation explicitly for phase. Eq. 2.11 can be rearranged to (see Appendix B)

$$\phi(\vec{r}) = -\bar{k}\nabla_{\perp}^{-2}\left(\nabla_{\perp}.\left(\frac{1}{I(\vec{r})}\right)\nabla_{\perp}\nabla_{\perp}^{-2}\frac{\partial I(\vec{r})}{\partial z}\right) \tag{2.12}$$

If we impose two conditions on this equation, that the field is monochromatic, or at least quasi-monochromatic, and that the irradiance is uniform across any individual xy-plane, but not of course between xy-planes in the z direction, then Eq 2.12 can be simplified to

$$\phi(\vec{r}) = -k\frac{1}{I_0}\nabla_{\perp}^{-2}\frac{\partial I(\vec{r})}{\partial z} \tag{2.13}$$

where the wave number is no longer averaged, due to the monochromatic condition, and the irradiance of the xy-plane is given by the constant I_0.

2.2 Materials and Methods

The methods presented here are based upon those used by Curl *et al* (2005) in calculating the refractive index of airway smooth muscle cells. This method differs from that of Curl *et al*

method in one crucial aspect. Since corneal stromal cells are more sensitive to changes in their environment than the cells studied by Curl *et al* (2005), a fluoroscopic material that could not penetrate the cell membrane was used to aid in determining the thickness of the cell within the medium, rather than within the cells themselves. This fluoroscopic dye emits light of a certain wavelength when stimulated by laser light, cell thicknesses were then measured by measuring the shadow thickness where no fluoroscopic material was present. A full account of this procedure is given in section 2.2.5

2.2.1 QPI Validation

The method of phase measurement was first tested using polystyrene microspheres traceable to the National Institute of Science and Technology (NIST) of a known refractive index (1.59 at 589nm) obtained from Thermo Scientific (Fremont, CA, USA). Spheres, of size 10.00±0.04µm and 15.02±0.08µm (size distributions are standard deviations) and suspended in distilled water were imaged under bright field transmitted light under Köhler illumination conditions, to satisfy the uniform irradiance assumption of equation 2.13. Initially, phase images were calculated using a white light source with a large bandwidth averaged at 550nm, as it was the manufacturer's opinion that this method would not result in a significant change in result. In later experiments a 540nm green filter of full width half maximum bandwidth of 90nm was used to restrict the bandwidth of the incident light as much as possible and so satisfy the monochromatic condition. Image stacks of increasing z through the focal plane were obtained using a Leica DM6000B upright microscope at 1µm intervals for a total distance of 30µm, using a 20x plan-apochromat air lens (Carl Zeiss AG, Jena, Germany) with a numerical aperture (NA) of 0.7, combined with a 1.6x additional magnification and a 0.7x camera mount. The CCD camera (Leica Cameras AG, Solms, Germany) mounted to the microscope had a pixel size of 6.45µm×6.45µm. The best focal plane was set at the centre of the bead by visual

inspection and minimising the out of focus diffraction rings surrounding the bead at the boundary. Images stacks were collected at either side of this plane. The focal image, combined with two out of focus images 2µm in the z-direction from the focal plane were imported into QPm software obtained from Iatia Ltd (Melbourne, Australia). The three images were input into the software, which calculated the irradiance gradient $\left(\frac{\partial I(\vec{r})}{\partial z}\right)$, and after image transforms were conducted according to equation 2.13, returned a quantitative phase image. Measurements were taken from pixels in straight lines across the centre of each bead at different angles. These values were then combined with the known thickness of the sphere as a function of the distance from the centre to determine the refractive index as per equation 2.3.

$$\Delta\phi = k\tau(n_2 - n_1) \tag{2.3}$$

The thickness of the sphere as a function of the distance from the centre was calculated by rearranging the standard equation for a circle to

$$\tau_s = 2(r^2 - x^2)^{½} \tag{2.14}$$

where τ_s is the vertical thickness of the sphere of radius r at a distance x from the central vertical axis (Fig 2.1).

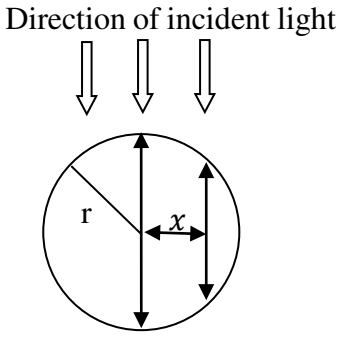

Figure 2.1: Schematic diagram showing how thickness of the sphere was calculated. The thickness (vertical double arrows), is calculated according to Eq. 2.14, using the known radius, r and the perpendicular distance from the central axis, x

The central pixel of each bead was taken to be where the maximum phase shift was recorded. Phase shift measurements near the edge of the sphere were discounted as the lensing effect of

the microspheres was most pronounced at the edge. These manifested as dark rings of no signal around the edge of the spheres which can be seen in Figures 2.2-2.5 in section 2.3.1.

As the monochromatic incident light condition was vital to the validity of the mathematical analysis, phase images were also calculated using bright field images acquired from a 538nm laser scanning microscope (Carl Zeiss, Jena, Germany). Use of this microscope would not only allow for images to be acquired with as small a bandwidth as is reasonably practicable, but would also allow for the magnification of the image to be tuned to virtually any setting without the need to increase the lens magnification. Excessive magnification with a conventional microscope would provide a greater sample of pixel values for the centre of the bead, but at a cost of decreasing the depth of focus, the measure of the size of the plane of focus in the z-axis. Maintaining a depth of focus that covers the extent of the bead, as much as is reasonably practicable, is critical to ensuring that visual artefacts do not plague the image at the chosen focal plane. A shallow depth of focus would increase the interference caused by the top and bottom of the object, which must necessarily lie outside of the central focal plane.

2.2.2 Cell Culture of Activated Bovine Keratocytes

Bovine eyes were obtained from local abattoirs. After cleaning and disinfecting with betadine solution the corneal epithelium and endothelium were removed and stromal pieces excised with a scalpel. Stromal tissue was then placed in well-plate with Dulbecco's modified Eagle's medium (DMEM) with added 10% foetal bovine serum (FBS) to stimulate cell growth and without phenol red indicator, so that the wavelength of the incident light of the bright field images is unaffected. The tissue cultures were stored in incubation at 37^{o}C in an atmosphere of 5% CO_2 until the stromal cells activated and migrated out of the tissue and onto the culture plate. The tissue pieces were then removed and the remaining cells trypsinised. The cell containing solution was twice centrifuged at 3000rpm for 8 minutes to separate cells from the

trypsin solution, with DMEM being replaced between centrifuges. The pellet that formed during the centrifuges was then redissolved and the solution transferred to a 25cm^3 cell culture flask. When the cells in the flask attained confluence after 2-3 days they were trypsinised again and split between additional flasks, with DMEM in the flask being replaced every 48 hours. During the splitting process some cells were seeded onto glass-bottomed Petri dishes obtained from MatTek Corporation (Ashland, MA, USA) ready for image collection.

2.2.3 Cell Culture of Inactive Bovine Keratocytes

Bovine eyes were obtained from local abattoirs and, after extraneous muscle and fat were removed, cleaned and disinfected with 2.5% betidine solution as before. The epithelium was removed using a scalpel and the entire cornea excised. Once removed, the endothelial tissue of the cornea was detached using tweezers and a scalpel, and the stromal tissue was cut into approximately 1mm^3 sections. These sections were placed in 50ml centrifuge tubes containing minimum essential medium with added 2mg/ml collagenase type I. After 2 hours, any remaining large pieces of stromal tissue were removed from the tube and the remaining solution was centrifuged at 500rpm for 5 minutes. The pellet that forms during the centrifuging process was then dissolved in 1ml of DMEM solution with added non-essential amino acids, RPMI vitamin mixture, glutathione, 1% penicillin and streptomycin mixture and 0.1% fungizone (amphotericin-B). This solution was then placed in incubation at 37ºC in an atmosphere containing 5% CO_2. Once the cells were observed to have attached to the flask, further DMEM containing the same additives was added, up to 5ml. Once the cells reached confluence, they were detached from the flask by agitation and transferred to glass bottomed petri dishes ready for imaging.

2.2.4 Quantitative Phase Image Collection

Quantitative phase images (QPI) of cells were obtained in the same way as with bead images. Stacks of bright field images were obtained in 1µm intervals using a Leica DM6000B with a Carl Zeiss HC Plan aprochromat 20x lens with 0.7 numerical aperture. Phase images were produced using the QPm software (Iatia Ltd), as with the beads. Pixel values were exported from 15x15 boxes placed in regions of the cell of the greatest intensity, rather than in lines, as this was assumed to be the area of greatest thickness. Mean values of phase retardation were calculated and used to calculate the refractive index, according to Eq 2.3.

2.2.5 Confocal image collection for thickness measurements

Unlike in the case of the beads, the thickness of the cells is unknown, and as such must be measured for the refractive index to be calculated. To make this measurement, fluorescent isothiocyanate (FITC) dextran was added to the dish containing the cells and DMEM medium. The cells were then imaged under fluoroscopic conditions using a 488nm Argon laser. In theory, since the dextran molecules were too large to penetrate through the cell membrane, this would create images of fluorescent background with void areas where the cells were located. In practice this was mostly true, with most of the cells successfully blocking the intrusion of the fluorescent dye. The few cells that appeared to have the dextran leak into them were not used for the purposes of measurements.

Stacks of images in the z-direction were then obtained from just under the coverslip to the point at which the void disappeared. Images were taken with a 20x air lens with NA of 0.8, at 0.05µm intervals using a Carl Zeiss LSM5 Pascal confocal microscope and Axiovert 200 inverted stand. The image stack was analysed by creating intensity profiles within and adjacent to the void, and the upper cell boundary was taken to be where the intensity returned to 50% of the

background level. Stacks were taken in periods of no more than one hour, to prevent changes in temperature from affecting the morphology of the cells as much as possible.

2.3 Results

2.3.1 Results of Investigation into the Phase Image Calculation Calibration

Results from the first attempted calibration produced a refractive index measurement of 1.421±0.008 (standard deviation, n=68). This significantly differed from the manufacturer's estimate of 1.59. For these images, Köhler illumination conditions were applied, but there was a lack of light filtering. Lensing effects of the spherical particles produced a point of light that was originally thought to be the focal plane. This effect is explained in more detail in section 2.4. Figure 2.2 shows the phase images that were obtained from these false focal planes. It is clear in these images that spurious areas of positive signal, which should indicate some amount of phase retardation in the light, can be seen.

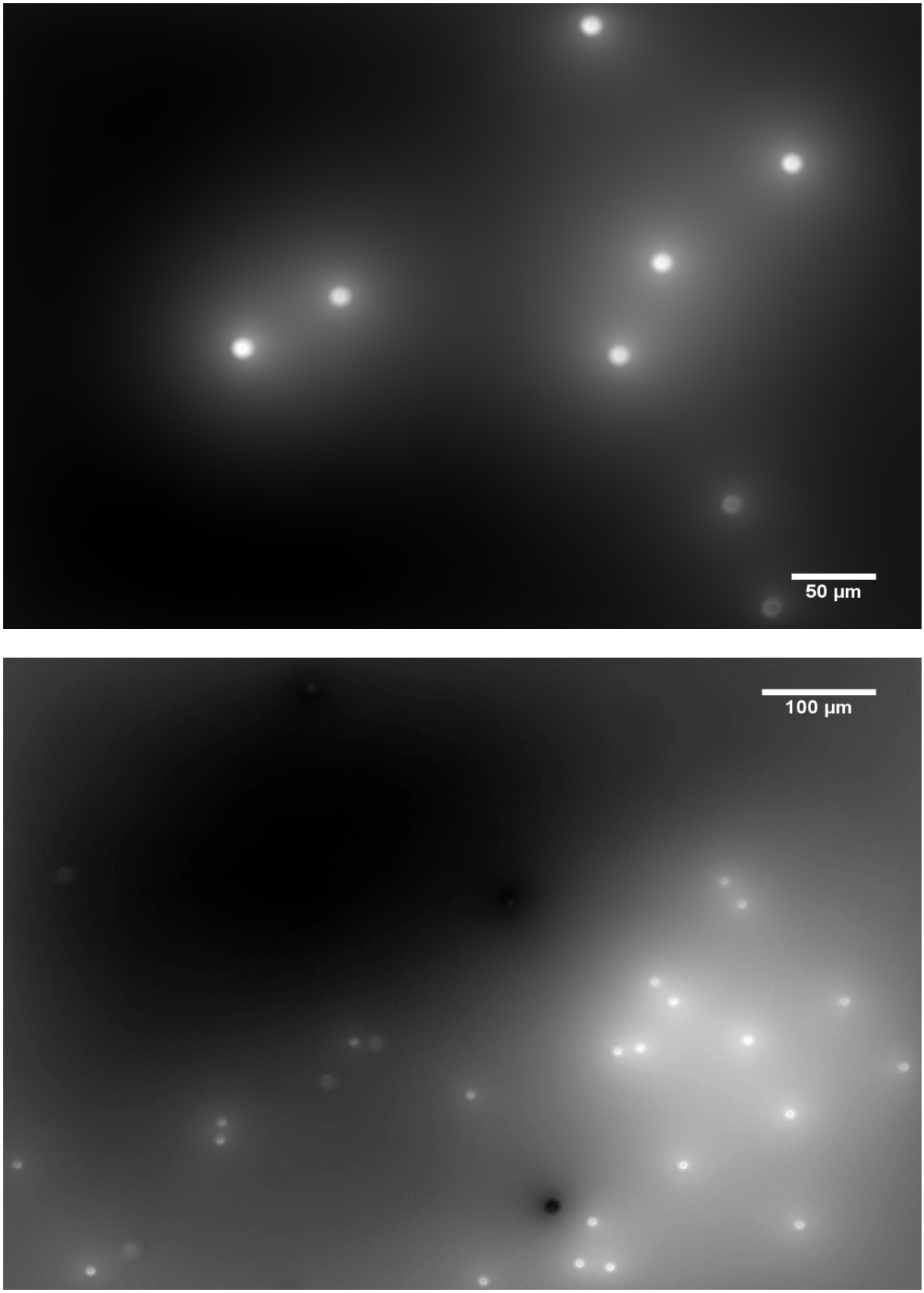

Figure 2.2: Phase images of 15µm (top) and 10µm (bottom) polystyrene beads, calculated using incorrect focal planes. Spurious halos can be seen in both images as well as areas of void signal in the 10µm image. Both images returned refractive index values in the range of 1.40-1.45, which was known to be incorrect.

Further calibrations were attempted using a more accurate focal plane, but with no incident light filtering. The use of the correct focal plane corrected and eliminated the spurious 'halos' of high signal that appeared in previous calibration attempts. However, the use of unfiltered white light as the incident source provided quantitative results that were incompatible with the manufacturer's estimate of 1.59. The returned result in the case of white incident light was 1.462±0.007 (standard deviation, n=81). The software manufacturer's claims that accurate quantitative results could be obtained with a large bandwidth white light source could not be verified in this case.

Results obtained from images from the laser-scanning microscope were disappointing. During the acquisition of the images, the microsphere appeared to be in a constantly moving state. The phase images produced were asymmetric and return a refractive index value of 1.435±0.009 (standard deviation, n=23). A sample image is shown in figure 2.3

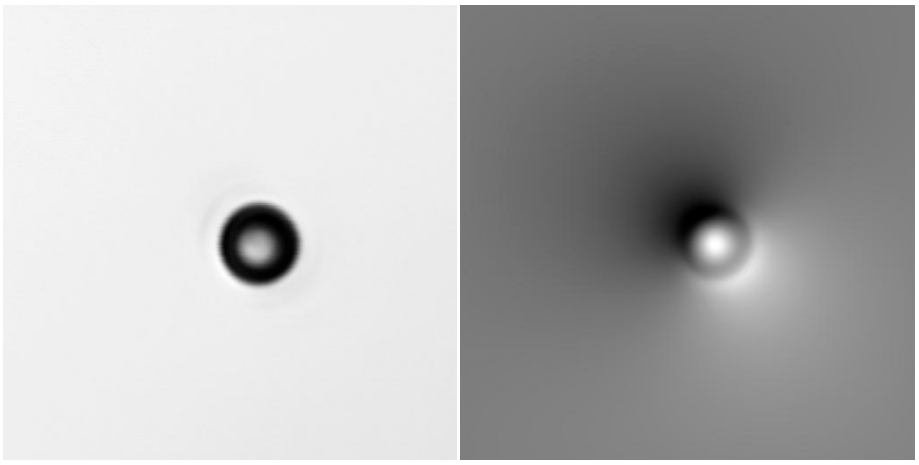

Figure 2.3: Bright field image of a 15µm polystyrene bead obtained from laser scanning microscopy (left) and the phase image that was produced using it (right). An obvious asymmetry was observed in the phase image, which was initially thought to be caused by Brownian motion during image acquisition.

In an attempt to correct the asymmetry, images were produced with the microspheres suspended inside a thermoreversible gel (CyGel), in its hardened state. Images from this method are shown in figure 2.4. Calculations of the refractive index of the beads from these images produced a result of 1.456±0.005 (standard deviation, n=10). The smaller sample size

was due to the experiment being terminated after the first batch of analysis produced unsatisfactory results.

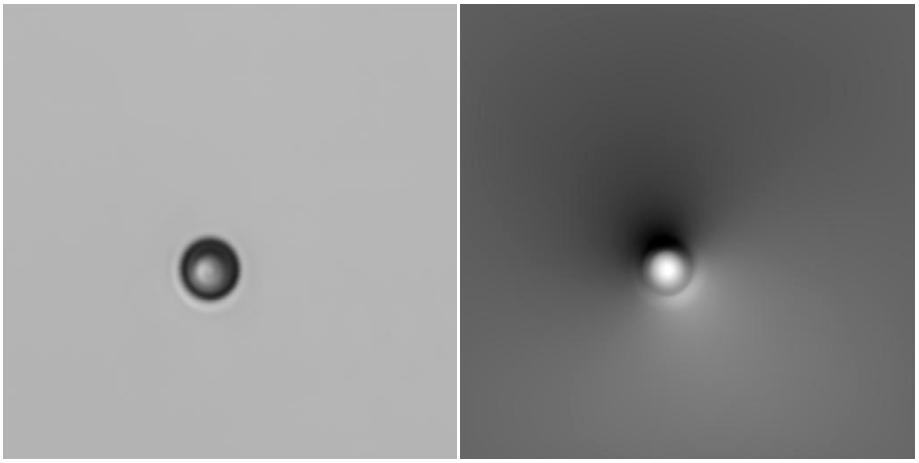

Figure 2.4: Bright field image of a 15µm bead embedded in hardened CyGel (left) and the phase image that was calculated from it (right). The asymmetry that was present in the phase image when beads were observe to move during the image acquisition was still observed when the motion was prevented.

When the incident light was filtered using a 540nm green filter with bandwidth of 90nm (full-width half-maximum), NIST traceable polystyrene beads acquired from Thermo Scientific were measured to have a refractive index of 1.591±0.004 (standard deviation, n=74). This matches the manufacturer's quoted value of 1.59 (no error was supplied). An example of the bright field and phase images are given in figure 2.5. The phase images calculated showed a minimum amount of haloing, and an expected increase in phase retardation between the edge and the central regions, due to the increase in thickness to the maximum at the centre of the sphere. In addition, although background areas were not completely flat as should be expected from a path that contained only medium, the variations in the background were of a magnitude small enough such that they did not significantly affect the phase calculations for the beads.

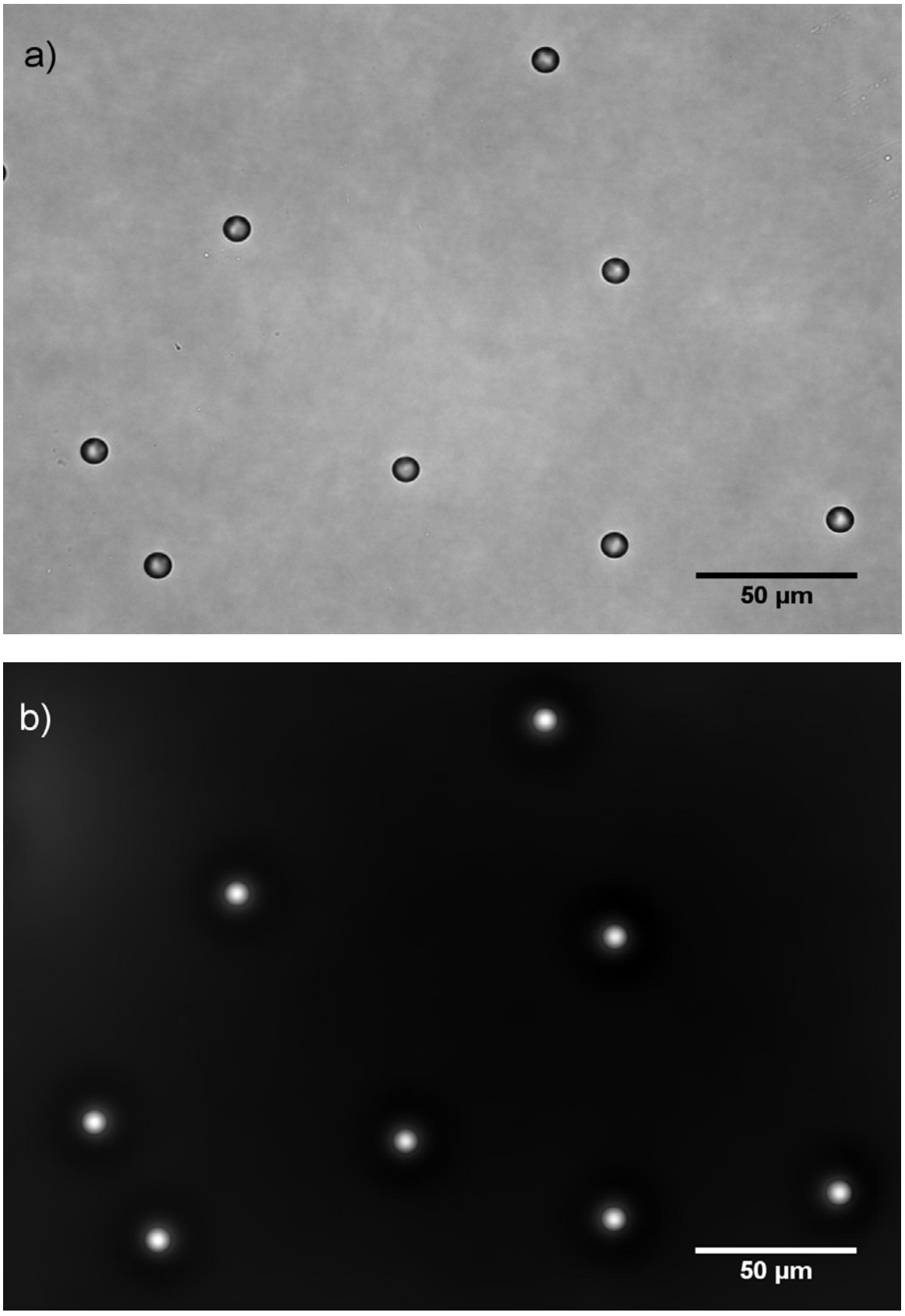

Figure 2.5: a) Bright field focal plane image of several 15µm polystyrene beads. The focal plane was chosen to be the plane that minimised the phase rings around the beads. b) Phase image calculated from the bright field images. It should be noted that in this case there are no large areas of void information, and halos around the beads are kept to a minimum.

2.3.2 Results of Bovine Keratocyte Cell Measurements

Figure 2.6 shows a bright field focal plane image for activated fibroblasts and the resulting quantitative phase image that was calculated from it. Arrows on the image are to indicate equivalent positions within the image. To improve visualisation, the contrast for cell phase images was reversed compared to the bead images of section 2.3.1. It should be noted therefore, that darker areas in the cell phase images indicate a greater phase retardation. The values of refractive index in table 2.2 were calculated using equation 2.3.

$$\Delta\phi = k\tau(n_2 - n_1) \tag{2.3}$$

The refractive index of the medium was taken to be 1.337 (Kemper et al. 2007). Cells are barely visible in figure 2.6a due to the focal plane of the bright field image being assumed to lie at the point of minimum contrast. It should also be noted that the increase in the observed background signal, which manifests as a background that is darker than it would be for a negative bead image, is due to the refractive index mismatch being less distinct than for the beads. The scale is calibrated such that the full range of greyscale is used no matter how great the range in phase retardation is. Pure white and pure black pixels will represent the minimum and maximum phase excursion respectively. Phase contrast images of keratocytes cultured in 25cm^3 culture flasks are shown in figure 2.7. Serum-free cultured keratocytes were determined by morphology. The cells exhibited small, flat cell bodies and interconnecting dendritic behaviour typical of this kind of cell. A bright field and calculated phase image are shown in figure 2.8. Cells in the bright field image are barely visible, but appear clearly within the phase image.

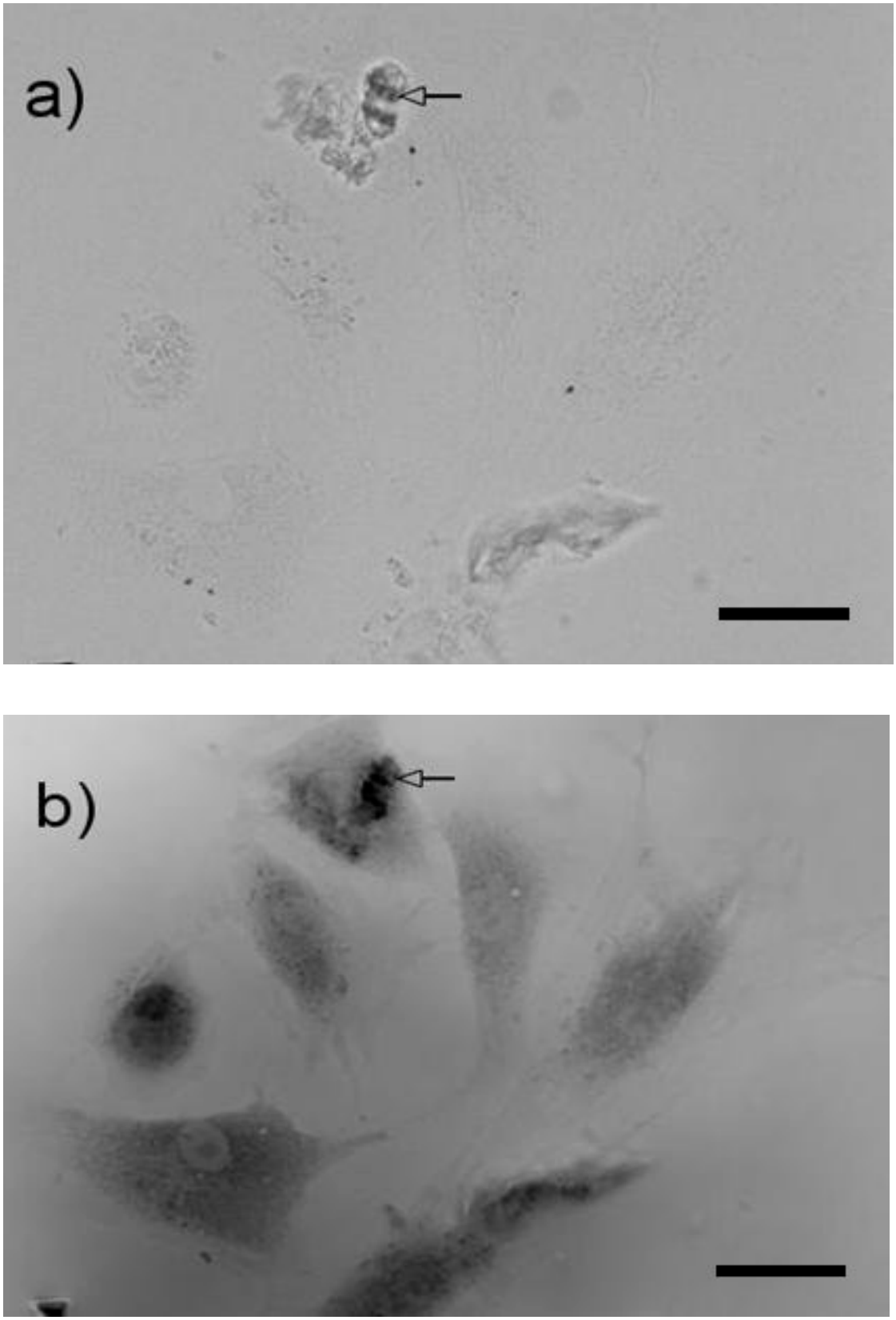

Figure 2.6: a) Bright field image of bovine fibroblast cells. As this is a bright field image, the focal plane was taken to be the plane of minimum contrast. b) Phase image calculated from the bright field images. Areas of greater phase retardation are shown as darker. Arrows represent equivalent areas in the two images to assist localisation, they do not show any specific feature. Scale bar = 20µm

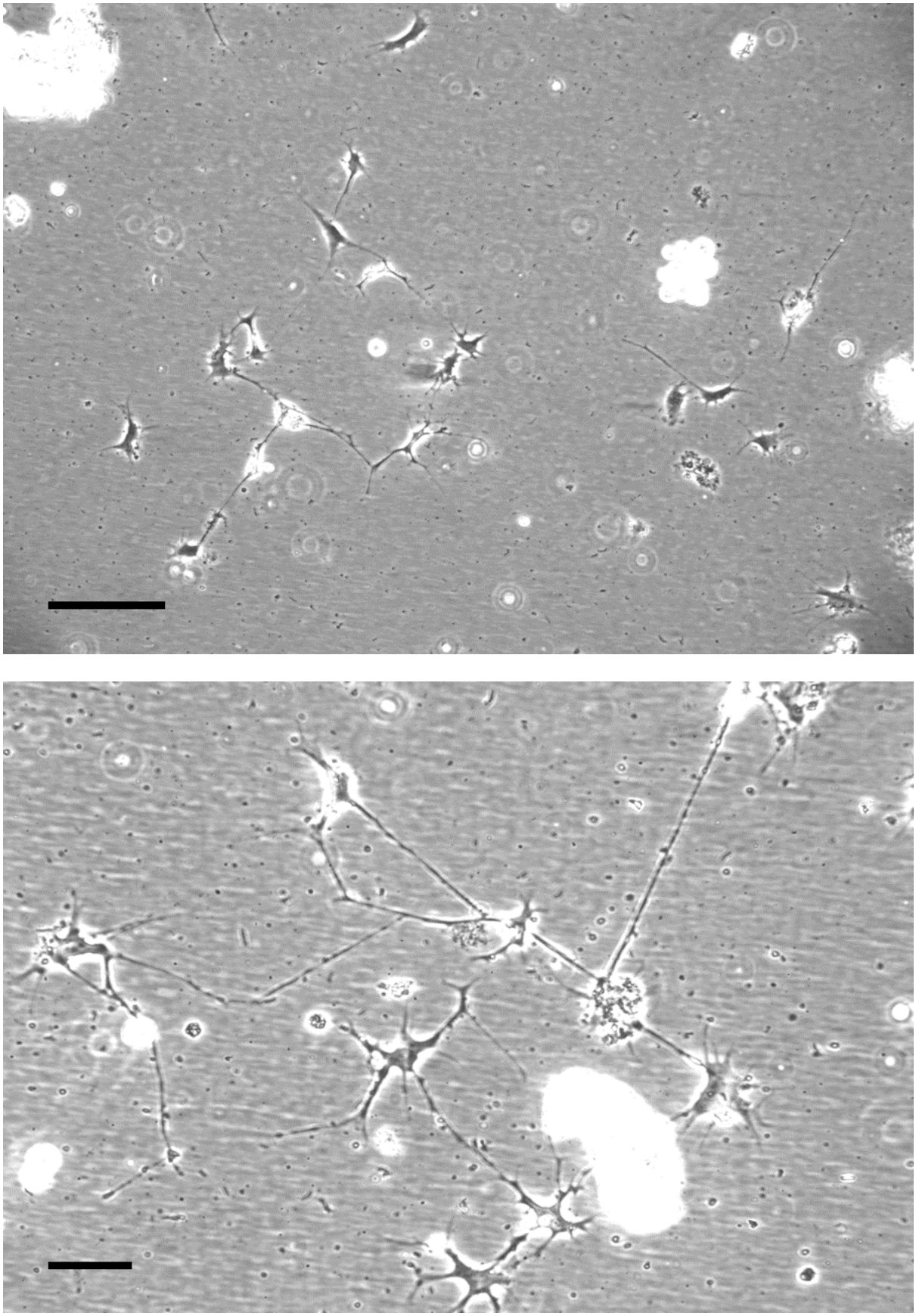

Figure 2.7: Phase contrast images of bovine keratocyte cells cultured in a serum free environment. Top image scale bar = 100µm, lower image scale bar = 25µm

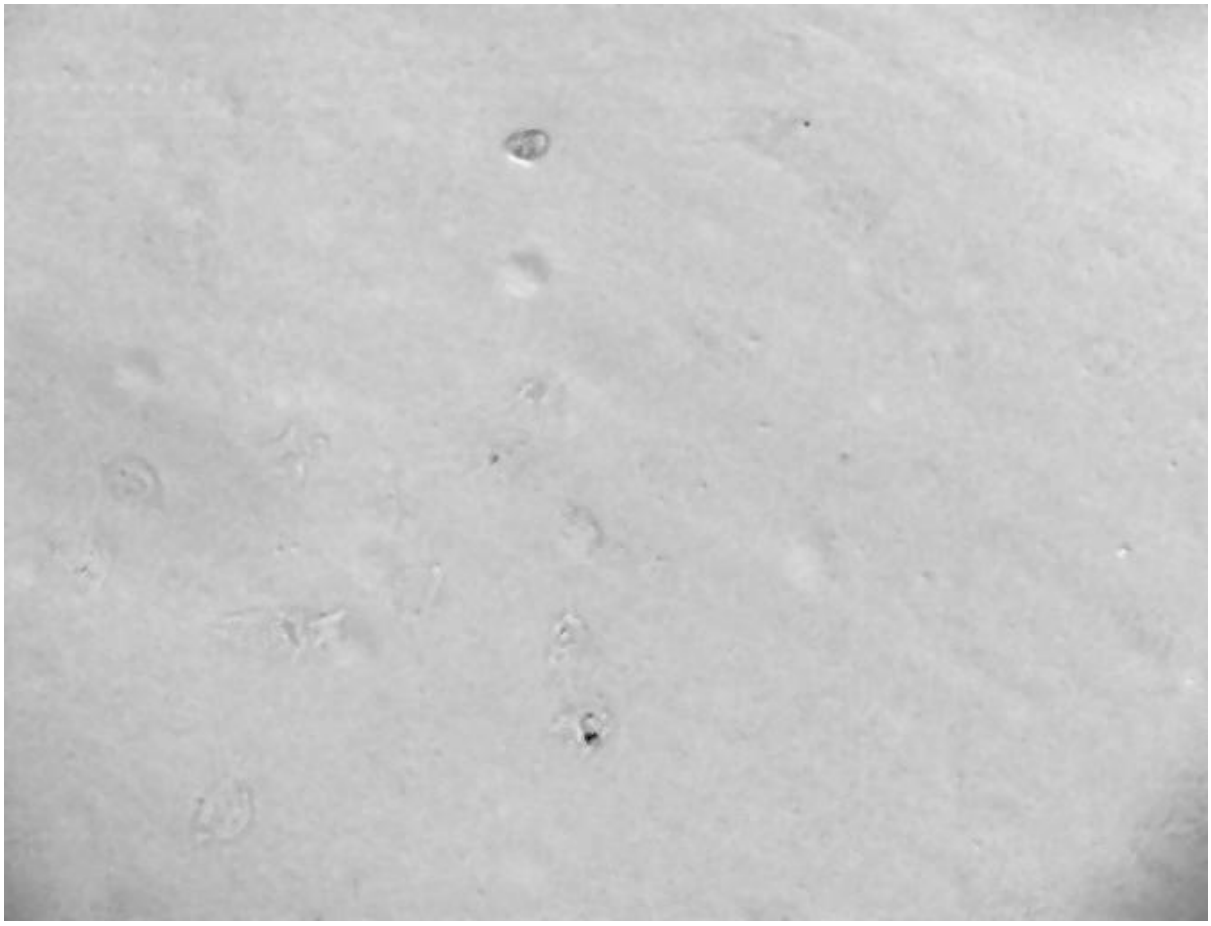

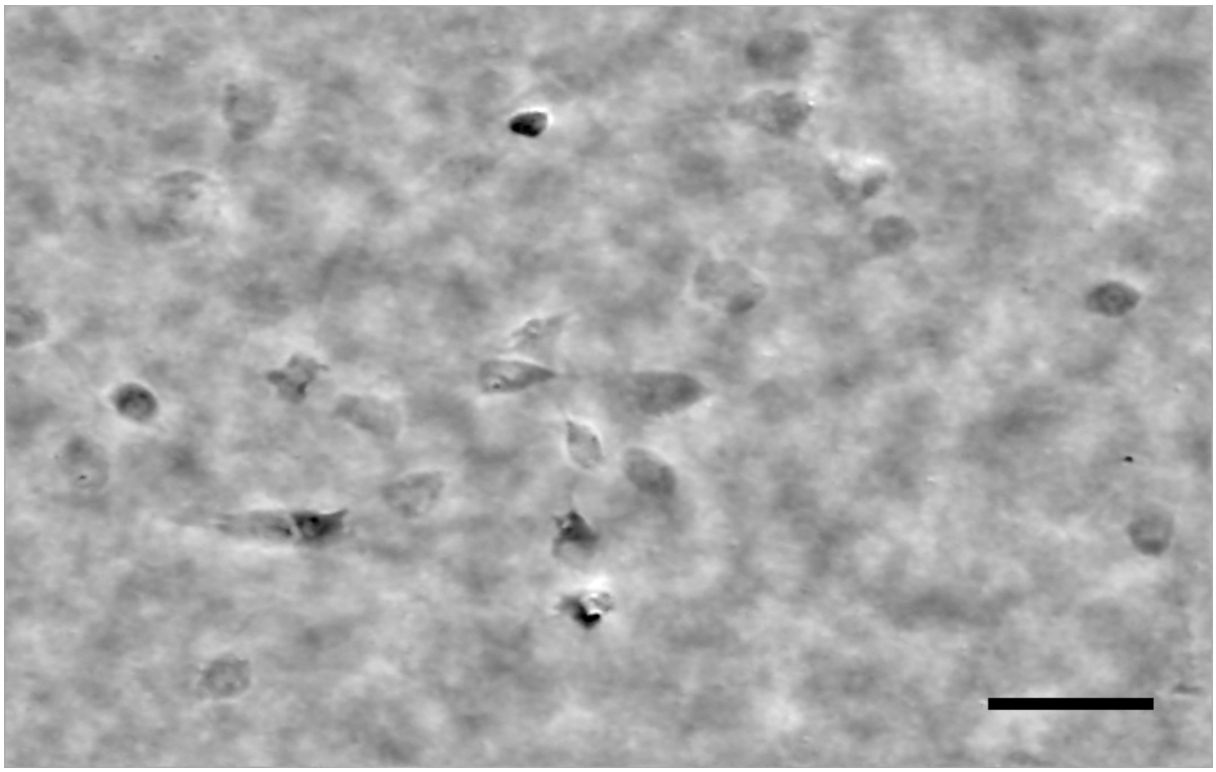

Figure 2.8: Bright field (top) and phase image (bottom) for bovine quiescent keratocytes cultured in MEM. Phase image has been put through a high pass filter to improve the contrast. Darker sections indicate a greater phase shift. Scale bar = 50µm

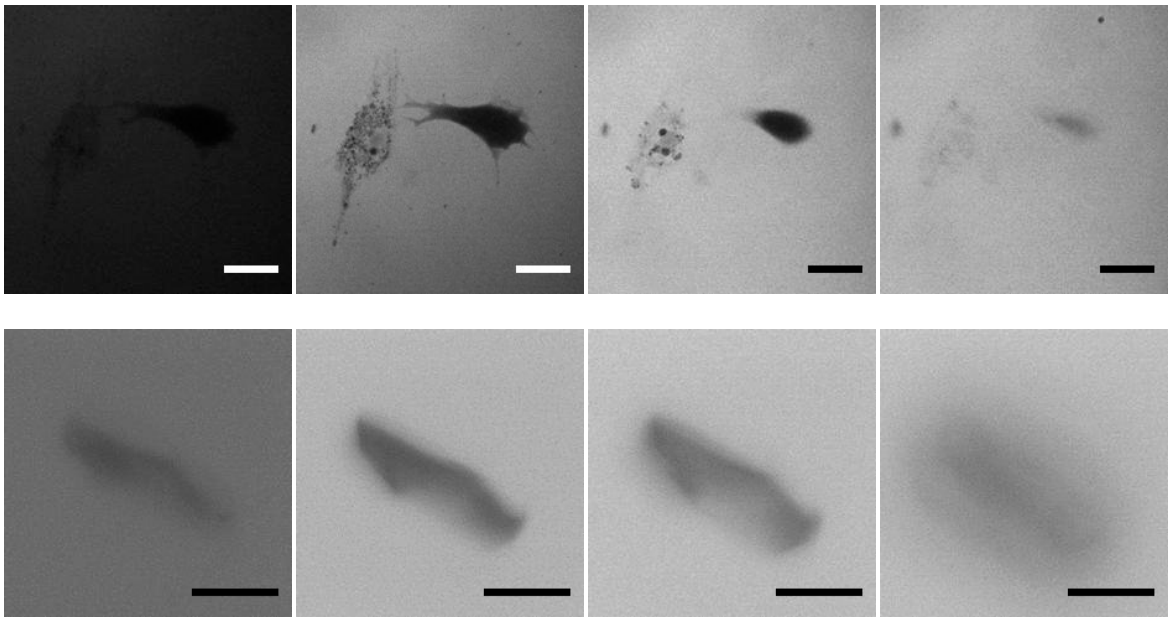

Figure 2.9: Confocal images of bovine fibroblasts (top) and a bovine keratocyte (bottom). Left to right represents an increase in the z-direction, the direction perpendicular to the plane of the image, and hence a movement from beneath to above the cell body. Scale bars = 20µm

Example images from thickness measurements are shown in figure 2.9. Cells that exhibited a leaky cell membrane, such as that shown on the left in the top half of images in figure 2.9, allowed the dextran to penetrate and so were not used in final analysis, it was assumed that these cells were dead and hence not suitable for inclusion. For the inactive keratocyte cells, only the cell body was visible. Thickness measurements were taken from 28 fibroblasts and 41 keratocyes, by measuring the relative intensity within the cell body compared to the background, after which a plot of intensity against z position could be produced. The thickness was taken to be where the intensity within the cell body returned to 50% of the value of the background image, to attempt to account for a possible shadow bleeding effect returning a spurious large thickness.

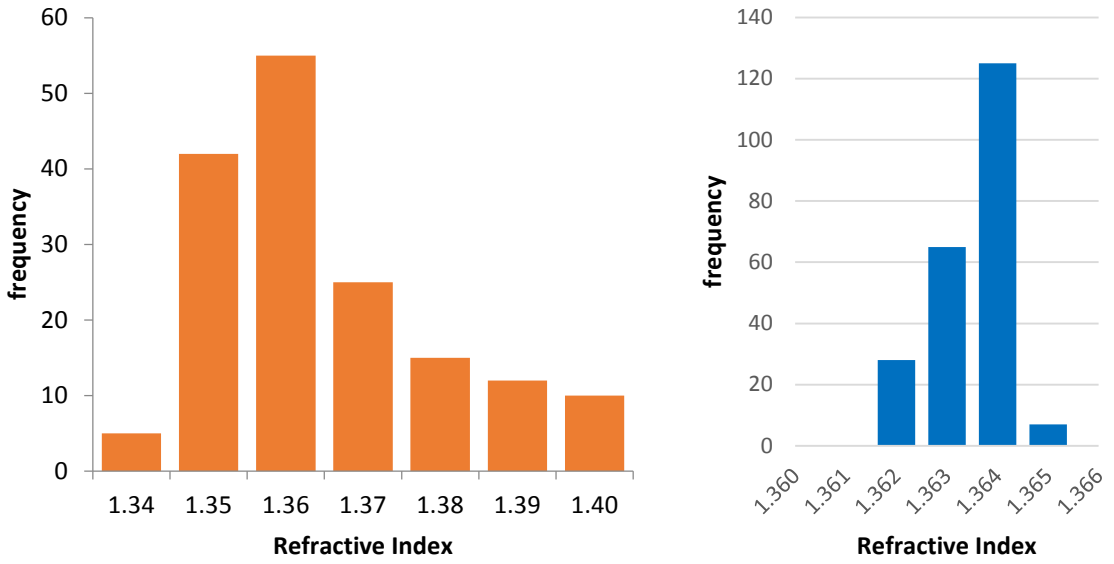

Figure 2.10: Left) Frequency histogram representing the calculated average refractive index of bovine fibroblasts (n=164). Right) Frequency histogram representing the refractive index calculated from measurements of one cell (n=225). Note that the intra-cell variance is much smaller than the inter-cell variance.

Figure 2.10 shows a plot of the calculated refractive index from the mean phase excursion measurements of all measured fibroblasts (n=164) and the results calculated from each pixel within the measured area of one cell (n=225). While inter cell measurements show a degree of variability, the intra cell measurements are extremely consistent. The precise reasons for this variability are unclear, but it is possibly due to variations in the background. Attempts to flatten biases in the camera proved to be ineffective. Flat field exposures were taken in the complete absence of a light source, and analysis of directional biases was carried out, but the pixel values returned were so small that this approach was abandoned as a possible explanation for the different values.

A summary of the results from this chapter are provided in table 2.2. The values presented are the mean phase excursion per cell. As the phase excursion itself is a mean of the 225 pixel values the error quoted is the standard error, the error on the mean of means. As thickness measurements were calculated only once per cell, the error values in that case are simple standard deviations. Refractive indices errors are calculated using the standard rules for error

propagation, where in this case the error on a calculated result (α_A) is found by adding errors on measurements (α_B, α_C) in quadrature

$$\alpha_A = ({\alpha_B}^2 + {\alpha_C}^2)^{\frac{1}{2}} \tag{2.16}$$

Table 2.2: Summary of results for phase excursion and thickness and the resulting refractive index (RI). Uncertainty values are the standard error for phase excursion, and standard deviation for thickness and refractive index measurements.

Cell Type	phase excursion (radians)	thickness (μm)	RI
Fibroblasts	3.10±0.09 (n=164)	9.5±0.3 (n=28)	1.365±0.003
Keratocytes	4.04±0.16 (n=118)	7.2±0.5 (n=41)	1.381±0.004

2.4 Discussion

As three dimensional objects clearly lack an absolute focus, the centre of the bead was taken to be the most focussed point. However the location of the precise centre of the bead by visual inspection was not trivial to ascertain. Even when traversing a stack of images, it was initially difficult to know precisely where the centre was located. This was partly owing to the natural lensing effect of the beads, which focussed the light to a central point located above the extent of the bead. When phase images were calculated from images using this false focal point, the result was an unusable and nonsensical image that contained spurious peaks and troughs that were located in obviously wrong locations. This effect can be seen in Figure 2.1.

As well as the focal plane, the condition for monochromaticity appears to be vital for the success of the algorithm. Only when a narrow band filter was used did the method produce results anything close to the manufacturer's quote of 1.59. Initially it was suspected that, due to the high relative refractivity of the beads to the surrounding water, reflections from the surface or within the bead might contribute to a significant loss of information, leading to a

lower than expected refractive index measurement. However, calculations using the Fresnel equation (Eq 2.17), which relates the reflectivity (R) to the refractive indices of the water $(n_1 = 1.333)$ and the microsphere $(n_2 = 1.590)$, showed that for light incident at 90º to the surface of the bead, the percentage of light reflected was around 0.6%.

$$R = \left(\frac{n_1 - n_2}{n_1 + n_2}\right)^2 \tag{2.17}$$

It was hoped that a laser scanning microscope would provide the necessary low bandwidth of incident light and hence improve the validity of the algorithm, as well as allowing both required measurements that needed to be made for cells to be taken simultaneously. Unfortunately the results obtained from this procedure were unsatisfactory. When this method was first trialled, the phase images that were produced suffered from a high degree of asymmetry, which was thought to be caused by the Brownian motion, the random motion of a large particle caused by the collisions of smaller particles within a fluid, which was observed during image collection. It is not precisely known why Brownian motion was visible for laser scanning images and not during bright field images. As the laser scanning microscope is inverted, it is possible that Brownian motion is visible only when the initial adhesion of the beads to the microscope slide was not aided by gravity. In an attempt to combat the problem of Brownian motion, the beads were re-suspended within a fully transparent hydromorphic gel. This gel was applied as a viscous liquid when kept at 0ºC, which hardened once warmed to room temperature. No Brownian motion was noticed during image acquisition but the phase images produced were not noticeably changed from their previous situation. The reason for the asymmetry is a problem that is so far unsolved. Any explanation offered would be mostly speculation, but it is possible that the conversions that were calculated to allow a laser scanned image to be used rather than a bright field image collected with a conventional CCD camera were incorrect. At the current time, the laser scanned images seem incompatible with the QPm software.

The results summarised in table 2.1 may be compared with the average value for the stroma as a whole determined by previous studies of close to 1.375 (Maurice 1957; Sivak 1988). This would fit well with the model proposed by Jester et al (1999; 2008) and Piatigorsky (2000, 2001) that keratocytes actively change their refractive index to match their surroundings while in their quiescent state. The significant difference ($p = 0.046$, student's t-test) between the stromal refractive index and that of stromal fibroblasts, when coupled with the fact that there is a lack of significant difference ($p = 0.55$, student's t-test) between the refractive index of keratocytes and that of the stroma, it can be claimed these results indicate that light scattering is indeed increased when these cells differentiate. The precise magnitude of this change will be explored in chapter 3. The findings of Jester et al (1999) showed the increase in scattering is most pronounced in the anterior section of the stroma, and this is consistent with our findings given that the anterior section is that which has the highest keratocyte cell density (Prydal et al. 1998; Patel et al. 2001; Popper et al. 2004; McLaren et al. 2010) and the highest refractive index mismatch (Patel et al. 1995). It must be noted that the refractive index of the stroma of 1.375 is a mean value, and that a large variance could have catastrophic effects on the clarity of the cornea even if the mean remains at a reasonable value. The refractive index gradient measured by Patel et al (1995) showed the stromal refractive index to decrease through the cornea from 1.380±0.005 in the anterior section to a minimum of 1.373 in the extreme posterior region, thus giving a maximum refractive index mismatch of 0.008 for quiescent keratocytes and 0.015 upon activation. Thickness measurements recorded from the confocal procedure gave a higher than anticipated thickness for keratocyte cells of both states. Measurements of around 1 micron are common in electron microscopy studies (Muller et al. 1995; Doughty et al. 2001), although this could be considered an underestimate for conditions in vivo. While it is currently believed that dehydration processes used to prepare corneal tissue samples have little effect on the collagen matrix, it is reasonable to suspect that these preparation methods

have devastating effects on the cells of the stroma, leading them to appear much smaller in electron micrographs than in fact is the case in vivo. This could not account for the total amount of the discrepancy between the two styles of measurements though, the larger thicknesses observed using the confocal technique may confirm that a measurement of cells in vitro is not representative of the system in vivo. Alternatively, the effects of 'bleeding' from the shadows in a lower section of the image stack might have contributed to a higher reading than would be expected under real conditions.

While the measurements of the polystyrene beads shows that there can be very little inaccuracy with the phase excursion measurements themselves, cells are not nearly as homogenous. Therefore while intra-cell measurements were very consistent there was a larger variation in inter-cell measurements of the phase excursion and thickness. This would not be a problem if both measurements could be taken simultaneously, or if it could be guaranteed that the different measurements of the phase excursion and thickness were applied to the same cell in the same state. Regrettably, with our current procedures this is not possible. Alternative methods of making simultaneous measurements were trialled, by attempting to create phase images from laser scanning images, allowing both measurements to be made at the same time on the same microscope. However, as a successful demonstration of the calibration could not be made for the reasons discussed earlier in this section this proposed method could not be trialled.

As the measurements are taken in two different ways using two different microscopes, it would be impossible to be completely sure that they are being applied to the same cell and in the same location. The added time taken to achieve this would also become a factor, since these are required to be live cultured cells in vitro and not static or preserved in any way, there is the potential for the conditions of the culture, and therefore the conditions under which a measurement is made, to change between observations, which would clearly not be acceptable. So far then we are restricted to calculating mean values over many different cells, and using

these mean values to calculate the mean refractive index. The legitimacy of this method, in essence, relies upon the cells displaying an acceptable degree of homogeneity. Since the 95% confidence limits of phase and thickness resulted in refractive index error values that presented at the third decimal place, it can be assumed that the cells are sufficiently homogenous for mean values to be suitable to be presented, and for use in future models.

3 Corneal Transparency Modelling

3.1 Introduction

The corneal stroma is fundamentally a vast interconnected array of cylindrical fibrils. It is thought that the unique way in which this matrix is formed and maintained is what gives the cornea its transparency. Early attempts to explain the transparency of the cornea credited the possible lack of refractive index differences within the tissue as the primary reason for this property. This was a reasonable assumption, as any change in refractive index would result in light scattering from the boundary which seemed incompatible with an observably transparent tissue. The idea of the cornea possessing a constant refractive index has now been abandoned, and the reasons why will be discussed in section 3.1.1, but the idea of scattering being reduced or absent due to low refractive index mismatches remains as a theory for why the stromal cells do not appear to scatter light in healthy corneas in line with theoretical predictions. While the early assumptions about the lack of refractive index differences within the cornea have been fully investigated and shown to be false, it would appear that the early assumption of the cornea being too acellular to give rise to any significant scatter has persisted (Maurice 1957; Goldman and Benedek 1967; Benedek 1971). The aim of this chapter is to challenge this assumption, and to use theoretical modelling to provide a picture of the properties required by stromal cells in order to avoid an opaque cornea.

3.1.1 A Synopsis of Corneal Transparency Models

As was alluded to in section 3.1, early assumptions regarding the refractive index of the cornea were made in order to explain its rare property of transparency. This theory fell short for two main reasons; first that there was a birefringence effect observed within the cornea under certain circumstances, which by itself should prove that differences in refractive index exist.

Adding the measurements of stromal refractive index, 1.375 mean across various species (Maurice 1957; Sivak 1988), when compared to dry collagen, 1.547 (Aurell and Holmgren 1953; Maurice 1957), and hydrated fibrils, 1.416 (Meek and Leonard 1993) confirmed the idea of a constant refractive index within the cornea to be false.

With the idea that the cornea was immune to light scatter proven false, theorists then turned to the structure of the lattice itself. Attempts had been made before to link the observed structure of the collagen in the stroma to the transparency properties, with little success. Caspersson and Engström (1946) developed a model that transparency was dependent of the alignment of rows of fibrils, however it only accounted for light propagating in the direction of the fibril alignment, and required fibril diameters an order of magnitude higher than was eventually measured. Maurice (1957) was the first to suggest that a perfect hexagonal lattice of fibrils could provide a large scale transparency by complete destructive interference of all the scattered light. The theory gained in popularity, due to it leading to intuitive explanations for a variety of observed phenomena. It could explain why loss of transparency occurs during swelling and under conditions of pressure delivered to an area of the cornea, the explanation in both cases being a temporary interruption of the lattice structure that dissipates on a return to a normal condition. Maurice also calculated a value for the refractive index of the ground substance that proved to be accurate. Detractors pointed to electron microscopy studies, which showed anything but a perfect lattice arrangement. It was also pointed out that measurements of dry collagen might not be representative of conditions in vivo, and the hydration of the collagen may lower its refractive index (Smith 1969), although it is difficult to envisage that full hydration would remove the mismatch entirely. Leonard and Meek (1997) were later able to show this was the case by making use of Gladstone and Dale's law of mixtures, which states that the refractive index of a mix of N different materials (n_{tot}) is equal to the sum of the products of the volume fraction of each material (f_i) and its refractive index (n_i).

$$n_{tot} = \sum_{i=1}^{N} n_i f_i \tag{3.1}$$

By using previously measured values for the refractive index of dry collagen and for that of the hydrated stroma, the volume fractions calculated by Leonard and Meek (1997) resulted in a refractive index for hydrated fibrils of 1.416 averaged across more than 40 different species.

The failure of electron micrographs to support the perfect lattice model of Maurice was originally thought to be an artefact caused by the processing of the samples that is necessary for their imaging in the vacuum of an electron microscope chamber. However proponents of electron microscopy believed the technique to be representative enough not to impart such drastic changes to the structure of the tissue as would be necessary if the perfect lattice existed in vivo. The work of Goldman and Benedek (1967) on aquatic animals also presented a conundrum. The dogfish they were studying had a much thicker Bowman's layer than was present in mammals, comprising about 15% of the total thickness of the cornea, which is thought to help prevent the cornea from swelling in an aquatic environment. The collagen present in Bowman's layer does not form fibrils that collect as lamellae and so cannot form a lattice. Using this as evidence, Goldman and Benedek (1967) proposed that the long range order of a lattice structure was not necessary for transparency, and that the range of order in the structure need only be near the wavelength of the light passing through it to be able to consider a tissue as optically homogenous. A subsequent study of swollen corneas (Goldman et al. 1968) found that the 'lakes' that form within the lamellae could be responsible for the observed opacity. By applying diffraction theory to reason that light could not resolve structures considerably smaller that its wavelength, the minimum resolvable distance (d) was found to be equal to half the wavelength of the light within the medium it was passing through $(\lambda/2n)$ (Goldman et al. 1968; Benedek 1971). For visible light in the cornea this distance is a minimum of 150nm.

3.1.2 Keratocyte Cells: A Missing Element of the Model

Previous attempts to explain the transparency of the cornea have focussed almost exclusively on the properties of the collagen matrix of the stroma and have assumed for the purposes of the model that the stroma is entirely acellular (Maurice 1957). This assumption was originally justified on the low percentage by volume of cells in the stroma. Confocal studies have shown that, in terms of paths through the cornea, it is much more likely for light waves to encounter keratocyte cells than not (Jester 2008). As their thickness is at least an order of magnitude higher than the minimum resolvable distance, it is natural to assume that some scattering would occur at the boundary between lamellae and the cell membrane. Additionally, the percentage by volume of cellularity within the cornea might be much higher than previously thought. Measurements in the posterior stroma have placed the figure at 5%, but that rises to 12% in the area just below Bowman's layer (Patel et al. 2001). In the developing cornea in chicks it has been estimated that the cell volume could be as much as 20% (Young et al. 2014) based on three-dimensional electron microscopy studies. The exact consequences to the magnitude of scatter within a cornea of such cellularity are as yet unknown. Providing a quantitative estimate of transmission through such a tissue is the aim of this chapter.

3.1.3 The Transparency of the Lens

To explain the transparency of the cornea as a cellular tissue, it may be possible to borrow ideas already well documented regarding the only other transparent tissue of the mammalian body. The lens is a biconvex structure located in the posterior chamber of the eye, just behind the iris. The main responsibility of the lens is to provide an additional, and most importantly, adjustable, refractive power in the eye's optical system. The lens is made up of cells, known as lens fibres, arranged in a concentric patterns that emanate out from the centre. This structure is then surrounded by a layer of epithelial cells. Lens fibre cells are known to utilise several methods

of improving their optical qualities. Mature lens fibre cells are completely without organelles, including a nucleus, in order to reduce scattering to the minimum possible level. This concession of function is acceptable in cells whose only responsibility is to reduce their scattering, but clearly could not be used by corneal keratocytes, which must balance their dual roles first as a low scattering cell body but also as a critical aspect of the wound healing response. As the cornea exists as the interface between the eye and the exterior world, wounds can be expected to be more likely than in the case of the lens, where a healing response, if it exists, would very rarely be required. Lens fibre cells also actively affect the optics of the lens with their function. The lens has long been known to exhibit a variable refractive index from periphery to central regions, with mean value of 1.380 at the surface and 1.406 at the core (Kasthurirangan et al. 2008). The progression of this change from surface to centre is known to be parabolic (Pierscionek 1995), and to change with age, with younger lenses displaying different contour patterns (Pierscionek 1997). This allows the lens to have a higher refractive power relative to its size, while also minimising scattering caused by a refractive index mismatch. These changes within the lens however could not be abrupt, or light would scatter and reflect at the boundary between regions. To circumvent this potential problem, lens fibre cells contain molecules in their cytoplasm that raises the refractive index, known collectively as crystallins. As cells mature and become more central in the lens, the amount of these lens crystallins contained in the cytoplasm increases, giving the effect of a continuous gradient of refractive index from periphery to centre. Crystallins are soluble proteins and make up around 90% of the total protein contained within the lens (Hoehenwarter et al. 2006). The extraordinarily high concentration of these proteins within the lens allow them to form structural units, known as refractons, that provides a short-range order which removes light scatter by destructive interference in an analogous way to the fibrils of the cornea. Lens crystallins also play a crucial role in refractive index matching. Measurements have been made

of the refractive index of the cytoplasm and cell membrane using immersion refractometry, for both the central fully mature lens fibre cells and the less mature cells of the outer cortex (Michael et al. 2003). The mismatch decreases from the surface to the centre and measured light scattering changes through the lens in the same way (van den Berg 1996; van den Berg and Spekreijse 1999), although this may also be partly due to the surface lens fibre cells still containing some organelles.

3.1.4 The Hypothesis of Corneal Crystallins

In order to reconcile the apparent paradox of keratocyte cells being both too large to continue the short range order of the collagen fibrils, but also having a measured low amount of scattering from their cytoplasm, it might be possible that the same mechanism that gives the highly cellular lens its transparency is also at work in the cornea. Silverman and Alexander (1981) discovered large amounts of soluble protein in the bovine cornea. This protein was later identified as an analogue of the enzyme aldehyde dehydrogenase (ALDH) (Cooper et al. 1990; Cooper et al. 1991). ALDH enzymes are involved in the catalysis of acetaldehyde, a by product of the oxidation of alcohols, and are commonly found in the liver. Within the cornea, ALDH enzymes would not appear to catalyse any biological pathway and so must exist in the tissue for some other passive purpose. It has been suggested that ALDH enzymes protect against damage from ultraviolet radiation (Manzer et al. 2003) and oxidative stress (Pappa et al. 2005; Lassen et al. 2006). However the main candidate function of the enzyme is to act as a corneal crystallin to change the refractive index of the stromal cell cytoplasm. This term was first coined in a paper by Cuthbertson, Tomarev and Piatigorsky (1992). The case for corneal crystallins was further strengthened by results from Jester et al (1999) who were the first to connect the crystalline hypothesis to corneal haze that followed freeze wounds in rabbits. Using in vivo confocal techniques it was demonstrated that under normal transparent conditions, light

scattering from stromal cells was minimal, but also crucially that the majority of the scattering that was present originated at the nucleus-cytoplasm boundary, with almost no scattering at all from the cell membrane. In a normal cell, the refractive index mismatch between cytoplasm and cell membrane, and cell membrane and extracellular material would be high enough for light scattering to be easily detected. That this is not the case in corneal stromal cells is strong evidence that the cytoplasm of keratocytes is not ordinary. When this fact is combined with the known optical properties of ALDH enzymes found in the cornea, a clear picture emerges. What may be even more interesting, however, is that in the days following the intentional wound, a haze developed and then slowly receded. When the same confocal technique was used to pinpoint the source of the increased scattering, it was found to originate within the anterior stroma. Fibroblast cells that had been activated during the wound healing pathway now appeared to be strongly scattering. This might indicate that the source of haze effects that develop in the days following wounding are the fibroblasts that are actively repairing the wound. It is possible that once activated, fibroblasts cease production of ALDH and begin to scatter, leading to the observed opacity. This would also provide a neat explanation for the recession of corneal haze effects in the weeks following wounding. It could also be possible that the production of collagen within fibroblasts itself causes an unavoidable increase in scattering, but whatever the precise mechanism is, two facts appear to be clear from the confocal evidence. First that there is a process that allows keratocyte cells to reduce the scattering that occurs from their cytoplasm when they are inactive and second that it is cellular processes, almost certainly related to the corneal wound healing response, that are the root cause of post-wounding haze.

3.2 Theoretical Modelling

Modelling was attempted using two different methods, a method purely focussing on the scattering of light from cells in the cornea, and a method that focussed on solving the wave equation for all points within the lattice. This section will outline the fundamental theory behind the models and how precisely results were obtained. It should be noted that these methods are purely theoretical and do not constitute an experiment as such. While the results obtained are based upon the results from the study detailed in chapter 2, the framework can stand alone. Should the results from chapter 2 prove to be inaccurate in any way, the models presented here would still be valid, it is only the outcomes, and the conclusions that are drawn from them that would change.

3.2.1 Light Scattering Within the Cornea

Light Scattering is the process that results from the interaction of the oscillating electromagnetic field of the radiation to the matter that it is passing through. Electromagnetic radiation induces an oscillating dipole at each point within the medium. This dipole then radiates energy in all directions at the same frequency, but not necessarily the same phase, of the incident radiation. The superposition of these waves from different spatial positions as they spread is known as the scattering pattern. The differences in phase between the different spatial positions can result in scatter that is non-isotropic, where there are directions of higher and lower amplitude. This process is also commonly called diffraction when beams of radiation are considered, and is often represented as a simple deflection of the beam, at several different orders, as they pass through a lattice.

The different types of light scattering are distinguished by the relative properties of the photon and scattering particle, and by whether the energy, and hence the wavelength, of the photon is

conserved. Scattering that causes a change in the wavelength of incident light is known broadly as inelastic scattering. Inelastic scattering can be observed in many forms, of which the most common are Compton scattering and Brillouin scattering. Compton scattering involves the deflection of photons from the electrons in a material. As the photon is not completely absorbed, and since momentum and mass-energy must be conserved in all collisions, the photon is deflected and the wavelength decreased by an amount corresponding to the increase in momentum of the electron according to the equation (Compton 1923)

$$\lambda_0 - \lambda = \frac{h}{m_e c}(1 - \cos\theta) \tag{3.2}$$

where λ_0 and λ are the wavelength of the incident and deflected photon respectively, θ is the angle of deflection, m_e is the rest mass of the electron, h is Planck's constant and c is the speed of light in a vacuum. What can be easily shown is that the maximum wavelength shift, when $\theta = 180^o$, corresponds to a wavelength change of only $4.86 \times 10^{-12} m$. As the wavelength of visible light is around 5 orders of magnitude larger than this, any Compton scattering effects in the cornea will be negligible. For the high energy X-rays used for the diffraction studies of a later chapter, this effect will become important.

Brillouin scattering is the inelastic scattering of light through crystal lattices (Brillouin 1922). Classically, vibrations in the lattice cause changes to the density, and hence refractive index, in different parts of the material. These changes cause a frequency shift in the light. Once again however, these changes are negligibly small compared to the wavelength of visible light. When modelling the interactions of the cornea with visible light, these inelastic components can be safely ignored. Elastic collisions therefore dominate at the visible wavelengths.

Elastic light scattering is usually divided into three main types, according to the relative size of the scattering particle to the wavelength of the incident light. This size parameter (α) can be defined as

$$\alpha = \frac{2\pi r}{\lambda} \tag{3.3}$$

Where r is the radius of the particle and λ the wavelength of the light. If $\alpha \ll 1$ then the effect of Rayleigh scattering dominates. Rayleigh scattering is a non-isotropic, elastic scattering of light by particles of small size. The probability of a scattering events is extremely dependent on the wavelength of light, being inversely proportional to the fourth power of wavelength. A change in incident wavelength of only 300nm between the long and short wavelength portions of the visible spectrum results in a fivefold increase in the probability of a scattering event, in favour of the shorter wavelength photons. The classic example of this wavelength dependence of Rayleigh scattering is the resultant blue colour of the Earth's atmosphere under the illumination of sunlight. Rayleigh scattering events for visible light would dominate when particles are of a size no larger than 40nm. As the wavelength is much larger than the particle size, the exact shape of the particle is not thought to affect the outcome and so no matter what the real shape is the particle can be approximated to a sphere.

Where $\alpha \approx 1$ the limit of Rayleigh scattering theory is reached and Mie scattering must be considered instead. Mie scattering is a solution to Maxwell's equations, named for its discoverer, Gustav Mie (1908), of the scattering of light photons from spherical dielectric particles. Mie scattering solutions are generally much more complicated than their Rayleigh equivalents, and cannot generally be expressed in terms of simple proportional relationships. Mie solutions for spherical particles generally produce infinite series, although these can be well approximated using iterative processes with the aid of computers. Mie solutions are not generally proportional to the wavelength of the incident light, and will scatter isotropically,

although in the limit of small particle size the Mie solution will reduce to the Rayleigh solution and wavelength dependence is recovered. Unlike in Rayleigh scattering, for Mie solutions the shape of the scattering particle is very important. So far, Mie solutions are only completely analytic for spherical particulates, although some progress has been made calculating solutions for ellipsoidal particles (Asano and Yamamoto 1975; Asano and Sato 1980; Asano 1983).

For particles with $\alpha \gg 1$ the Mie solution reduces to the geometric limit, at which point the laws of geometric optics, reflection and refraction, take over and light propagation can be modelled by the system of ray optics. Geometric optics is often used to describe the properties of the eye as a whole, but when considering only the components of the cornea individually the model will fail to predict the observed levels of scattering from smaller areas of transitioning refractive index.

3.2.2 Cell Morphology and the Implications for the Model

The dimensions of a typical cell are usually measured in a small number of microns, the exact dimensions of keratocytes are not expected to differ significantly from this very rough estimate. Before we begin to construct the model system, we must first calculate the upper and lower bounds of the size of the particle for the different types of elastic scattering. If we assume a Rayleigh limit where $\alpha = 0.1$ and the geometric limit where $\alpha = 100$ it can be shown using Eq 3.2 that Mie scattering will be significant for a spherical cell radius of between 8nm and 11μm. Measurements from section 2.3 show that this is clearly the case.

Currently, Mie scattering models are only completely analytic for spherical particles. If we are trying to approximate the shape of cells, spheres may not be an accurate representation of the system in vivo. Cells in the stroma lie flat between collagen lamella, with a reasonably constant anterior to posterior thickness, according to electron micrographs (Doughty et al. 2001). For a volume matched spherical representation of cells, the light path would be on average greater

than the real scenario. However, if the path length of the sphere were matched with the expected thickness of the cell, then the spherical particles would be too small to be representative. Table 3.1 shows the results of scattering calculations using volume and path length matched spheres using a publically available Mie scattering calculator (Prahl 2012), using best case scenario inputs for each case.

Table 3.1: Results of scattering calculations that model cells as both volume matched (d=7.26µm) and path matched (d=1.34µm) spheres.

	Refractive Index	Diameter (µm)	Scattering Cross-Section (μm^2)	Concentration (%)	Transmission (%)
Inactive	1.381	7.26	5.26	5	48.5
Inactive	1.381	7.26	5.26	10	23.6
Activated	1.365	7.26	14.1	5	14.4
Activated	1.365	7.26	14.1	10	2.1
Inactive	1.381	1.34	0.006	5	87.7
Inactive	1.381	1.34	0.006	10	77.0
Activated	1.365	1.34	0.017	5	69.0
Activated	1.365	1.34	0.017	10	47.6

Clearly then another shape is needed for the model to be properly representative. However, it is already known that Mie scattering is strongly dependent upon the shape of the particle, and that any attempts to apply Mie theory to particles with less symmetry will result in calculations that are prohibitively complex. The added complexity of non-spherical particles can be partially spared in this case by making use of the anomalous diffraction approximation (ADA). The ADA simplifies the calculation of the scattering cross section, while losing information only from secondary and higher orders of structure (Van de Hulst 1957). The ADA was originally applied to non-absorbing spheres in a system where the wavelength is much smaller than the

diameter of the particle and the ratio of refractive indices inside and outside of the particle is close to 1. Van de Hulst (1957) showed that the effect of loss of information has little effect on the magnitude of the scattering cross section under these conditions even for refractive index values as high as 1.7. The ADA continues to be used widely, a recent example being a study on the recovery of the size of spheriodal particles from their scattering profile, a process that is essentially the inverse of the aims of this model. The study showed that even with the approximation in effect, the introduced errors were negligible when the conditions of the approximation were satisfied, although when the real and the imaginary part of refractive index, a measure of the absorption effect of the medium, were increased the errors introduced by the approximation increased by as much as 20% (Sun et al. 2008). As the refractive index ratio of the cells to the ground substance does not approach the level of 1.33 tested, and since we are using the reasonable assumption of no absorption of visible light within the cornea these errors that are introduced at the limits of the conditions for the ADA should not affect the results.

Due to the nature of the morphology of the keratocyte cells, the most accurate representation of their shape would be a flat cuboidal structure, following the work of Napper (1967), the ADA can be used to simplify the calculation of the Mie scattering cross section from cubic particles. This work may then be extended to particles of cuboidal prism shapes. Starting from the definition of scattering cross section as the ratio of total flux scattered per unit flux

$$\sigma(\alpha) = \iint_{G(\alpha)} \left|1 - e^{-i\delta(\alpha)}\right|^2 dxdy \tag{3.4}$$

where $\sigma(\alpha)$ is the scattering cross section, $\delta(\alpha)$ is the phase shift of the transmitted light on refraction through the particle and $G(\alpha) = \iint dxdy$ is the geometric shadow cast by the particle. For a face-incident cube of cross sectional area A, the scattering cross section (σ_c) is given by

$$\sigma_c = 2A(1 - \cos\rho_c) \tag{3.5}$$

where $\rho_c = 2\pi\tau(m - 1)/\lambda$, the phase shift of light of wavelength λ caused by a refractive index ratio of m along a path of length τ.

Once the scattering cross section has been calculated, we can calculate the transmission through the whole of the cornea using the relation

$$T = I/I_0 = exp(-\varepsilon_c \sigma t/V_c) \tag{3.6}$$

for a cornea of thickness t and volume fraction of ε_c cells of volume V_c. The values I and I_0 represent the transmitted and incident irradiance respectively. An interesting result of this for cuboidal cells is that the transmission through it is independent of the cross sectional area of the cell. This can be clearly seen by substituting Eq 3.5 into Eq 3.6.

$$T = exp(-\varepsilon_c \sigma\tau/V_c) = exp(-2\varepsilon_c \tau(1 - \cos\rho_c)/\tau_c) \tag{3.7}$$

Where the thickness of the cell, $\tau_c = V_c/A$. In order to be able to use only the transmission as the measure of transparency, it is important to establish what the consequences of a scattering event from a corneal cell will be. It has already been shown that scattering in of itself need not cause a loss in transparency, if destructive interference effects remove the scattered light from the information pool. With cell scattering this is very unlikely, since cells have never been shown to arrange themselves in any particular formation in the cornea.

For a scattering event to cause a loss in transparency, it has to deflect the light such that the scattered path differs from the unscattered path by more than the distance across a retinal photoreceptor. If the deflection is less than this, then the light is detected in the same way as it would have been and the scattering event does not affect the image that is projected on the retina. If we take the effective centre of the optics of the eye to be 17mm from the retina, and the width of cone photoreceptors in the fovea to be 2.5μm (Wandell 1995, Chapter 3) then

simple trigonometry gives the solid angle subtended by a single photoreceptor to be 0.008 degrees. Even given the large forward direction bias associated with Mie scattering, it is very unlikely that a scattering event will deflect a photon by less than this angle. For this reason, we take any scattering event to be detrimental and so consider the percentage of unscattered light to be the same as the transmission through the cornea.

For the model, cells were approximated as cuboidal slabs of constant anterior-posterior thickness (Figure 3.1) and constant refractive index, surrounded by extracellular material of refractive index 1.375, as reported in the literature (Maurice 1957; Sivak 1988). Transmission through a cornea of thickness 550µm, close to that reported in the literature (Ambrosio et al. 2006; Cervino et al. 2009), was calculated according to Eq 3.6. Two different cell thicknesses were used, to represent the upper and lower limit on the size of a cell in vivo. Thickness measurements of the order of 1 micron reported from electron microscopy studies (Muller et al. 1995; Doughty et al. 2001) were considered to represent the lower limit of cell thickness, as while the micrographs represent the cells in a more natural environment, the processing required to produce them, in particular the dehydration and fixation stages, is known to cause shrinkage. Even though steps were taken to minimise the possible effects of shadow bleeding during the thickness measurements associated with section 2.2.5, they still could have contributed to an increase in the thickness measurement. As such, the thickness reported in section 2.3.2 were considered, for the purposes of the modelling work, to be an upper limit on the thickness.

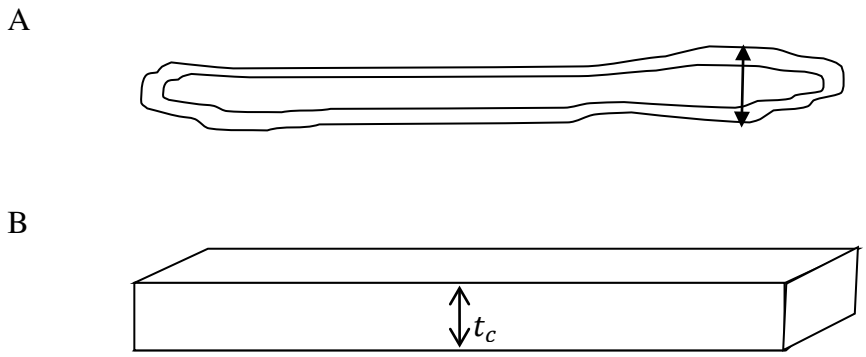

Figure 3.1: Schematic diagram to show transverse section of a typical keratocyte in vivo (A) and the particulate shape used in the scattering model (B). Arrow in A indicates the point of maximum thickness, which was used as the basis of t_c

3.2.3 The Finite Difference Time Domain Method

The work of Maxwell in the 19th Century and the formulation of his set of partial differential equations has allowed physicists to predict and model a wide variety of wave phenomena. The equations, given in their differential form, are shown in equations 3.7 to 3.10.

$$\nabla . E = \frac{\rho}{\varepsilon_0} \tag{3.7}$$

$$\nabla . B = 0 \tag{3.8}$$

$$\nabla \times E = -\frac{\partial B}{\partial t} \tag{3.9}$$

$$\nabla \times B = \mu_0 \left(J + \varepsilon_0 \frac{\partial E}{\partial t} \right) \tag{3.10}$$

Where ∇ is the three dimensional differential operator, E and B and the electric and magnetic vector fields respectively, ρ represents the charge density, J is the electric current density, and ε_0 and μ_0 represent the fundamental constants of the permittivity and permeability of free space, respectively.

In all aspects of wave phenomena, solutions to these equations provide the theoretical prediction of the behaviour of the system. However, finding exact analytic solutions to these equations is not always trivial, and in complex systems these solutions may need to be calculated hundreds of times. These type of intense calculations are the realm of computers, but in order for them to be performed a numerical iterative method is required. Originally, frequency domain techniques involving solutions calculated from integral equations using linear algebra were the preferred mode of operation. With the increase in power, and more importantly the decrease in the cost of computer memory, time domain techniques have come to dominate.

These time domain solutions can be combined with a finite difference method for approximating differentials. Finite difference methods discretise a continuous function into points, and approximate the derivative by applying a central difference of the form; $f(x + h/2) - f(x - h/2)$, where h is the distance between the points. Dividing the central difference by h forms an expression that can be used as an accurate approximation for the differential of $f(x)$ (Eq 3.11). This provides another advantage of finite-difference methods, the errors are well defined and calculable. As with the definition of a differential (Eq 3.12), as h approaches zero so does the error

$$\frac{f(x + h/2) - f(x - h/2)}{h} \approx f'(x) \tag{3.11}$$

$$\lim_{h \to 0} \frac{f(x - h) - f(x)}{h} = f'(x) \tag{3.12}$$

The finite difference time domain (FDTD) technique was first proposed by Yee (1966), and involves approximating solutions to Maxwell's equations by applying them to a grid that is discretised in space and time. This process can be shown more easily by applying these conditions to the one dimensional scalar wave equation (Taflove and Hagness 2005, pp. 21-28)

$$\frac{\partial^2 u}{\partial t^2} = c^2 \frac{\partial^2 u}{\partial x^2} \tag{3.13}$$

Where u is the wavefunction, c is the speed of light in a vacuum and $\partial^2/\partial t^2$ and $\partial^2/\partial x^2$ are the second partial derivatives of time and position respectively. By making use of Taylor expansions of the functions $u(x_m + \Delta x)$ and $u(x_m - \Delta x)$:

$$u(x_m + \Delta x) = u(x_m) + \Delta x \frac{\partial u}{\partial x} + \frac{(\Delta x)^2}{2!}\frac{\partial^2 u}{\partial x^2} + \frac{(\Delta x)^3}{3!}\frac{\partial^3 u}{\partial x^3} + \ldots\ldots \tag{3.14}$$

$$u(x_m - \Delta x) = u(x_m) - \Delta x \frac{\partial u}{\partial x} + \frac{(\Delta x)^2}{2!}\frac{\partial^2 u}{\partial x^2} - \frac{(\Delta x)^3}{3!}\frac{\partial^3 u}{\partial x^3} + \ldots\ldots \tag{3.15}$$

The space derivative can be found by adding together Eq. 3.14 and Eq. 3.15, and rearranging in terms of the second spatial derivative.

$$\frac{\partial^2 u}{\partial x^2} = \frac{u(x_m + \Delta x) - 2u(x_m) + u(x_m - \Delta x)}{(\Delta x)^2} + O[(\Delta x)^2] \tag{3.16}$$

Where $O[(\Delta x)^2]$ is a remainder term from the Taylor expansion. The cumbersome notation can be compacted by representing space and time steps in superscripts and subscripts such that u_m^n represents the wavefunction $u(x)$ at space increment $m\Delta x$ and time increment $n\Delta t$. Thus, equation 3.14 can be rewritten as

$$\frac{\partial^2 u}{\partial x^2} = \frac{u_{m+1}^n - 2u_m^n + u_{m-1}^n}{(\Delta x)^2} + O[(\Delta x)^2] \tag{3.17}$$

An analogous equation can be derived for the time derivative. By substituting these two expressions into the scalar wave equation (Eq 3.13) and neglecting the remainder terms it is possible to form an expression for the wavefunction evaluated at the (n+1)th time step purely in terms of the solutions that are already known.

$$u_m^{n+1} = (c\Delta t)^2 \left(\frac{u_{m+1}^n - 2u_m^n + u_{m-1}^n}{(\Delta x)^2} \right) + 2u_m^n - u_m^{n-1} \tag{3.18}$$

If the discretisation is chosen such that $\Delta x = c\Delta t$ then equation 3.18 can be even further simplified to

$$u_m^{n+1} = u_{m+1}^n + u_{m-1}^n - u_m^{n-1} \tag{3.19}$$

This means it is possible to calculate the propagation at the next time interval by a simple addition of the wave quantities at position either side of the grid and from the previous time step. The solutions for all time points can then be derived in an iterative fashion. During such iterative processes small errors can propagate and may be a cause for concern. In principle, any discretisation can be chosen, but care must be taken that both Δx and Δt are chosen to be sufficiently small such that the remainders, which scale with their squares and which we have so far neglected, do not become problematic. In the specific case that $c\Delta t = \Delta x$ however, it can be shown that Eq 3.19 is an exact solution, even though remainder terms have previously been neglected. The full proof of this statement can be found in Appendix C, or alternatively consult Taflove and Hagness (2005, pp. 27-29).

Finite difference time domain simulations were performed on a linux operating system (Ubuntu) running the MIT electromagnetic equation propagation (MEEP) program version 1.2.1. The model was set up in two dimensions first as a purely hexagonal lattice of infinite height dielectric cylinders, arranged normal to the plane of the wave. Perfectly absorbing boundary conditions were in effect around the boundary of the test space in order to prevent

reflections from the edges. The lattice was created by placing a cylinder that is considered to be infinite in the *z* direction and duplicating the cylinder a fixed number of times. This row of cylinders was then itself duplicated to form a square lattice (Figure 3.2).

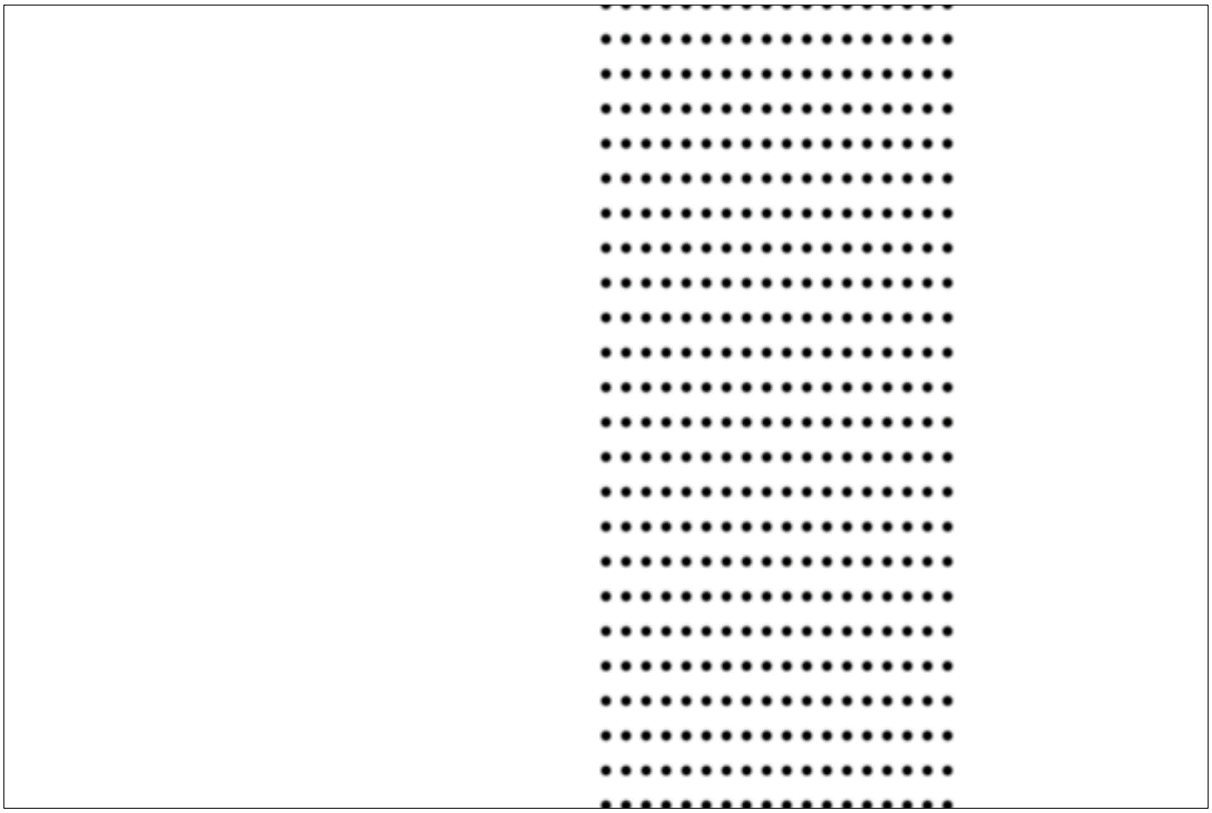

Figure 3.2: Schematic of base square lattice

The hexagonal lattice was produced by introducing a new square lattice in the same way that was offset from the first by $\left(0.5\ , \frac{\sqrt{3}}{2}\right)$, in accordance with the trigonometry of a hexagon of side 1 unit. The final lattice was such that the fibril spacing was exactly one unit (Figure 3.3).

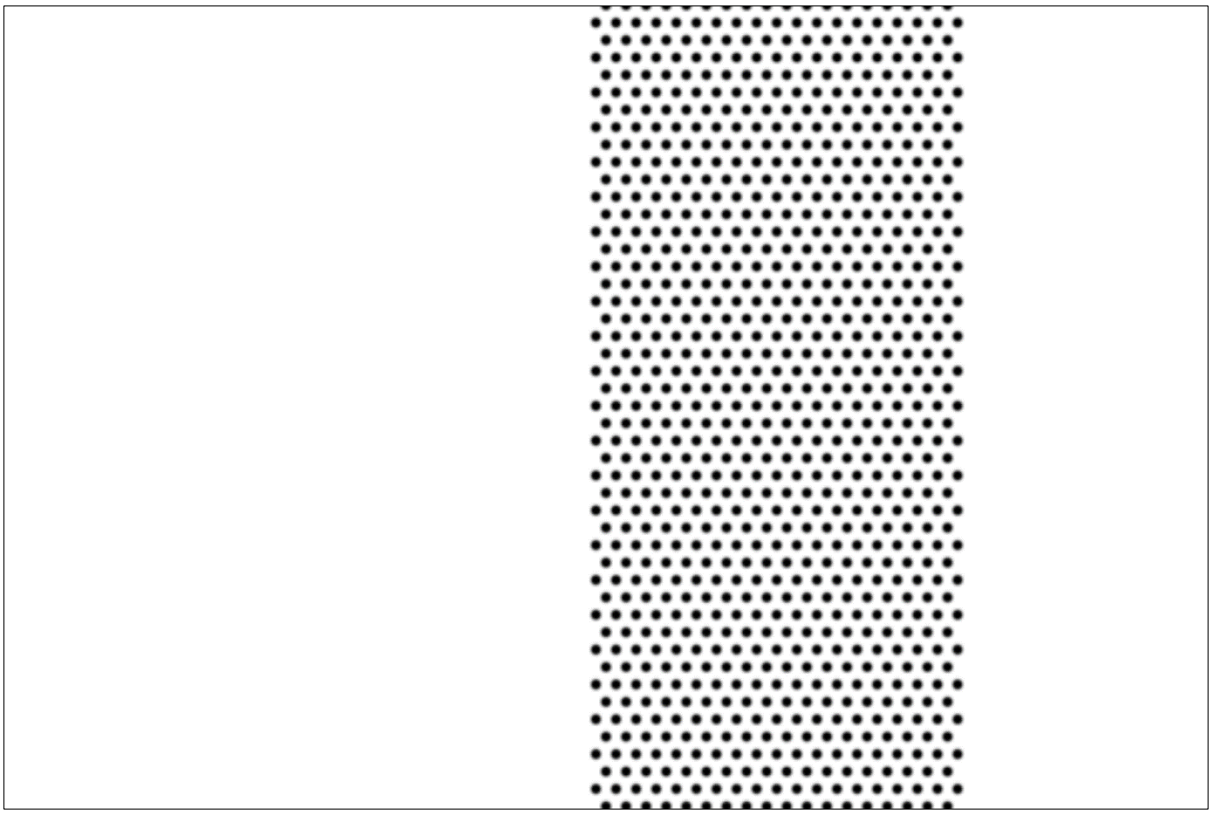

Figure 3.3: Schematic of final lattice

Wave sources were chosen to have a wavelength of between 7 and 15 times that of the fibril spacing, in accordance with the bandwidth of the visible spectrum, assuming a centre-to-centre fibril spacing of 50nm. The flux was calculated at 500 different frequencies within this band by the program at a position to the right of the lattice (Figure 3.4).

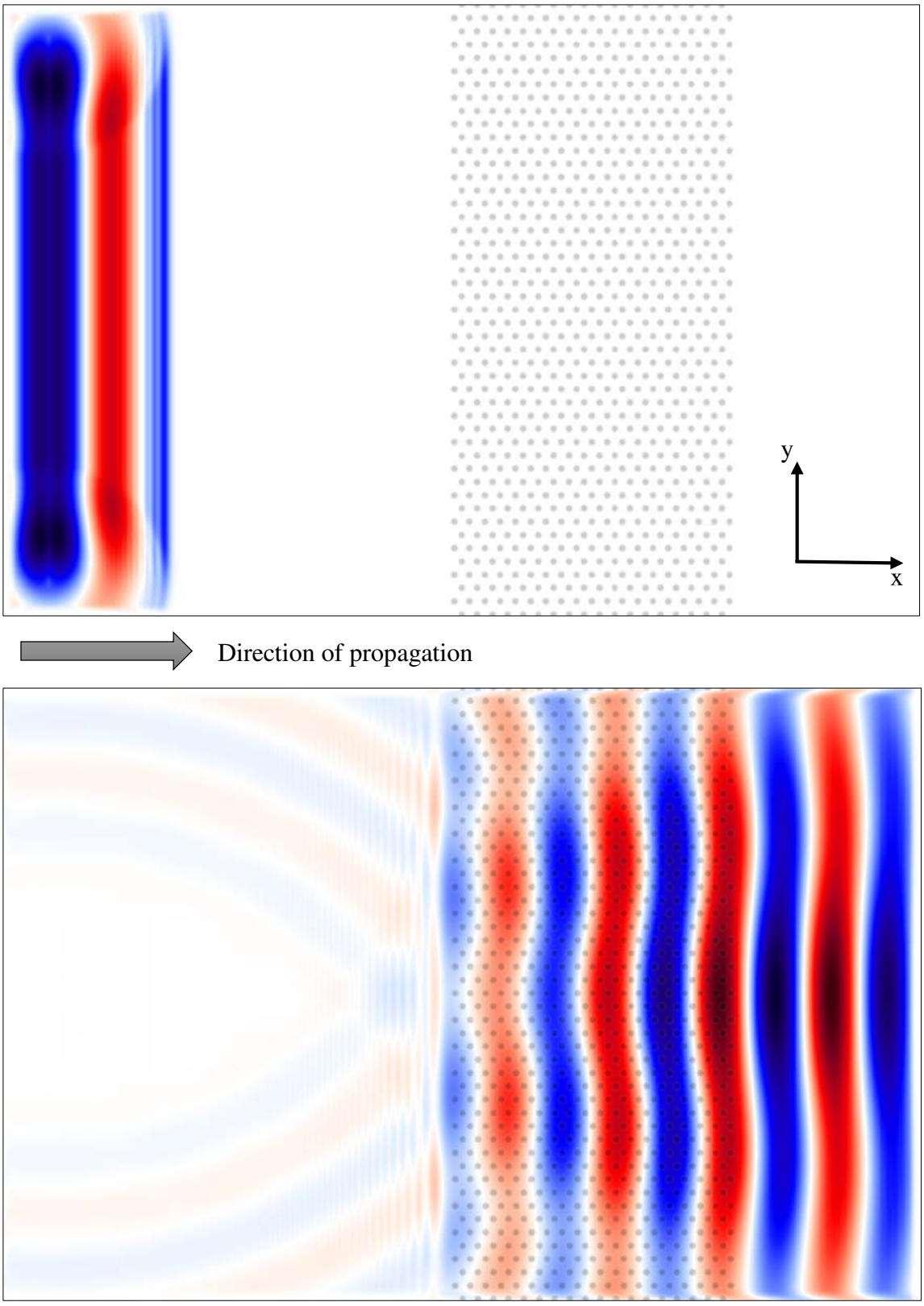

Figure 3.4: Colour maps, showing example of transmitted wave propagating from left to right at t=82 (top) and t=250 (bottom). Amplitude in the z-direction is represented from blue (negative) through white (neutral) to red (positive). Wavelength is set at 7 units in this case.

To test transmission through the unaltered lattice, the results of the measured flux with the lattice present were compared with the transmitted flux when no lattice was present. The program was set such that the generation of a lattice was the default setting. This could be overridden at the command line of the operating system when the control file was run. Declaring the parameter $lattice?$ to be false would result in the program generating a system identical in every way, except with the lack of a hexagonal lattice of cylinders. Once results had been obtained for the unaltered lattice structure, holes were introduced into the lattice. This was done by creating a series of eight different square lattices, positioned so that it appeared to be the same size but with a section of fibrils missing. This section was then given a different refractive index to the background and the results taken in the same way (Figure 3.5).

Figure 3.5: Schematic of lattice with a hole introduced of size x=8 and y=4, placed at the centre of the lattice

For multiple simulations the parameters defined at the start of the program were changed manually before the program was run.

Results from these simulations can be found in section 3.3.2. The raw program code, written in the scheme language and run within the MEEP program, is provided in Appendix D.

3.3 Results

3.3.1 Mie Scattering Model

The plots of transmission against cell volume fraction are given in figure 3.6, in both plots the single difference between the two scenarios is the refractive index of the cells, with the activated fibroblasts set at 1.365 and the keratocytes at 1.381, according to the results presented in section 2.3. The transmission of a cornea populated by inactive cells remains above 85% well beyond normal volume fraction concentrations, which are known to range from 3-5% in the posterior stroma up to 12% just below Bowman's layer (Prydal et al. 1998), for cell thicknesses of 1.34 microns. The second plot in figure 3.6 is based on cell thicknesses from table 2.2 in section 2.3. Transmission drops with increased volume fraction far more quickly in this case, which may indicate that in vitro thicknesses are not suitable for modelling situations in vivo. Figure 3.7 shows how transmission would change for different cell thicknesses given the refractive index gradient of the cornea, which ranges from 1.373 to 1.380, from posterior to anterior respectively. Transmission in the anterior section of the cornea remains high for both keratocyte cell thickness values, and falls dramatically when the refractive index value is lowered. In the posterior section, the values for both cell types become much closer. This reflects the more similar refractive index difference between both types of cells in the posterior section.

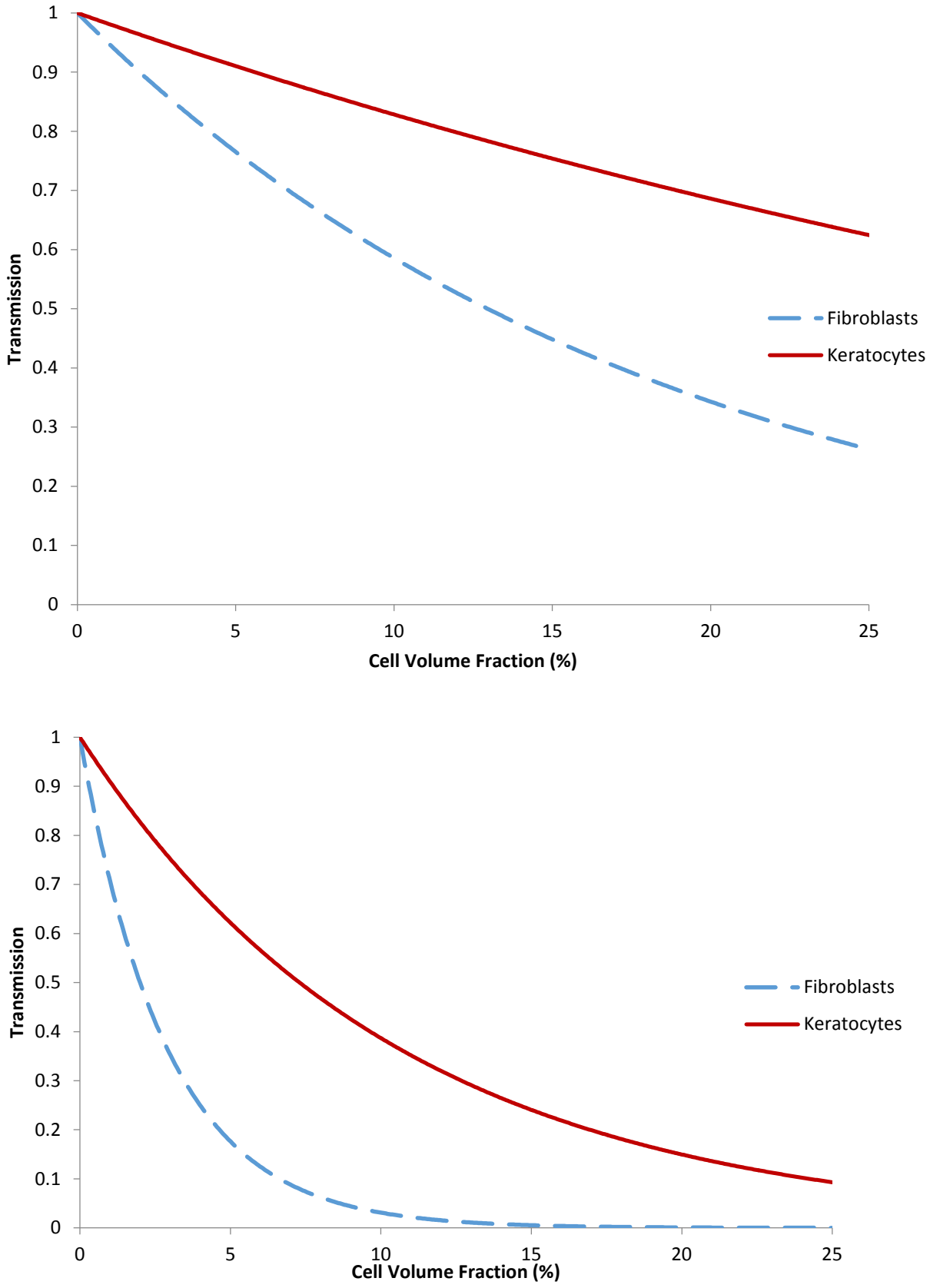

Figure 3.6: Plots showing transmission through a cornea of thickness 0.55mm for increasing volume fraction of keratocytes and fibroblasts for mean cell thickness of 1.34 microns as measured by Doughty et al (2001) (top) and for cell thicknesses from table 2.2, 9.5µm for active fibroblasts and 7.2µm for inactive keratocytes (p60) (bottom).

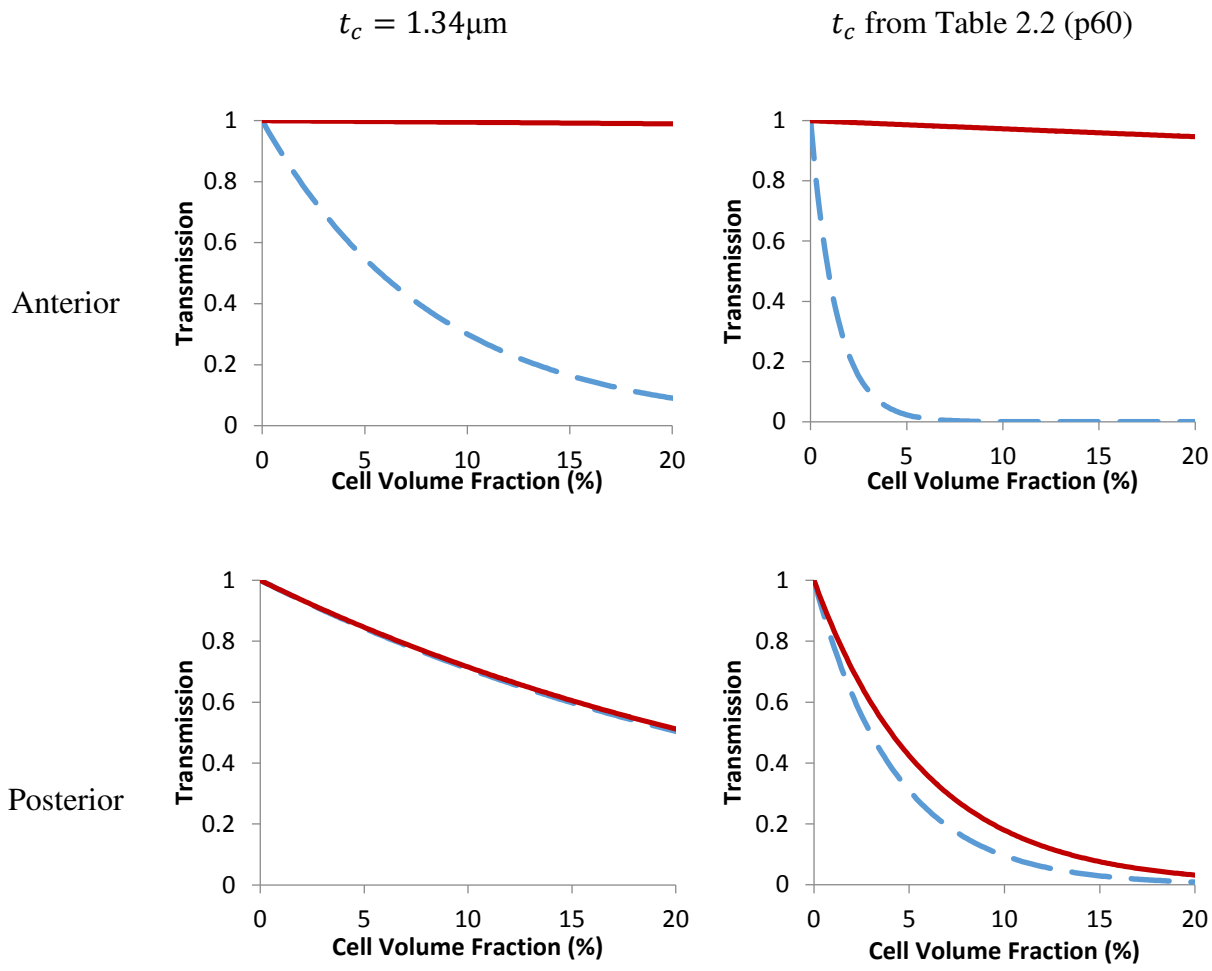

Figure 3.7: Plots to show theoretical transmissions through a cornea of 0.55mm of refractive index as measured by Patel et al (1995) populated by cells of refractive index presented in Table 2.2 and of upper and lower limits on cell thickness. These plots show the transmission given a cornea of maximum and minimum refractive index through the full thickness. Red and blue lines represent inactive keratocytes and activated fibroblasts, as with figure 3.6. t_c values used in right hand side plots are 9.4µm for fibroblasts and 7.2µm for keratocytes. Background refractive index values used are 1.380 for anterior plots and 1.373 for posterior plots. Transmission through the anterior section of the cornea appears to be much more greatly affected by the change in RI of the stromal cells than the posterior section.

3.3.2 FDTD Model

Figures 3.8 to 3.12 show the flux measured for different frequencies through a perfect hexagonal lattice of size 40x60 fibrils with holes of various sizes placed at the centre. Total flux results are presented relative to a lattice with no hole set and so can be thought of as the transmission change that is as a result of the presence of the gap in the lattice. The size of 40 units in the x direction would correspond to a lamella thickness of 2μm, giving a total number of lamellae at between 250 and 300 for a stromal thickness of between 0.5 and 0.6 millimetres. The plots show how the transmission of such lamellae would be expected to change given holes of different sizes in both x and y. Plots are presented with holes constant in the x-direction (the horizontal axis) with changes applied in the y-direction (the vertical axis). Table 3-2 shows the collated transmission data, averaged across all measured frequencies. The frequencies measured ranged from 0.07 to 0.13 units in 500 steps.

Figure 3.13 shows the results of the relative transmission of a perfect hexagonal lattice compared to a system with no lattice present. Transmission remains at around 100% for all frequencies measured, with the exception of some outlying peaks that will be address in section 3.4. This plot provides evidence that a model of a perfect hexagonal lattice will transmit perfectly as should be expected given the work of Maurice (1957), and hence that any changes from these results are solely the result of the changes that have been made to the lattice.

Figure 3.14 shows theoretical values for total transmission given different values for a single lamella and the percentage of lamellae that would be expected to be interrupted by cells. In constructing this plot, it is assumed that any uninterrupted lamella would give a perfect transmission and that a gap within a single lamella and that between two different lamellae would result in the same magnitude of loss of transmission. The output frequency is specified

in units of $2\pi c$, which are equivalent to the inverse of the wavelength. Thus by setting the fibril spacing of one unit to be 50nm, the frequency of red light corresponds to 1/14 units, or around 0.07, with blue light being around 1/8 units, or 0.0125.

Figures 3.15 to 3.20 show the change in transmission when the epsilon value of the refractive index is altered from 1 to 4 in 0.1 steps. The epsilon value represents the square of the refractive index of the dielectric medium. It was assumed for the purposes of the simulation that the fibrils were non-absorbing and so the imaginary component of their refractive index was taken to be zero. Transmission values are given relative to the natural case of fibrils with an epsilon of 1.991, which corresponds to a refractive index of 1.411. These simulations were designed to explore the results of a system with a vastly different refractive index for the fibrils, as a purely theoretical curiosity. These plots highlight one of the major strengths of the FDTD method; the model can be set up in many different ways and tested under many different conditions that could not be achieved by practical experiments. It was hoped that it may highlight some previously unconsidered aspect of the system of the cornea that in fact turns out to be critically important.

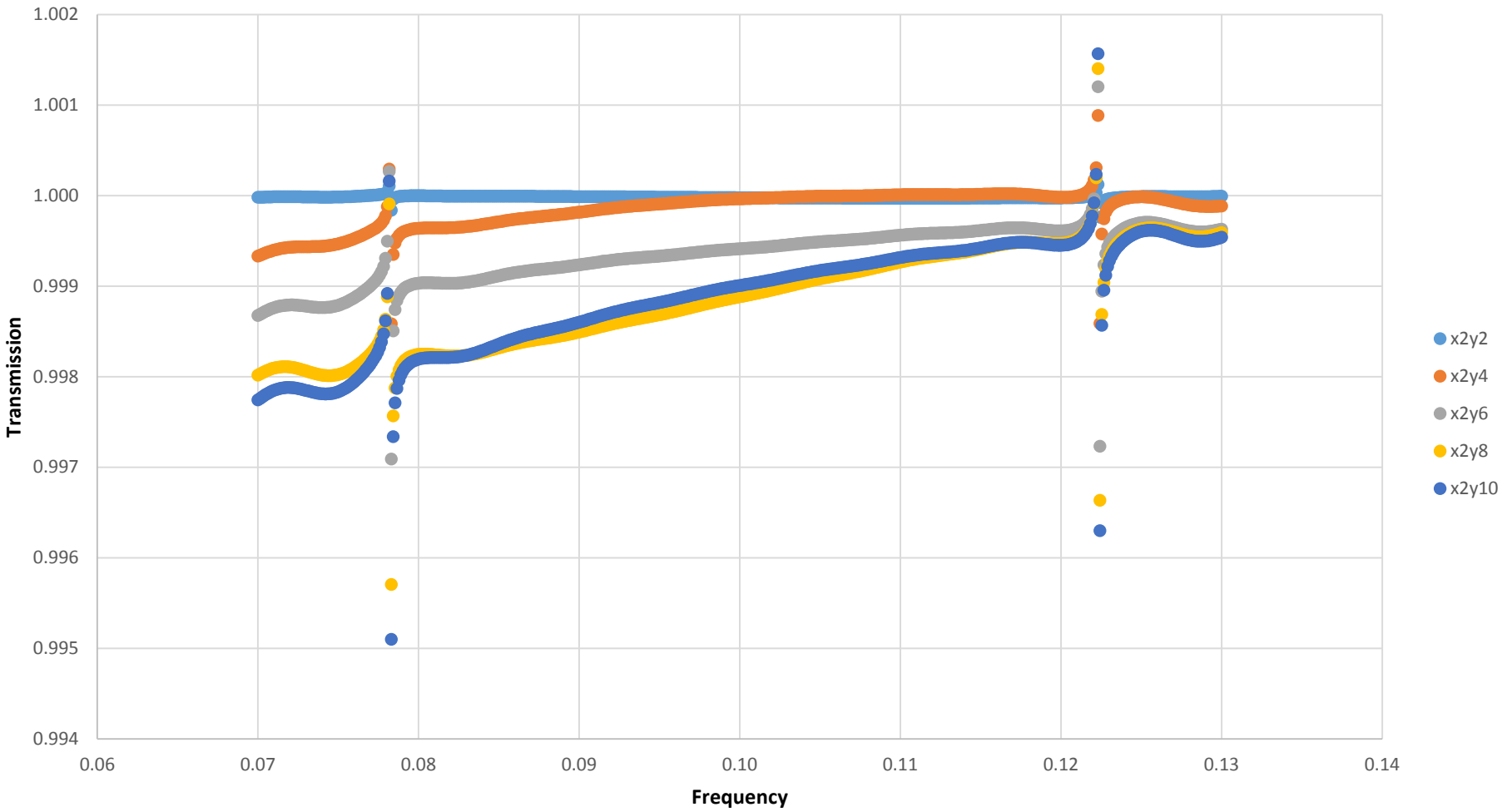

Figure 3.8: Graph showing relative transmission vs frequency through a 40x60 lattice for a hole of x=2, relative to a lattice of the same size with no hole. Frequency readings for this and all subsequent graphs in this chapter are such that 0.07 corresponds to red light of wavelength 700nm, and 0.13 corresponds to blue light of wavelength 400nm. See section 3.2.2 for more explicit details. Different colours represent differences in the size of the hole in the y-direction, with the x-direction remaining constant.

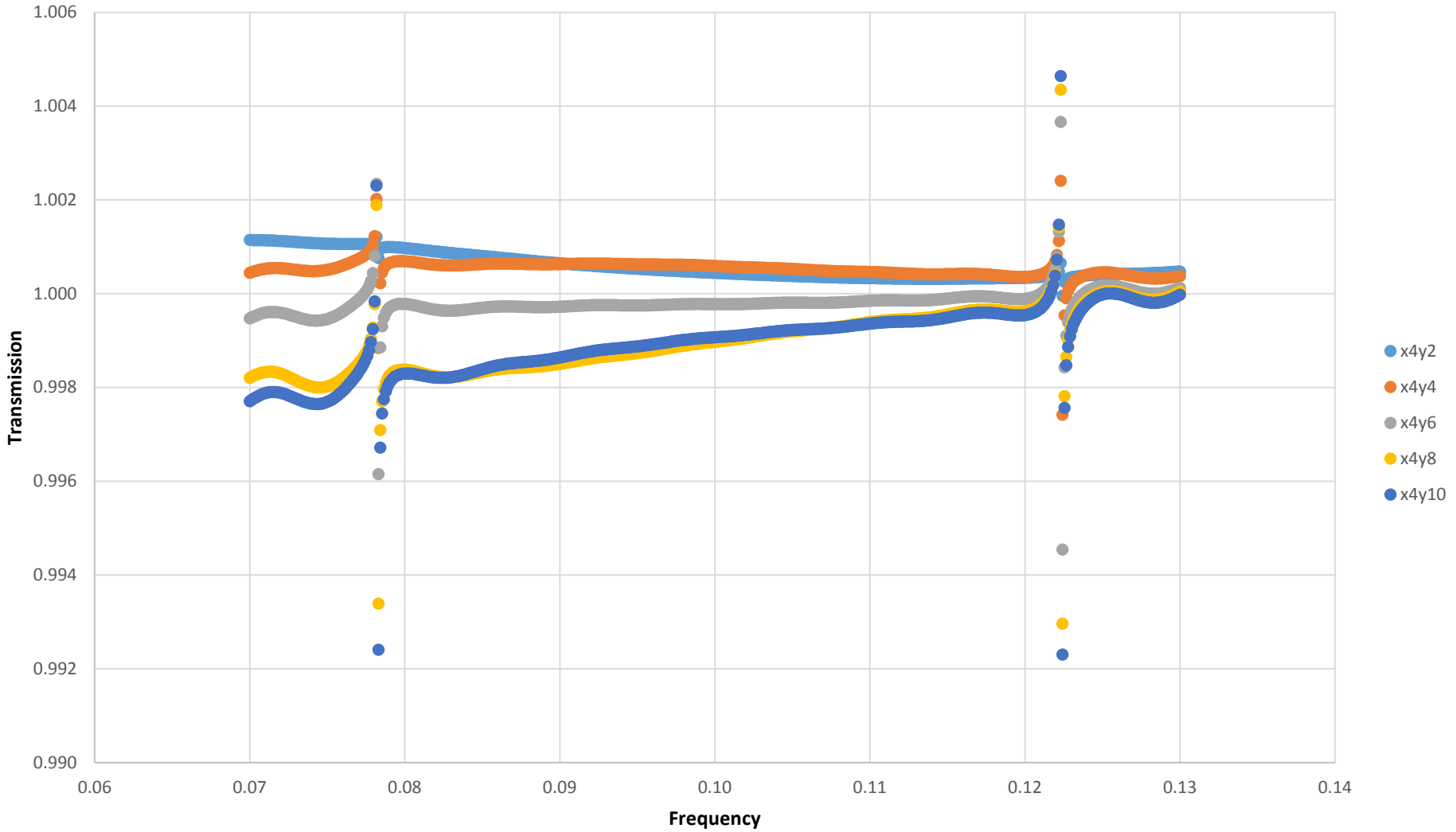

Figure 3.9: Graph showing relative transmission vs frequency through a 40x60 lattice for a hole of x=4, compared with a lattice of the same size with no hole.

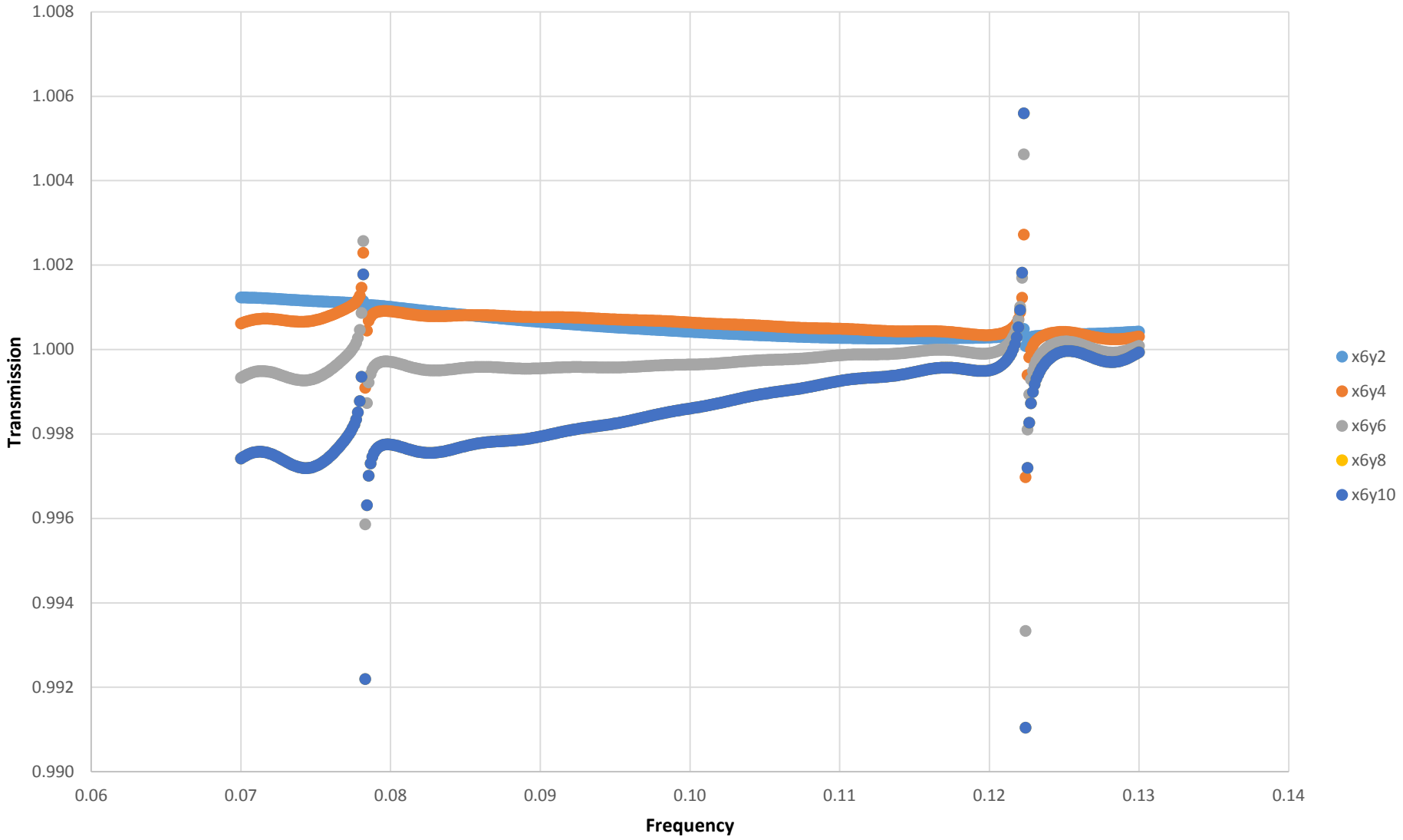

Figure 3.10: Graph showing relative transmission vs frequency through a 40x60 lattice for a hole of x=6, compared with a lattice of the same size with no hole.

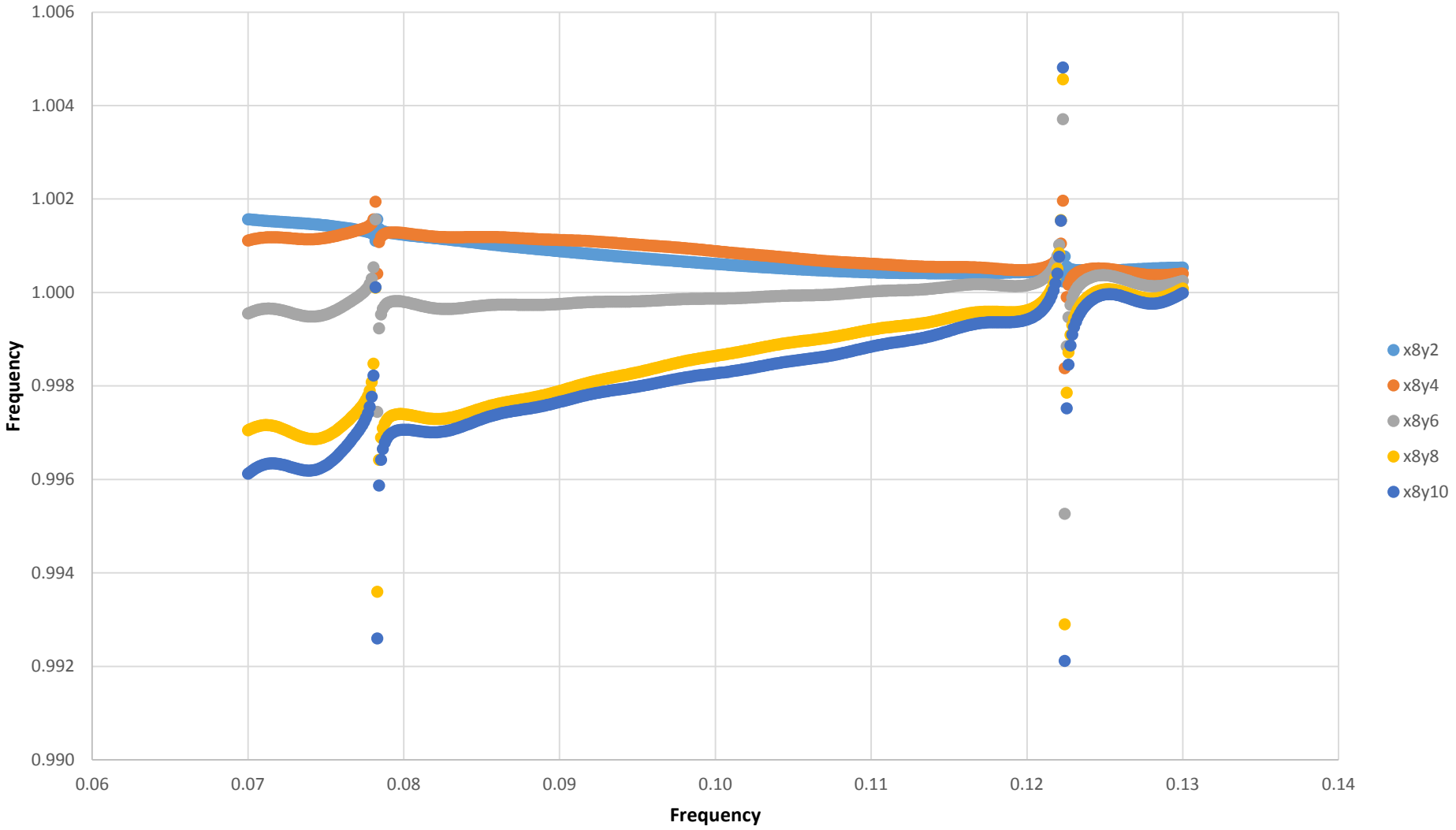

Figure 3.11: Graph showing relative transmission vs frequency through a 40x60 lattice for a hole of x=8, compared with a lattice of the same size with no hole.

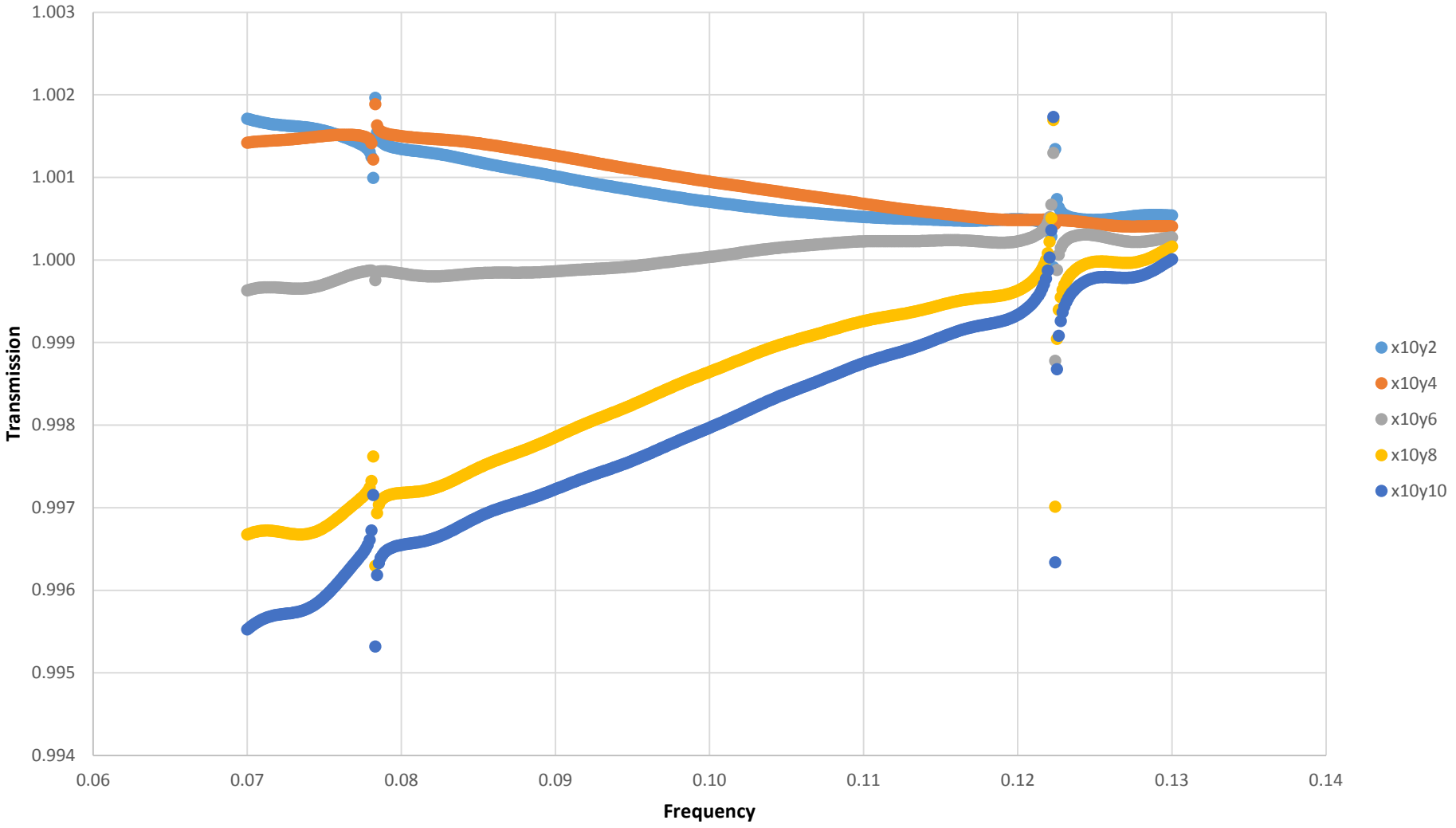

Figure 3.12: Graph showing relative transmission vs frequency through a 40x60 lattice for a hole of x=10, compared with a lattice of the same size with no hole.

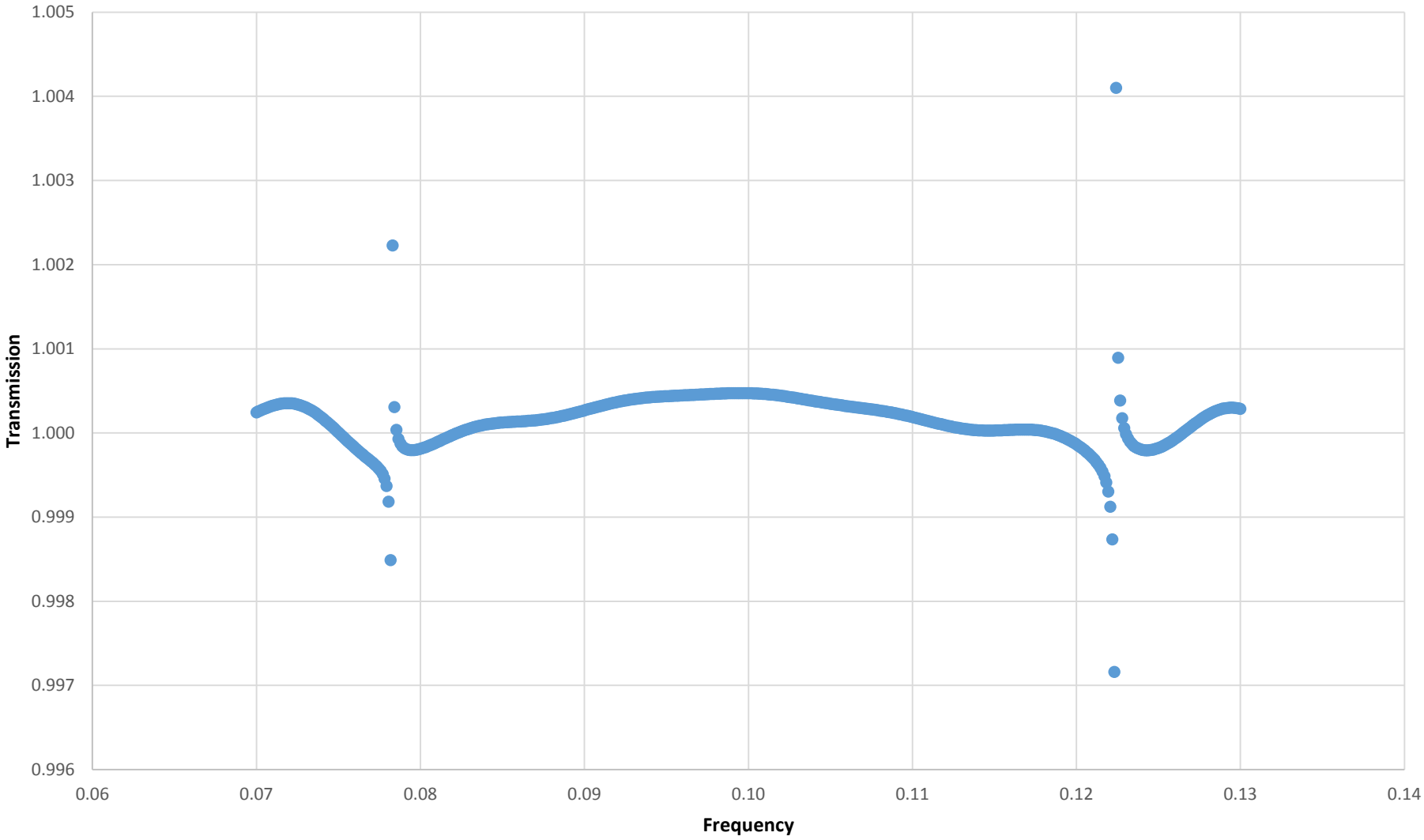

Figure 3.13: Plot showing relative transmission against frequency for a perfect hexagonal lattice of 60x40 fibrils compare to a system with no lattice present.

Table 3.2: Table showing average relative percentage transmission across all frequencies from 0.07 to 0.13 units as a function of gap dimensions.

		size of gap in x direction (units)				
		2	4	6	8	10
size of gap in y direction (units)	2	100	100.06	100.06	100.08	100.09
	4	99.98	100.05	100.06	100.09	100.1
	6	99.93	99.98	99.97	99.99	100
	8	99.89	99.9	99.86	99.85	99.85
	10	99.89	99.89	99.86	99.82	99.79

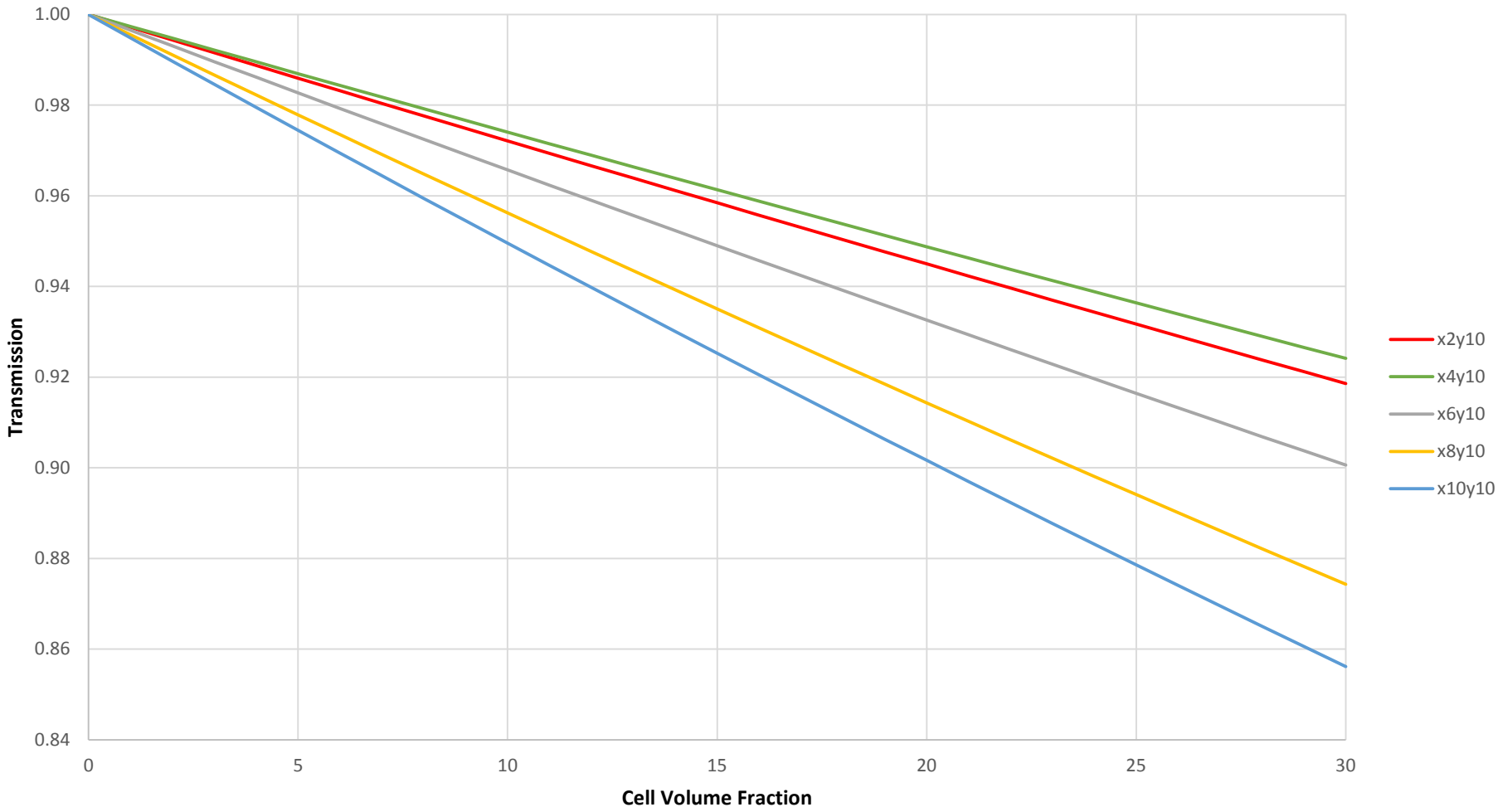

Figure 3.14: Plot showing transmission vs cell volume fraction for a cornea comprised of 200 lamellae of size 60x40, with the cell size, which is modelled by the size of the hole in the single lamella simulations, indicated in the legend.

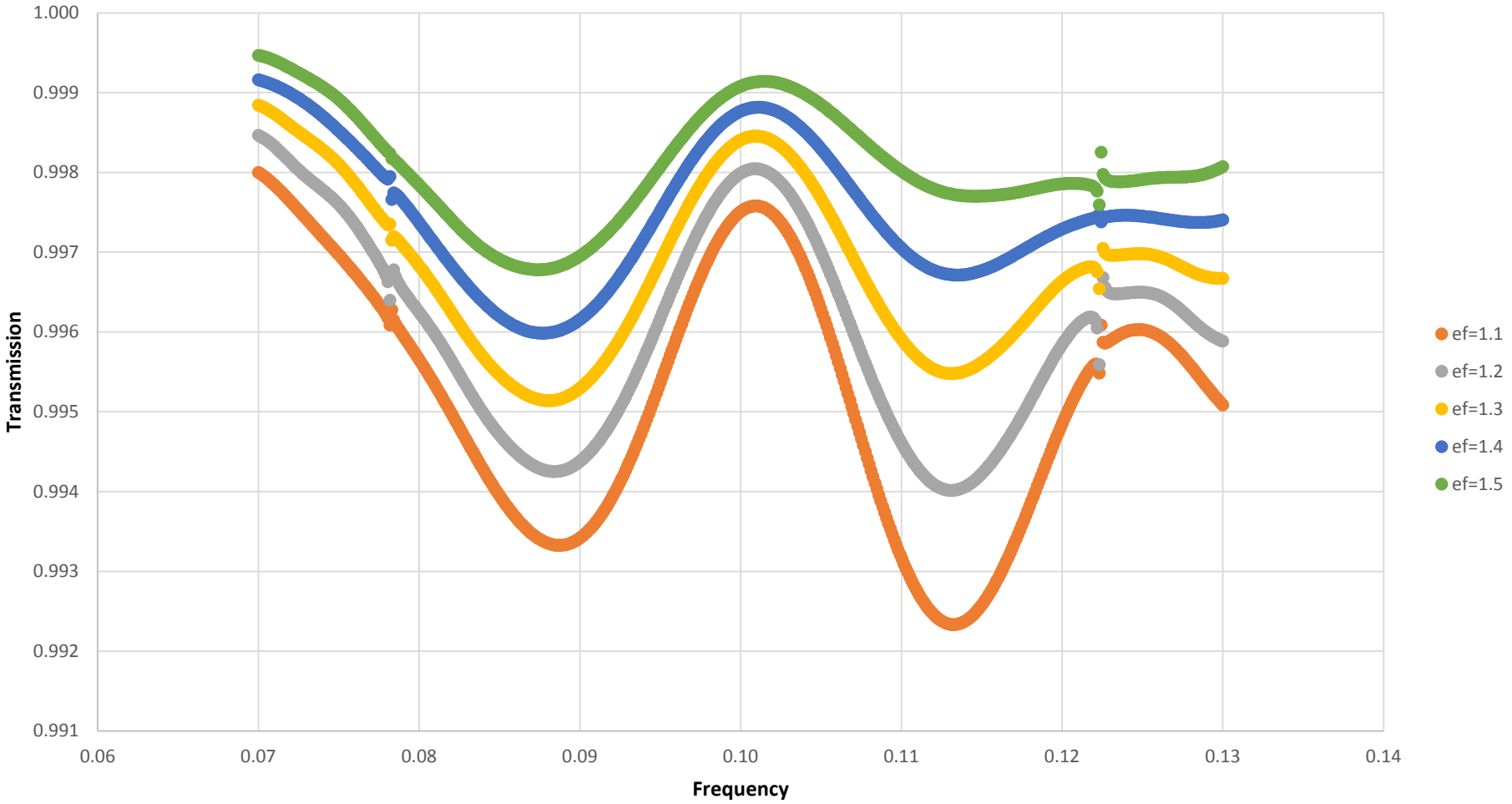

Figure 3.15: Plot showing relative transmission vs frequency for a 40x60 lattice of fibril with epsilon value between 1.1-1.5. In the legend of this and all subsequent figures in this chapter, ef refers to the epsilon value of the fibrils used in the model. The epsilon value of a material is equal to the square of its refractive index.

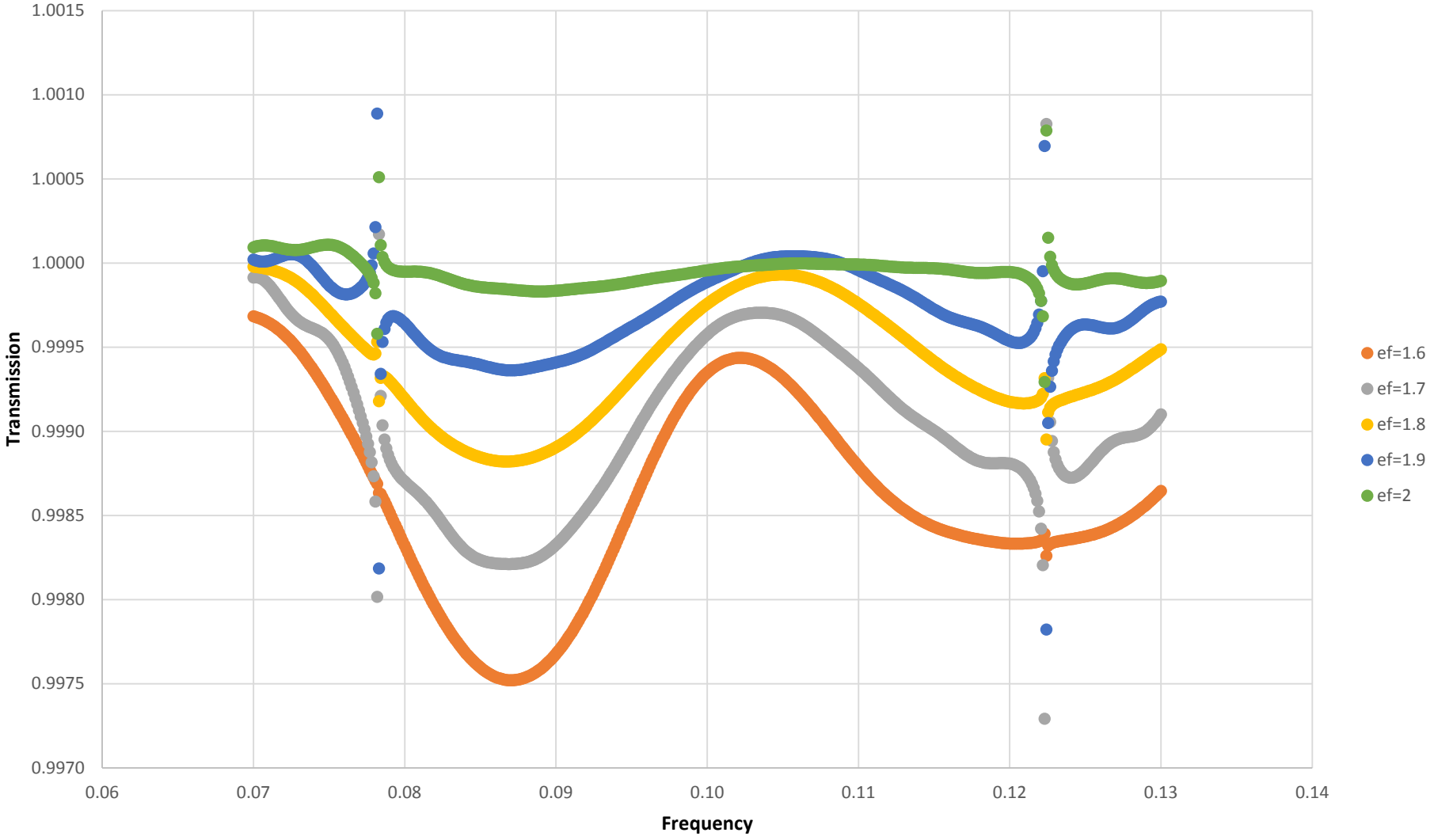

Figure 3.16: Plot showing relative transmission vs frequency for a 40x60 lattice of fibril with epsilon value between 1.6-2

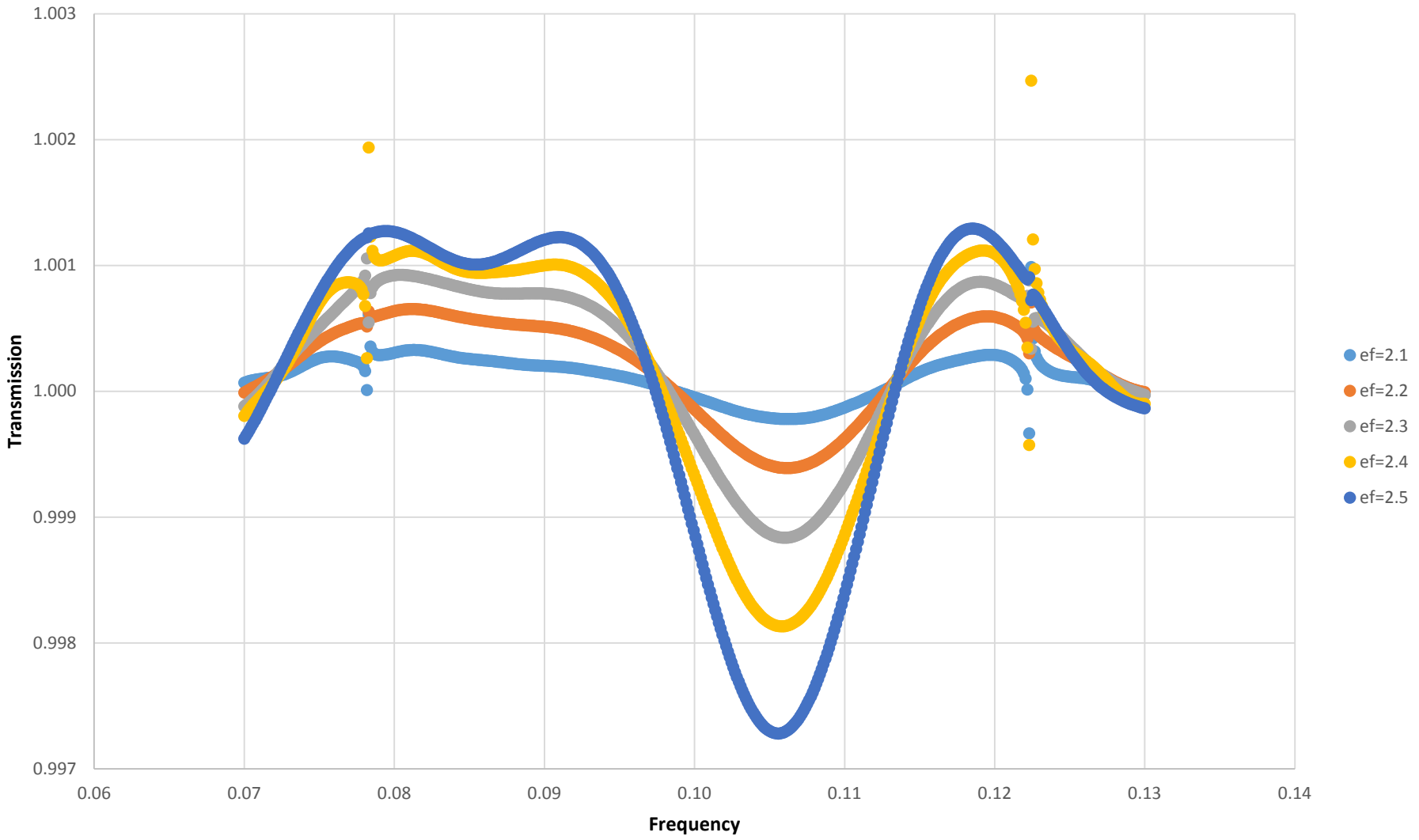

Figure 3.17: Plot showing relative transmission vs frequency for a 40x60 lattice of fibril with epsilon value between 2.1-2.5

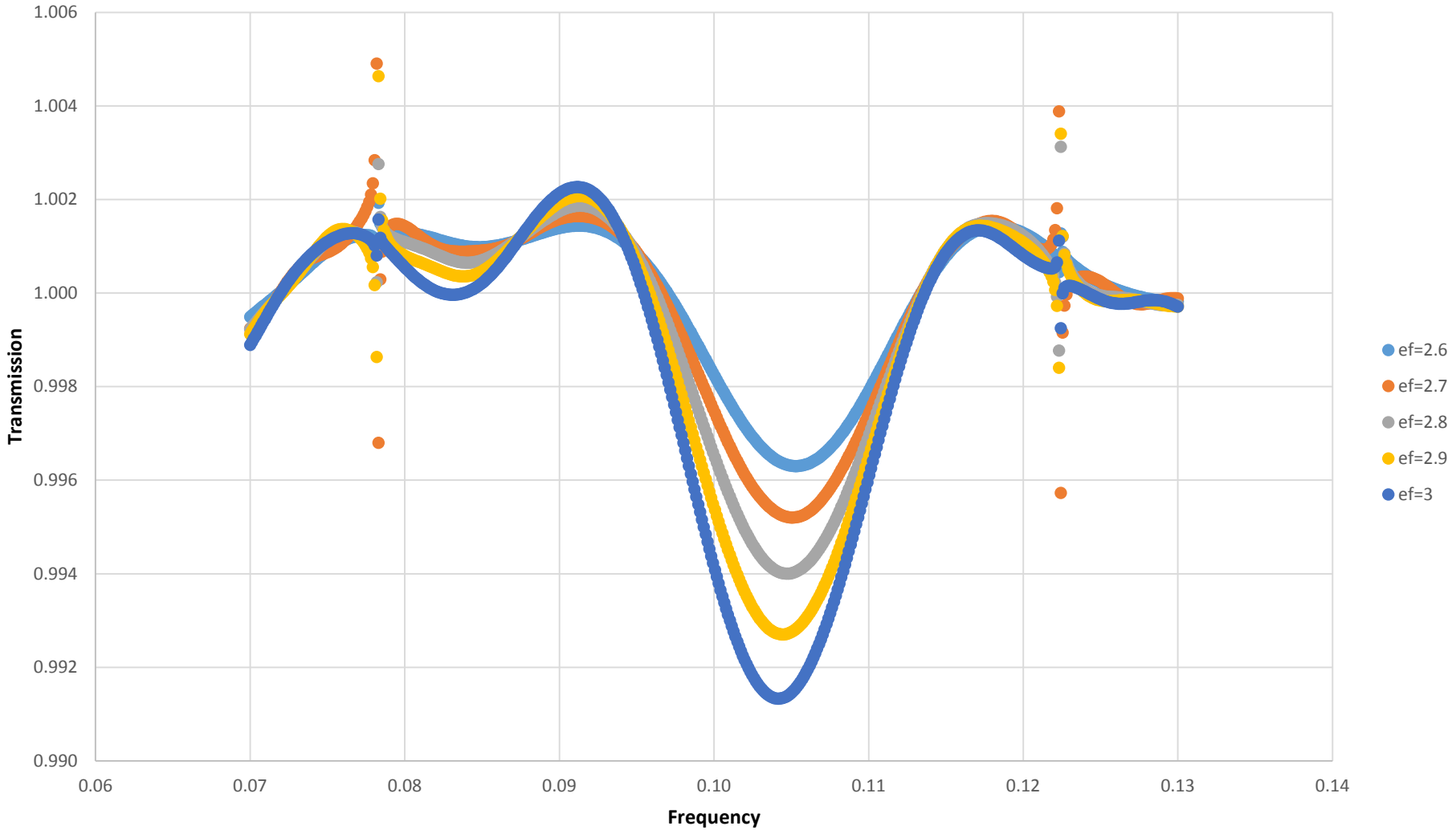

Figure 3.18: Plot showing relative transmission vs frequency for a 40x60 lattice of fibril with epsilon value between 2.6-3

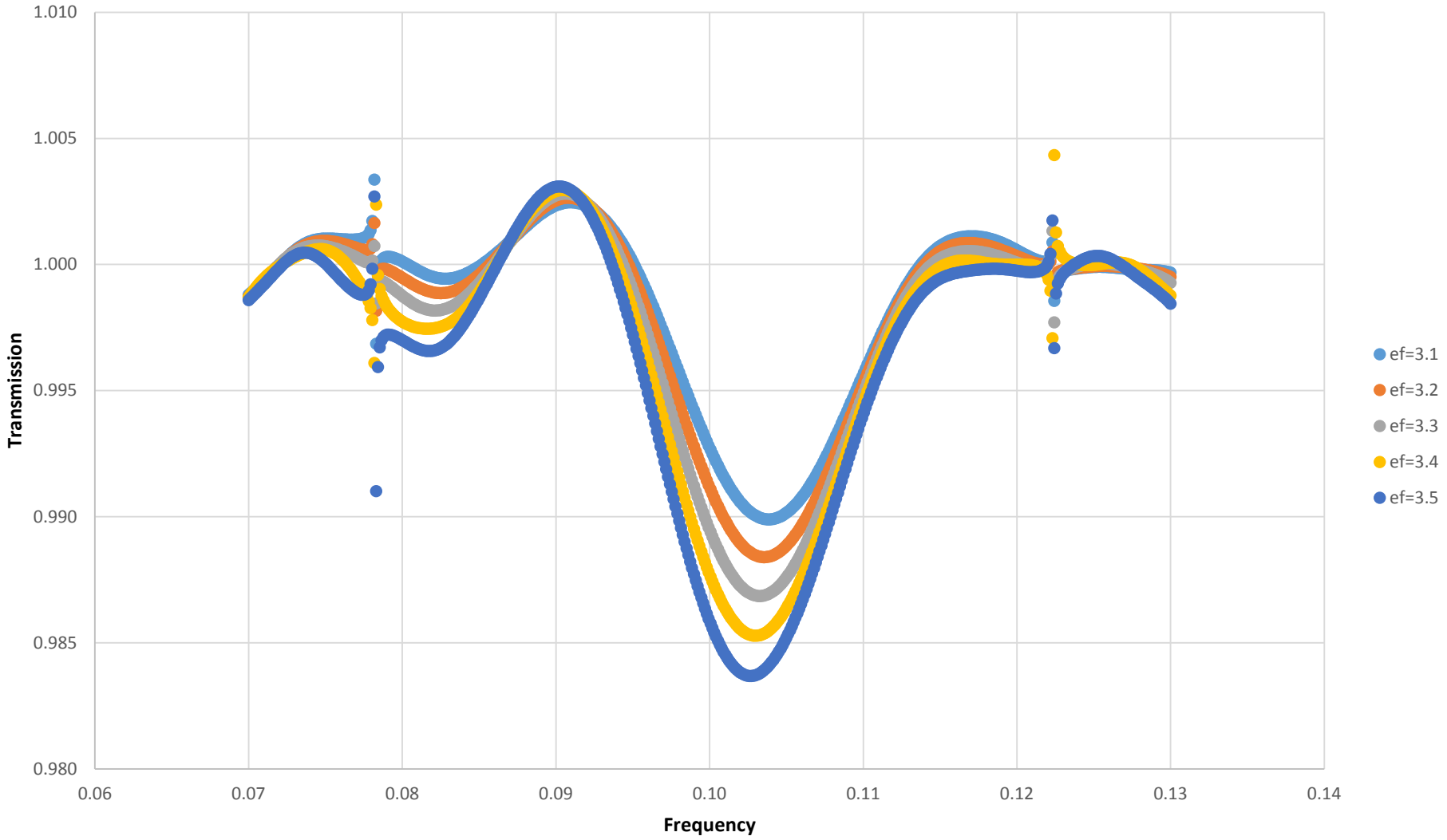

Figure 3.19: Plot showing relative transmission vs frequency for a 40x60 lattice of fibril with epsilon value between 3.1-3.5

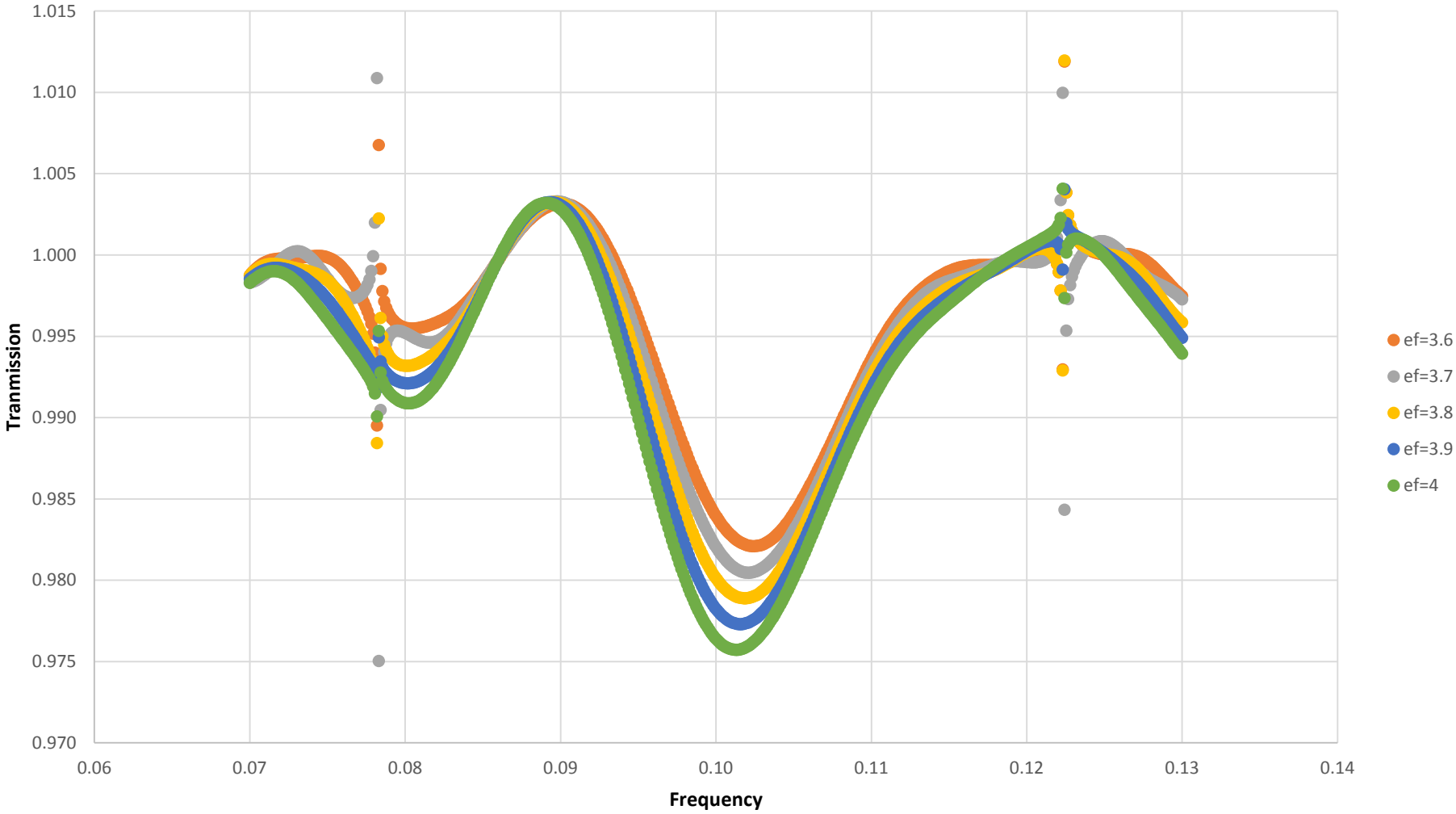

Figure 3.20: Plot showing relative transmission vs frequency for a 40x60 lattice of fibril with epsilon value between 3.6-4

3.4 Discussion

At face value, it would be natural to assume that a change in the refractive index of just 0.016±0.005 could not account for the dramatic drop in transparency that has been observed in previous experimental studies. However, even though this difference is small the results from the theoretical model show that if the volume fraction of cells were more than 10% as is observed in the anterior section of the cornea, then a change of this magnitude alone could cause the increase in scattering measured by Jester et al (1999), as well as that observed in post-operative case reports (Hafezi and Seiler 2010; Vaddavalli et al. 2012) and animal models. At concentrations of the order of 5% in the posterior section the calculated 70% transmission for a cornea populated by activated fibroblasts shows that the cells would still be a large factor in the observed haze, even if they could not account for total opacity. If however, we also take into account the increase in the cell density at the site of the wound, due to both the mobility of the newly activated fibroblasts and their propensity for mitosis during the wound healing response, the opacity could be fully explained. This would also account for the disappearance of the phenomenon after the cells either disperse, undergo apoptosis or return to their quiescent state on completion of the wound healing process. The increase in scattering being most pronounced in the anterior section of the stroma is also consistent with the results of the model, since the anterior section is that which has the highest keratocyte cell density (Prydal et al. 1998; Patel et al. 2001; Popper et al. 2004; McLaren et al. 2010) and the highest refractive index mismatch (Patel et al. 1995). It must be noted that the value of refractive index of the cornea of 1.375 is a mean value, and that a large variance could have catastrophic effect on the clarity of the cornea even if the mean remains at a reasonable value. The refractive index gradient measured by Patel et al (1995) showed the stromal refractive index to decrease through the cornea from 1.380±0.005 in the anterior section to a minimum of 1.373±0.001 in the posterior region, thus giving a maximum refractive index mismatch of 0.008 for keratocytes

and 0.015 for fibroblasts. Since the maximum keratocyte mismatch occurs in the more sparsely populated posterior region the transmission remains relatively unaffected for cell thicknesses reported from electron microscopy studies (Muller et al. 1995; Doughty et al. 2001). The larger reduction in transmission for thicknesses reported in section 2.3 may confirm that the measurement in vitro is not perfectly representative of the system in vivo, although it should be noted that figure 3.2 shows the consequence of the minimum refractive index as measured by Patel et al (1995) being represented through the full thickness of the cornea, and not just in the posterior section. As such this is an absolute lower limit for transmission through a healthy cornea populated with quiescent cells. Figure 3.3 shows the refractive index mismatch for fibroblasts is always consistent with the observed haze and also shows that, no matter the thickness of the cells, is always more pronounced in the anterior section where the mismatch is greatest.

The results acquired from the FDTD model showed both expected and unexpected effects. The most glaring feature of the figures in section 3.3.2 is the asymptotic behaviour that can be seen in every simulation at two particular frequencies. The discontinuities appeared at frequencies of around 0.122 and 0.078, corresponding to a wavelengths of approximately 410nm and 640nm respectively. At this time this effect is unexplained. If some internal resonance were the cause of the peaks, one should expect to find only one resonant mode within a specifically arranged lattice. With no further explanations forthcoming, this is left as an open question. However since the presence of the peaks is consistent throughout all the simulations, it does not appear to significantly detract from the comparative assessment of the results. The presence throughout all simulations appears to suggest the origin lies as an artefact of the process. The rest of this discussion will ignore these peaks for the purposes of qualitative and quantitative comparisons.

The presence of a lattice does not in of itself effect the transmission results, as Figure 3.9 shows. Transmission relative to the lack of a lattice structure remains at close to 100% throughout all frequencies. This result agrees with the theoretical predictions of Maurice (1957) who proved mathematically that a perfect hexagonal lattice would transmit perfectly, due to the interference from multiple fibrils being totally destructive in all directions except the direction of propagation.

Figures 3.8 to 3.12 give the transmission of a lattice with holes of increasing size. As expected, increasing the size of the hole does in general appear to affect the total transmission through the lattice structure, with the transmission decreasing for holes of increased size in the direction perpendicular to the propagation. The size of the gap in the direction parallel to the propagation direction appears to be less important, with transmission remaining quite static for constant y. This is in direct conflict with the findings of section 3.2.2, where the cell thickness was considered to be the dependent variable. The total magnitude of the transparency loss however is of the same order. Figure 3.14 shows the transparency loss that could be expected if the cornea were populated by 250 lamellae with various cell volume fractions. The plot shows similar transparency losses as that shown by the Mie scattering model for keratocytes in figures 3.6 and 3.7. Even with the very largest gap in the lattice, the transmission remains above 90% at the 5-15% range that represents the most recent measurements of the cellularity of the cornea, and remains above 85% even at concentrations of 30%, double the highest measured values.

Also unexpected was the apparent frequency dependence of the transparency loss. Much more loss was measured at the longer wavelength red end of the visible spectrum, for nearly all simulations, with the effect becoming more pronounced for larger gap sizes. This is also in conflict with the Mie scattering model, since Mie scattering is usually considered to be isotropic, with no strong wavelength dependence.

Transmission changes as a result of the epsilon value of the fibrils were more in line with expectations. Values become more uniformly close to 100% the closer the fibrils are to an epsilon of around 2, which corresponds to a refractive index in the region of 1.4. At values much higher and much lower, transparency drops overall, although there appears again to be a curious frequency dependence for all epsilon values. The presence of transmission values of much greater than 100% for fibril epsilon values of between 2 and 3 might indicate a form of inelastic scattering is causing a redistribution of the flux between different frequencies. If this is the case, it might indicate that the cornea cannot be modelled only in terms of Mie scattering, since this kind of process is considered to be purely elastic, and that a secondary inelastic series of scattering events should also be included. Whatever the cause of this phenomenon, it is of more importance that these peaks are more than cancelled out by the troughs in the 0.095 to 0.115 frequency range. This causes the maximally efficient lattice over the total visible range to be the scenario with fibrils having a refractive index of near 1.41, and the extracellular material having a refractive index of around 1.38. The question that has been overlooked so far throughout these experiments and the literature is concerning the importance of the refractive index of the fibrils. The FDTD model presented here seems to suggest that a fine-tuned refractive index is very important.

This model is so far limited to the case of a perfect lattice, which does not fully represent the real world situation of the system in vivo. Future work could focus on the possibility of adding a small perturbation to each cylinder within the lattice, to test the theory that only a short range order is a necessary condition for a transparent cornea. A further improvement could focus on the transfer from two to three dimensions. This would not only bring the model closer to the real system, but it would also allow the gap in the structural lattice to be placed between lamellae rather than within it. It is unclear so far whether the absolute position of the gap is of paramount importance. There is at this point no obvious reason to suspect the position of the

cell within or between lamellae should in of itself have an effect on the overall transmission though it, but having a system that allowed multiple different directions of lamellae would permit the movement of the gap to answer this question definitively.

4 Keratoconus Tissue Study

4.1 Introduction

4.1.1 Aarhus University Hospital Bank Donated Tissue

The structural biophysics research group secured the donation of corneal samples provided by the Danish Cornea Bank (Aarhus, Denmark), under the auspices of the Aarhus University Hospital. These samples were rare in that they were provided from a donor that had previously been diagnosed with keratoconus, and treated with a penetrating keratoplasty (PK) transplant, which was the standard method of treatment for advanced cases at the time. The samples received consisted of a 16mm diameter button of which between 11-13mm was corneal tissue, surrounded by 3-5mm of sclera. The corneal tissue consisted of an outer section of original, and therefore keratoconic, tissue surrounding an inner clear section where the transplanted tissue had been grafted. At the interface between the two tissues was an opaque scar that was clearly visible. The patient underwent PK operations in both eyes, 12 years before death in the case of the left eye and 28 years in the right.

The characteristics of such a tissue make it the ideal candidate for the study of both corneal scarring and the possibility for the investigation into the mechanisms of recurrence of keratoconus after PK. Despite the high success rate of PK operations, 98.9% successful (n=93) at 46 months, with a postoperative visual acuity of 20/40 or better in 86% of cases (Lim et al. 2000) and 94% success with a mean failure time of 13 years (n=112) (Pramanik et al. 2006) are among the rates quoted in the literature, there have been a number of reports of failures owing to the suspected recurrence of the disease within the grafted tissue (Abelson et al. 1980; Nirankari et al. 1983; Thalasselis and Etchepareborda 2002; Patel et al. 2005). The reasons for this are not well understood, with suggested explanations ranging from a genetic predisposition

(Stoiber et al. 2000) to vigorous eye rubbing as a result of irritation (Koenig 2008; Yeniad et al. 2009). It is possible of course that the cornea simply may never recover its structural integrity after drastic full thickness wounds, and this is what causes the grafts to fail in a manner resembling keratoconus. The literature already contains a large body of evidence showing that normal stromal structure is not recovered with full PK grafts as it is with wounds that are more superficial (Morrison and Swan 1982a, b, 1983; Lang et al. 1986; Farley and Pettit 1987; Melles and Binder 1990; Hayes et al. 2010). What is not known is if the failures of PK grafts are being caused by a failure of the recovery of the structure of the stroma, in which case the reason for the failure may be attributed to surgical techniques, or if the grafts are being adversely affected by the surrounding tissue until they exhibit keratoconus symptoms. If abnormal features can be found within a graft that had never been diagnosed as a failure, then it could be possible to link the failures of other grafted tissue to the abnormalities found. Any abnormality would likely be extremely subtle, since even in the small cases where recurrent keratoconus has been suspected the disease has not presented until years after the initial PK.

The scarred area of the Danish eye bank samples, where the graft was sutured in place together with the original tissue, would also be of great interest. Scarring in the cornea is normally seen in transmission electron microscopy studies as a disorganised arrangement of corneal fibrils, as opposed to the regular repeating lamella structure of healthy transparent tissue, even after healing for many months (Connon and Meek 2004). The scar in this tissue had many years to heal and yet was still clearly visible. Long term studies of scar tissue generally only run to a number of months in animal models, up to 21 months in Rawe et al (1994) for example, so it is not currently known if micrographs of tissue allowed to heal for many years will show a similar structure or any signs of a continuous healing process. Given that the scar tissue is still clearly visible, the latter is considered unlikely, indeed it might be more sensible to expect scar

tissue from this graft to exhibit an increase in disorder, due to the long term pressure put upon the cornea in everyday situations.

4.1.2 Electron Microscopy

As part of this study, electron microscopy (EM) was used in order to qualitatively compare healthy and diseased samples. The full introduction to electron microscopy has already been given in section 1.8. However, qualitative analysis by its very nature is open to interpretation, so, in addition, quantitative analysis, in the form of fibril radial distribution functions, was also carried out. In a healthy cornea, calculations of the number of fibrils found at a given distance from any reference fibril (radial distribution function) would be expected to show a nearest neighbour peak, demonstrating the short range order within the lattice. Fibrils do not usually coalesce and remain uniformly spaced. However, even in healthy corneas, there is no long range order evident from electron micrographs, thus there are very few peaks in the radial distribution function after the first. Instead, beyond the nearest neighbour peak, the fibril number density reduces and begins to oscillate around a stable line corresponding to the overall fibril number density in the tissue.

Examples of normalised radial distribution functions from a system with short-range order (corresponding to a healthy cornea) and a system with a random distribution of fibrils (representative of a severely pathological cornea) are shown in Figures 4.1 and 4.2, respectively.

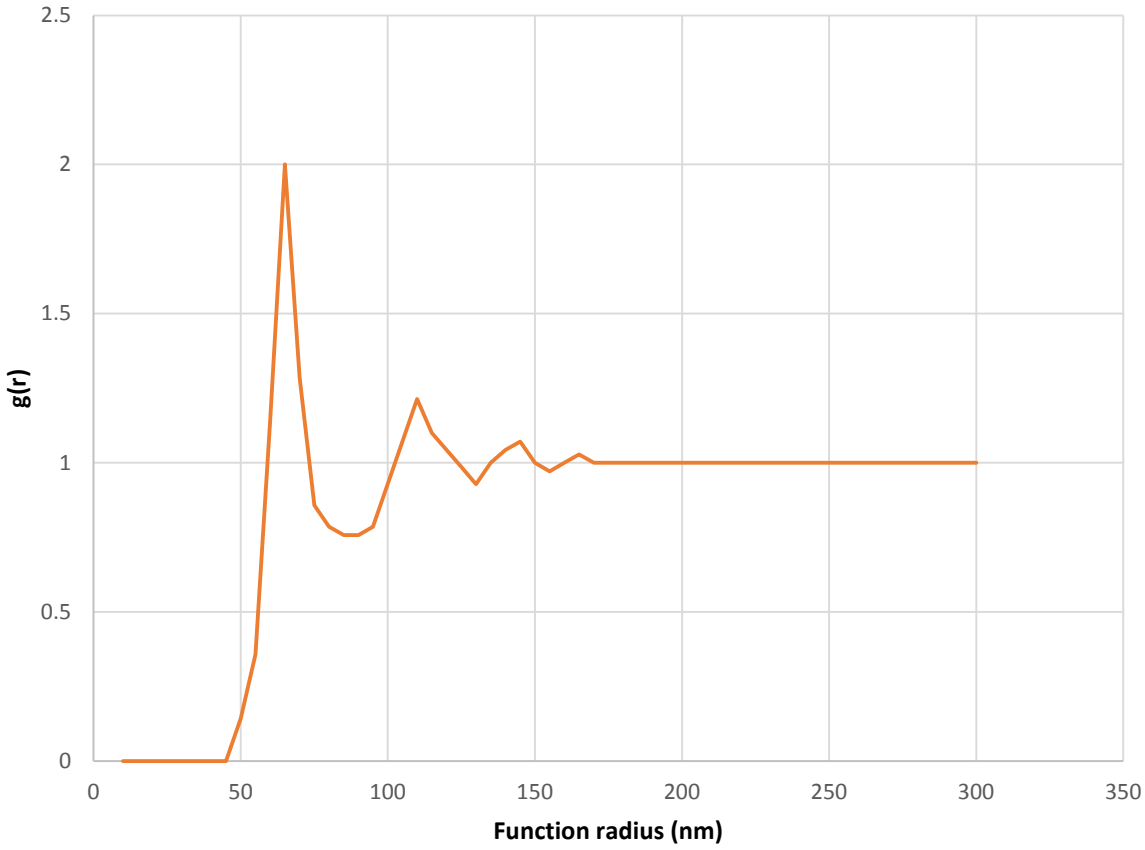

Figure 4.1: Example of fibril spacing function that would be expected of a healthy sample. There is an exclusion zone at lower separations corresponding to the space between the surfaces of adjacent fibrils. After this there is a strong nearest–neighbour peak corresponding to the average centre-to-centre spacing of nearest neighbours. The function then quickly shows damped oscillations about the average number density. Here the data are normalised such that this value equals one, such that g(r) is the relative probability of finding a fibril within a certain radius.

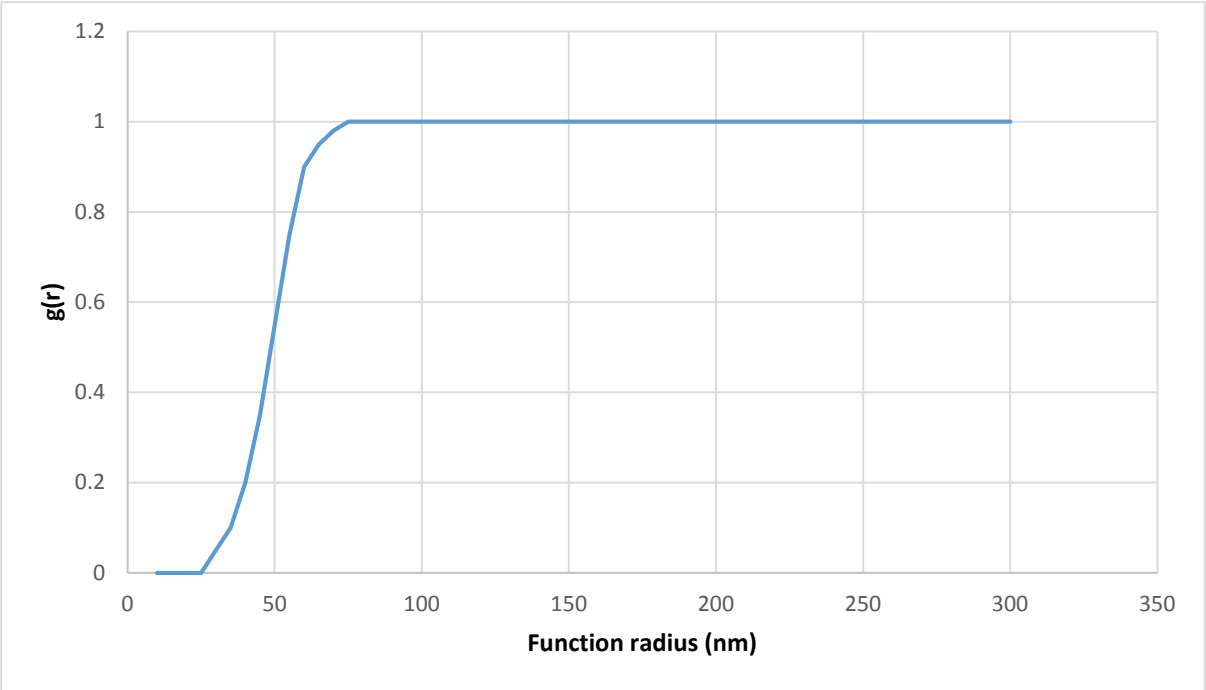

Figure 4.2: Example of fibril spacing that would be expected from a cornea with no short term order. This is assuming that proteoglycans still act to provide a minimum separation. If no proteoglycans were present then the signal at lower spacings would increase.

4.1.3 X-ray Scattering

The improvement of technology regarding x-ray radiation has allowed modern researchers to be able to direct intensely focussed beams of x-rays on a timescale that is significantly quicker than when the first diffraction patterns were produced. X-ray scattering allows direct measurement of interfibrillar spacings that is an average of the whole tissue through which the x-ray beam passes, and is therefore more representative of the bulk tissue than electron microscopic measurements. In addition, there are no processing requirements such as dehydration and embedding of the tissue. X-ray scattering was therefore used to supplement the electron microscopy (Boote et al. 2013; Appendix C). It was also used to quantify changes in the bulk organisation of the collagen lamellae in the specimens.

4.2 Materials and Methods

4.2.1 Tissue Details

One pair of post-mortem eyes was obtained from The Danish Cornea Bank of Aarhus University Hospital (Aarhus, Denmark). The patient had a history of bilateral keratoconus which was treated in both eyes with penetrating keratoplasty (PK). The age of the recipient at death was 79 years. Unfortunately the age of the donor was not available. PK grafts had been completed 12 and 28 years prior to death in the left and right eye, respectively. The whole corneas and some scleral tissue were removed from the globes as a 16mm diameter button, with the position marked with a suture at the 8 o'clock position in the right eye and the 4 o'clock position in the left eye from the point of view of the observer. These buttons were then immediately wrapped in polyvinylidene chloride film to prevent dehydration, and stored at -80ºC. The buttons were observed and photographed prior to their use in X-ray diffraction and EM studies, and showed a distinct and obvious discontinuity presumed to be the boundary between the original tissue and that of the donor. In addition, both eyes showed regions of abnormal opacity in the peripheral cornea, in the temporal section of the left eye and in both the superior and inferior sections of the right eye (Figures 4.3 and 4.4).

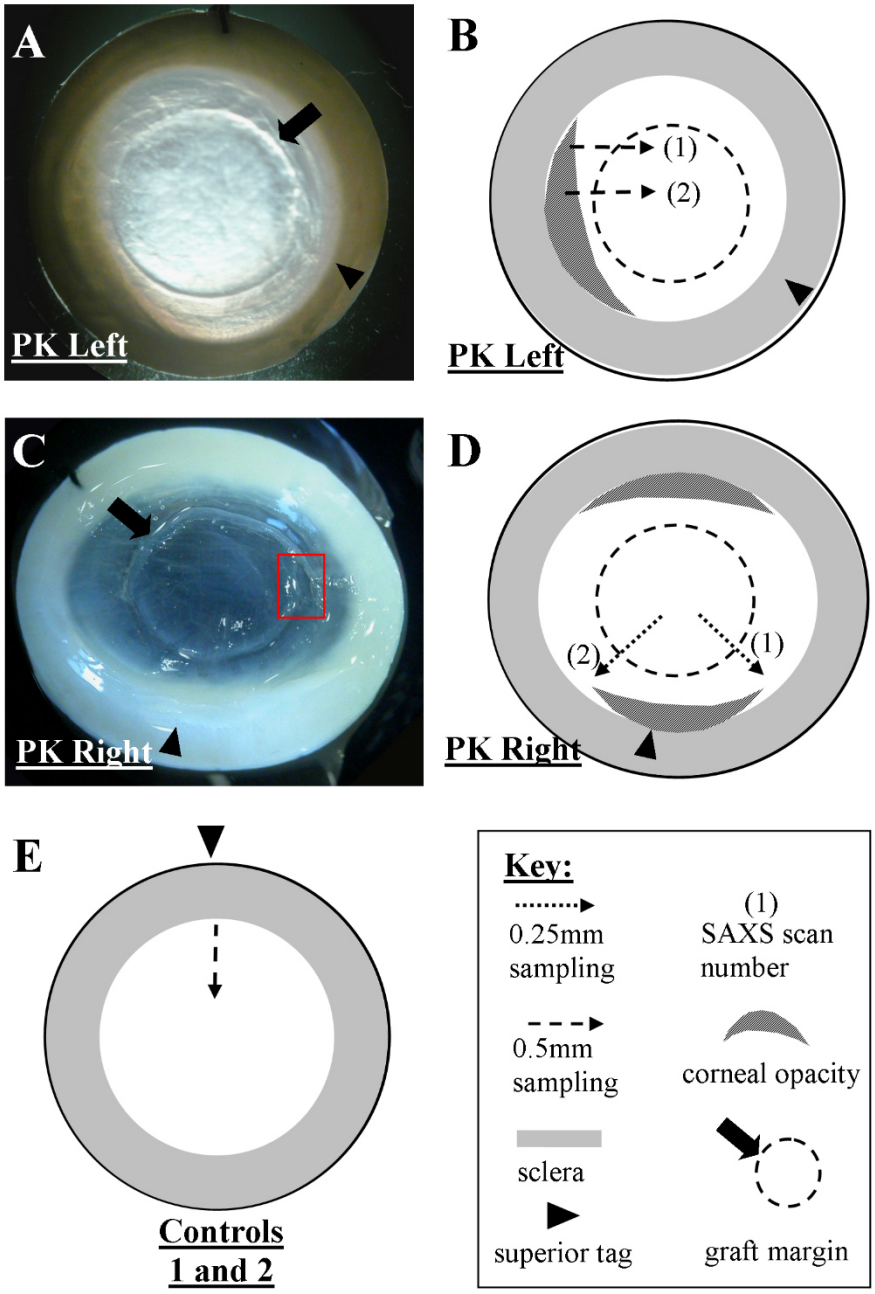

Figure 4.3: Appearance of specimens for WAXS and SAXS studies of left (A) and right (C) eyes. Red rectangle in C indicates a discontinuity at the wound margin (Boote et al. 2013).

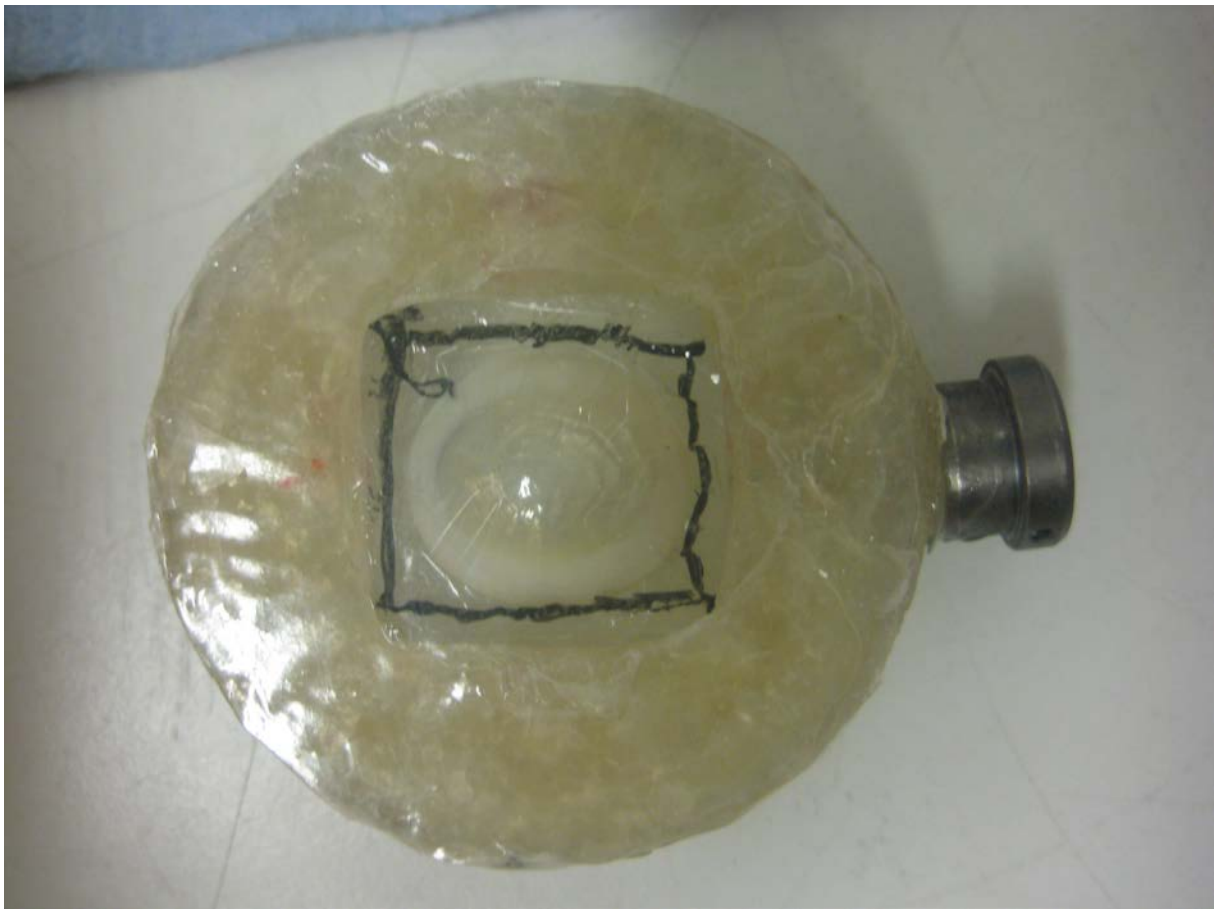

Figure 4.4: Image showing tissue from right eye within a holding case that was used during x-ray diffraction pattern acquisition. Tissue was wrapped in conventional wrapping film (polyvinylidene chloride) to prevent dehydration.

No diagnostic history was available for the right eye. For the left eye, the apex of the keratoconus cone was located in the inferior/temporal section of the cornea. Quantitative measurements of both thinning and the resulting astigmatism were not possible due to irregularities on the corneal surface. Vascularisation in the peripheral cornea was reported five months after PK as far as the sutures, which were removed after 12 months. No further complications were reported after a follow up examination at 14 months post-PK.

Control tissue was provided by Bristol Eye Bank. The patient was a male aged 65 years at time of death, from liver failure, and no history of corneal diseases was recorded in his medical history. The tissue was excised 20 hours post mortem, and quarantined for one month in DMEM solution.

4.2.2 Preparation of Electron Microscopy Samples

Samples were cut from three areas from the Danish Eye Bank donated tissue, after WAXS and SAXS studies had been completed. Sections were taken from the nasal section of the scar region of the left eye and the centre of the transparent graft (Figure 4.5).

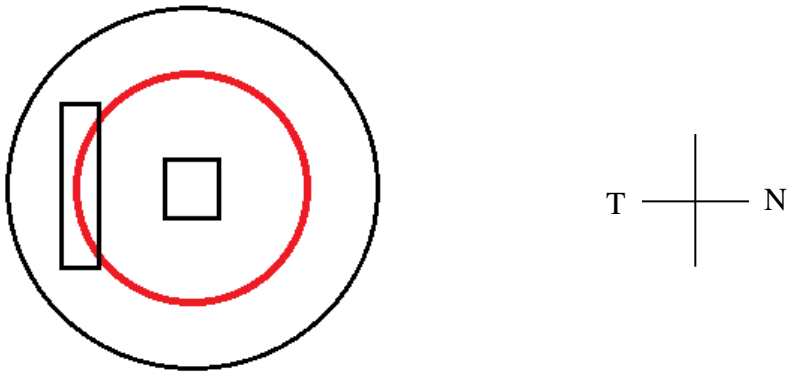

Figure 4.5: Schematic diagram showing the areas where tissue was taken from the original donor cornea. The red line indicates the scar, inside of which was the clear grafted tissue from the PK operation. Compass indicates nasal (N) and temporal (T) directions.

These samples were prepared according to the methods developed by Scott (1980; Scott and Orford 1981). Samples were fixed overnight in 2.5% glutaraldehyde in 25mM sodium acetate buffer containing 0.1M $MgCl_2$, 0.05% cuprolinic blue stain, a cationic stain developed by Scott (1981), and 0.1M HCl to adjust the pH to 5.7. Samples were then placed in sodium acetate buffer for three 5 minutes intervals consecutively and then placed in a 0.5% sodium tungstate solution a total of three times for 5 minutes each time. After the third wash the tissue was dehydrated using increasing concentrations of ethanol, from 50% up to 100%, for 15 minutes at each concentration. After the 100% ethanol wash, the ethanol was replaced with propylene oxide for two 15 minute intervals and then a 1:1 mixture of propylene oxide and araldite resin

for 1 hour. The araldite resin was made by mixing a 46.7:53.3 solution of araldite monomer CY212 and DDSA hardener with 0.6% BDMA accelerator, until a highly viscous resin of a red-orange colour was produced. The tissue was then placed in the resin for 2-3 hours, with the resin then replaced. This replacing of the resin is carried out 5 more times. At each stage the vials were placed in an automatic rotator (Agar Scientific, Stanstead, UK) for the time between solution and resin changes. Tissue samples were then placed in moulds and warmed in an oven at 60ºC for 24 hours until the resin became solid.

These solid blocks were then cut to size using a razor blade until a trapezoidal platform was fashioned around the embedded tissue and ultra-thin (90nm) sections of the tissue were cut using an ultramicrotome and glass knife. These sections were sliced from the block by slowly passing it past the glass knife while the block fixed to a mounted arm, such that a ribbon of trapezoidal sections were formed. The gold interference colour to the section confirmed the correct thickness. These thin sections were then floated onto a small water lake attached to the triangular glass knife, and were then mounted onto a copper grid. These section were subsequently stained with 0.5% uranyl acetate solution for 5 minutes and 1% phosphotungstic acid for 30 seconds. Excess stain was removed by placing the grid on a water droplet for 1 minute, for 4 times each. Images were produced using a transmission electron microscope (JEOL 1010) operating at 80kV and a Gatan ORIUS SC1000 CCD camera.

4.2.3 Wide Angle X-ray Diffraction Study

Following the small-angle x-ray scattering (SAXS) data collection carried out by Boote et al (2013), the samples were placed in 4% paraformaldehyde and stored at 4ºC until used for wide-angle x-ray scattering (WAXS). Previous studies have established that fixation in paraformaldehyde does not affect the corneal collagen parameters measures by WAXS studies (Boote et al. 2006). WAXS patterns were subsequently recorded using the I02 beamline at the

Diamond Synchrotron (Didcot, UK) across the whole of the specimen at 0.25mm intervals in both horizontal and vertical directions. The x-ray beam was tuned to a wavelength of 0.98Å and cross-sectional diameter of 0.2mm, with an exposure time of 8 seconds. The specimen was mounted in a holder with the anterior surface orientated towards the x-ray beam, and translated to various positions using an integrated motorised stage. The original curvature of the specimen was preserved and dehydration was prevented with the use of polyethylene film. The precise alignment was achieved in real time using a microscope mounted to point along the x-ray beam. WAXS patterns were recorded using a CCD detector placed 550mm behind the specimen.

4.2.4 Fibril Orientation Mapping

The WAXS pattern from cornea consists of a diffraction ring corresponding to the reflection from the 1.6nm spacing of the collagen molecules within the fibrils, background scatter from non-collagenous components, and water scatter. These patterns were analysed as described in detail elsewhere (Meek and Boote 2009). In brief, the program Optimus 5.1 was used to analyse a complete set of patterns by measuring the x-ray scatter intensity in concentric circles outward from the central point of each pattern. In-house macros were then used, first to remove background scatter from non-collagenous components of the tissue, and then to integrate the intensity of the reflection arising from the collagen intermolecular spacing, which was plotted as a graph of scatter intensity versus angle around the diffraction ring. This allowed the data to be split into two areas, the aligned scatter associated with the preferred orientation of a proportion of the collagen fibrils, and the isotropic scatter arising from fibrils that are equally disposed at all angles within the plane of the cornea as viewed from the direction of the x-ray beam (i.e. as viewed from the front). The isotropic scatter could then be removed and the remaining data plotted in the form of a polar plot, which represents the preferred direction of collagen. Polar plots were colour co-ordinated according to their magnitude to allow for the

large spread in the intensity of scatter from aligned collagen in different areas of the cornea. These individual plots were assembled together by a further macro, to form an overall graphic showing the preferred direction of the collagen across the cornea, and where available the peripheral sclera.

4.2.5 Fibril Spacing Calculations

Fibril spaces were calculated directly from electron micrographs. Coordinates of fibrils that appeared perpendicular to the plane of the image were manually assigned in ImageJ, and the coordinates of each fibril were imported into a spreadsheet. A macro was then designed to automatically calculate the distance between any two fibrils in the grid using simple Pythagorian trigonometry. Distances were than grouped and plots were made of frequency against fibril spacing. The expectation for a healthy sample was that fibril spacing would peak at a value, and then level out at all higher values of separation, thus showing the short range order of the lattice and the lack of long range order. In practice, since the amount of fibrils within a lamella is finite, it would also be expected that as the separation increased to greater than the thickness of the lamella the frequency would decrease sharply, as there are no more fibrils within the specified radius.

4.3 Results

4.3.1 Electron Microscopy Images of Aarhus Eye Bank Tissue

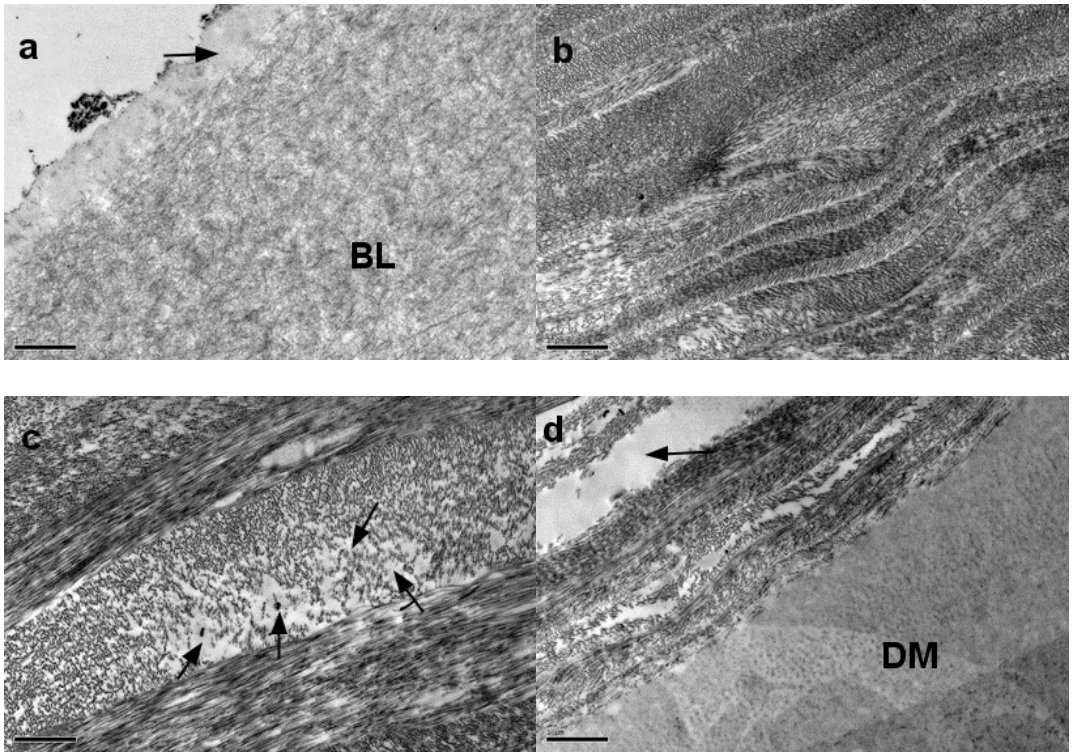

Figure 4.6: Images from the central graft portion of the tissue showing a) Bowman's layer (BL) and missing epithelium b) the anterior stroma c) the posterior stroma and d) Descemet's membrane (DM) and posterior stroma. Black arrows indicate a) surface layer of unknown material in place of missing epithelium c) intra-lamella swelling d) inter-lamella lake. Scale bar represents 1µm.

Figure 4.6 shows images obtained from the central graft region of the cornea that was received from Aarhus Eye bank. Figure 4.6a shows a complete Bowman's membrane with no breaks seen, and a surface of unknown material. Epithelial cells that would normally lie adjacent to Bowman's layer were missing across the length of the sample. Figure 4.6b shows the anterior stroma, no swelling was noticed and the lamellae in this region appeared normal. Figure 4.6c and 4.6d show a sample of the posterior stroma. In this region, some intra-fibril swelling can be seen (black arrows, Figure 4.6c) and large inter-lamellae lakes were common (arrow, Figure

4.6d), Descemet's membrane was left intact. Further examples of inter fibrillar lakes within the central graft can be seen in figure 4.8, and to a lesser extent in figure 4.7.

Figure 4.7: Section of anterior lamellae in central graft region. Scale bar represents 1 micron.

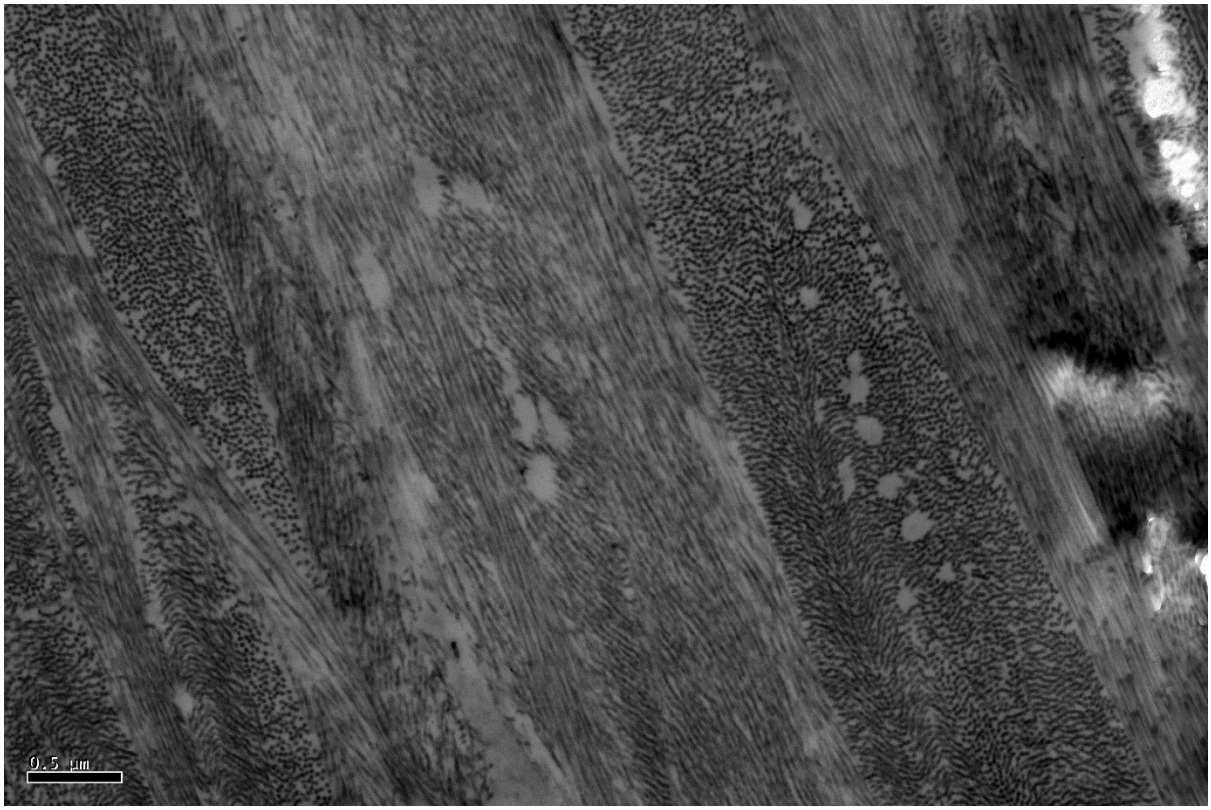

Figure 4.8: Section of anterior lamellae of donated graft. Scale bar represents 500nm.

Unfortunately, the samples cut from the blocks from the scarred region did not contain any features from the external layers of the cornea, so exact positional information regarding the depth of the lamellae could not be established. However, some features shown in figure 4.9 could not be directly related to any potential positioning of the lamellae. Figure 4.9a shows an example of the thin lamellae that were prevalent throughout the sample. Figures 4.9b and 4.9c show lamellae that have developed a kink, a feature that was not present in the samples from the central region of the cornea.

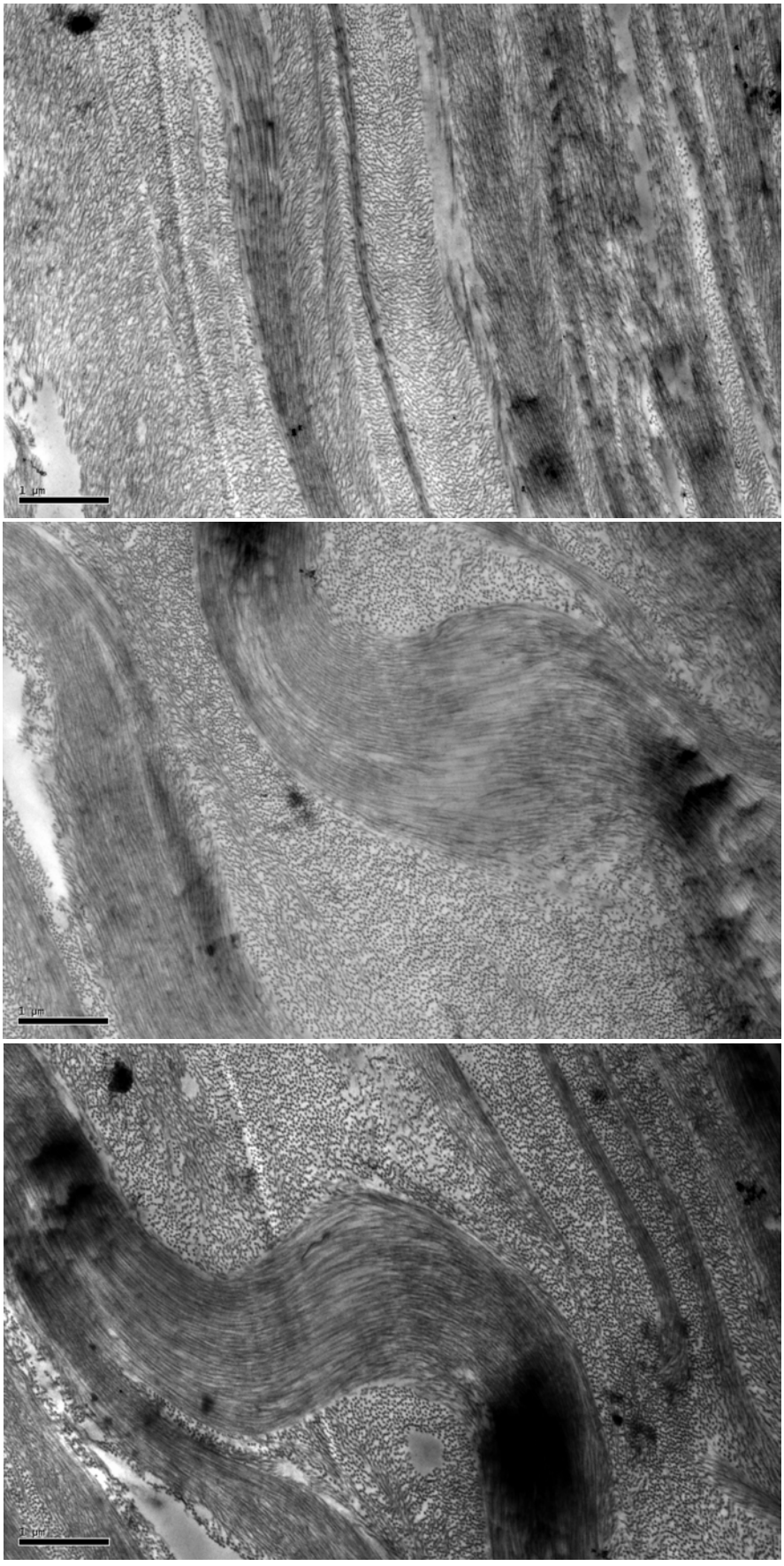

Figure 4.9: Images taken from the scarred region of the cornea sample, relative positional information could not be determined from the sample. Scale bar represents 1µm.

Although stained at the same time and for the same length of time, the scarred samples appear to uptake much more of the uranyl acetate stain. The reason for this is unknown, but unfortunately this led to dark patches covering parts of all of the sample.

4.3.2 Control Tissue Electron Micrographs

Figure 4.10 to 4.12 show example electron micrographs are control stromal tissue. No interfibrillar lakes were present. Collagen aligned parallel to the plane of the image appeared to stain more strongly than the collagen that ran transverse to the plane of the image. However since these images were being used to calculate fibril spacings, and therefore only the transverse collagen was required to be properly stained, this did not present a problem. Proteoglycans also appeared to have failed to absorb the stain, but again since this was not the main reason for the acquisition of the images this was not an issue.

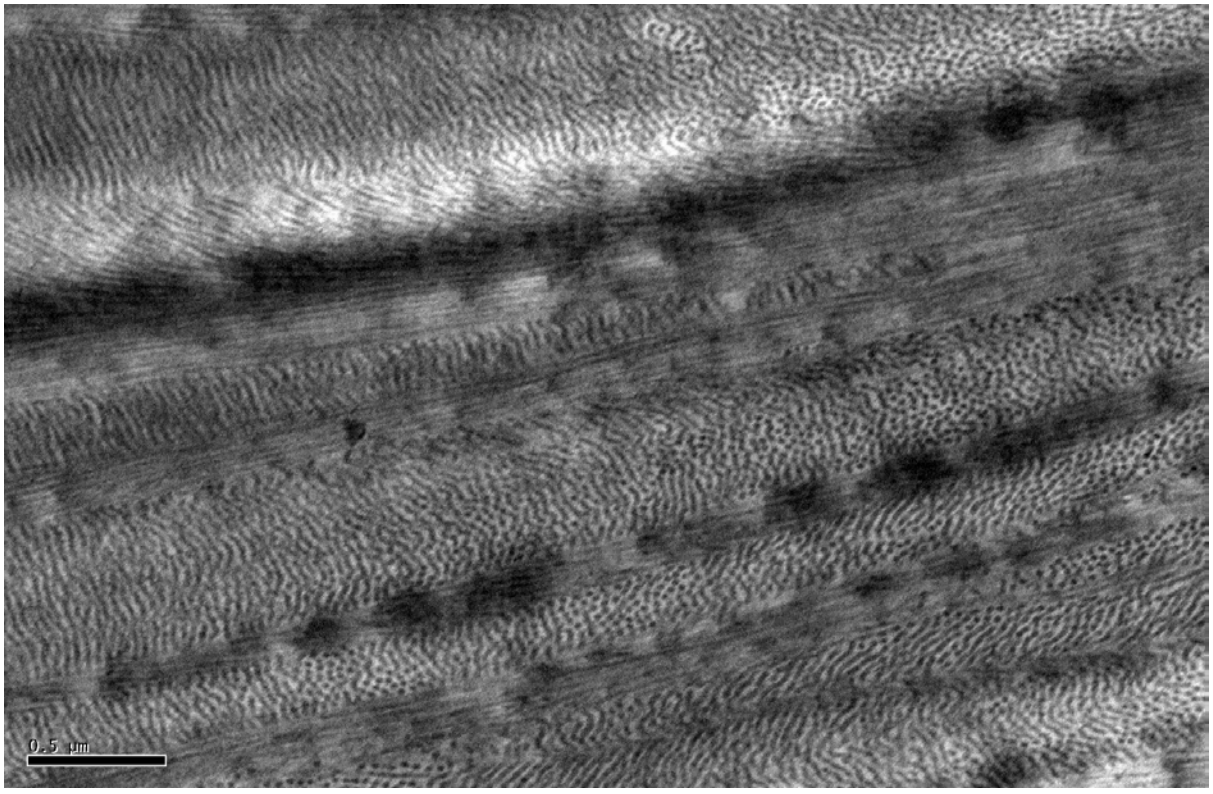

Figure 4.10: Electron micrograph of control corneal stroma. Scale bar represents 500nm.

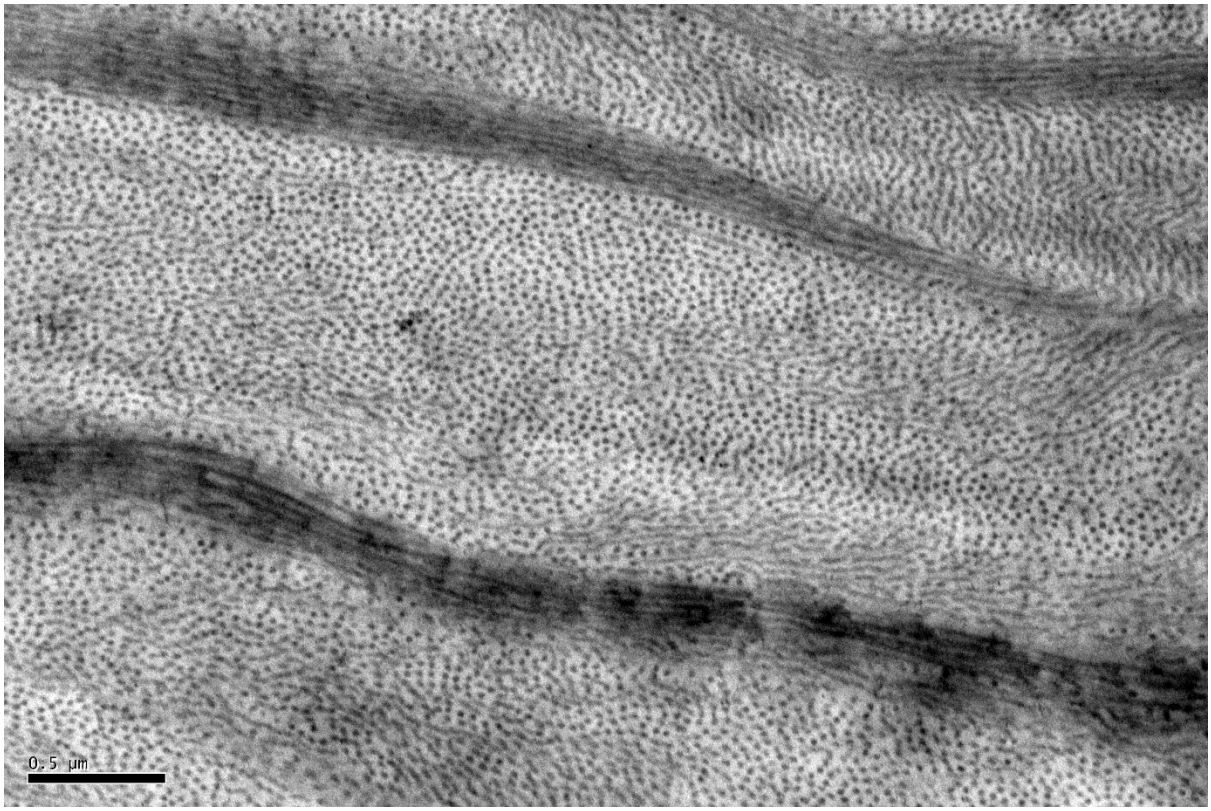

Figure 4.11: Example of electron micrograph used for fibril spacing calculations of control tissue. Scale bar represents 500nm.

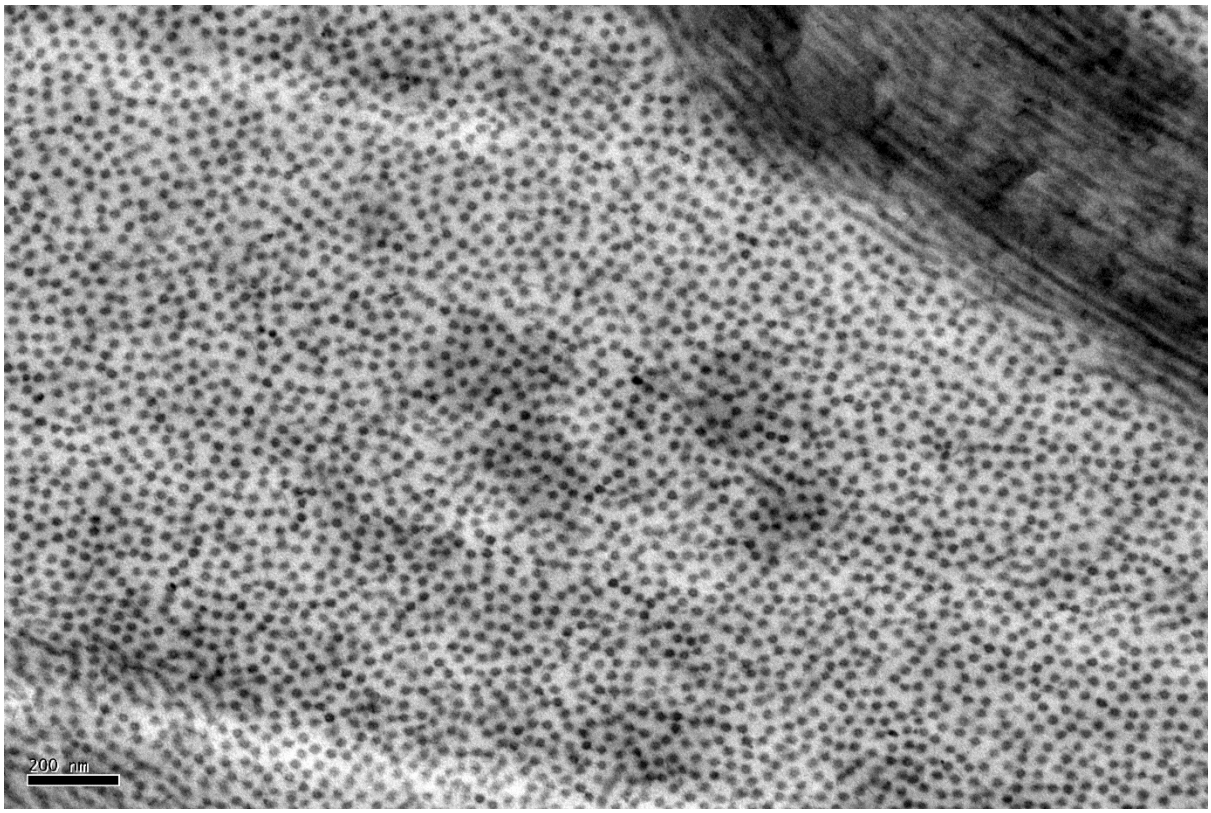

Figure 4.12: Example of electron micrograph of control tissue. No interfibrillar lakes were present within the control tissue. Scale bar represents 200nm.

4.3.3 Wide Angle X-ray Scattering Study

Figures 4.13 and 4.14 show complete maps of collagen alignment for both left and right eyes. Within each map, the individual polar plots show the preferential direction or directions of the collagen lamellae located at that place in the tissue, as deduced from analysis of the x-ray diffraction pattern from that position. Both maps show the expected areas of low anisotropy in the central clear regions, with some preferential directions that lie perpendicular to each other. Normally these directions would run in the nasal-temporal and inferior-superior directions. In the case of the right eye, however, this does not appear to be the case, suggesting that the grafted tissue was not correctly orientated during surgery. The grafted section is mainly surrounded by an annulus of highly aligned collagen in the limbus region that has been seen in many such studies. However, again in the right eye, this annulus is interrupted in an area consistent with the wound left by the graft (Figure 4.13). The section of the map of the right eye corresponding to the area of the scar shows a distinct delineation, possibly as a result of the wound edge slightly separating. In the opaque sections of both eyes, the collagen appears to align tangentially in a similar manner that would normally be expected in the sclera. Figure 4.15 shows contour maps of total and aligned collagen for both left and right eyes. Abnormal features are present in the scarred and opaque sections of both eyes, with localised elevations of collagen mass present in the areas of noticeable opacity and at the graft margin.

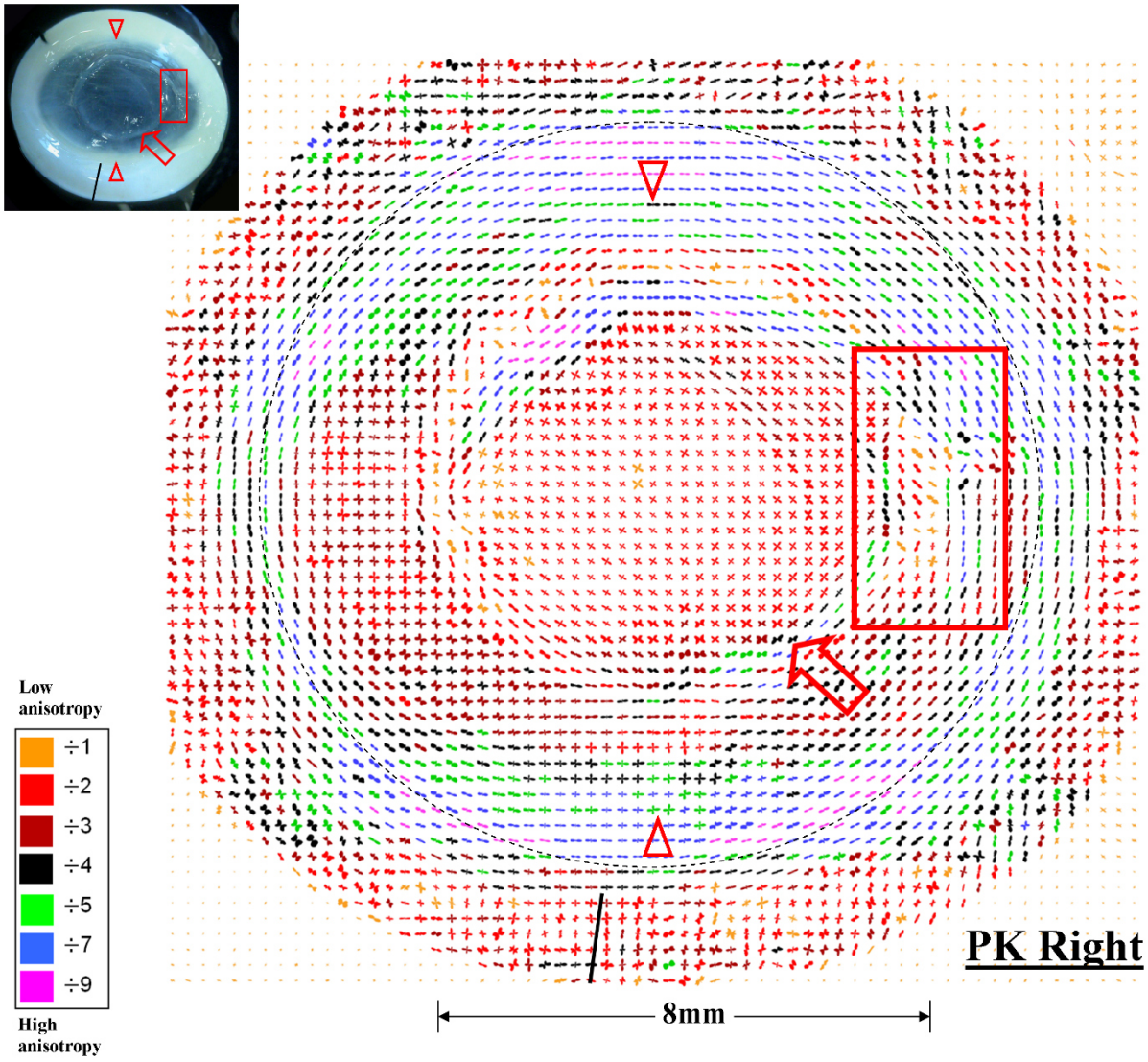

Figure 4.13: Polar vector map of collagen fibril alignment of right eye, including both the central grafted region and the original keratoconic limbus and sclera. Plots are scaled to appear the same size, with the extent of the scaling indicated by colour coding. The dashes circle indicates the location of the limbus. The larger arrow shows tangential fibril alignment along the graft margin. Smaller arrowheads indicate regions of abnormal opacity within the limbus margin. Rectangle surrounds a region where fibril alignment delineates the separated wound edges. Superior tag of the original tissue, which is not necessarily the same as the graft, is marked by a solid black line at the approximately 6 o' clock position.

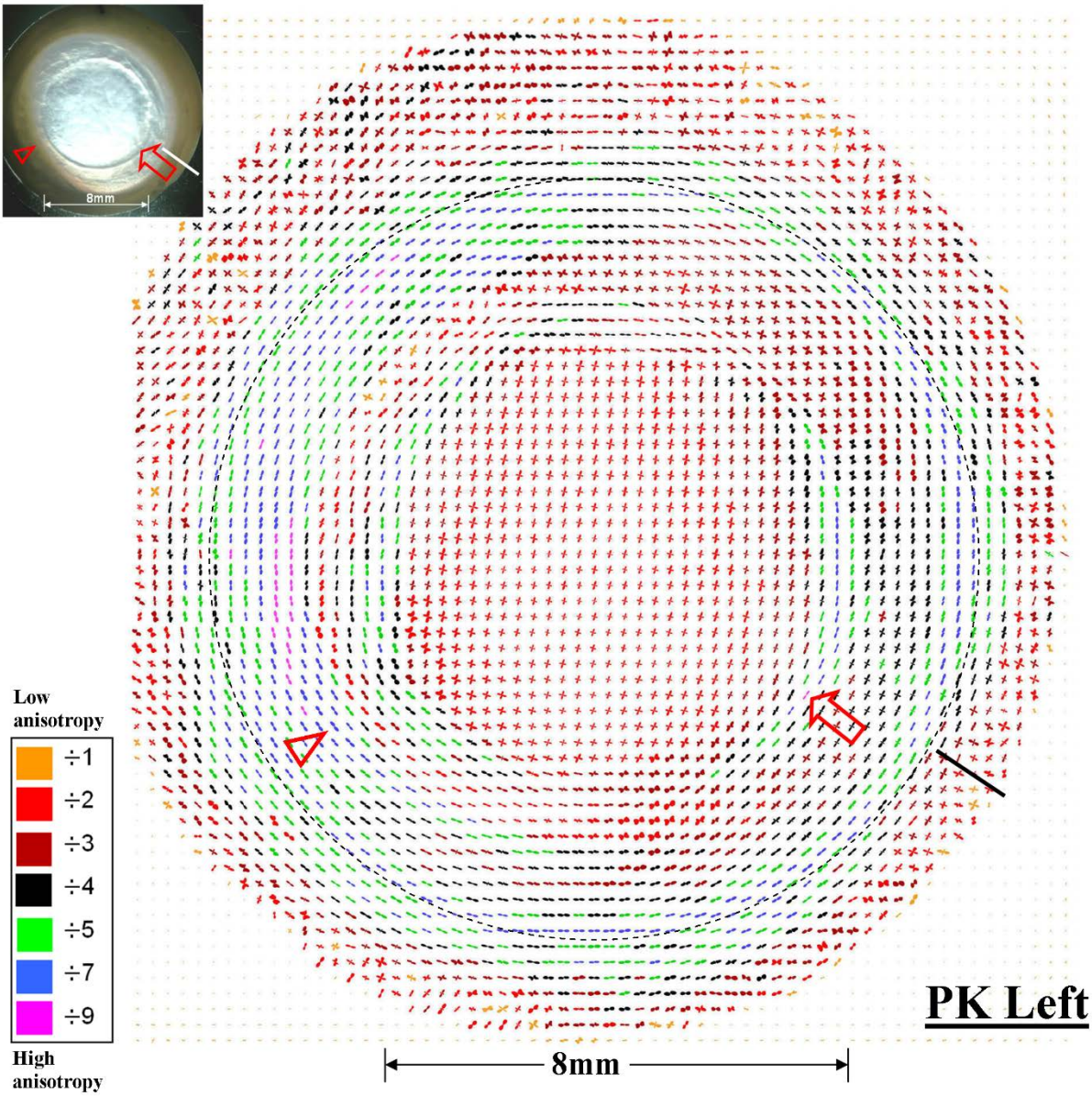

Figure 4.14: Polar vector map of collagen fibril alignment of left eye, including both the original pathological tissue and the healthy grafted central region. As with figure 4.6, larger plots, indicating regions of greater alignment, are scaled down, with the extent of the scaling shown by colour coding. Dashed circle indicates the extent of the limbus. Arrow indicates tangential fibril alignment along the graft margin. Arrowhead corresponds to an area of opacity within the limbus. Superior tag of the original tissue is marked with a solid line at approximately the 4 o' clock position (Dooley 2012).

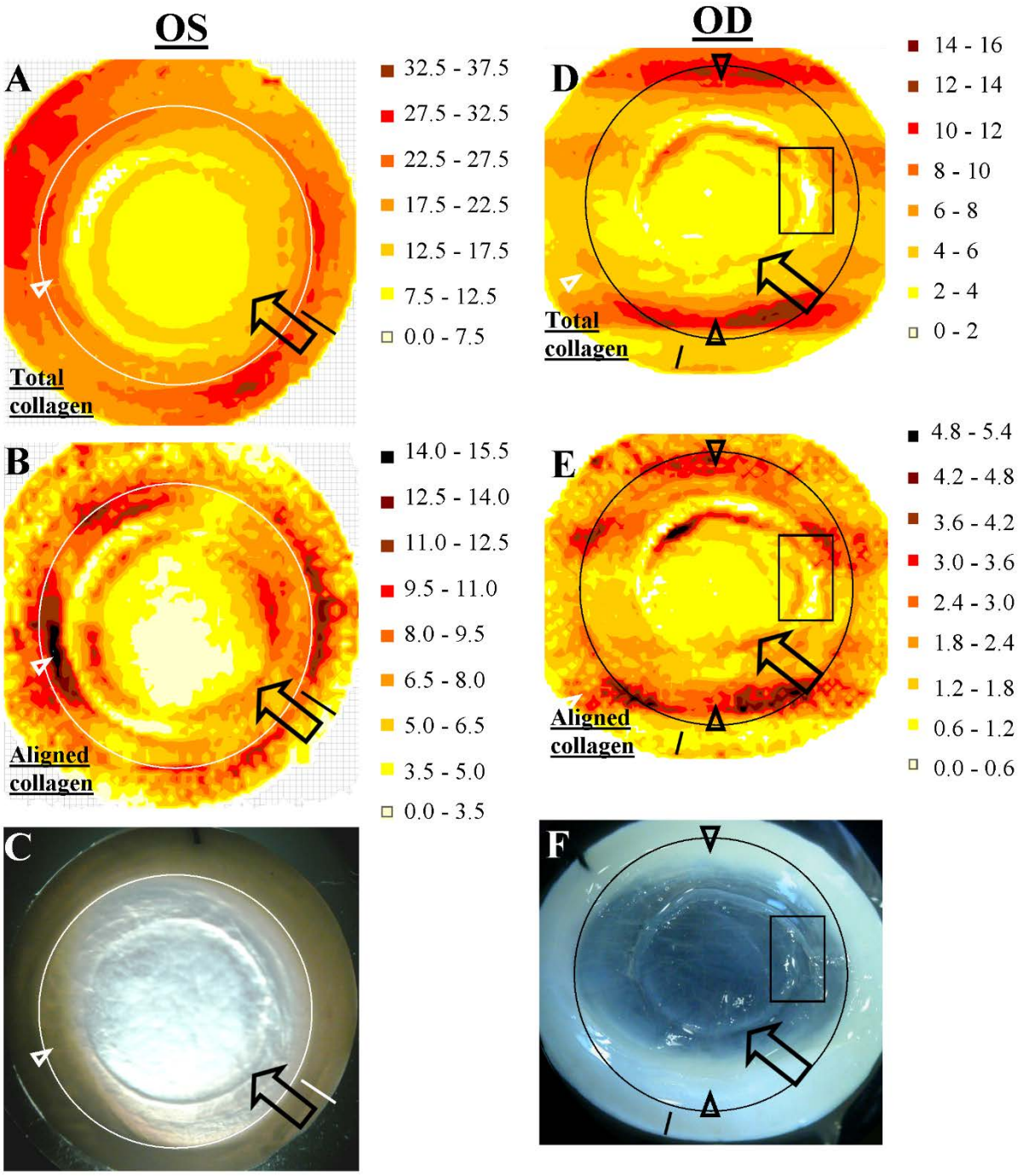

Figure 4.15: Distribution maps showing the total (A&D) and aligned (B&E) collagen across the tissue specimens. Arrows show a local increase in total and aligned collagen at the graft margin. Solid circles indicate the limbus and solid lines the superior position. Rectangles in E and F highlight an area where the wound had begun to separate.

4.3.4 Fibril Spacing Calculations

Figure 4.16 shows the results of fibril spacing calculations for the scarred and grafted regions of the donor tissue, and a healthy control tissue. g(r) was calibrated such that the average of the baseline data point was set at 1. Baseline points are defined as those larger than 100nm. A decrease in the size of the nearest neighbour peak was observed in both the scarred region and the transplanted central graft. Control tissue exhibited the expected characteristics of the radial distribution function for corneal tissue.

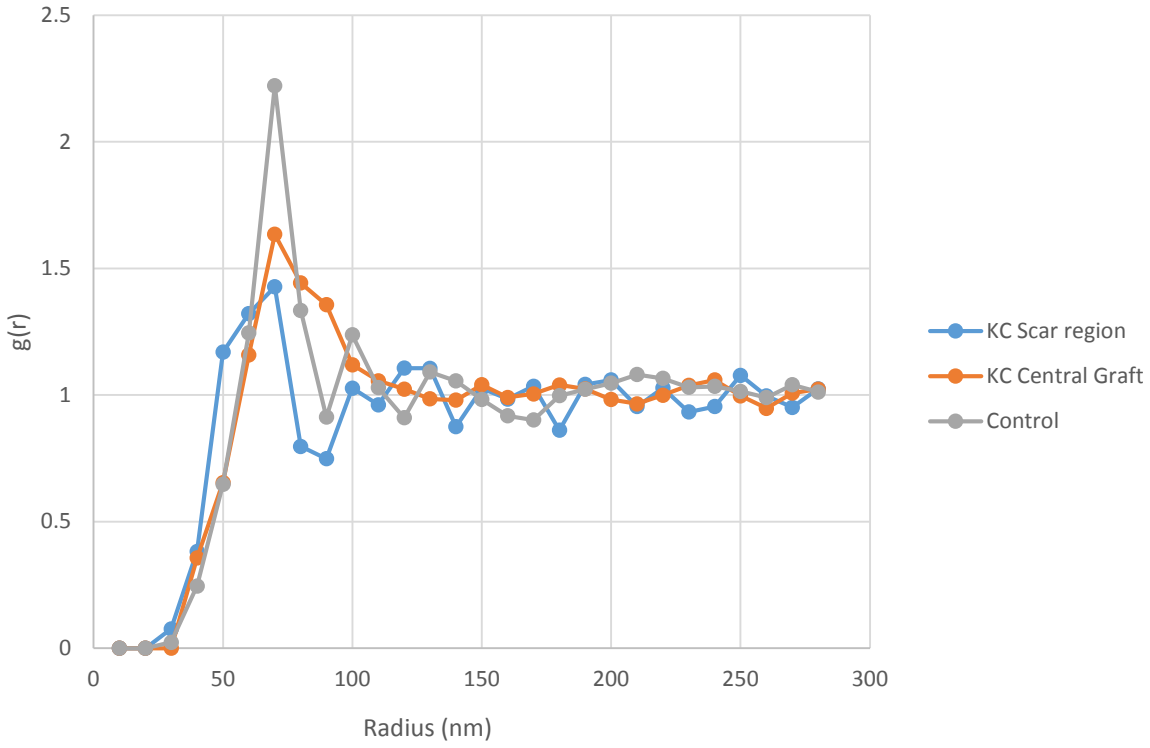

Figure 4.16: Graph showing fibril spacings in Danish keratoconus cornea at the scarred region, the central region and the control tissue, calculated from measurements made from electron micrographs.

4.4 Discussion

The images from the central region of the cornea sample showed no obvious signs of recurrent keratoconus that have been observed in reported cases of graft failure. The lamellae in the

stroma looked normal, with the exception of some swelling in the posterior layers, which was probably caused by the organ culture medium in which the sample was first stored. Swelling in posterior regions preferentially has been noted in pathologically abnormal cornea samples before (Palka et al. 2010), but these finding might not necessarily be applicable to grafts. The grafted section showed a thick layer of an unknown material, which could be a thick basement membrane, and a complete lack of epithelial cells. Normally, the lack of epithelial cells would not be unusual for samples that are transported frozen. However, the thick layer of basement membrane would suggest that the cells may have been unable to properly anchor to Bowman's layer. This observation is not consistent with cases of recurrent keratoconus, which more often manifests as breaks in the Bowman's layer and the epithelial basement membrane (Nirankari et al. 1983; Unal et al. 2007). However, this is only true in the cases where the recurrence of the disease had been diagnosed, and this diagnosis was confirmed many years after the initial PK surgery. These samples had been donated 14 years after PK operations had been performed, so it is possible that any recurrence had not had time to show the pathological changes described in the literature, which were investigated between 22 and 40 years after PK. The rarity of such donated samples make the acquisition of data to investigate this possible effect extremely difficult. It may be that we have to rely on other publications reporting the same or similar effects before we can be sure this is a sign of recurrent keratoconus, and not simply and effect of the storage conditions. After the initial storage of the tissue in organ culture medium, the tissue was frozen before being used in x-ray diffraction studies. This freezing process is not considered to be detrimental to the collagen lattice, but is known to destroy the keratocyte cells that populate the stroma. It is this method of storage that was thought to be the origin of the inter-lamellar lakes that were observed in the sample. The freezing process, while necessary, was unfortunate as the destruction of the keratocytes made it impossible to determine if they were the normal cells that had originally populated the graft, or abnormal cells from the exterior

section that had invaded the graft tissue. Whether or not keratocytes can traverse the scarred section remains an open question at this time.

In the scarred region of the sample, the lamellae in the stroma that were observed appeared much thinner than usual. Initially it was unclear whether this was an effect of the scarring, or if it is more simply a normal feature of tissue that is taken from an area away from the centre. As tissue is not normally taken from this area of the cornea for EM study, suitable reports that could be used for comparison could not be found in the literature.

While lamellae do interweave, especially in the anterior layers of the stroma, to provide structural support for the cornea (Roberts 2000; Dupps and Roberts 2001), the anatomy that was present in the scarred samples appeared to differ from normal healthy corneal tissue. Large kinks in the some lamellae were observed, as if they had ruptured in places. If this is evidence for a failed repair system, it would explain the apparent opacity of the scar that was evident before the tissue was processed. It may be that the rebuilding process includes an increase in the interweaving so the structural integrity of the cornea is maintained at the expense of transparency. This would seem to complement the long-standing idea that fibroblasts play an important role in the wound healing response (Jester and Jin 2003) although their reduced transparency due to an decrease of corneal crystallins could not contribute directly to the loss of transparency of the scar in this case, since the fibroblasts that are active for the initial wound healing response have been shown to disappear after several weeks either by migration or apoptosis (Helena et al. 1998; Netto et al. 2006).

The WAXS study of the tissue of both eyes showed multiple abnormalities when compared with the results of healthy controls. Scarring and areas of slight limbal opacity notwithstanding, the central grafted region appeared to have maintained both an acceptable level of structural integrity and clarity, and as such could not be considered a failure. PK remains a highly

successful treatment option for cases of severe keratoconus (Pramanik et al. 2006). Full thickness wounds are thought to never fully heal (Morrison and Swan 1982b; Lang et al. 1986; Farley and Pettit 1987; Melles and Binder 1990; Hayes et al. 2010), and the collagen maps presented here do not dispute this view. Abnormalities were restricted to areas where the scarring and opacity could be observed. With respect to the scarring, it is presently unknown if the tangential orientation of the collagen observed in the right eye (Figure 4.13) is caused by a wound healing response, or a lack of proper healing to the initial surgical wound (Connon and Meek 2003). It is possible that the kinks observed in the micrographs of the scarred areas could account for the reduction in aligned collagen in those areas.

The lack of clear nasal-temporal and superior-inferior orientations within the graft in both eyes is almost certainly the result of the graft being inserted at an angle during the PK procedure. During the time both surgeries were performed, structural information was not kept in transplanted tissue as a matter of routine. It has since been postulated that maintaining a consistent lattice could be very important, not only with the correct orientation of the grafted tissue but also bilateral consistency as well, since the collagen matrices do not appear to be internally symmetrical (Boote et al. 2010). The axial and sagittal preferential directions are thought to protect the cornea from damaged caused by the actions of the ocular muscles (Daxer and Fratzl 1997; Meek and Newton 1999; Boote et al. 2005; Abahussin et al. 2009), so an oblique orientation may lead to a weakened cornea. It would be natural for the damage to be observed at the weakest point, which could explain the observed separation site in the right eye that can be seen in the photographs in figures 4.15 (F) and 4.3 (C). Rather than intraocular pressure, the action of the extraocular muscles could be causing the separation, or more likely it is some combination of both effects. Correct alignment of the graft would mitigate one of these effects at least and lead to a lowering of the graft failure rate. With the graft being completed so many years before the donation of the tissue, it might be expected that the

collagen orientation might have changed to match the new position of the grafted tissue with respect to the nasal-temporal and superior-inferior axes, as would seem reasonable in more dynamic tissues. That this is not the case demonstrates that large scale changes within the collagen matrix once it has been formed are not possible, even after 28 years. The precise reason for this is unclear. Either the turnover of the unaltered collagen is extremely slow, or even non-existent (Smelser et al. 1965), or the turnover rate is irrelevant because the keratocytes are unable to distinguish absolute direction, and lay collagen according only to the local conditions that are already present.

Additionally, any radical changes to the collagen matrix at the site of the scar could have a large impact upon the structural integrity of the tissue. After prolonged handling and experimental use, it was noticed that in the left eye the seam where the scar was located did separate in places under small amounts of pressure, and the right eye had a noticeable visible separation in the temporal region of the scar. These traits had not been deemed serious enough to cause the graft to be regarded as having failed during the lifetime of the patient, but they do show that both scars were abnormally weak when compared with a healthy tissue both before and especially after excision. The difference in the conditions of both the eyes was most likely due to the right PK having been performed 16 years earlier than the left. In the right eye, collagen distortion at the site of the separation was noted, with fibrils aligning radially to the graft. This anisotropy was generally low, and so possibly did not contribute to the mechanical failure of the tissue, although a similar pattern of behaviour has been noted in previous specimens that did fail after 13 years (Hayes et al. 2010). Measurements at the scar of the left eye suggest that only 10% of the collagen was aligned orthogonally to the wound, which could not be expected to provide enough resistance to a tear if pressure were applied in this direction. The annular fibril alignment that we see from the WAXS maps could also contribute to undesirable deformations, or even complete separation of graft and host tissue, under normal

intraocular forces. With a lack of meridional collagen, an annular only configuration has been predicted to be weakened (Boyce et al. 2008), which could explain the tendency of wounds to be more susceptible to separation (Calkins et al. 1981) even after long periods post PK (Farley and Pettit 1987; Pettinelli et al. 2005). From these results, it would seem to be beneficial for the corneal collagen matrix to contain more fibrils that ran perpendicular to the circular wound surface, in both the nasal-temporal and superior-inferior axes, but this is not what is observed. This confirms the view that the corneal matrix has a limited ability to remodel following a wound. Some amount of transverse collagen is observed, but not enough to maintain structural integrity. Once the matrix has been formed, it remains in approximately the same state for life, with only the most superficial wounds able to be fully repaired.

Both eyes presented with regions of extensive abnormal opacity in the periphery, on the temporal side of the left eye and both the superior and inferior sections of the right. WAXS data presented here showed those regions to contain areas of highly aligned collagen that is more normally found within the limbus and sclera (Figures 4.13 and 4.14). This pathology has the classic appearance of sclerisation which has been previously studied and shown to present both bilaterally and asymmetrically (Sen et al. 1969). To date, this condition has not had a cause linked with the diagnosis of keratoconus, and so it is expected that the two conditions have developed independently. It is not known when this sclerisation has occurred during the patient's lifetime.

The fibril spacing calculations for the Danish tissue were broadly in line with expectations. It has been previously shown that fibril spacings in healthy tissue peak in a short range area, and then decay to a baseline value that persists for the remainder of the function (Hart and Farrell 1969). This peak thusly shows that even in the absence of a perfect lattice the matrix retains a short range order that is necessary for transparency, as was discussed in chapter 3. This is what we see in spacing calculations of healthy controls. A peak is reached in the region of 70nm that

is between two and three times the size of the baseline, with no signal before 30nm. This reflects the disastrous consequences of fibril spacing being too low. As well as serving to stabilise the matrix, proteoglycans also are needed to maintain a minimum fibril spacing, which the zero signal at very low spacing shows to be the case. In the absence of PGs, the minimum signal would begin at a centre-to-centre spacing that is equal to the fibril diameter, since at that spacing the surface of the fibrils are touching. This would occur at a minimum of around 30nm. As a non-pathological tissue, it appears strange that the central graft does not exhibit the same features as the control tissue. There did not appear to be any sign of abnormality or loss of transparency within the grafted tissue on initial inspection. The results from scarred area of the cornea show a similar change. The peak in the nearest neighbour region persists, but it is much lower compared to the baseline than the control. The peak also appears to have shifted towards a smaller spacing in the case of the scar. This could be a consequence of the areas of missing fibrils that could be observed within the electron micrographs of both tissues. Gaps in the lamellae could be caused by a shift in the fibril spacing to the extremes of the range, which would flatten the peak. A shift in the short range order from around 70nm by itself should not cause troublesome transparency losses, with the peak still located within the maximum acceptable spacing for transparency that has been calculated to be 120nm, so long as the spacing does not become low enough for fibrils to aggregate. What is more undesirable for transparency is the large decrease is the relative size of the peak compared to the size of the baseline. This would appear to indicate a much weaker overall ordering of the matrix, which would have unwanted implications on the transparency of the tissue.

5 Macular Corneal Dystrophy Study

5.1 Introduction

As with most tissues of the body, the study of the causes of abnormalities, diseases and disorders of the cornea allows an insight into the inner workings of the healthy specimen. By comparing the structure and function of diseased corneas to that of a healthy control, it is possible to determine exactly how important certain structures are in the case of the transparency of the cornea. Macular corneal dystrophy (MCD) is a genetic disorder that affects the structure and function of the proteoglycans in the stroma specifically, and so is a useful comparison model for the study of the precise functions of the proteoglycans. MCD has been extensively studied in the literature and an overview of the background has already been provided in section 1.7.2. During one of these studies, it was noticed by Quantock et al (1991) that one of the many irregular features of MCD tissue that could be seen in electron micrographs was an abundance of 'lakes' throughout the tissue. These lakes contained substantial amounts of proteoglycans, which were unconnected to any collagen fibrils. Furthermore, these proteoglycans appear to exist in a mesh, with a large amount of interconnections between them. To date, these lakes have remained largely unstudied, and have been considered a curiously unusual pathology with a lack of clinical relevance. They are clearly not useful in terms of the diagnosis of the disease, since more obvious signs, such as the gradual clouding of the tissue, are a less invasive method of diagnosis. However, a study of how the abnormal proteoglycans interact with each other in the absence of collagen may be able to be applied to the structure of the lamellae in either MCD corneal tissue or for other abnormal pathologies, and possibly for healthy tissue as well. The method by which these interactions will be modelled will be based on reconstructed three dimensional tomography

calculated from a series of two-dimensional transmission electron micrographs by a method of filtered back-projection.

5.1.1 Three-Dimensional Tomography from Transmission Electron Microscopy

Transmission electron microscopy (TEM) produces two-dimensional images of a three dimensional, albeit very thin, specimen. This naturally results in the loss of some spatial and contextual information. For a long time this was considered to be a necessary obstacle inherent to the process, but with the rise in the power of computers and their ability to store and manipulate larger amounts of information, this previously lost information can be recovered using the technique of tomography. Generally, tomographic techniques produce a three-dimensional reconstruction from a series of two dimensional images. In most of these applications, such as in medical fields of x-ray computed tomography and magnetic resonance imaging, the series of two dimensional images is a complete set of information, limited only by the time it takes to collect and reconstruct the images, the number of two-dimensional slices needed to construct a reasonably representative three-dimensional image, or in the case of x-ray CT, the dose delivery to the patient. Slices are taken by changing the position only, leaving the plane of the image identical for each one. Regrettably, this is not the case for TEM reconstructions. Attempts to take slices of a thicker sample would impact upon the ability to focus the images, leading to a blurred and useless image. With the requirement to use an ultrathin sample to maintain the visual contrast, a different method must be used to provide the information for the reconstruction. Rather than attempting to resolve thin sections, this information can be provided by taking a series of images at different angles. When the specimen is tilted, structures in the images will move depending on where precisely they are located on the grid, an effect known as parallax, but so long as this can be accounted for through the different angles, usually by using markers placed on the top and bottom of the grid, a

reconstruction is possible. The main disadvantage of this procedure is that information is more limited than in purely sectional methods. The practicalities of the arrangement of the electron microscope precludes very large angles from becoming part of a reconstruction. Even if imaging could be performed, the amount of structural information returned suffers from diminishing returns at higher angles, and so may not contribute any useful information to the process anyway. In practice these so called tilt series are usually constructed from images taken at every 1 or 2 degrees of arc between extremes of ±60º, where 0º is defined as the plane that is perpendicular to the direction of the electron beam.

A further potential problem of taking images at an increased angle is due to the electrons having to pass through a thicker overall portion of the specimen as the angle between sample and electron beam is decreased (Figure 5.1). This has two non-desirable effects, first that the thicker portion of the specimen becomes more difficult to focus, and the intensity of the beam often needs to be increased to compensate, and also that there is more energy imparted to the sample by the electron beam. This added energy causes heating within the sample, and is only exacerbated by the increase in intensity that is often required to produce a clear image. Samples melting or having holes burned in them from a beam that is too intense are common occurrences from the author's early attempts at conducting a tilt series, although a greater proficiency was achieved with practice. The results of these problems from a practical perspective is that tilt series operations must be performed quickly, before the sample begins to break down under heat stress. These effects also place limitations on how many times a specific grid can be reused. The precise area used for a tilt series can realistically only be used once, with perhaps one or two other areas that can be fully imaged before the sample becomes too damaged to be useable. With practice, the entire 120 image series can be collected within 2 hours.

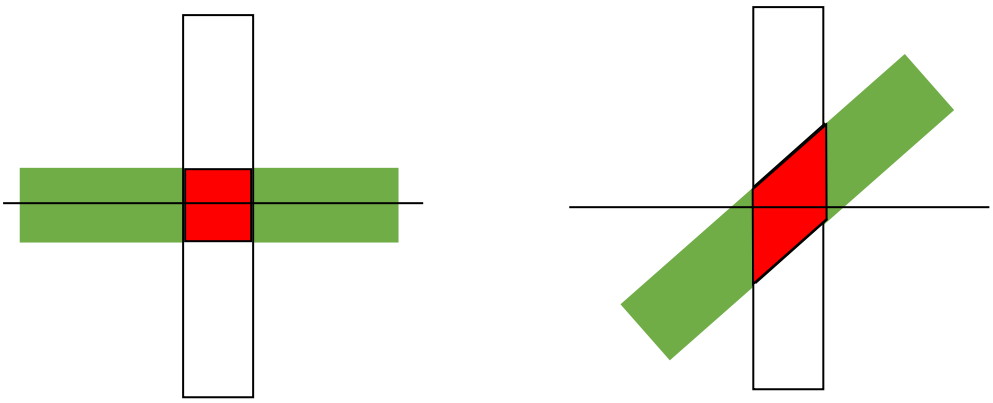

Figure 5.1: Schematic diagram to show the effect on tilting a sample (green) with respect to an electron beam (white). As the tilt with respect to the horizontal becomes more pronounced, the volume and perpendicular thickness which the beam must pass through both become larger (red), resulting in a greater amount of energy being transferred to the sample and it becoming increasingly difficult to adequately focus on the desired plane.

In order to perform the reconstruction, the grids are previously coated on both sides with colloidal gold, a suspension of gold particles in liquid solution. The particles can be used as tracers during image acquisition, but their main role is as markers to provide information as to the extent of the parallax of the system. By making use of computer software, the parallax at different points within the image series can be traced and the reconstruction is built, turning a series of images of different angles into a series of planar images. These reconstructions are then often artificially segmented to represent the relative positions of the fibrils and proteoglycans in a clearer manner.

This tomography method has been used in a number of publications to model the structure of the cornea in both healthy and pathologic corneas of both bovine (Lewis et al. 2010) and mouse corneas (Parfitt et al. 2010), and has become a well-established tool for recovering the three dimensional information that is normally lost in transmission electron microscopy.

5.1.2 MCD: Effects and Treatments

Macular corneal dystrophy (MCD) is a disorder of the cornea that manifests as small areas of opacity that become progressively larger with age. In most cases, MCD is thought to be caused by a mutation in the CHST6 gene, which leads to a complete absence of the keratan sulphate glycosaminoglycan (GAG) in the cornea. The cornea is transparent at birth, but opacities become detectable in the second decade of life and in many cases, by the fifth decade, patients diagnosed with MCD have corneas that are nearly opaque. MCD has been diagnosed throughout the world, but, unsurprisingly as a recessive congenital disorder, there are areas where MCD is more common due to genetic predispositions and semi-isolated communities, such as Iceland (Jonasson et al. 1989). Recent surveys of corneal dystrophies put the number affected by MCD in the USA at around 1 in 30,000 (Musch et al. 2011).

Unlike in the case of keratoconus, MCD affects not only the stroma but is also known to affect Descemet's membrane and the corneal endothelium. It is for the reason that the most common treatment, once opacity has rendered the tissue unusable, is penetrating keratoplasty (PK). The more recent technique of lamellar keratoplasty, where Descemet's membrane and the endothelium are left intact, would leave behind pathological tissue, running the risk of a recurrence of the disease and the need for further grafts to be required. As well as the endothelium, the keratocytes are also often abnormal when compared to healthy controls. They usually contain granular vacuoles within the cytoplasm, which sometimes contain fibrillar material and GAGs (Klintworth 2009). The corneal epithelial cells are spared of any abnormalities, the reason for this is currently unknown.

5.2 Materials and Methods

5.2.1 Tissue details

Tissue samples were obtained from the laboratory of biology and pathology, located within the Institute of Inherited Metabolic Disorders at Charles University, Prague, Czech Republic. Tissue samples were excised and stained in Prague, with the School of Optometry receiving two approximately 2mm cube sections of the original tissue. The samples used in this study were provided by a 37 year old female donor of white Czech and Morrocan ethnicity. Tissue was obtained after a penetrating keratoplasty (PK) procedure was performed on the subject's right eye only. Onset of MCD symptoms occurred 18 years prior to the PK. No family history of MCD was recorded. The tissue was not tested for presence of keratan sulphate and so no information on the type of MCD was available.

5.2.2 Preparation of Electron Microscopy Samples

The samples described in section 5.2.1 had already been stained with cationic cuprolinic blue stain (Scott and Orford 1981; Scott 1985). The samples were washed with 25mM sodium acetate buffer containing 0.1M $MgCl_2$ for 5 minutes and then dehydrated with increasing concentrations of ethanol for 5x15 minute periods. Once the dehydration was complete, ethanol was replaced with propylene oxide solvent for a further 2x15 minutes and then placed in a 1:1 mixture of propylene oxide and araldite resin for 1 hour. The araldite resin was made by mixing a 46.6:53.3 solution of araldite monomer CY212 and DDSA hardener with 0.6% BDMA accelerator, until a highly viscous resin of a red-orange colour was produced. The tissue was then places in the resin a total of six times for 2-3 hours at a time. At each stage the vials were placed in an automatic rotator (Agar Scientific, Stanstead, UK) for the time between solution

and resin changes. Tissue samples were then placed in moulds and warmed in an oven at 60ºC for 24 hours until the resin became solid.

These solid blocks were then cut to size using a razor blade until a trapezoidal platform was fashioned around the embedded tissue and ultra-thin (90nm) sections of the tissue were cut using an ultramicrotome and glass knife. These sections were by slowly passing the block, which was fixed to a mounted arm, past the glass knife, such that a ribbon of trapezoidal sections was formed. A gold colour to the section, owing to interference of light passing through it, was used to confirm the correct thickness. These thin sections were then floated onto a small water lake attached to the triangular glass knife, and mounted onto a copper grid. These section were then stained, with the section placed face down, with 0.5% uranyl acetate (UA) solution for 5 minutes and 1% phosphotungstic acid (PTA) for 30 seconds. Excess stain was removed by placing the grid on a water droplet for 1 minute, for 4 times each. At the conclusion of this process, the grid was stained on both sides for four minutes each side with a 10nm colloidal gold suspension to implant fiducial markers that would be used in the reconstruction process.

5.2.3 EM Imaging Methods

Collagen lamellae from a variety of stromal regions were imaged at x15,000 magnification in 1º steps from -60º to +60º, where 0º defined the plane perpendicular to the path of the electron beam. Regions of interest were chosen based on their position within the grid, as regions closer to the central axis will suffer from a reduced parallax error. Course focus was determined by visual inspection and fine focus achieved using fast Fourier transforms. Images were roughly aligned during acquisition by aligning a chosen fiducial marker with a region of interest specified when the series was initiated. Images were produced using a transmission electron microscope (JEOL 1010) operating at 80kV and a Gatan ORIUS SC1000 CCD camera.

5.2.4 Structural Reconstruction of MCD Tissue

Image tilt series were first aligned more accurately using IMOD software (Kremer et al. 1996), which produced a fully aligned tilt series from the raw images. Reconstructions were then performed using EM3D . IMOD tracks the fiducial markers in the series and uses the varying parallax that is apparent for markers in different positions within the image, and on different sides of the grid. This process was repeated through a number of iterations until the reported errors in the position of the markers was within an acceptable margin. EM3D was then used to produce tomograms by a method of filtered back-projection. Once the reconstruction was complete, features of interest were segmented either by manually telling the program a general area where a feature was located and allowing it to track the feature through the other planes of the program, or by manually tracking the feature through all the planes in which it appears. In general, collagen fibrils were segmented automatically, and proteoglycans were segmented manually.

5.3 Results

5.3.1 Reconstructions of MCD Stromal Collagen Matrix

A raw electron micrograph of the area that has been reconstructed is shown in figure 5.2. The image shown was taken with no angle of tilt applied to the loading mechanism.

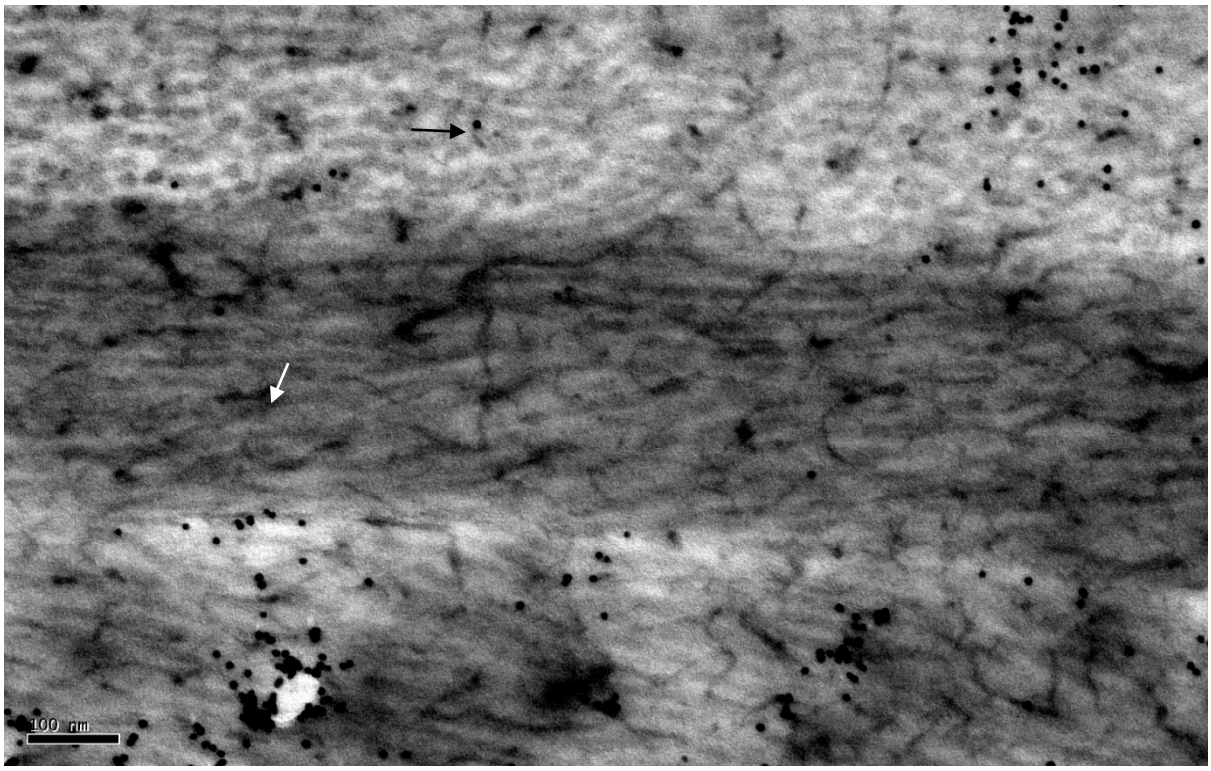

Figure 5.2: Image showing section through an anterior lamella of a cornea diagnosed with macular dystrophy. Dark circles within the image are absorbing fiducial markers of colloidal gold (black arrow). Stained proteoglycan filaments are abundant (white arrow).

Planar reconstruction data are shown in Figure 5.3. As part of the reconstruction process, the images are mirrored in the x-axis compared with their raw counterparts. Reconstruction images have also been slightly rotated in the xy plane as a result of the automatic alignment of the raw micrographs. PGs from this reconstruction were measured to have a mean length of 45±13nm and a mean thickness of 9.1±2.6nm. The maximum recorded length was 80nm and the minimum was 22nm. The maximum recorded thickness was 12nm and the minimum as 5.0nm.

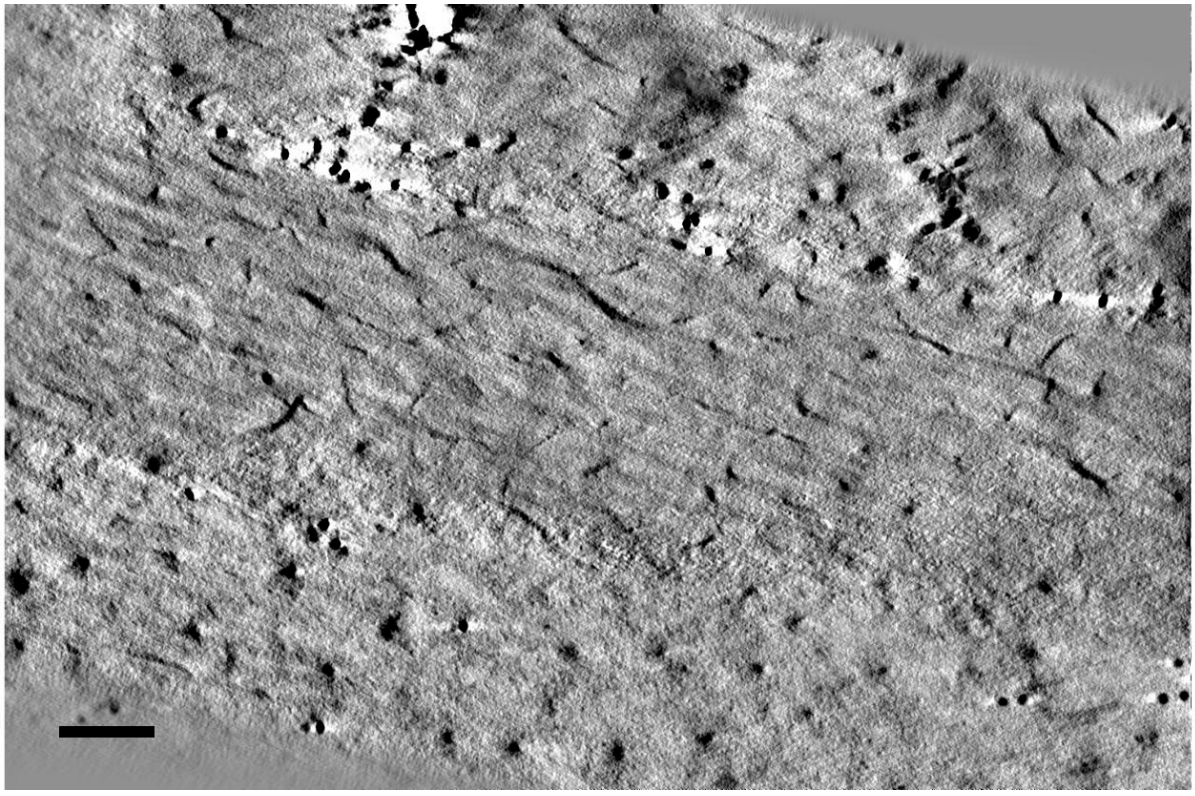

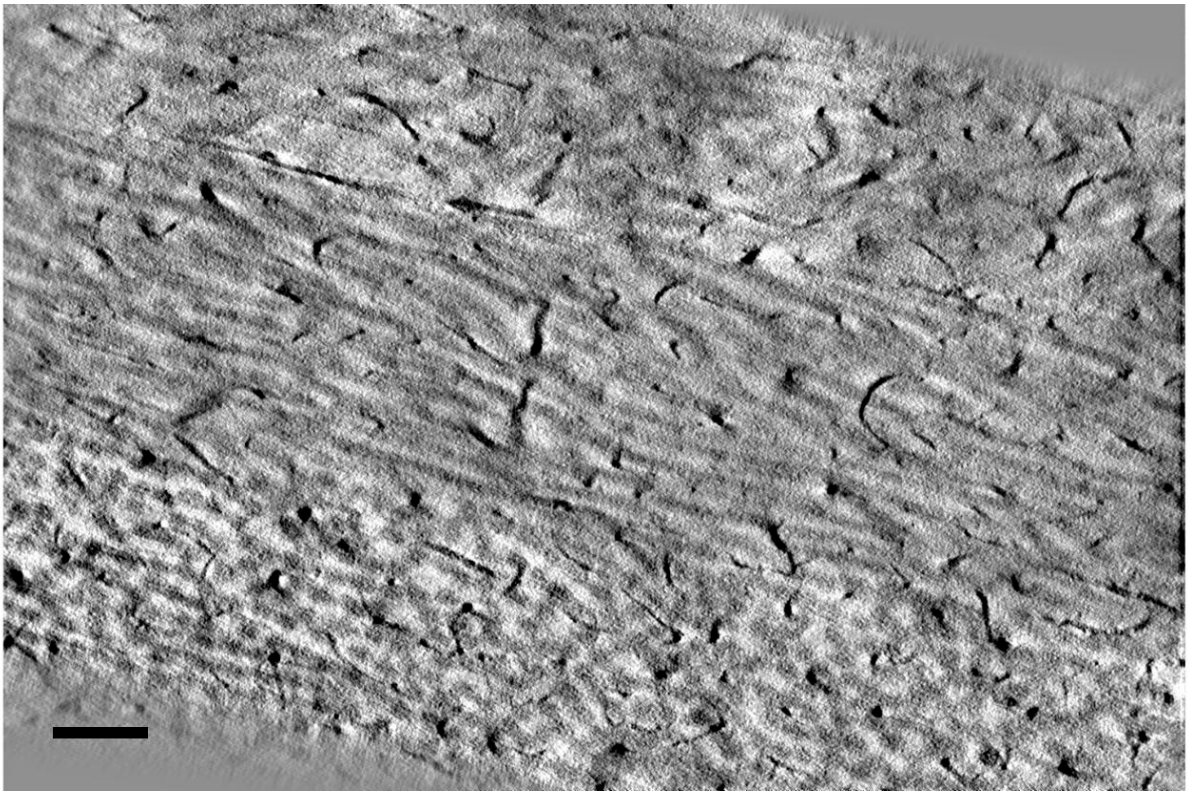

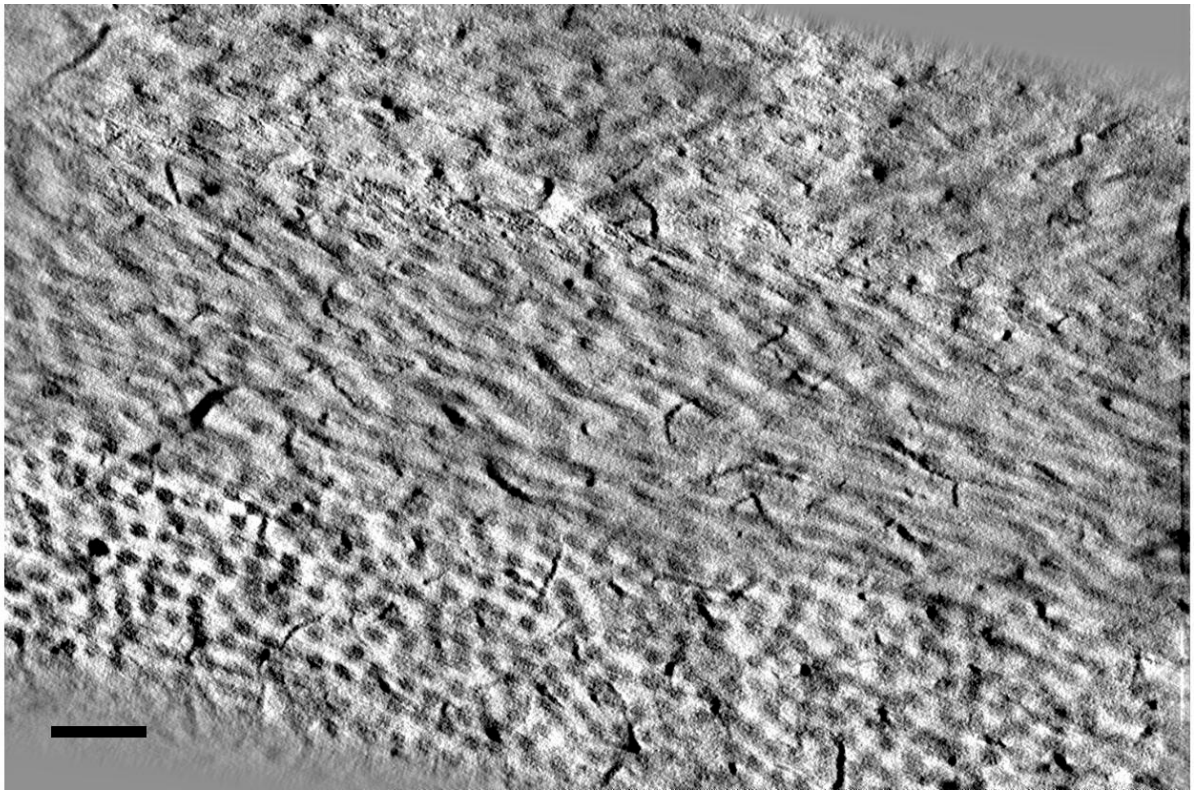

Figure 5.3: Images from a planar reconstruction acquired from a tilt series taken in 1 degree steps from -60 to +60. Images are shown from the anterior, centre and posterior sections of the reconstruction respectively. Scale bar = 100nm

Figure 5.4 shows a rendered reconstruction of an area of the tilt series. Collagen fibrils are shown in blue and proteoglycans in gold. The image was rendered by segmenting the proteoglycan structures manually through the planes of the reconstructed image in which it appeared. Collagen fibrils were segmented using an automated process.

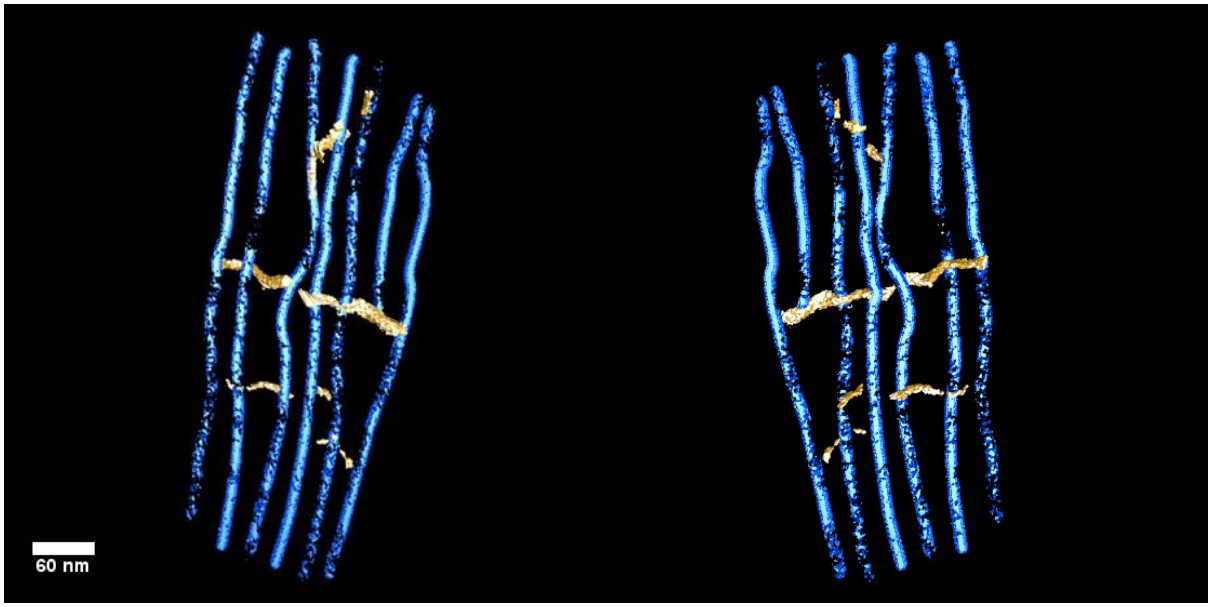

Figure 5.4: Reconstruction of section from figure 5.2. Collagen fibrils are coloured blue with proteoglycans in gold. Viewpoints are given from opposite directions of the same structure.

5.3.2 Reconstructions of MCD Proteoglycan filled voids

An electron micrograph image taken of a collagen free lake is shown in figure 5.5. Two-dimensional planes of the reconstruction that was created from it are shown in figure 5.6. Three-dimensional segmentations of proteoglycans within this area are presented in figure 5.7. The views are of the same section of the proteoglycan matrix, with the first orientated such that the beam is perpendicular to the plane of the image, and the second is the same rendered section that has been slightly rotated about the y-axis in order to show the lack of bonding between the molecules. Colours that have been assigned to some of the proteoglycans are meant to indicate how one viewpoint would map onto the other. The slightly rotated view of figure 5.7 shows that there are no direct overlaps of the proteoglycans, despite the previous image in figure 5.7, the plane perpendicular to the beam pathway, appearing to show that to be the case. PGs located within the lakes were measured to have a mean length of 47±12nm and thickness of 9.8±2.8nm.

The maximum recorded length was 113nm and the minimum was 29nm. The maximum recorded thickness was 17nm and the minimum was 5.0nm

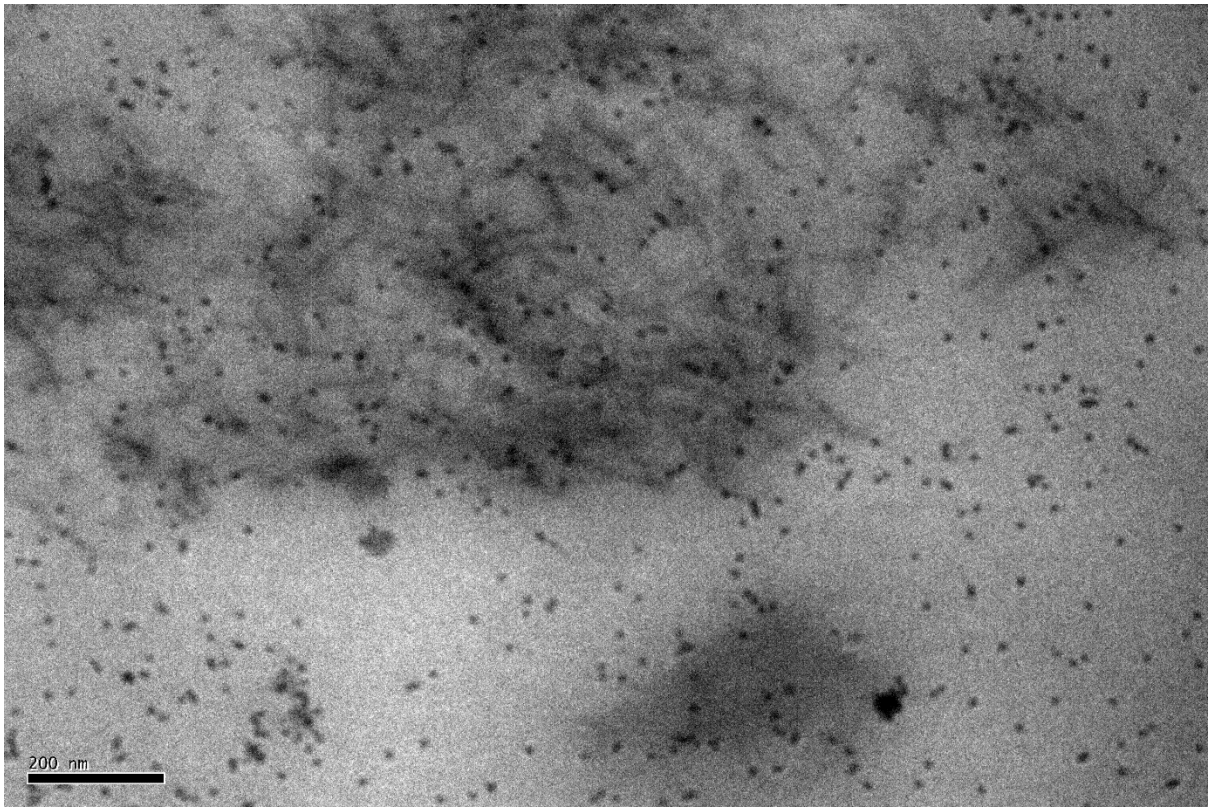

Figure 5.5: Electron micrograph of region of MCD sample populated only by proteoglycans. Dark circles on the image are colloidal gold fiducial markers.

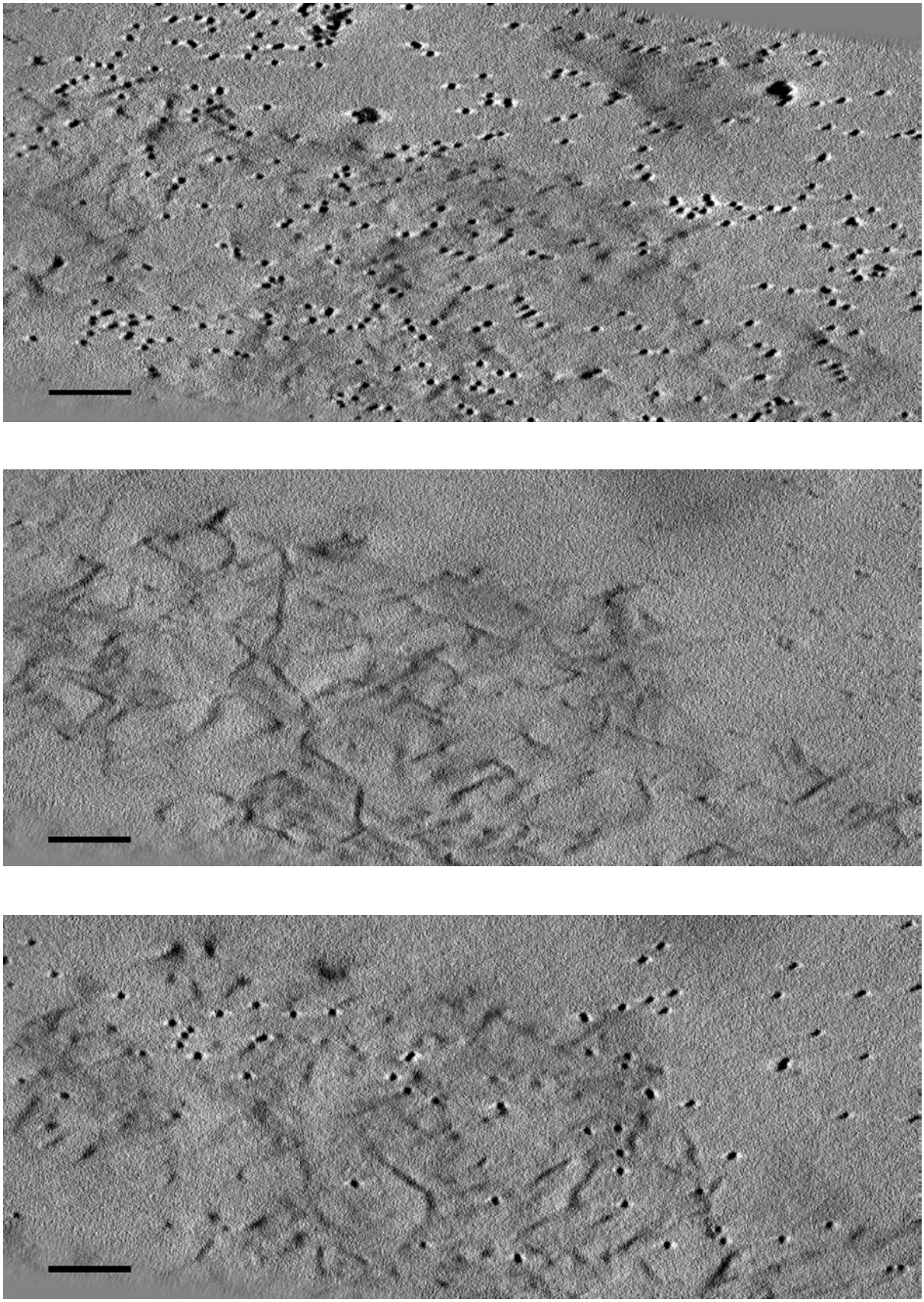

Figure 5.6: 2D planes of 3D reconstruction, showing fiducial markers on the top of the grid (top), the proteoglycans in the middle of the reconstruction (middle), and the fiducial markers on the opposite side of the grid (bottom). Scale bar represents 100nm.

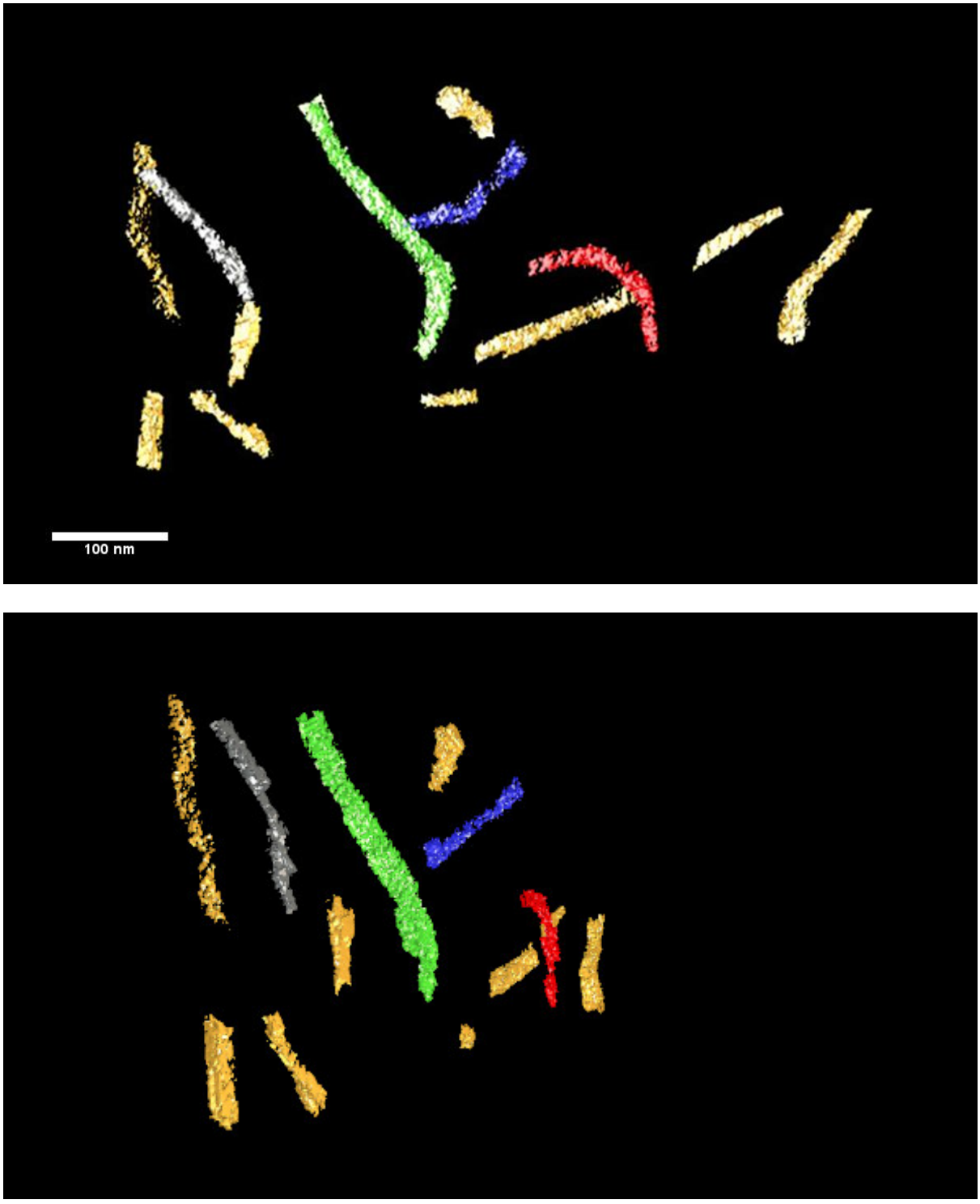

Figure 5.7: Segmentation of void reconstruction, showing proteoglycans. The plane shown in the top segmentation is the plane perpendicular to the beam path. The lower segmentation is of the same PGs but rotated about the y-axis to show their lack of interaction with each other. Colours identify specific proteoglycans for comparison.

5.4 Discussion

Reconstructions of MCD tissue show a larger average length for proteoglycans than would be expected of healthy tissue, in line with expectations given the genetic mutation that is known to disrupt keratan sulphate production (Quantock et al. 1997). Keratan sulphate is known to be the shortest of the PGs from measurements of bovine and rabbit tissue (Scott 1992). An average length equivalent to that of dermatan sulphate would indicate a larger relative abundance compared to keratan sulphate, which is what should be expected of MCD tissue. The structure of the collagen matrix was typical of that expected in cases of MCD (Meek et al. 1989; Quantock et al. 1993; Palka et al. 2010). Lakes were common, and collagen arrangement appeared abnormal. Cases of MCD would also typically show abnormal keratocytes that exhibit unusual cytoplasmic vacuoles (Klintworth 2009). Unfortunately no keratocytes were observed within the electron micrographs obtained, so it was not possible to determine their condition.

In the human cornea the proteoglycans containing keratan sulphate are usually shown to run predominantly orthogonal to the collagen fibrils. From animal studies they are known to be short proteoglycans that interconnect two neighbouring fibrils, so their absence might result in more complicated bonding arrangements (Parfitt et al. 2010). As it is unknown what type of MCD the tissue in the present study is afflicted with, it is not possible to know absolutely whether any keratan sulphate PGs are present within the matrix. What is certain is that their relative abundance will be lower than that would be expected of healthy tissue. Unless aggregation of keratan sulphate is common, we can surmise from the average lengths that these PGs are based on dermatan sulphate. The more elaborate systems of bonding, necessary for a matrix without keratan sulphate, likely result in larger proteoglycan complexes, as more bonds must be made to compensate for the lack of the adjacent fibril bonding usually achieved with

the use of keratan sulphate. The maximum measured length of 80nm is probably an indication of dermatan sulphate PG bonding longitudinally. The reconstruction presented in section 5.3.1 shows some isolated cases of abnormally large proteoglycan complexes. One notable case shown in figure 5.3 appears to bond 5 different fibrils together, although it is probable that this is actually two separate chains that have happened to bond close together. In any case, it seems to be that longer complexes of dermatan sulphate PGs appear within the landscape of MCD tissue much more so than in healthy stromal tissue. Further evidence for this compensatory bonding is that the whole reconstruction seems to be lacking in total proteoglycan number. There appear to be far fewer proteoglycans than would be expected in a healthy tissue reconstruction. This could simply be due to the idea that without sulphated keratan sulphate the stromal matrix is forced to develop with more complex bonding processes.

The number of proteoglycans that have absorbed the cuprolinic blue stain appears to be quite low. This might not be unusual in MCD tissue, since there are no sulphated bonding sites in the keratan PGs, which are of vital importance to the organization of the matrix (Hayashida et al. 2006). However, there is evidence in the literature to suggest that the low or absent sulphation of keratan PGs in MCD is compensated by an increase in sulphation of chondroitin and dermatan sulphate (Nakazawa et al. 1984). From analysis of the lengths of the proteoglycans within the lakes, it would appear that a fraction of the dermatan sulphate PGs that are formed by the keratocyte cells do not find binding sites within the collagen matrix. This could explain why they end up in lakes within the tissue, they are superfluous. This could be due to there being a limited number of potential binding sites, or possibly due to the oversulphation of chondroitin/dermatan sulphate PGs (Nakazawa et al. 1984) preventing its incorporation into the matrix.

In addition to the seemingly abnormal proteoglycans that populate the reconstruction, the organisation of the collagen fibrils is also altered. In several places the fibrils appear to collapse

together until they are close to converging (figure 5.4). This could also be attributed to the lack of keratan sulphate that is the primary result of MCD. Without small scale adjacent fibril bonding being an option, the entire matrix will be inherently less stable, which will lead to the kind of aggregation that is observed in figure 5.4. Following the hypothesis of Lewis et al (2010), without keratan sulphate being present between fibrils to attract the positive ions and water, there exists an imbalance of charge between the fibrils. This action would normally be analogous to the Donnan effect, where a charge imbalance persists on either side of a semi-permeable barrier. With a lack of immobile positive ions provided by the keratan sulphate to repel the collagen fibrils, the attractive forces dominate and the fibrils will aggregate in places (Quantock et al. 1990; Palka et al. 2010). The consequences of this are potentially disastrous. Without a consistent short range order, scattered light from the fibrils will not destructively interfere, and the cornea as a whole will tend more towards greater opacity (Maurice 1957; Hart and Farrell 1969). A further abnormal presentation of the collagen segmentation in figure 5.4 is the presence of one fibril that appears to end within the picture. At the time of writing, no author has successfully claimed to have witnessed the termination of a collagen fibril within an electron micrograph and unfortunately, this cannot be conclusively inferred from Figure 5.4 either. The position of this fibril coincided with a regrettable segment of noise that led to the rest of the fibril being impossible to track. Given the relative position of the neighbouring fibrils it is probable that the one in question continued in a different plane. Without better reconstruction data, it is not possible to know absolutely. The fibril was left in the rendered segmentation as an interesting anomaly.

With regard to the proteoglycan reconstruction, in the two-dimensional planar views, it appears that the proteoglycans that populate the lakes within the stroma are bonding with each other and forming a collagen-free matrix. However, the three-dimensional reconstructions show that not to be the case. The rotated view clearly shows that none of the proteoglycans that appear

to cross over each other in the perpendicular view are actually bonded. This is just one view of course, but it is representative of the whole reconstruction that was partly presented in section 5.3.2. Cases where proteoglycans appeared to be in a bonded state were largely outnumbered by those that just appeared to cross in the two dimensional viewpoint normal to the image. The proteoglycans that were present in the images were also generally smaller, and did not show the larger scale aggregation that was present in the MCD lamellae of section 5.3.1. This has some interesting implications. It is possible that proteoglycans will only bond longitudinally with each other in the presence of collagen. There does not appear to be an obvious reason otherwise for free proteoglycans not to bond longitudinally with each other on contact. There are potential advantages that could be surmised if this were the case. A healthy cornea would benefit from proteoglycans being prevented from forming bonds in the absence of collagen fibrils, because there may be the potential for it to clump together in large numbers rather than fulfil its proper function of maintaining the stability of the matrix. Even if larger scale bonding of many different proteoglycans is not possible, there still might be advantages to having them only bond together when they have already bonded to the fibrils first. This would avoid a situation where the wrong system of bonds has already formed before the proper place in the matrix and the type of bond required has been established. Alternatively, it is also possible that the PGs present in the voids could be fundamentally different from those in the matrix. Chondroitin sulphate in MCD is suspected to be unaffected (Hassell et al. 1980), but if oversulphation of the GAG chains causes the chondroitin/dermatan sulphate to lose their ability to bind to the matrix, it might also cause them to lose the ability to bond longitudinally with each other as well. The maximum PG length recorded does show that some longitudinal bonding is possible, as a PG of 113nm in length must be an aggregated combination of at least two and possibly three different PGs, but these extreme lengths were not very common, and were completely swamped by the PG that were of a length consistent with a lack of bonding.

This effect would might follow logically from the findings of Parfitt et al (2010), who suggested that a lack of sulphation of PGs would encourage longitudinal aggregation. It could follow that oversulphation would therefore have the opposite effect, although this extrapolation has yet to be tested. Of course, if oversulphation were to prevent longitudinal bonding, then the PGs in the matrix must not be oversulphated, as then the entire matrix would break down and one might assume that transparency could not be achieved at all, rather than the gradual losses than we observe to occur.

6 Conclusions

The cornea is a tissue with many different responsibilities, all of which need to be prioritised according to the given situation. Ideally, a cornea is perfectly transparent, resistant to intra-ocular pressure, resistant to extra-ocular mechanical stresses, impervious to infection and shaped such that fine focus can be achieved in tandem with the lens. Which of these properties is given the highest priority is partially situation-dependent. Some amount of transparency for example, might be willingly sacrificed in the form of a scar in order to best preserve structural integrity. It is a decision that is not only made at the unconscious level. Procedures to modify the shape of the cornea, principally to correct visual defects, using laser ablation have become extremely popular since their inception in the 1990s. Understanding how these kind of modifications to the collagen matrix will affect its ability to perform its most important duties is critical when volunteers are so widespread. The unaltered cornea appears to prioritise transparency and structural integrity over its refractive function. Millions around the world are born with, or develop, visual defects that require the addition of corrective lenses. The reasoning for this appears sensible, from an evolutionary standpoint, poor vision is better than no vision at all. Perhaps a more interesting question is in what circumstances, through active mechanisms in the cornea as a response to stimulus, or through passive mechanisms that are a result of abnormal pathology, does the cornea prioritise structure above transparency? This question has been the primary focus for this thesis, presenting experiments designed to test why the transparency sometimes breaks down, and others to attempt to explain in part how abnormal pathology sometimes reorganises this priority order.

The results presented in chapters 2 and 3 appear to lend credence to the hypothesis that keratocytes are adapted to their environment to the point that they actively change their refractive index to match it. The calculated value of refractive index closely matches the known

values for the extra-cellular matrix (ECM) in the stroma, and this value was observed to be different for activated highly mitotic cells. This would suggest that a larger mismatch between the activated cells and the ECM could increase the amount of undesirable scattering and cause a decrease in the transparency of the cornea. In addition, it has been shown what impact the cessation of this mechanism could theoretically have on a cornea using a Mie scattering model. While the model predicts a loss in transparency with only small RI differences, this loss when reasonable parameters are used cannot totally account for the post-operative haze it is thought to cause. Instead this thesis proposes that the cessation of active RI management is compounded by the influx of additional activated cells to the wounded area in question, which would provide a level of additional scattering consistent with the effect observed.

The FTDT model provided interesting results, though they were difficult to interpret. In some respects they provide agreement with the Mie scattering model about the transmission loss that exists solely due to a hole of different RI appearing within the lattice, but in others they disagree with other well established techniques, such as with the differences in transmission with frequency being the reverse of that found by direct summation of fields methods (Leonard 1996). Finite-difference methods may well be the most promising future direction for investigations of the system of corneal transparency, as the results are both more explicitly defined, with fewer assumptions made in the methods, and the system is easier to manipulate for any reason to investigate a multitude of results. However, the extra complications in the calculation has led to the results being difficult to analyse. This might end up being an inevitable trade-off for more complex methods of calculation.

The disorder of keratoconus is one that forces the cornea to give up parts of its structural integrity and shape without compromising transparency, at least initially. As was discussed within chapter 4, the tissue having been grafted out years before donation gave a unique opportunity to study the proposition of recurrent keratoconus within previously donated tissue.

Fibril orientation results for the grafted area showed no obvious abnormalities beyond the suspected incorrect original orientation of the graft, although this result does show that the lack of plasticity of a graft and hence the importance of maintaining the correct orientation for the grafted tissue during surgery. The results for the grafted region for the fibril spacing calculations, however, showed a notable reduction in short-range order when compared with the control tissue. The reduction was not total, some short-range order was retained, which should explain why transparency was still maintained at least superficially. This surprising reduction in short-range order might indicate some amount of recurrent keratoconus, but the effect is not dramatic enough for this to be conclusively shown. Qualitative analysis of micrographs from the same region again appear to indicate some element of abnormal morphology, with some gaps in the lamellae noticed, though again instances were rare enough to not be able to show conclusively. Overall, while some abnormal features were noted within the grafted area, these features were subtle enough to not be able to show as being a conclusive proof of recurrent keratoconus.

With the scarred region, it was clear from visual inspection of the tissue that transparency had been compromised, the TEM results showed both qualitatively and quantitatively that the short-range order was reduced. WAXS studies showed abnormal sections where collagen had aligned tangentially to the annulus, and areas which lacked any meridional collagen at all. It was clear from the condition of the tissue that even after nearly two decades, the scar had not healed to the extent that structural strength had returned to normal, as other tissues would. This again would appear to confirm that the cornea is a tissue that is very adverse to change once its development stages have ended. Whether the changes to the matrix can definitely be said to be responsible for the transparency loss is difficult to show conclusively.

The three-dimensional reconstructions in chapter 5 showed the expected reduction in observed PGs, presumably because the tissue was missing sulphated keratan sulphate PG due to MCD.

This thesis presents a bonding model that suggests that bonding is more complex between PGs in MCD compared to healthy tissue, since it is lacking the sulphated KS that, as a short proteoglycan, would normally bond consecutive fibrils together.

The three-dimensional reconstructions of previously observed PG filled voids showed that although the PGs appear to interact and form a mesh in two-dimensional micrographs, they actually do not bond with each other within the void areas. This thesis presents the possible hypotheses that either PGs may only interact in the presence of collagen, or these voids act as a spare parts storage space for PGs that have been created by the keratocytes without having any place to bond to the matrix. Testing these two hypotheses may become the basis for future research.

6.1 Proposed Future Work

6.1.1 Keratocyte Refractive Index and Scattering Model

The most intriguing area of potential future work is in the methods to obtain the original measurements of phase and thickness. At present, these measurements had to be made at two different times using two different microscopes and two different cell cultures. This is undesirable as using averages to perform the calculations almost certainly contributed to a higher standard error than could be achieved by taking simultaneous measurements of the same cell. Ideally, measurements of bright field intensity could be performed over time in the manner of a time lapse, by setting up an incubated microscope to track the movements, if any, of the cells and taking images at regularly scheduled intervals automatically. If thickness measurements could also be performed on the same cell and at the same time, it would be possible to know exactly how phase difference varies with cell thickness, rather than just assuming it must vary as is the case currently. While the limitations of the measurements as

outlined in this thesis have been discussed and are not expected to invalidate the results, there is obvious scope to improve the method by which they are obtained. Time lapse methods might also suggest just how quickly a refractive index change is achieved, and if this time is of the similar order to the presentation of post-operative haze, the link between the two effects could be made even more strongly.

6.1.2 Keratoconus Study

Due to the nature of the experiments the Danish tissue has already been subjected to, further work on that particular tissue seems unlikely. The tissue has been damaged by high intensity X-rays and the remaining pieces not used for EM have been frozen, which could reasonably be expected to alter the matrix. Additionally, the specific set of situations that led to the tissue existing are quite rare, so it might be unlikely that a tissue with the same history will be secured in the future. However, in the event that a similar tissue is secured, all of the studies that were conducted as part of this thesis should be repeated. This is to ensure that the characteristics that have been highlighted can be repeatedly measured across different tissues. It may also be worth looking more closely at a wider array of situations within the umbrella of penetrating keratoplasty grafts. While the failure rate is known to be low, what is not known is how the original pathology affects the failure rate. If recurrent keratoconus were the suspected cause of these graft failures, it might be expected that PK grafts that carried out for late-stage keratoconus should fail more often that those carried out for other pathologies. Unfortunately for investigations in this area, full PK transplants might become very rare in the future. With surgeons beginning to recognise the extent of the consequences of the damage that a full thickness wound causes, pathologies that affect only a part of the cornea have begun to be treated with only partial transplants, such as with endothelial replacements in Fuch's dystrophy for example.

6.1.3 Macular Corneal Dystrophy Study

Future work on MCD tissue should focus on the interactions of PGs within the tissue, and comparisons with it to other pathologies. The most important comparison that should be made is between tissues diagnosed with different types of MCD. This would allow a comparison to be made between the collagen matrices for different levels of sulphated keratan PGs that are known to exist within the tissue. This might help confirm the role that KS PGs play in the formulation of the matrix and the lengths that MCD afflicted tissue goes to when compensating for their absence within the structure. Comparisons might also be made between the void sections with differing amounts of sulphated KS, to provide further insights into the bonding states of free PGs. Further research may also test the hypothesis that PGs do not normally bond together outside of the collagen matrix. If it were possible to remove the collagen fibrils, possibly by collagenase digestion, it might be possible to study the interaction of proteoglycans directly.

Appendix A: Derivation of Equation 2.8

Starting with Eq. 2.5 and 2.6

$$S_{coh}(\vec{r}) = -\frac{1}{8\pi}\left(\nabla U(\vec{r},t)\frac{\partial}{\partial t}U^*(\vec{r},t) + \nabla U^*(\vec{r},t)\frac{\partial}{\partial t}U(\vec{r},t)\right) \tag{2.5}$$

$$U(\vec{r},t) = \sqrt{I_{coh}}exp\big(i(\phi(\vec{r}) - \omega t)\big) \tag{2.6}$$

By substituting Eq. 2.6 into Eq 2.5 we obtain

$$S_{coh}(\vec{r}) = -\frac{1}{8\pi}\left(\nabla\left(\sqrt{I_{coh}}\frac{e^{i\phi(\vec{r})}}{e^{i\omega t}}\right)\frac{\partial}{\partial t}\left(\sqrt{I_{coh}}\frac{e^{i\omega t}}{e^{i\phi(\vec{r})}}\right)\right.$$

$$\left. + \nabla\left(\sqrt{I_{coh}}\frac{e^{i\omega t}}{e^{i\phi(\vec{r})}}\right)\frac{\partial}{\partial t}\left(\sqrt{I_{coh}}\frac{e^{i\phi(\vec{r})}}{e^{i\omega t}}\right)\right)$$

As the irradiance is constant, it can be removed from the derivatives

$$S_{coh}(\vec{r}) = -\frac{1}{8\pi}\left(I_{coh}\nabla\frac{e^{i\phi(\vec{r})}}{e^{i\omega t}}\frac{\partial}{\partial t}\frac{e^{i\omega t}}{e^{i\phi(\vec{r})}} + I_{coh}\nabla\frac{e^{i\omega t}}{e^{i\phi(\vec{r})}}\frac{\partial}{\partial t}\frac{e^{i\phi(\vec{r})}}{e^{i\omega t}}\right)$$

Exponential terms that only depend on time can be removed from the spatial derivatives and vice versa.

$$S_{coh}(\vec{r}) = -\frac{I_{coh}}{8\pi}\left(e^{-i\omega t - i\phi(\vec{r})}\nabla e^{i\phi(\vec{r})}\frac{\partial}{\partial t}e^{i\omega t} + e^{i\omega t + i\phi(\vec{r})}\nabla e^{-i\phi(\vec{r})}\frac{\partial}{\partial t}e^{-i\phi(\vec{r})}\right)$$

The spatial derivatives can be found by using implicit derivatives and the chain rule

$$S_{coh}(\vec{r}) = -\frac{I_{coh}}{8\pi}\left(e^{-i\omega t - i\phi(\vec{r})}\left(ie^{i\phi(\vec{r})}\nabla\phi(\vec{r})\right)\left(i\omega e^{i\omega t}\right)\right.$$
$$\left. + e^{i\omega t + i\phi(\vec{r})}\left(-ie^{-i\phi(\vec{r})}\nabla\phi(\vec{r})\right)\left(-i\omega e^{-i\omega t}\right)\right)$$

By cancelling exponentials and making use of the definition $i^2 = (-i)^2 = -1$ this reduces to Eq. 2.8, as required

$$S_{coh}(\vec{r}) = -\frac{I_{coh}}{8\pi}\big(-i\omega\nabla\phi(\vec{r}) - i\omega\nabla\phi(\vec{r})\big)$$

$$S_{coh}(\vec{r}) = \frac{\omega}{4\pi} I_{coh} \nabla\phi(\vec{r})$$

Q.E.D

Appendix B: Derivation of Equation 2.12

Starting with the TIE

$$-\bar{k}\frac{\partial I(\vec{r})}{\partial z} = \nabla_{\perp}.\left(I(\vec{r})\nabla_{\perp}\phi(\vec{r})\right) \tag{2.11}$$

This equation can be rearranged to make the phase the subject first by using the definition that $\nabla^2\nabla^{-2} \equiv 1$

$$-\bar{k}\nabla_{\perp}^2\nabla_{\perp}^{-2}\frac{\partial I(\vec{r})}{\partial z} = \nabla_{\perp}.\left(I(\vec{r})\nabla_{\perp}\phi(\vec{r})\right)$$

Since $\nabla^2 \equiv \nabla.\nabla$, this can be further rearranged to

$$-\bar{k}\nabla_{\perp}.\left(\nabla_{\perp}\nabla_{\perp}^{-2}\frac{\partial I(\vec{r})}{\partial z}\right) = \nabla_{\perp}.\left(I(\vec{r})\nabla_{\perp}\phi(\vec{r})\right)$$

$$-\bar{k}\nabla_{\perp}\nabla_{\perp}^{-2}\frac{\partial I(\vec{r})}{\partial z} = I(\vec{r})\nabla_{\perp}\phi(\vec{r})$$

$$-\bar{k}\frac{1}{I(\vec{r})}\nabla_{\perp}\nabla_{\perp}^{-2}\frac{\partial I(\vec{r})}{\partial z} = \nabla_{\perp}\phi(\vec{r})$$

Progression is achieved by exploiting the identity $\nabla^2(\nabla A) \equiv \nabla(\nabla^2 A)$

$$-\bar{k}\nabla_{\perp}^2\frac{1}{I(\vec{r})}\nabla_{\perp}\nabla_{\perp}^{-2}\frac{\partial I(\vec{r})}{\partial z} = \nabla_{\perp}^2\left(\nabla_{\perp}\phi(\vec{r})\right)$$

$$-\bar{k}\nabla_{\perp}^2\frac{1}{I(\vec{r})}\nabla_{\perp}\nabla_{\perp}^{-2}\frac{\partial I(\vec{r})}{\partial z} = \nabla_{\perp}\left(\nabla_{\perp}^2\phi(\vec{r})\right)$$

$$-\bar{k}\nabla_{\perp}\left(\nabla_{\perp}.\left(\frac{1}{I(\vec{r})}\right)\nabla_{\perp}\nabla_{\perp}^{-2}\frac{\partial I(\vec{r})}{\partial z}\right) = \nabla_{\perp}\left(\nabla_{\perp}^2\phi(\vec{r})\right)$$

$$-\bar{k}\nabla_{\perp}.\left(\frac{1}{I(\vec{r})}\right)\nabla_{\perp}\nabla_{\perp}^{-2}\frac{\partial I(\vec{r})}{\partial z} = \nabla_{\perp}^2\phi(\vec{r})$$

$$-\bar{k}\nabla_{\perp}^{-2}\left(\nabla_{\perp}.\left(\frac{1}{I(\vec{r})}\right)\nabla_{\perp}\nabla_{\perp}^{-2}\frac{\partial I(\vec{r})}{\partial z}\right) = \phi(\vec{r})$$

Which is Eq 2.13

Q.E.D

Appendix C: Proof of the Exact Solution Theorem

Starting with Eq. 3.17, which is repeated here for convenience.

$$u_i^{n+1} = u_{i+1}^n + u_{i-1}^n - u_i^{n-1} \tag{3.17}$$

In chapter 3, this equation was reached by making use of a Taylor expansion. The remainder term of the expansion was neglected as negligible. However, by expanding all the terms in both sides of Eq 3.17, it can be shown that no approximation is actually made. By rewriting the wavefunctions as exact solutions of the wave equation such that, $u_i^n = F(x_i + ct_n) + G(x_i - ct_n)$, the RHS of Eq 3.17 becomes

$$RHS = [F(x_{i+1} + ct_n) + G(x_{i+1} - ct_n)] + [F(x_{i-1} + ct_n) + G(x_{i-1} - ct_n)] - [F(x_i + ct_{n-1}) + G(x_i - ct_{n-1})]$$

By discretising our space and time grids such that $x_i = i\Delta x$ and $t_n = n\Delta t$ we can expand the previous equation

$$RHS = \big[F\big((i+1)\Delta x + cn\Delta t\big) + G\big((i+1)\Delta x - cn\Delta t\big)\big] + \big[F\big((i-1)\Delta x + cn\Delta t\big) + G\big((i-1)\Delta x - cn\Delta t\big)\big] - [F(i\Delta x + c(n-1)\Delta t) + G(i\Delta x - c(n-1)\Delta t)]$$

In the specific case that $\Delta x = c\Delta t$ this relation becomes

$$RHS = \big[F\big((i+1)\Delta x + n\Delta x\big) + G\big((i+1)\Delta x - n\Delta x\big)\big] + \big[F\big((i-1)\Delta x + n\Delta x\big) + G\big((i-1)\Delta x - n\Delta x\big)\big] - [F(i\Delta x + (n-1)\Delta x) + G(i\Delta x - (n-1)\Delta x)]$$

$$RHS = \left[F\big((i+n+1)\Delta x\big) + G\big((i-n+1)\Delta x\big)\right] + \left[F\big((i+n-1)\Delta x\big) + G\big((i-n-1)\Delta x\big)\right] - \left[F\big((i+n-1)\Delta x\big) + G\big((i-n+1)\Delta x\big)\right]$$

After cancellations this reduces to

$$RHS = F\big((i+n+1)\Delta x\big) + G\big((i-n-1)\Delta x\big)$$

Expanding the LHS

$$LHS = u_i^{n+1} = F(x_i + ct_{n+1}) + G(x_i - ct_{n+1})$$

$$LHS = F(i\Delta x + c(n+1)\Delta t) + G(i\Delta x - c(n+1)\Delta t)$$

Again by setting the steps of the grid such that $\Delta x = c\Delta t$

$$LHS = F(i\Delta x + (n+1)\Delta x) + G(i\Delta x - (n+1)\Delta x)$$

$$= F\big((i+n+1)\Delta x\big) + G\big((i-n-1)\Delta x\big)$$

This is identical to the final form for the RHS, and so Eq 3.17 must be an exact equation.

Appendix D: Program Code

FDTD model, written in Scheme and run within meep 1.2.1

```
(define-param x 60) ; x-size of system
(define-param y 20) ; y-size of system
(define-param fxnum 16) ; number of fibrils in lattice rows
(define-param fynum 14); number of fibrils in lattice columns
(define-param xgapnum 7); size of fibril gap in x-direction
(define-param ygapnum 4); size of fibril gap in y-direction
(define-param frad 0.3) ; fibril radius
(define-param fxspace 1.732) ; x fibril spacing
(define-param fyspace 0.5) ; y fibril spacing
(define-param epsf 1.991); epsilon of fibrils
(define-param epsc 1.891); epsilon of extrafibrillar material
(define-param endtime 300); number of iterations
(define-param sampletime 0.5); time between each sample
(define-param freq 0.05); frequency of pulse
(define-param df 0.05); width of pulse
(define-param latcenx -4); lattice cylinder center x co-ord
(define-param latceny 10); lattice cylinder centre y co-ord
(define-param lattice? true); default with lattice in place
(define-param hole? false); default with no hole in lattice
(define v1 (vector3 1 0))
(define v2 (vector3 0 -1.732))

(set! geometry-lattice (make lattice (size x y no-size)))
(set! default-material (make dielectric (epsilon epsc)))

(set! geometry
        (if lattice?
        (if hole?
        (append
        (geometric-objects-duplicates v1 0 (- (/ fxnum 2) 1)
        (geometric-object-duplicates v2 0 (- fynum 1)
                (make cylinder (center latcenx latceny)(height infinity)(radius frad)
                (material (make dielectric(epsilon epsf)
);end make dielectric
);end material
);end make cylinder
);end geometric-object-duplicates
);end geometric-objects-duplicates

        (geometric-objects-duplicates v1 0 (- (/ fxnum 2) 1)
        (geometric-object-duplicates v2 0 (- fynum 1)
                (make cylinder (center (- latcenx 0.5) (+ latceny 0.866))(height infinity)(radius frad)
                (material (make dielectric(epsilon epsf)

);end make dielectric
);end material
);end make cylinder
);end geometric-object-duplicates
);end geometric-objects-duplicates
        (geometric-objects-duplicates v1 0 (- (/ fxnum 2) 1)
        (geometric-object-duplicates v2 0 (- fynum 1)
                (make cylinder (center (+ (+ latcenx xgapnum) fxnum) latceny)(height infinity)(radius frad)
                (material (make dielectric(epsilon epsf)

);end make dielectric
);end material
);end make cylinder
);end geometric-object-duplicates
);end geometric-objects-duplicates
```

```
(geometric-objects-duplicates v1 0 (- (/ fxnum 2) 1)
        (geometric-object-duplicates v2 0 (- fynum 1)
                (make cylinder (center (+ (+ (+ latcenx xgapnum) fxnum) 0.5) (+ latceny 0.866))(height infinity)(radius
frad)
                (material (make dielectric(epsilon epsf)

);end make dielectric
);end material
);end make cylinder
);end geometric-object-duplicates
);end geometric-objects-duplicates
(geometric-objects-duplicates v1 0 (- (+ (/ fxnum 2) xgapnum) 1)
        (geometric-object-duplicates v2 0 (- (/ fynum 2) ygapnum)
                (make cylinder (center (+ latcenx (/ fxnum 2) ) latceny)(height infinity)(radius frad)
                (material (make dielectric(epsilon epsf)
);end make dielectric
);end material
);end make cylinder
);end geometric-object-duplicates
);end geometric-objects-duplicates

(geometric-objects-duplicates v1 0 (+ (+ (/ fxnum 2) xgapnum) 1)
        (geometric-object-duplicates v2 0 (- (/ fynum 2) ygapnum)
                (make cylinder (center (- (+ latcenx (/ fxnum 2)) 0.5 ) (+ latceny 0.866))(height infinity)(radius frad)
                (material (make dielectric(epsilon epsf)
);end make dielectric
);end material
);end make cylinder
);end geometric-object-duplicates
);end geometric-objects-duplicates

(geometric-objects-duplicates v1 0 (- (+ (/ fxnum 2) xgapnum) 1)
        (geometric-object-duplicates v2 0 (- (/ fynum 2) ygapnum)
                (make cylinder (center (+ latcenx (/ fxnum 2)) (+ (- (- latceny (/ fynum 2)) ygapnum) 0.866))(height
infinity)(radius frad)
                (material (make dielectric(epsilon epsf)
);end make dielectric
);end material
);end make cylinder
);end geometric-object-duplicates
);end geometric-objects-duplicates

);end append (if hole?=true)
        (append
        (geometric-objects-duplicates v1 0 (- fxnum 1)
        (geometric-object-duplicates v2 0 (- fynum 1)
                (make cylinder (center latcenx latceny)(height infinity)(radius frad)
                (material (make dielectric(epsilon epsf)
);end make dielectric
);end material
);end make cylinder
);end geometric-object-duplicates
);end geometric-objects-duplicates

        (geometric-objects-duplicates v1 0 (- fxnum 1)
        (geometric-object-duplicates v2 0 (- fynum 1)
                (make cylinder (center (- latcenx 0.5) (+ latceny 0.866))(height infinity)(radius frad)
                (material (make dielectric(epsilon epsf)

);end make dielectric
);end material
);end make cylinder
);end geometric-object-duplicates
);end geometric-objects-duplicates

);end append (if lattice?=true) (if hole?=false)
);end if hole
```

```
            (list
            (make block
            (center 0 0)
            (size x y infinity)
            (material (make dielectric (epsilon epsc)
);end make dielectric
);end material
);end make block
);end list (if lattice?=false)
);end if lattice
);end set geometry

(define-param i 0)
;(let loop ((i 0))
;(if (< i 200)
;(begin

(set! sources          (append sources
                       (list
                       (make source
                                  (src (make gaussian-src (frequency freq)
                                  (fwidth df)
                                  (start-time i)
                                  (end-time (+ 10 i)
);end end-time
);end make continuous-src
);end src
                                  (component Ez)
                                  (size 0 16)
                                  (center -28 0)
);end make source
);end list
);end append sources
);end set sources

(set! pml-layers (list (make pml (thickness 1.0))))

(set! resolution 10)

(define-param nfreq 300) ; number of frequencies to compute pulse
(define trans ; transmitted flux
            (add-flux freq df nfreq
            (make flux-region
            (center (- (/ x 2) 5) 0)(size 0 (- y 4))
); end make flux-region
); end add-flux
); end define

(define refl ; reflected flux
            (add-flux freq df nfreq
            (make flux-region
            (center  (- latcenx 4) 0)(size 0 (- y 4))
); end make flux-region
); end add-flux
); end define



(run-until endtime
            (at-beginning output-epsilon)
            ;(to-appended "ez" (at-every sampletime output-efield-z)
);end to-appended
);end run-until

(display-fluxes trans refl)
```

Code for the polar plot montage program, written in Visual Basic and run in Microsoft Excel 2009 and 2013

```
Sub GraphMont()


Dim n As Object
Dim ex, why, i, sfile, j, jex As Integer
Dim t, l As Double
Dim WB As Workbook

Set WB = Excel.Workbooks.Open("F:\Kc1\Kc1map.xlsx") 'Insert path of destination spreadsheet here.

why = InputBox("Number of Rows?")
ex = InputBox("Number of Columns?")

Flip = MsgBox("Does the data need to be flipped?", vbYesNo)

If Flip = vbYes Then

sfile = 1

For j = 1 To why 'Loop to change between rows

jex = j * ex
jmex = (j - 1) * ex

For i = sfile To jex 'Loop to fill rows

Set n = ActiveSheet.Pictures.Insert("F:\Kc1\Kc1mapj " & i & ".jpg") 'Insert Filepath of polar plots here and in the same place in the second half of the if decision
With Cells(6 * j, 3 * ((ex + 1) - (i - jmex))) 'This set up fills rows from right to left
l = .Left
t = .Top
End With
With n
.Top = t
.Left = l
End With
n.Select
Selection.ShapeRange.ScaleWidth 0.47, msoFalse, msoScaleFromTopLeft 'Scaling factors. To make final plot square, change the size of the cells in the spreadsheet first to 20x40 pixels
Selection.ShapeRange.ScaleHeight 0.47, msoFalse, msoScaleFromTopLeft

Next i

sfile = sfile + ex

'MsgBox ("Row " & j & " is complete") If montage is very big, use this line to insert a message box after every row, thus confirming the program is still running, comment out if unnecessary

Next j

Else

sfile = 1

For j = 1 To why

jex = j * ex
jmex = (j - 1) * ex

For i = sfile To jex

Set n = ActiveSheet.Pictures.Insert("F:\Kc1\Kc1mapj " & i & ".jpg")
With Cells(6 * j, 3 * (i - jmex)) 'In this case, plot will be inserted from left to right
```

```
l = .Left
t = .Top
End With
With n
.Top = t
.Left = l
End With
n.Select
Selection.ShapeRange.ScaleWidth 0.47, msoFalse, msoScaleFromTopLeft
Selection.ShapeRange.ScaleHeight 0.47, msoFalse, msoScaleFromTopLeft

Next i

sfile = sfile + ex

'MsgBox ("Row " & j & " is complete") used for big files, in order to break up the running of the program

Next j

End If

MsgBox ("Montage is complete")

End Sub
```

Appendix E: Published Work

OPEN ACCESS Freely available online

PLOS ONE

Quantification of Collagen Ultrastructure after Penetrating Keratoplasty – Implications for Corneal Biomechanics

Craig Boote[1☯], Erin P. Dooley[1☯], Steven J. Gardner[1], Christina S. Kamma-Lorger[1], Sally Hayes[1], Kim Nielsen[2], Jesper Hjortdal[2], Thomas Sorensen[3], Nicholas J. Terrill[3], Keith M. Meek[1]*

1 Structural Biophysics Group, School of Optometry and Vision Sciences, Cardiff University, Cardiff, United Kingdom, **2** Department of Ophthalmology, Aarhus University Hospital, Aarhus, Denmark, **3** Diamond Light Source, Didcot, Oxfordshire, United Kingdom

Abstract

Purpose: To quantify long-term changes in stromal collagen ultrastructure following penetrating keratoplasty (PK), and evaluate their possible implications for corneal biomechanics.

Methods: A pair of 16 mm post-mortem corneo-scleral buttons was obtained from a patient receiving bilateral penetrating keratoplasty 12 (left)/28 (right) years previously. Small-angle x-ray scattering quantified collagen fibril spacing, diameter and spatial order at 0.5 mm or 0.25 mm intervals along linear scans across the graft margin. Corresponding control data was collected from two corneo-scleral buttons with no history of refractive surgery. Wide-angle x-ray scattering quantified collagen fibril orientation at 0.25 mm (horizontal)×0.25 mm (vertical) intervals across both PK specimens. Quantification of orientation changes in the graft margin were verified by equivalent analysis of data from a 13 year post-operative right PK specimen obtained from a second patient in a previous study, and comparison made with new and published data from normal corneas.

Results: Marked changes to normal fibril alignment, in favour of tangentially oriented collagen, were observed around the entire graft margin in all PK specimens. The total number of meridional fibrils in the wound margin was observed to decrease by up to 40%, with the number of tangentially oriented fibrils increasing by up to 46%. As a result, in some locations the number of fibrils aligned parallel to the wound outnumbered those spanning it by up to five times. Localised increases in fibril spacing and diameter, with an accompanying reduction in matrix order, were also evident.

Conclusions: Abnormal collagen fibril size and spatial order within the PK graft margin are indicative of incomplete stromal wound remodelling and the long term persistence of fibrotic scar tissue. Lasting changes in collagen fibril orientation in and around PK wounds may alter corneal biomechanics and compromise the integrity of the graft-host interface in the long term.

Citation: Boote C, Dooley EP, Gardner SJ, Kamma-Lorger CS, Hayes S, et al. (2013) Quantification of Collagen Ultrastructure after Penetrating Keratoplasty – Implications for Corneal Biomechanics. PLoS ONE 8(7): e68166. doi:10.1371/journal.pone.0068166

Editor: Michael E. Boulton, University of Florida, United States of America

Received April 16, 2013; **Accepted** May 30, 2013; **Published** July 5, 2013

Funding: Medical Research Council (Grants G0600755 and MR/K000837/1). The funders had no role in study design, data collection and analysis, decision to publish, or preparation of the manuscript.

Competing Interests: The authors have declared that no competing interests exist.

* E-mail: meekkm@cf.ac.uk

☯ These authors contributed equally to this work.

Introduction

The biomechanical properties of the cornea are influenced significantly by the organization of collagen fibrils that form the bulk of the corneal stroma [1]. Alterations in the alignment [2,3,4], diameter [5,6,7] and spatial order [5,6] of stromal fibrils occurs after penetrating injury, and there is evidence that some of these changes persist long-term in and around the wound margin following some types of corneal surgery [3,8,9]. Some of these findings may be related to the observation that the mechanical strength of corneal scar tissue never fully reaches uninjured levels [10]. A number of investigators have examined the appearance of the graft margin following penetrating keratoplasty (PK) [3,9,11,12,13,14,15]. All of these studies reported significant demarcation or abnormalities in the stroma at the graft-host interface, suggesting a limited stromal healing response. However, the majority of this literature featured either histological or confocal microscopic findings, while quantitative, ultrastructural studies of collagen architecture following penetrating corneal wounds remain scarce.

Here we have used x-ray scattering to quantify stromal collagen ultrastructure in a pair of post-mortem human eyes from a patient who underwent bilateral PK for keratoconus 12 (left eye) and 28 (right eye) years previously, and a 8.5 mm post-operative corneal button from the right eye of a second patient who required re-graft 13 years after originally undergoing PK. The availability of tissue

of this kind is extremely limited. This study therefore afforded us a rare opportunity to investigate the long-term effects of penetrating injury on corneal ultrastructure by carrying out the first quantitative study of collagen organisation across whole corneal specimens featuring PK wounds.

Methods

The research presented in this manuscript was approved by the Human Science Ethical Committee (School of Optometry and Vision Sciences, Cardiff University, UK) and the South East Wales Research Ethics Committee (Cardiff, UK). The institutional review board approved the use of all corneas described in this study; a waiver of consent was given for the donor corneas. All tissue used in this study was obtained in accordance with the tenets of the Declaration of Helsinki, and local ethical rules were adhered to throughout. All experimental procedures were performed in accordance with the Declaration of Helsinki.

PK Patient 1 Tissue Details

A pair of post-mortem eyes with history of bilateral PK for keratoconus was obtained from The Danish Cornea Bank, Aarhus University Hospital (Aarhus, Denmark). The age of the PK recipient at death was 79 yrs. The donors' ages were not available. 16 mm diameter corneo-scleral buttons were excised and the orientation within the eye marked with a scleral suture. The specimens were then immediately wrapped in polyvinylidene chloride film to prevent dehydration, frozen and stored at −80°C until the time of x-ray experiments. Inspection of the PK tissue using light microscopy prior to the x-ray experiments disclosed that both specimens displayed prominent regions of opacity in the peripheral cornea, located on the temporal side in the left eye and inferior/superior in the right, and that the graft margins were still visibly demarcated (Fig. 1A,C). Additionally, a marked discontinuity of the wound edge was visible on the temporal side of the right eye (Fig. 1C). *Left eye history:* Underwent 8.2 mm/8.0 mm PK for keratoconus 12 years previously. The apex was thinned and located inferior/temporal. However, thinning and astigmatism could not be accurately quantified due to irregularity of the corneal surface. 5 months after PK there was vascularization into the donor cornea as far as the sutures. The sutures (superior: 5 loops parallel to the suture, inferior: 4 loops) were removed after 12 months, and at 14 months there were no reported complications. *Right eye history:* Underwent PK for keratoconus 28 years previously. No further information was available.

PK Patient 2 Tissue Details

A 8.5 mm diameter post-operative corneal button from a 51 year old patient who required re-graft following suspected recurrence of keratoconus 13 years after initial 7.5 mm/7.25 mm PK surgery. A detailed structural examination of this specimen was published by our lab previously and concluded that corneal ectasia at 13 years may have recurred due to a mechanical failure of the graft rather than keratoconus recurrence [3]. In the current study, a portion of the raw x-ray scatter data was re-analysed in order to verify results from patient 1.

Control Tissue Details

Two post-mortem corneo-scleral buttons from donors aged 71 yrs (Control 1) and 47 yrs (Control 2), with no history of keratoconus or refractive surgery, were obtained from Bristol Eye Hospital (Bristol, UK). The specimens were wrapped in polyvinylidene chloride film, frozen and stored at −80°C until the time of x-ray experiments. Further control results were obtained via re-analysis of raw x-ray data from a normal cornea (Control 3) examined in detail in a previous publication by our lab [16].

Small-angle x-ray Scattering

Small-angle x-ray scattering [17] (SAXS) was performed on Beamline I22 at the Diamond Light Source (Didcot, UK), using an x-ray beam (wavelength: 0.1 nm) with a cross-sectional diameter of 0.25 mm. Each film-wrapped specimen was thawed and placed into sealed Perspex® (Lucite Group Ltd, Southampton, UK) chambers with Mylar® (DuPont-Teijin, Middlesbrough, UK) windows. The incident x-ray beam was directed towards the anterior specimen surface, perpendicular to the corneal apex, and the specimens were allowed to retain their natural curvature. Specimen alignment was achieved by an initial exposure of x-ray sensitive film placed in the specimen chamber to locate the position of the incident beam. SAXS patterns, each resulting from an x-ray exposure of 10 s, were collected along multiple linear scans across the graft-host interface of each specimen at, 0.25 mm (PK left) or 0.5 mm (PK right) sampling intervals (Fig. 1B,D), and recorded electronically on an x-ray detector placed 6 m behind the specimen position. Equivalent data from corresponding locations on the control specimens were also collected (Fig. 1E). Specimen translation between exposures was achieved using a motorized stage integrated with the x-ray camera shutter. Analysis of corneal SAXS patterns allows quantification of the average separation, diameter and index of spatial order of collagen fibrils in the stromal volume sampled by the x-ray beam [17]. Measurements of all three collagen parameters were obtained at each sampled point in the specimens, as described previously [18,19,20].

Wide-angle x-ray Scattering

Following SAXS experiments, the PK specimens were immediately placed in 4% paraformaldehyde and stored at 4°C for subsequent characterization using wide-angle x-ray scattering (WAXS). Our previous work has established that this mild fixation method does not affect corneal/scleral collagen parameters as measured by WAXS [16]. Diamond Beamline I02 was used to record WAXS patterns across the whole of each PK specimen at 0.25 mm (horizontal)×0.25 mm (vertical) intervals, using an x-ray beam of wavelength 0.098 nm and a cross-sectional diameter of 0.2 mm. For data collection each specimen was mounted in the same way as for SAXS, such that the incident x-ray beam was directed at the anterior surface and perpendicular to the corneal apex, and the tissue's natural curvature was retained. Initial specimen alignment was achieved via an in-line microscope directed along the incident x-ray beam direction. WAXS patterns, each resulting from an x-ray exposure of 8 s, were recorded electronically on a CCD detector (ADSC, Poway, USA) placed 550 mm behind the specimen position. Specimen translation was achieved using integrated motor stages.

Analysis of corneal/scleral WAXS patterns provides a quantitative measure of bulk collagen fibril orientation, as an average value within the stromal volume sampled by the x-ray beam [21]. For every sampled location in the PK specimens, we obtained three measurements: 1) the relative number of fibrils preferentially aligned at a given angle within the tissue plane (over and above the population of fibrils that are arranged isotropically), 2) the total x-ray scatter integral (a measure of the total mass of fibrous collagen), 3) the aligned x-ray scatter integral (a measure of the mass of preferentially aligned collagen). A detailed account of the data analysis may be found in a previous publication [21].

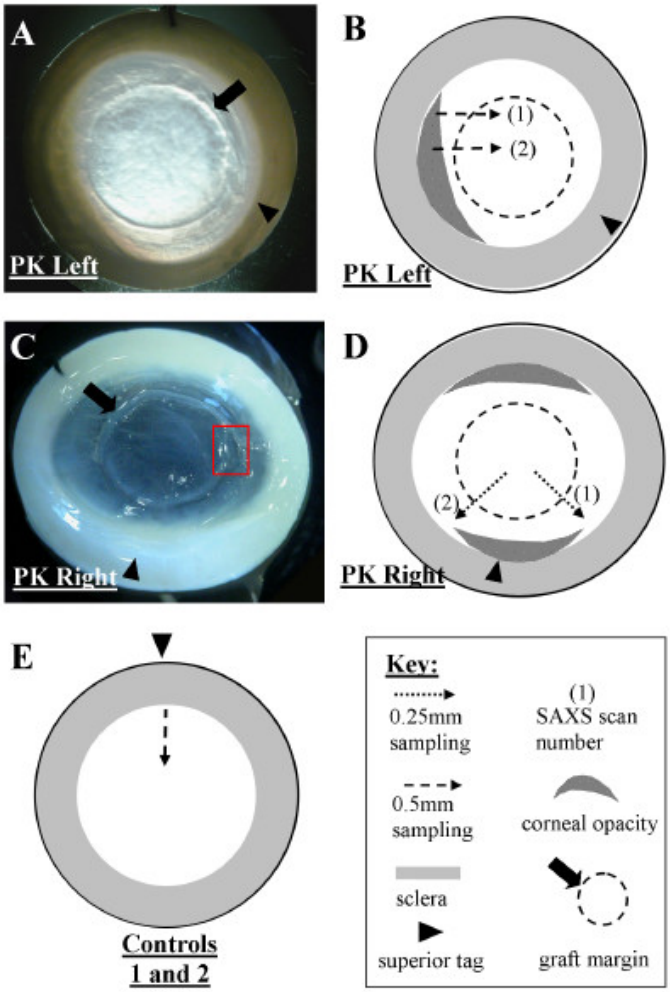

Figure 1. Appearance of specimens and SAXS sampling locations. A) Left and **C)** right PK specimens from Patient 1. Red rectangle in C) shows discontinuity of the wound edge in the right eye. **B–E)** SAXS scans performed on the PK and control specimens.
doi:10.1371/journal.pone.0068166.g001

Results

Collagen Spatial Organisation

Fig. 2 shows SAXS results from two linear scans across the graft-host interface of the left PK specimen of Patient 1. Similar to previous findings in normal human corneas using transmission electron microscopy [22] and SAXS [18,23], average fibril spacing and diameter generally displayed minimum values in the central cornea and increased with proximity to the limbus, with fibril order index displaying the opposite trend. However, notably, additional local elevations in fibril spacing and decreased levels of fibril spatial order were also consistently observed in the region of the graft margin. In some scans, these alterations were also accompanied by corresponding increases in fibril diameter. Fig. 2 also presents corresponding data from two scans across the graft margin of the right PK specimen from the same patient, in which similar observations were noted. Analysis of the control data confirmed that the localised alterations in fibril ultrastructure noted in the graft margin of both PK specimens were not present in corresponding regions of unwounded corneas (Fig. 2), consistent with previous studies of normal human tissue [18,22,23].

Collagen Orientation and Mass Distribution

Fig. 3 presents a map of predominant collagen fibril alignment across the left PK specimen, determined using WAXS. Each

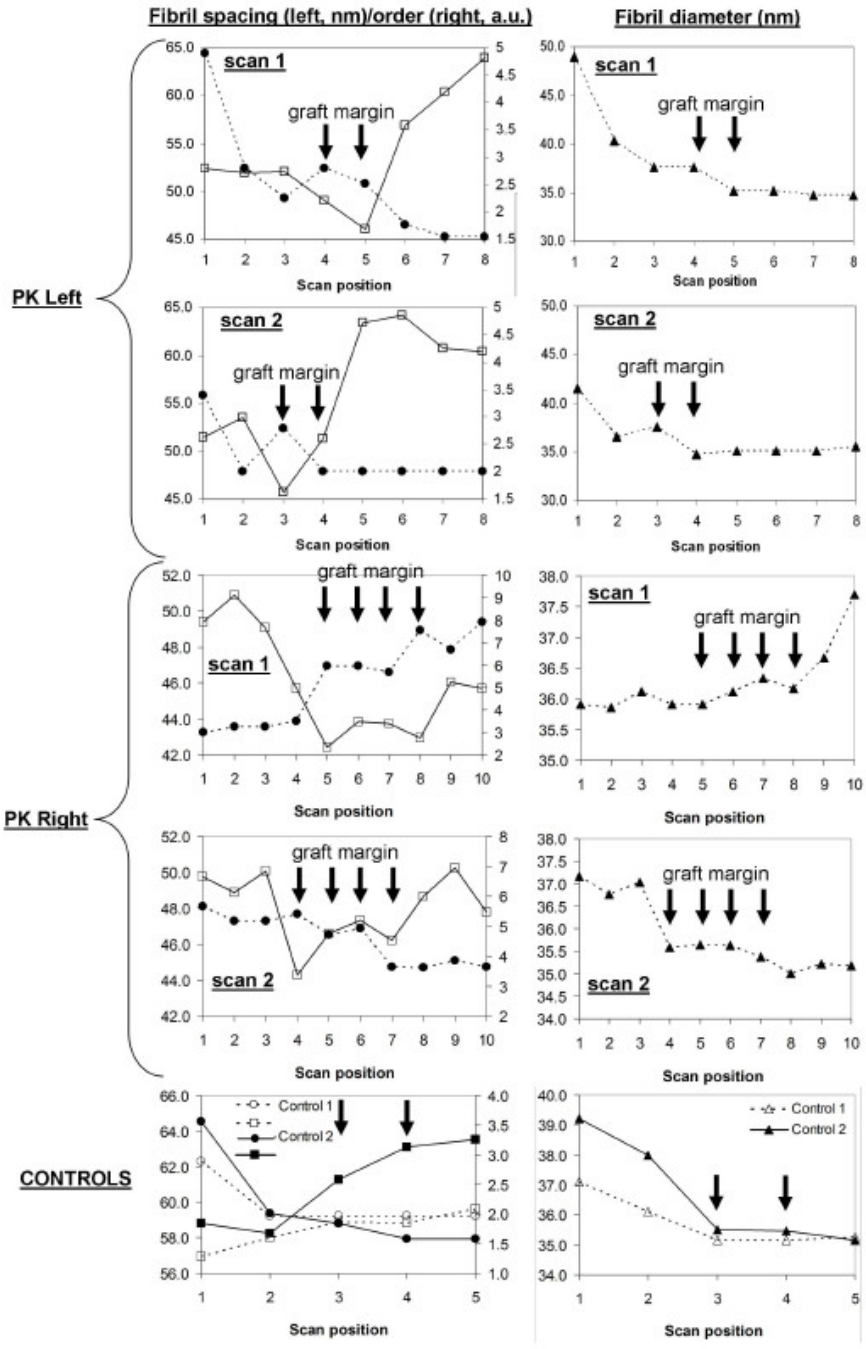
Fibril spacing (left, nm)/order (right, a.u.)
Fibril diameter (nm)
PK Left
PK Right
CONTROLS
scan 1
scan 2
graft margin
Control 1
Control 2
Scan position

Figure 2. SAXS data across the graft-host interface of the PK specimens from Patient 1, showing measurements of collagen fibril spacing (circles), spatial order index (squares) and diameter (triangles) along the scans indicated in Fig. 1. Corresponding data is also shown for control specimens. Arrows indicate scan positions lying on the PK graft margin and their equivalent positions on the controls. Note local increase in fibril spacing and diameter, and accompanying decrease in spatial order, in the graft margin for the PK specimens.
doi:10.1371/journal.pone.0068166.g002

sampled point is represented by an individual polar vector plot, in which the distance from the plot centre to periphery in a given direction represents the relative amount of preferentially aligned collagen lying in that direction [21]. The same technique has been used extensively to map collagen orientation across normal human corneas [16,24]. This previous work has shown that, centrally, the normal cornea is characterised by a preponderance of fibrils oriented along the superior-inferior and nasal-temporal meridians, while towards the periphery these preferred directions gradually alter to become predominantly tangential at the limbus [16,24]. Reference to Fig. 3 shows that this overall pattern was also evident in the left PK specimen. However several additional features, not present in normal tissue, were also noted.

Firstly, the circumferential collagen which characterises the normal human limbus and perilimbal sclera had extended into the peripheral cornea on the temporal side, corresponding in location

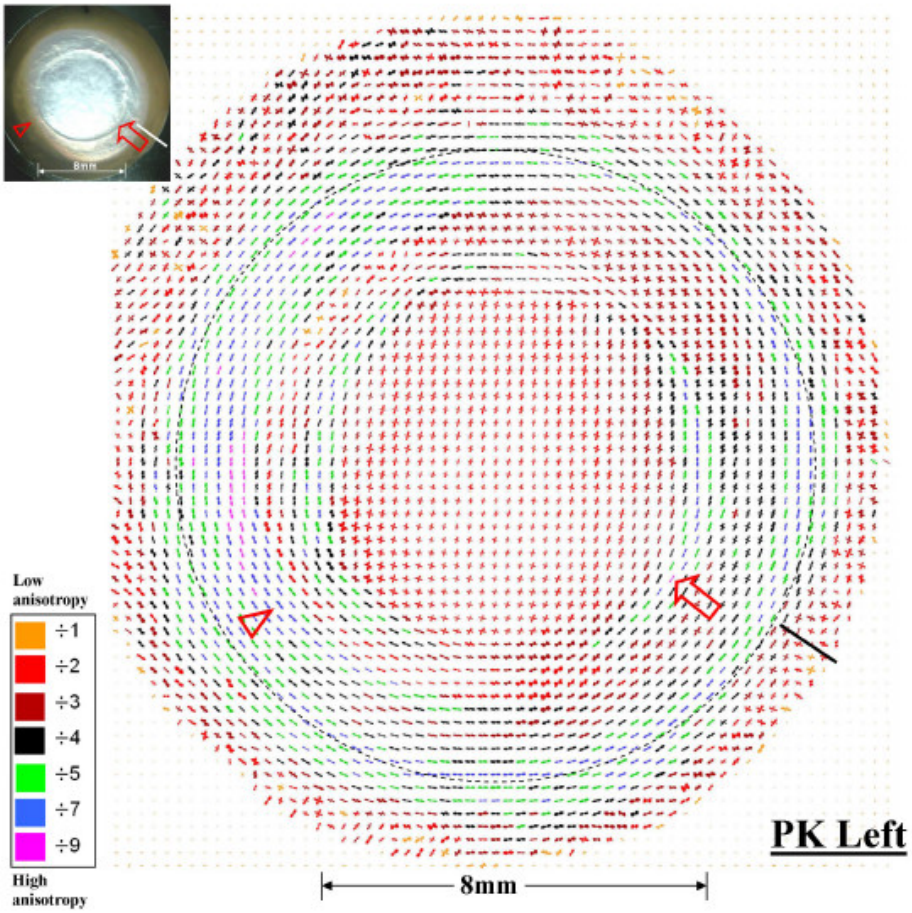

Figure 3. Polar vector map of preferential collagen fibril alignment across the left PK specimen of Patient 1, determined using WAXS. The larger plots (indicative of greater fibril alignment) have been scaled down for montage display by factors indicated in the colour key. Broken circle: limbus. Arrow: tangential fibril alignment along the graft margin. Arrowhead: abnormal inward extension of tangential limbal fibrils into the peripheral cornea, corresponding to region of prominent corneal opacity. Solid line: superior tag. Inset: location of noted features on actual specimen.
doi:10.1371/journal.pone.0068166.g003

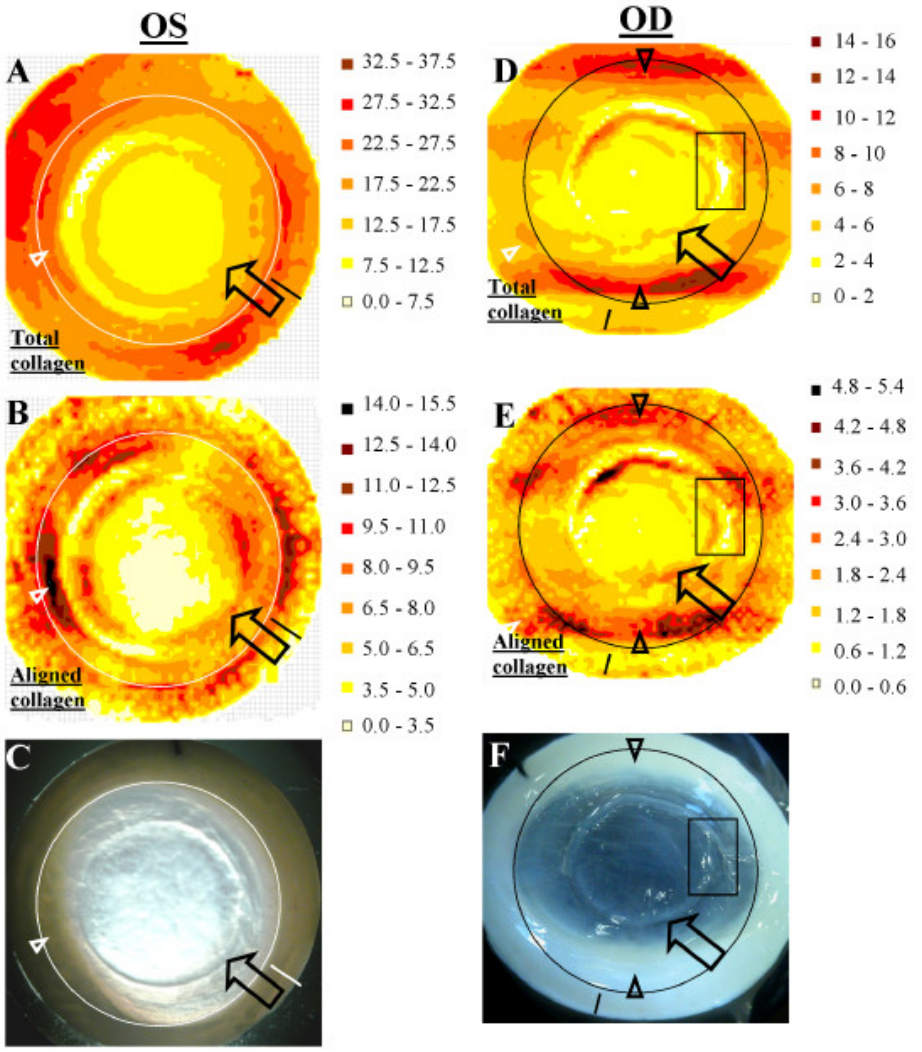

Figure 4. Distribution maps of A,D) total and B,E) preferentially aligned collagen across the PK specimens from Patient 1, determined using WAXS (arbitrary units). Arrows: local elevation in collagen mass at the graft margin. Arrowheads: abnormal elevation of collagen mass in the peripheral cornea, corresponding to the prominent regions of corneal opacity. Solid circles: limbus. Solid lines: superior tag. Rectangles: Elevated collagen mass delineates the separated wound edges of the right PK specimen, with a reduction in the intervening tissue. **C,F)** Location of noted features on actual specimens.
doi:10.1371/journal.pone.0068166.g004

with the region of prominent corneal opacity (Fig. 3 - arrowhead). This region was also notable for displaying elevated collagen mass in comparison with the nasal side of the eye (Fig. 4A–C - arrowheads), an increase which was proportionately greater for aligned, compared to total, collagen. Secondly, along the majority of the graft margin there were marked alterations to normal collagen orientation, characterised by fibrils aligned predominantly tangential to the wound edge (Fig. 3 - arrow). In this region an approximately two-fold local increase in total collagen scatter was measured (Fig. 4A - arrow), consistent with an overlap of the donor button and host bed. Aligned collagen scatter in this region showed a proportionately greater elevation, measuring up to four-fold higher than in adjacent regions inside and outside of the graft

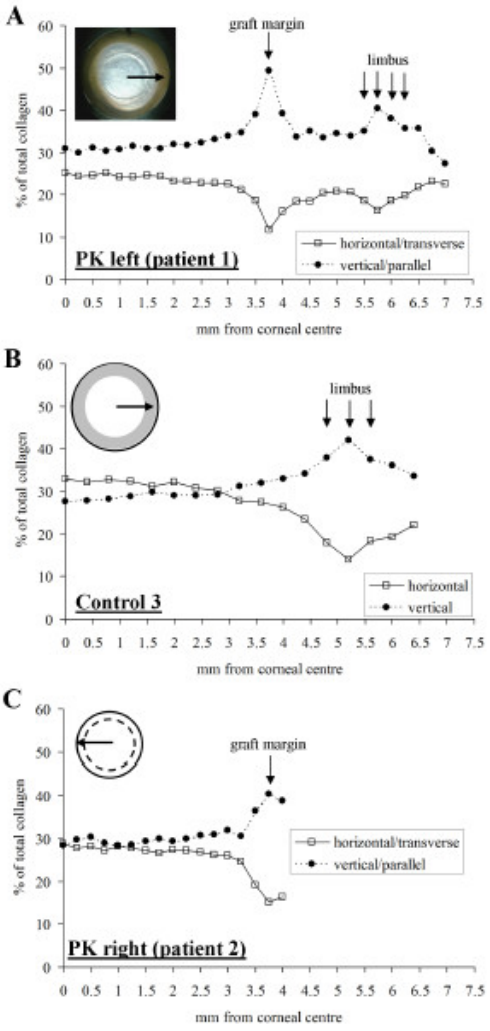

Figure 5. Proportion of total collagen oriented within 45° sectors of the horizontal (transverse to the wound edge) and vertical (parallel to the wound edge) directions as a function of distance from the corneal centre in A) Patient 1, left PK specimen (sampling interval: 0.25 mm), B) normal control cornea (sampling interval 0.4 mm) and C) Patient 2, right PK specimen (sampling interval: 0.25 mm). Note marked increase/decrease in collagen oriented parallel/transverse to the wound edges in A) and C).
doi:10.1371/journal.pone.0068166.g005

margin (Fig. 4B - arrow), indicating considerable reinforcement of aligned collagen around the wound edge.

In order to quantify further the change in normal alignment of collagen across the graft margin, we compared the relative proportions of collagen oriented transversely and parallel to the wound edge. This was done by calculating from the WAXS patterns [25] the proportion (relative to total collagen) of fibrils oriented within 45° sectors of the horizontal (i.e. transverse) and vertical (i.e. parallel) directions, when approaching the wound along a horizontal corneal semi-meridian (Fig. 5A - *inset*). These results are shown in Fig. 5A, and compared to equivalent data from a normal human cornea (Control 3) examined in a previous WAXS study [16] in Fig. 5B. The measurements disclose an abrupt 15% increase in the proportion of collagen aligned parallel to wound edge, and an accompanying 11% decrease in the proportion of transversely oriented collagen, at this particular location on the graft margin, resulting in approximately five times as much fibrous collagen edging the wound as that spanning it. Inspection of the corresponding raw x-ray scatter intensity values confirmed that this effect arose from a combination of a 46% absolute increase in parallel collagen and a 40% absolute decrease in transverse collagen (data not shown). A similar trend was confirmed at a corresponding location on the PK graft margin of Patient 2, in which the number of collagen fibrils edging the wound was approximately 3-fold higher than those spanning it (Fig. 5C).

Figs. 6 and 4D,E present maps of preferential collagen orientation and collagen mass distribution, respectively, across the right PK specimen. Within the donor button, two orthogonal dominant directions of collagen were again evident (Fig. 6). However, unlike the donor button of the left PK specimen (Fig. 3), and the central cornea of normal human eyes [16,24,26], these preferred directions did not correspond to the superior-inferior and nasal-temporal meridians of the recipient eye (Fig. 6), suggesting that in this case the donor button was grafted obliquely. The graft margin was again notable for the presence of markedly reinforced collagen aligned tangential to the wound edge (Figs. 6 and 4D–F - arrows). Furthermore, the visible discontinuity of the wound margin on the temporal side was clearly reflected in the pattern of collagen organisation in this region, with dominant fibril orientation and elevated collagen mass delineating the separated graft margin, and fibrillar distortion and reduction of collagen mass in the tissue between the separated wound edges (Figs. 6 and 4D–F - rectangles). The prominent regions of corneal opacity in the inferior and superior peripheral cornea were again characterised by an abnormal inward extension of the highly aligned circumferential limbal/perilimbal scleral collagen (Figs. 6 and 4D–F - arrowheads).

Discussion

Although PK is a highly successful long-term treatment option in cases of severe corneal scarring and advanced pathology, late-onset complications can present in a minority of patients. In the case of PK for advanced keratoconus, the indication presented by the patients studied herein, graft failure occurs in around 6% of cases at a mean time of 13 years post-op [27]. To what extent, if any, collagen structural changes contribute to the mechanisms underlying graft failure remains to be established. However, there is a large body of evidence to suggest that normal stromal architecture may never be fully recovered in full-thickness graft wounds [3,9,11,12,13,14,15,28,29]. The current results align well with this view, demonstrating extensive long-term abnormalities in collagen fibril orientation and spatial organisation around the entire graft margin following PK. Firstly, we noted that collagen orientation was predominantly tangential to the wound edge, consistent with findings reported in previous long-term PK follow-ups [3,9]. It is possible that this observation could be partly a legacy of a mechanical distortion of existing collagen during

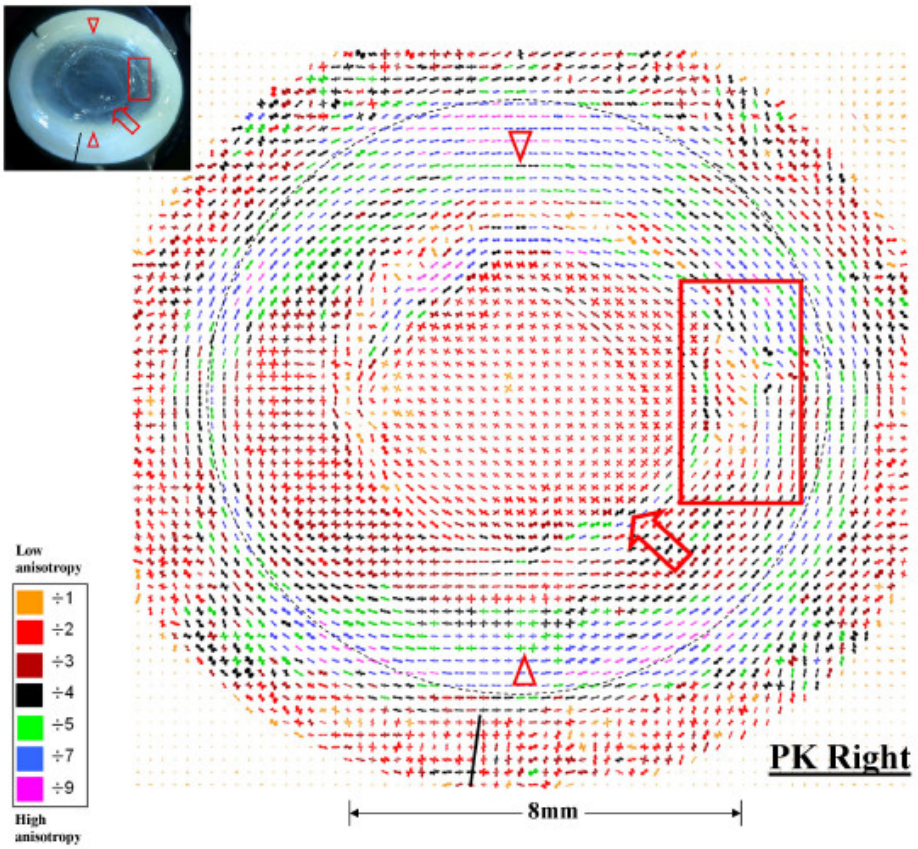

Figure 6. Polar vector map of preferential collagen fibril alignment across the right PK specimen of Patient 1, determined using WAXS. The larger plots (indicative of greater fibril alignment) have been scaled down for montage display by factors indicated in the colour key. Broken circle: limbus. Arrow: tangential fibril alignment along the graft margin. Arrowhead: abnormal inward extension of tangential limbal fibrils into the peripheral cornea, corresponding to regions of prominent corneal opacity. Rectangle: fibril alignment delineates separated wound edges and is disturbed in intervening tissue. Solid line: superior tag. Inset: location of noted features on actual specimen.
doi:10.1371/journal.pone.0068166.g006

trephination [2], likely augmented by new collagen secreted by infiltrating activated host keratocytes aligning with the donor button edge via contact guidance [30].

Significant changes in collagen alignment around the wound margin could impact on the mechanical stability of the graft-host interface. Specifically, at the examined location in the left PK graft margin of Patient 1, our measurements indicated that only around 10% of the total collagen was aligned transversely to the wound edge. Such a relative lack of meridional fibrils spanning the graft margin might be reasonably expected to encourage a wound under tension to reopen. In contrast, over 50% of the collagen at this point was aligned parallel to the wound edge. Notably, a predominantly circumferential arrangement of fibrils is predicted, from biomechanical considerations, to maximise out-of-plane corneal deformation under intraocular pressure [31]. This could potentially exacerbate the tendency of an already weakened donor-host tissue interface to separate. With this in mind, it is relevant to note that traumatic wound dehiscence has been reported up to 19 years after PK [11,29], while stress analysis experiments have indicated that the graft-host interface remains weak even after the tissue appears fully healed [28].

Although neither eye of Patient 1 examined herein suffered a reported failure, the wound margin of the patient's right eye did display a prominent visible separation on the temporal side, which was confirmed by the collagen orientation pattern in this region. It may be significant that this graft was performed earlier and hence had been in the eye some 16 years longer than the fellow eye, which showed no such changes. Moreover, we also noted a distortion of the collagen in the tissue between the separated wound edges, in which fibrils had aligned radially, i.e. along the direction of the apparent outward migration of the wound edge and perpendicular to the edge itself. The altered collagen alignment here may not have resulted in a significant local mechanical effect because the degree of anisotropy was generally

low (indicated by the orange color coding of the vector plots). However, interestingly a similar pattern of radial collagen alignment abutting the wound edge was previously noted by the same technique in the specimen from Patient 2, in which an initially successful PK graft had seemingly mechanically failed after 13 years [3]. With respect to these observations, it is unfortunate that no follow-up ophthalmic records were available for the right eye of Patient 1.

The long-term persistence of circumferential collagen in the graft margin we report here is compatible with the general view of stromal collagen after penetrating corneal injury having a limited capacity to remodel following initial wound repair, and this is further supported by our observation of altered collagen spatial organisation in the graft margin of Patient 1. Specifically, we noted localised increases in collagen spacing and diameter, and a reduced level of spatial order, observations which are all consistent with the presence of fibrotic scar tissue deposited early in wound healing [5,6,20]. This could be a contributing factor to the visible opacity of the wound margin in these specimens [32], and may also be expected to further alter the biomechanical properties of the tissue in this region [18].

A final observation of the current study of potential importance to corneal biomechanics is that, with reference to the dominant fibril directions of the donor and host collagen, the right PK donor button appeared to have been grafted obliquely. It has been suggested that the superior-inferior and nasal-temporal preferred collagen orientation in the central human cornea may reflect a mechanical adaptation of the tissue to forces imposed by the extraocular muscles [25,26,33,34]. In this context, it is interesting that the orthogonal fibril directions in the right PK specimen of Patient 1 examined herein had remained oblique to the rectus muscle insertions, with apparently no significant re-alignment after 28 years as may have been expected on the basis of the abovementioned criteria. This may reflect the extremely slow rates of collagen turnover in the quiescent stroma [35]. Alternatively, it could be linked to the observation that the inflation behaviour of the cornea under normal conditions has been shown to be insensitive to the collagen structure of the central region [36]. A further interpretation could be that any new collagen deposited during wound healing has been laid down mainly in register with the donor lamellae, possibly indicating that infiltrating cells have taken their directional cues largely from the existing collagen scaffold irrespective of mechanical stimuli.

The peripheral (keratoconic) tissue of both eyes of Patient 1 displayed prominent peripheral corneal opacity, located temporally in the left eye and inferior/superior in the right. The WAXS data from this these regions revealed abnormal levels of highly aligned tangential collagen, resembling that normally restricted to the limbus and perilimbal sclera [16,24]. Taken together with the physical appearance of the tissue, this suggests peripheral scleralization had occurred. To our knowledge there is no specific documented association of corneal scleralization and keratoconus. Therefore we contend that this may be a case of isolated peripheral sclerocornea which, as is the case here, usually presents bilaterally and asymmetrically [37], as opposed to an abnormality linked directly to the keratoconus itself.

In summary, this paper documents the first quantitative, long-term follow-up of collagen organisation across whole transplanted corneas. In principle, the changes noted in and around the graft margin could affect corneal biomechanical behaviour and graft stability. However further research, possibly focussing on the application of structural data in numerical simulation of corneal biomechanics, may help to establish any definitive link that may exist between the ultrastructural changes presented herein and the instances of PK graft dehiscence and mechanical failure documented in the clinical literature.

Acknowledgments

The authors thank Val Smith of the Bristol Eye Hospital for provision of specimens. Presented in part as a poster at the ARVO annual meeting, May 2011.

Author Contributions

Conceived and designed the experiments: CB KMM. Performed the experiments: CB EPD CSK SH TS NJT. Analyzed the data: CB EPD SJG. Contributed reagents/materials/analysis tools: KN JH TS NJT. Wrote the paper: CB KN JH KMM.

References

1. Meek KM (2009) Corneal collagen–its role in maintaining corneal shape and transparency. Biophysical Reviews 1: 83–93.
2. Connon CJ, Meek K (2003) Organization of corneal collagen fibrils during the healing of trephined wounds in rabbits. Wound Repair Regen 11: 71–78.
3. Hayes S, Young R, Boote C, Hawksworth N, Huang Y, et al. (2010) A structural investigation of corneal graft failure in suspected recurrent keratoconus. Eye 24: 728–734.
4. Kamma-Lorger CS, Hayes S, Boote C, Burghammer M, Boulton ME, et al. (2009) Effects on collagen orientation in the cornea after trephine injury. Molecular Vision 15: 378–385.
5. Cintron C, Schneider H, Kublin C (1973) Corneal scar formation. Exp Eye Res 17: 251–259.
6. Rawe IM, Meek KM, Leonard DW, Takahashi T, Cintron C (1994) Structure of corneal scar tissue: an X-ray diffraction study. Biophys J 67: 1743–1748.
7. Kamma-Lorger CS, Boote C, Hayes S, Albon J, Boulton ME, et al. (2009) Collagen ultrastructural changes during stromal wound healing in organ cultured bovine corneas. Experimental Eye Research 88: 953–959.
8. Dawson DG, Edelhauser HF, Grossniklaus HE (2005) Long-term histopathologic findings in human corneal wounds after refractive surgical procedures. Am J Ophthalmol 139: 168–178.
9. Melles GR, Binder PS (1990) A comparison of wound healing in sutured and unsutured corneal wounds. Arch Ophthalmol 108: 1460–1469.
10. Steele C (2009) Corneal wound healing: a review. Optometry Today 24: 28–32.
11. Farley MK, Petrit TH (1987) Traumatic wound dehiscence after penetrating keratoplasty. Am J Ophthalmol 104: 44–49.
12. Lang GK, Green WR, Maumenee AE (1986) Clinicopathologic studies of keratoplasty eyes obtained post mortem. Am J Ophthalmol 101: 28–40.
13. Morrison JC, Swan KC (1982) Full-thickness lamellar keratoplasty. A histologic study in human eyes. Ophthalmology 89: 715–719.
14. Morrison JC, Swan KC (1982) Bowman's layer in penetrating keratoplasties of the human eye. Arch Ophthalmol 100: 1835–1838.
15. Morrison JC, Swan KC (1983) Descemet's membrane in penetrating keratoplasties of the human eye. Arch Ophthalmol 101: 1927–1929.
16. Boote C, Hayes S, Abahussin M, Meek KM (2006) Mapping collagen organisation in the human cornea: left and right eyes are structurally distinct. Invest Ophthalmol Vis Sci 47: 901–908.
17. Meek KM, Quantock AJ (2001) The use of X-ray scattering techniques to determine corneal ultrastructure. Prog Retin Eye Res 20: 95–137.
18. Boote C, Dennis S, Newton RH, Puri H, Meek KM (2003) Collagen fibrils appear more closely packed in the prepupillary cornea: optical and biomechanical implications. Investigative Ophthalmology and Visual Science 44: 2941–2948.
19. Meek K, Quantock AJ, Boote C, Liu CY, Kao WWY (2003) An X-ray scattering investigation of corneal structure in keratocan deficient mice. Matrix Biology 22: 467–475.
20. Boote C, Du Y, Morgan SR, Harris J, Kamma-Lorger CS, et al. (2012) Quantitative Assessment of Ultrastructure and Light Scatter in Mouse Corneal Debridement Wounds. Invest Ophthalmol Vis Sci 53: 2786–2795.
21. Meek KM, Boote C (2009) The use of x-ray scattering techniques to quantify the orientation and distribution of collagen in the corneal stroma. Prog Retin Eye Res 28: 369–392.
22. Borcherding MS, Blacik LJ, Sittig RA, Bizzel JW, Breen M, et al. (1975) Proteoglycans and Collagen Fibre Organisation in Human Corneoscleral Tissue. Experimental Eye Research 21: 59–70.
23. Boote C, Kamma-Lorger CS, Hayes S, Harris J, Burghammer M, et al. (2011) Quantification of collagen organization in the peripheral human cornea at micron-scale resolution. Biophys J 101: 33–42.

24. Aghamohammadzadeh H, Newton RH, Meek KM (2004) X-ray scattering used to map the preferred collagen orientation in the human cornea and limbus. Structure 12: 249–256.
25. Boote C, Dennis S, Huang Y, Meek K (2005) Lamellar orientation in human cornea in relation to mechanical properties. Journal of Structural Biology 149: 1–6.
26. Daxer A, Fratzl P (1997) Collagen fibril orientation in the human corneal stroma and its implications in keratoconus. Investigative Ophthalmology and Visual Science 38: 121–129.
27. Pramanik S, Musch DC, Sutphin JE, Farjo AA (2006) Extended long-term outcomes of penetrating keratoplasty for keratoconus. Ophthalmology 113: 1633–1638.
28. Calkins JL, Hochheimer BF, Stark WJ (1981) Corneal wound healing: holographic stress-test analysis. Invest Ophthalmol Vis Sci 21: 322–334.
29. Pettinelli DJ, Starr CE, Stark WJ (2005) Late traumatic corneal wound dehiscence after penetrating keratoplasty. Arch Ophthalmol 123: 853–856.
30. Vrana E, Builles N, Hindie M, Damour O, Aydinli A, et al. (2008) Contact guidance enhances the quality of a tissue engineered corneal stroma. J Biomed Mater Res A 84: 454–463.
31. Boyce BL, Grazier JM, Jones RE, Nguyen TD (2008) Full-field deformation of bovine cornea under constrained inflation conditions. Biomaterials 4: 4.
32. Farrell RA, McCally RL (2000) Corneal Transparency. In: Albert DM, Jakobiec FA, editors. Principles and Practice of Ophthalmology. Philadelphia: W.B. Saunders Company. 629–643.
33. Abahussin M, Hayes S, Knox Cartwright NE, Kamma-Lorger CS, Khan Y, et al. (2009) 3D collagen orientation study of the human cornea using X-ray diffraction and femtosecond laser technology. Invest Ophthalmol Vis Sci 50: 5159–5164.
34. Meek KM, Newton RH (1999) Organization of collagen fibrils in the corneal stroma in relation to mechanical properties and surgical practice. Journal of Refractive Surgery 15: 695–699.
35. Smelser GK, Polack FM, Ozanics V (1965) Persistence of donor collagen in corneal transplants. Exp Eye Res 4: 349–354.
36. Nguyen TD, Boyce BL (2011) An inverse finite element method for determining the anisotropic properties of the cornea. Biomech Model Mechanobiol 10: 323–337.
37. Sen DK, Mohan H, Gupta DK (1969) Bilateral peripheral sclero-cornea. Acta Ophthalmol (Copenh) 47: 1041–1043.

References

Abahussin, M. and Hayes, S. and Knox Cartwright, N. E. and Kamma-Lorger, C. S. and Khan, Y. and Marshall, J. and Meek, K. M. 2009. 3D collagen orientation study of the human cornea using X-ray diffraction and femtosecond laser technology. *Invest Ophthalmol Vis Sci* 50(11), pp. 5159-5164.

Abelson, M. B. and Collin, H. B. and Gillette, T. E. and Dohlman, C. H. 1980. Recurrent keratoconus after keratoplasty. *American Journal of Ophthalmology* 90(5), pp. 672-676.

Aghamohammadzadeh, H. and Newton, R. H. and Meek, K. M. 2004. X-ray scattering used to map the preferred collagen orientation in the human cornea and limbus. *Structure* 12(2), pp. 249-256.

Akama, T. O. and Nishida, K. and Nakayama, J. and Watanabe, H. and Ozaki, K. and Nakamura, T. and Dota, A. and Kawasaki, S. and Inoue, Y. and Maeda, N. and Yamamoto, S. and Fujiwara, T. and Thonar, E. and Shimomura, Y. and Kinoshita, S. and Tanigami, A. and Fukuda, M. N. 2000. Macular corneal dystrophy type I and type II are caused by distinct mutations in a new sulphotransferase gene. *Nature Genetics* 26(2), pp. 237-241.

Akhtar, S. and Bron, A. J. and Salvi, S. M. and Hawksworth, N. R. and Tuft, S. J. and Meek, K. M. 2008. Ultrastructural analysis of collagen fibrils and proteoglycans in keratoconus. *Acta Ophthalmol* 86(7), pp. 764-772.

Alexander, C. M. and Werb, Z. 1989. Proteinases and extracellular matrix remodelling. *Currant Opinions in Cell Biology* (1), pp. 974-982.

Alexander, R. J. and Silverman, B. and Henley, W. L. 1981. Isolation and characterization of BCP-54, the major soluble protein of bovine cornea. *Experimental Eye Research* 32(2), pp. 205-216.

Ambrosio, R. and Alonso, R. S. and Luz, A. and Velarde, L. G. C. 2006. Corneal-thickness spatial profile and corneal-volume distribution: Tomographic indices to detect keratoconus. *Journal of Cataract and Refractive Surgery* 32(11), pp. 1851-1859.

Asano, S. 1983. Light scattering by horizontally orientated spheroidal particles. *Applied Optics* 22(9), pp. 1390-1396.

Asano, S. and Sato, M. 1980. Light scattering by randomly oriented spheroidal particles. *Applied Optics* 19(6), pp. 962-974.

Asano, S. and Yamamoto, G. 1975. Light scattering by a spheroidal particle. *Applied Optics* 14(1), pp. 29-49.

Aspden, R. M. and Hukins, D. W. L. 1979. Determination of the direction of preferred orientation and the orientation distribution function of collagen fibrils in connective tissues from high angle x-ray diffraction patterns. *Journal of Applied Crystallography* 12(JUN), pp. 306-311.

Aurell, G. and Holmgren, H. 1953. On the metachromatic staining of the corneal tissue and some observations on its transparency. *Acta Ophthalmol* 31((1)), pp. 1-28.

Bao, W. and Smith, C. F. and Al-Rajhi, A. and Chandler, J. W. and Karcioglu, Z. A. and Akama, T. O. and Fukuda, M. N. and Klintworth, G. K. 2001. Novel mutations in the CHST6 gene in Saudi Arabic patients with macular corneal dystrophy. *Investigative Ophthalmology & Visual Science* 42(4), pp. S483-S483.

Bartholomew, L. R. and Pang, D. X. and Sam, D. A. and Cavender, J. C. 1997. Ultrasound biomicroscopy of globes from young adult pigs. *American Journal of Veterinary Research* 58(9), pp. 942-948.

Beales, M. P. and Funderburgh, J. L. and Jester, J. V. and Hassell, J. R. 1999. Proteoglycan synthesis by bovine keratocytes and corneal fibroblasts: Maintenance of the keratocyte phenotype in culture. *Investigative Ophthalmology & Visual Science* 40(8), pp. 1658-1663.

Benedek, G. B. 1971. The theory of the transparency of the eye. *Applied Optics* 10(3), pp. 459-473.

Bettelheim, F. A. and Plessy, B. 1975. The hydration of proteoglycans of bovine cornea. *Biochimica Et Biophysica Acta* 381(1), pp. 203-214.

Birk, D. E. 2001. Type V collagen: heterotypic type I/V collagen interactions in the regulation of fibril assembly. *Micron* 32(3), pp. 223-237.

Birk, D. E. and Fitch, J. M. and Babiarz, J. P. and Doane, K. J. and Linsenmayer, T. F. 1990. Collagen fibrillogenesis in vitro: Interaction of type I and type V collagen regulates fibril diameter. *Journal of Cell Science* 95, pp. 649-657.

Blochberger, T. C. and Cornuet, P. K. and Hassell, J. R. 1992. Isolation and partial characterization of lumican and decorin from adult chicken corneas - a keratan sulfate containing isoform of decorin is developmentally regulated. *Journal of Biological Chemistry* 267(29), pp. 20613-20619.

Boettner, E. A. and Wolter, J. R. 1962. Transmission of the ocular media. *Investigative Ophthalmology* 1(6), pp. 776-783.

Boote, C. and Dennis, S. and Huang, Y. and Quantock, A. J. and Meek, K. M. 2005. Lamellar orientation in human cornea in relation to mechanical properties. *J Struct Biol* 149(1), pp. 1-6.

Boote, C. and Dennis, S. and Meek, K. 2004. Spatial mapping of collagen fibril organisation in primate cornea - an X-ray diffraction investigation. *Journal of Structural Biology* 146(3), pp. 359-367.

Boote, C. and Dennis, S. and Meek, K. M. 2003. Collagen organisation in adult and foetal marmoset cornea. *Investigative Ophthalmology & Visual Science* 44, pp. U246-U246.

Boote, C. and Dooley, E. P. and Gardner, S. J. and Kamma-Lorger, C. S. and Hayes, S. and Nielsen, K. and Hjortdal, J. and Sorensen, T. and Terrill, N. J. and Meek, K. M. 2013. Quantification of Collagen Ultrastructure after Penetrating Keratoplasty - Implications for Corneal Biomechanics. *Plos One* 8(7).

Boote, C. and Elsheikh, A. and Kassem, W. and Kamma-Lorger, C. S. and Hocking, P. M. and White, N. and Inglehearn, C. F. and Ali, M. and Meek, K. M. 2010. The Influence of Lamellar Orientation on Corneal Material Behaviour - Biomechanical and Structural Changes in an Avian Corneal Disorder. *Invest Ophthalmol Vis Sci*.

Boote, C. and Hayes, S. and Abahussin, M. and Meek, K. M. 2006. Mapping collagen organization in the human cornea: left and right eyes are structurally distinct. *Invest Ophthalmol Vis Sci* 47(3), pp. 901-908.

Boyce, B. L. and Grazier, J. M. and Jones, R. E. and Nguyen, T. D. 2008. Full-field deformation of bovine cornea under constrained inflation conditions. *Biomaterials* 29(28), pp. 3896-3904.

Bragg, W. H. and Bragg, W. L. 1913. The structure of the diamond. *Nature* 91, pp. 557-557.

Bragg, W. L. 1913. The specular reflection of X rays. *Nature* 90, pp. 410-410.

Bredrup, C. and Knappskog, P. M. and Majewski, J. and Rodahl, E. and Boman, H. 2005. Congenital stromal dystrophy of the cornea caused by a mutation in the decorin gene. *Investigative Ophthalmology & Visual Science* 46(2), pp. 420-426.

Brillouin, L. 1922. Diffusion de la lumiere et des rayonnes X par un corps transparent homogene; influence del'agitation thermique. *Ann. Phys.* 88(17).

Brissette-Storkus, C. S. and Reynolds, S. A. and Lepisto, A. J. and Hendricks, R. L. 2002. Identification of a novel macrophage population in the normal mouse corneal stroma. *Investigative Ophthalmology & Visual Science* 43(7), pp. 2264-2271.

Calkins, J. L. and Hochheimer, B. F. and Stark, W. J. 1981. Corneal wound healing: holographic stress test analysis. *Investigative Ophthalmology & Visual Science* 21(2), pp. 322-334.

Canty, E. G. and Kadler, K. E. 2005. Procollagen trafficking, processing and fibrillogenesis. *Journal of Cell Science* 118(7), pp. 1341-1353.

Caspersson, T. and Engstrom, A. 1946. The transparency of the corneal tissue. *Nordisk Medicin* 30(23), pp. 1279-1282.

Caterson, B. and Christner, J. E. and Baker, J. R. 1983. Identification of a monoclonal antibody that specifically recognizes corneal and skeletal keratan sulfate. Monoclonal antibodies to cartilage proteoglycan. *Journal of Biological Chemistry* 258(14), pp. 8848-8854.

Cavanagh, H. D. and Ladage, P. M. and Li, S. L. and Yamamoto, K. and Molai, M. and Ren, D. H. and Petroll, W. M. and Jester, J. V. 2002. Effects of daily and overnight wear of a novel hyper oxygen-transmissible soft contact lens on bacterial binding and corneal epithelium - A 13-month clinical trial. *Ophthalmology* 109(11), pp. 1957-1969.

Cervino, A. and Gonzalez-Meijome, J. M. and Ferrer-Blasco, T. and Garcia-Resua, C. and Montes-Mico, R. and Parafita, M. 2009. Determination of corneal volume from anterior topography and topographic pachymetry: application to healthy and keratoconic eyes. *Ophthalmic and Physiological Optics* 29(6), pp. 652-660.

Chakravarti, S. and Magnuson, T. and Lass, J. H. and Jepsen, K. J. and LaMantia, C. and Carroll, H. 1998. Lumican regulates collagen fibril assembly: Skin fragility and corneal opacity in the absence of lumican. *Journal of Cell Biology* 141(5), pp. 1277-1286.

Chien, C. C. and Tseng, P. Y. and Chen, H. H. and Hua, T. E. and Chen, S. T. and Chen, Y. Y. and Leng, W. H. and Wang, C. H. and Hwu, Y. and Yin, G. C. and Liang, K. S. and Chen, F. R. and Chu, Y. S. and Yeh, H. I. and Yang, Y. C. and Yang, C. S. and Zhang, G. L. and Je, J. H. and Margaritondo, G. 2013. Imaging cells and sub-cellular structures with ultrahigh resolution full-field X-ray microscopy. *Biotechnology Advances* 31(3), pp. 375-386.

Chinnery, H. R. and Humphries, T. and Clare, A. and Dixon, A. E. and Howes, K. and Moran, C. B. and Scott, D. and Zakrzewski, M. and Pearlman, E. and McMenamin, P. G. 2008. Turnover of bone marrow-derived cells in the irradiated mouse cornea. *Immunology* 125(4), pp. 541-548.

Compton, A. H. 1923. A quantum theory of the scattering of x-rays by light elements. *Physical Review* 21(5), pp. 0483-0502.

Connon, C. J. and Meek, K. M. 2003. Organization of corneal collagen fibrils during the healing of trephined wounds in rabbits. *Wound Repair Regen* 11(1), pp. 71-78.

Connon, C. J. and Meek, K. M. 2004. The structure and swelling of corneal scar tissue in penetrating full-thickness wounds. *Cornea* 23(2), pp. 165-171.

Conrad, G. and Dessau, W. and Vondermark, K. 1980. Synthesis of type-III collagen by fibroblasts from the embryonic chick cornea. *Journal of Cell Biology*, pp. 501-512.

Cooper, D. L. and Baptist, E. W. and Enghild, J. and Lee, H. and Isola, N. and Klintworth, G. K. 1990. Partial amino acid sequence determination of bovine corneal protein 54K (BCP54). *Current Eye Research* 9(8), pp. 781-786.

Cooper, D. L. and Baptist, E. W. and Enghild, J. J. and Isola, N. R. and Klintworth, G. K. 1991. Bovine corneal protein 54K (BCP54) is a homolog of the tumor associated (class 3) rat aldehyde dehydrogenase. *Gene* 98(2), pp. 201-207.

Corpuz, L. M. and Funderburgh, J. L. and Funderburgh, M. L. and Bottomley, G. S. and Prakash, S. and Conrad, G. W. 1996. Molecular cloning and tissue distribution of keratocan - Bovine corneal keratan sulfate proteoglycan 37A. *Journal of Biological Chemistry* 271(16), pp. 9759-9763.

Cox, J. L. and Farrell, R. A. and Hart, R. W. and Langham, M. E. 1970. The transparency of the mammalian cornea. *Journal of Physiology-London* 210(3), pp. 601-616

Critchfield, J. W. and Calandra, A. J. and Nesburn, A. B. and Kenney, M. C. 1988. Keratoconus I: Biochemical studies. *Experimental Eye Research* 46(6), pp. 953-963.

Curl, C. L. and Bellair, C. J. and Harris, T. and Allman, B. E. and Harris, P. J. and Stewart, A. G. and Roberts, A. and Nugent, K. A. and Delbridge, L. M. D. 2005. Refractive index measurement in viable cells using quantitative phase-amplitude microscopy and confocal microscopy. *Cytometry Part A* 65A(1), pp. 88-92.

Cuthbertson, R. A. and Tomarev, S. I. and Piatigorsky, J. 1992. Taxon specific recruitment of enzymes as major soluble proteins in the corneal epithelium of three mammals, chicken and squid. *Proceedings of the National Academy of Sciences of the United States of America* 89(9), pp. 4004-4008.

Dawson, D. G. and Randleman, J. B. and Grossniklaus, H. E. and O'Brien, T. P. and Dubovy, S. R. and Schmack, I. and Stulting, R. D. and Edelhauser, H. F. 2008. Corneal Ectasia After

Excimer Laser Keratorefractive Surgery: Histopathology, Ultrastructure, and Pathophysiology. *Ophthalmology* 115(12), pp. 2181-2191.

Daxer, A. and Fratzl, P. 1997. Collagen fibril orientation in the human corneal stroma and its implication in keratoconus. *Investigative Ophthalmology & Visual Science* 38(7), pp. A4-A4.

Delaye, M. and Tardieu, A. 1983. Short range order of crystallin proteins accounts for eye lens transparency. *Nature* 302(5907), pp. 415-417.

Dooley, E. P. 2012. *Ultrastructural evaluation of pathological and acutely injured mammalian corneas.* Cardiff University.

Doughty, M. J. and Seabert, W. and Bergmanson, J. P. G. and Blocker, Y. 2001. A descriptive and quantitative study of the keratocytes of the corneal stroma of albino rabbits using transmission electron microscopy. *Tissue & Cell* 33(4), pp. 408-422.

Dua, H. S. and Faraj, L. A. and Branch, M. J. and Yeung, A. M. and Elalfy, M. S. and Said, D. G. and Gray, T. and Lowe, J. 2014. The collagen matrix of the human trabecular meshwork is an extension of the novel pre-Descemet's layer (Dua's layer). *Br J Ophthalmol* 0, pp. 1-7.

Dua, H. S. and Faraj, L. A. and Said, D. G. and Gray, T. and Lowe, J. 2013. Human Corneal Anatomy Redefined A Novel Pre-Descemet's Layer (Dua's Layer). *Ophthalmology* 120(9), pp. 1778-1785.

Dunlevy, J. R. and Neame, P. J. and Vergnes, J. P. and Hassell, J. R. 1998. Identification of the N-linked oligosaccharide sites in chick corneal lumican and keratocan that receive keratan sulfate. *Journal of Biological Chemistry* 273(16), pp. 9615-9621.

Dupps, W. J. and Roberts, C. 2001. Effect of acute biomechanical changes on corneal curvature after photokeratectomy. *Journal of Refractive Surgery* 17(6), pp. 658-669.

Edward, D. P. and Yue, B. Y. and Sugar, J. and Thonar, E. J. and Sunderraj, N. and Stock, E. L. and Tso, M. O. M. 1988. Heterogeneity in macular corneal dystrophy. *Archives of Ophthalmology* 106(11), pp. 1579-1583.

Elliott, G. F. 1980. Measurements of the electric charge and ion-binding of the protein filaments in intact muscle and cornea, with implications for filament assembly. *Biophysical Journal* 32(1), pp. 95-97.

Farley, M. K. and Pettit, T. H. 1987. Traumatic wound dehisence after penetrating keratoplasty. *American Journal of Ophthalmology* 104(1), pp. 44-49.

Fraser, R. D. B. and Macrae, T. P. and Miller, A. and Suzuki, E. 1983. Molecular conformation and packing in collagen fibrils. *Journal of Molecular Biology* 167(2), pp. 497-521.

Funderburgh, J. L. and Corpuz, L. M. and Roth, M. R. and Funderburgh, M. L. and Tasheva, E. S. and Conrad, G. W. 1997. Mimecan, the 25-kDa corneal keratan sulfate proteoglycan, is a product of the gene producing osteoglycin. *Journal of Biological Chemistry* 272(44), pp. 28089-28095.

Goldman, J. N. and Benedek, G. B. 1967. The relationship between morphology and transparency in the nonswelling corneal stroma of the shark. *Investigative Opthalmology* 6(6), pp. 574-600.

Goldman, J. N. and Benedek, G. B. and Dohlman, C. H. and Kravitt, B. 1968. Structural alterations affecting transparency in swollen human corneas. *Investigative Ophthalmology* 7(5), pp. 501-519.

Goodfellow, J. M. and Elliott, G. F. and Woolgar, A. E. 1978. X-ray diffraction studies of corneal stroma. *Journal of Molecular Biology* 119(2), pp. 237-252.

Gordon, M. and Foley, J. and Linsenmayer, T. and Fitch, J. 1996. Temporal expression of types XII and XIV collagen mRNA and protein during avian corneal development. *Developmental Dynamics*, pp. 49-58.

Gordon, M. K. and Hahn, R. A. 2010. Collagens. *Cell and Tissue Research* 339(1), pp. 247-257.

Gottsch, J. D. and Sundin, O. H. and Liu, S. H. and Jun, A. S. and Broman, K. W. and Stark, W. J. and Vito, E. C. L. and Narang, A. K. and Thompson, J. M. and Magovern, M. 2005. Inheritance of a novel COL8A2 mutation defines a distinct early-onset subtype of Fuchs corneal dystrophy. *Investigative Ophthalmology & Visual Science* 46(6), pp. 1934-1939.

Green, H. S. and Wolf, E. 1953. A scalar representation of electromagnetic fields. *Proceedings of the Physical Society of London Section A* 66(408), pp. 1129-1137.

Hafezi, F. and Seiler, T. 2010. Persistent Subepithelial Haze in Thin-flap LASIK. *Journal of Refractive Surgery* 26(3), pp. 222-225.

Hahnel, C. and Somodi, S. and Weiss, D. G. and Guthoff, R. F. 2000. The keratocyte network of human cornea: A three-dimensional study using confocal laser scanning fluorescence microscopy. *Cornea* 19(2), pp. 185-193.

Hamada, R. and Graf, B. and Giraud, J. P. and Poulique.Y. 1972. Analytical and statistical study of lamellae, keratocytes and collagen fibrils of the central region of the normal human cornea. *Archives D Ophtalmologie* 32(8-9), pp. 563-570.

Hanna, C. and Bicknell, D. S. and O'Brien, J. E. 1961. Cell turnover in adult human eye. *Archives of Ophthalmology* 65(5), pp. 695-698.

Hart, R. W. and Farrell, R. A. 1969. Light scattering in the human cornea. *Journal of the Optical Society of America* 59(6), pp. 766-774.

Hassell, J. R. and Birk, D. E. 2010. The molecular basis of corneal transparency. *Experimental Eye Research* 91(3), pp. 326-335.

Hassell, J. R. and Newsome, D. A. and Krachmer, J. H. and Rodrigues, M. M. 1980. Macular corneal dystrophy: Failure to synthsize a mature keratan sulfate proteoglycan. *Proceedings of the National Academy of Sciences of the United States of America-Biological Sciences* 77(6), pp. 3705-3709.

Hay, E. D. and Revel, J. P. 1969. Fine structure of the developing avian cornea. *Monographs in developmental biology* 1, pp. 1-144.

Hayashida, Y. and Akama, T. O. and Beecher, N. and Lewis, P. and Young, R. D. and Meek, K. M. and Kerr, B. and Hughes, C. E. and Caterson, B. and Tanigami, A. and Nakayama, J. and Fukada, M. N. and Tano, Y. and Nishida, K. and Quantock, A. J. 2006. Matrix morphogenesis in cornea is mediated by the modification of keratan sulfate by GlcNAc 6-O-sulfotransferase. *Proc Natl Acad Sci U S A* 103(36), pp. 13333-13338.

Hayes, S. and Boote, C. and Lewis, J. and Sheppard, J. and Abahussin, M. and Quantock, A. J. and Purslow, C. and Votruba, M. and Meek, K. M. 2007. Comparative study of fibrillar collagen arrangement in the corneas of primates and other mammals. *Anat Rec (Hoboken)* 290(12), pp. 1542-1550.

Hayes, S. and Young, R. and Boote, C. and Hawksworth, N. and Huang, Y. and Meek, K. M. 2010. A structural investigation of corneal graft failure in suspected recurrent keratoconus. *Eye (Lond)* 24(4), pp. 728-734.

Helena, M. C. and Baerveldt, F. and Kim, W. J. and Wilson, S. E. 1998. Keratocyte apoptosis after corneal surgery. *Investigative Ophthalmology & Visual Science* 39(2), pp. 276-283.

Hodson, S. A. and Miller, F. 1976. The biocarbonate pump in the endothelium which regulates hydration of rabbit cornea. *J Physiol* 263, pp. 563-577.

Hoehenwarter, W. and Klose, J. and Jungblut, P. R. 2006. Eye lens proteomics. *Amino Acids* 30(4), pp. 369-389.

Holmes, D. and Kadler, K. 2004. The precision of lateral size control in the assembly of corneal collagen fibrils. *J Mol Biol* 345, pp. 773-784.

Holt, W. S. and Kinoshita, J. H. 1973. Soluble proteins of bovine cornea. *Investigative Ophthalmology* 12(2), pp. 114-126.

Hong, J. W. and Liu, J. J. and Lee, J. S. and Mohan, R. R. and Woods, D. J. and He, Y. G. and Wilson, S. E. 2001. Proinflammatory chemokine induction in keratocytes and inflammatory cell infiltration into the cornea. *Investigative Ophthalmology & Visual Science* 42(12), pp. 2795-2803.

Ihanamaki, T. and Pelliniemi, L. and Vuorio, E. 2004. Collagens and collagen-related matrix components in the human and mouse eye. *Progress in Retinal and Eye Research*, pp. 403-434.

Iozzo, R. V. 1998. Matrix proteoglycans: From molecular design to cellular function. *Annual Review of Biochemistry* 67, pp. 609-652.

Jacobsen, I. E. and Jensen, O. A. and Prause, J. U. 1984. Structure and composition of Bowman's membrane - study by frozen resin cracking. *Acta Ophthalmologica* 62(1), pp. 39-53.

Jester, J. V. 2008. Corneal crystallins and the development of cellular transparency. *Seminars in Cell & Developmental Biology* 19(2), pp. 82-93.

Jester, J. V. and BarryLane, P. A. and Cavanagh, H. D. and Petroll, W. M. 1996. Induction of alpha-smooth muscle actin expression and myofibroblast transformation in cultured corneal keratocytes. *Cornea* 15(5), pp. 505-516.

Jester, J. V. and Jin, H. C. 2003. Modulation of cultured corneal keratocyte phenotype by growth factors/cytokines control in vitro contractility and extracellular matrix contraction. *Experimental Eye Research* 77(5), pp. 581-592.

Jester, J. V. and Moller-Pedersen, T. and Huang, J. Y. and Sax, C. M. and Kays, W. T. and Cavangh, H. D. and Petroll, W. M. and Piatigorsky, J. 1999. The cellular basis of corneal transparency: evidence for 'corneal crystallins'. *Journal of Cell Science* 112(5), pp. 613-622.

Jester, J. V. and Murphy, C. J. and Winkler, M. and Bergmanson, J. P. G. and Brown, D. and Steinert, R. F. and Mannis, M. J. 2013. Lessons in Corneal Structure and Mechanics to Guide the Corneal Surgeon. *Ophthalmology* 120(9), pp. 1715-1717.

Johnson, D. H. and Bourne, W. M. and Campbell, J. 1982. The Ultrastructure Of Descemet's Membrane Changes With Age In Normal Corneas. *Archives of Ophthalmology* 100(12), pp. 1942-1947.

Jonasson, F. and Johannsson, J. H. and Garner, A. and Rice, N. S. C. 1989. Macular corneal dystrophy in Iceland. *Eye* 3, pp. 446-454.

Kasner, L. and Mietz, H. and Green, W. R. 1993. Agenesis of Bowman's layer - A histopathological study of four cases. *Cornea* 12(2), pp. 163-170.

Kasthurirangan, S. and Markwell, E. L. and Atchison, D. A. and Pope, J. M. 2008. In vivo study of changes in refractive index distribution in the human crystalline lens with age and accommodation. *Investigative Ophthalmology & Visual Science* 49(6), pp. 2531-2540.

Kay, E. P. and Lee, M. S. and Seong, G. J. and Lee, Y. G. 1998. TGF-beta s stimulate cell proliferation via an autocrine production of FGF-2 in corneal stromal fibroblasts. *Current Eye Research* 17(3), pp. 286-293.

Kemper, B. and Kosmeier, S. and Langehanenberg, P. and von Bally, G. and Bredebusch, I. and Domschke, W. and Schnekenburger, J. 2007. Integral refractive index determination of living suspension cells by multifocus digital holographic phase contrast microscopy. *Journal of Biomedical Optics* 12(5), p. 5.

Kern, P. and Menasche, M. and Robert, L. 1991. Relative rates of biosythesis of collagen type-I, type-V and type-VI in calf cornea. *Biochemical Journal*, pp. 615-617.

Kirby, M. C. and Aspden, R. M. and Hukins, D. W. L. 1988. Determination of the orientation distribution function for collagen fibrils in a connective tissue site from a high angle x-ray diffraction pattern. *Journal of Applied Crystallography* 21, pp. 929-934.

Klintworth, G. K. 2009. Corneal dystrophies. *Orphanet Journal of Rare Diseases* 4(7).

Klintworth, G. K. and Meyer, R. and Dennis, R. and Hewitt, A. T. and Stock, E. L. and Lenz, M. E. and Hassell, J. R. and Stark, W. J. and Kuettner, K. E. and Thonar, E. 1986. Macular corneal dystrophy: Lack of keratan sulfate in serum and cornea. *Ophthalmic Paediatrics and Genetics* 7(3), pp. 139-143.

Klintworth, G. K. and Oshima, E. and al-Rajhi, A. and al-Saif, A. and Thonar, E. J. and Karcioglu, Z. A. 1997. Macular corneal dystrophy in Saudi Arabia: A study of 56 cases and recognition of a new immunophenotype. *American Journal of Ophthalmology* 124(1), pp. 9-18.

Klintworth, G. K. and Smith, C. F. and Bowling, B. L. 2006. CHST6 mutations in North American subjects with macular corneal dystrophy: a comprehensive molecular genetic review. *Molecular Vision* 12(18), pp. 159-176.

Koenig, S. B. 2008. Bilateral Recurrent Self-Induced Keratoconus. *Eye & Contact Lens-Science and Clinical Practice* 34(6), pp. 343-344.

Komai, Y. and Ushiki, T. 1991. The 3-dimensional organization of collagen fibrils in the human cornea and sclera. *Investigative Ophthalmology & Visual Science* 32(8), pp. 2244-2258.

Krachmer, J. H. 2004. Eye rubbing can cause keratoconus. *Cornea* 23(6), pp. 539-540.

Kremer, J. R. and Mastronarde, D. N. and McIntosh, J. R. 1996. Computer visualization of three-dimensional image data using IMOD. *Journal of Structural Biology* 116(1), pp. 71-76.

Lang, G. K. and Green, W. R. and Maumenee, A. E. 1986. Clinicopathological studies of keratoplasty eyes obtained postmortem. *American Journal of Ophthalmology* 101(1), pp. 28-40.

Larabell, C. A. and Nugent, K. A. 2010. Imaging cellular architecture with X-rays. *Current Opinion in Structural Biology* 20(5), pp. 623-631.

Lassen, N. and Pappa, A. and Black, W. J. and Jester, J. V. and Day, B. J. and Min, E. and Vasiliou, V. 2006. Antioxidant function of corneal ALDH3A1 in cultured stromal fibroblasts. *Free Radical Biology and Medicine* 41(9), pp. 1459-1469.

Lee, R. E. and Davison, P. F. 1981. Collagen composition and turnover in ocular tissues of the rabbit. *Experimental Eye Research* 32(6), pp. 737-745.

Lee, R. E. and Davison, P. F. 1984. The collagens of the developing bovine cornea. *Experimental Eye Research* 39(5), pp. 639-652.

Leonard, D. W. 1996. *The ultrastructure of the corneal stroma and its implications for corneal transparency.* Open University.

Leonard, D. W. and Meek, K. M. 1997. Refractive indices of the collagen fibrils and extrafibrillar material of the corneal stroma. *Biophys J* 72(3), pp. 1382-1387.

Lewis, P. N. and Pinali, C. and Young, R. D. and Meek, K. M. and Quantock, A. J. and Knupp, C. 2010. Structural interactions between collagen and proteoglycans are elucidated by three-dimensional electron tomography of bovine cornea. *Structure* 18(2), pp. 239-245.

Li, D. Q. and Tseng, S. C. G. 1995. Three patterns of cytokine expression potentially involved in epithelial fibroblast interactions of human ocular surface. *Journal of Cellular Physiology* 163(1), pp. 61-79.

Li, W. and Vergnes, J. P. and Cornuet, P. K. and Hassell, J. R. 1992. cDNA clone to chick corneal chondroitin dermatan sulfate proteoglycan reveals identity to decorin. *Archives of Biochemistry and Biophysics* 296(1), pp. 190-197.

Lim, L. and Pesudovs, K. and Coster, D. J. 2000. Penetrating keratoplasty for keratoconus: Visual outcome and success. *Ophthalmology* 107(6), pp. 1125-1131.

Liu, N. P. and Dew-Knight, S. and Rayner, M. and Jonasson, F. and Akama, T. O. and Fukuda, M. N. and Bao, W. J. and Gilbert, J. R. and Vance, J. M. and Klintworth, G. K. 2000. Mutations in corneal carbohydrate sulfotransferase 6 gene (CHST6) cause macular corneal dystrophy in Iceland. *Molecular Vision* 6(33), pp. 261-264.

Maatta, M. and Heljasvaara, R. and Sormunen, R. and Pihlajaniemi, T. and Autio-Harmainen, H. and Tervo, T. 2006a. Differential expression of collagen types XVIII/endostatin and XV in normal, keratoconus, and scarred human corneas. *Cornea* 25(3), pp. 341-349.

Maatta, M. and Vaisanen, T. and Vaisanen, M. and Pihlajaniemi, T. and Tervo, T. 2006b. Altered expression of type XIII collagen in keratoconus and scarred human cornea - Increased expression in scarred cornea is associated with myofibroblast transformation. *Cornea*, pp. 448-453.

Manzer, R. and Pappa, A. and Estey, T. and Sladek, N. and Carpenter, J. F. and Vasiliou, V. 2003. Ultraviolet radiation decreases expression and induces aggregation of corneal ALDH3A1. *Chemico-Biological Interactions* 143, pp. 45-53.

Marchini, M. and Morocutti, M. and Ruggeri, A. and Koch, M. H. J. and Bigi, A. and Roveri, N. 1986. Differences in the fibril structure of corneal and tendon collagen. An electron microscopy and x-ray diffraction investigation. *Connective Tissue Research* 15(4), pp. 269-281.

Matsuda, M. and Ubels, J. L. and Edelhauser, H. F. 1985. A larger corneal epithelial wound closes at a faster rate. *Investigative Ophthalmology & Visual Science* 26(6), pp. 897-900.

Maurice, D. M. 1957. The structure and transparency of the cornea. *Journal of Physiology-London* 136(2), pp. 263-286.

McDermott, G. and Le Gros, M. A. and Knoechel, C. G. and Uchida, M. and Larabell, C. A. 2009. Soft X-ray tomography and cryogenic light microscopy: the cool combination in cellular imaging. *Trends in Cell Biology* 19(11), pp. 587-595.

McLaren, J. W. and Bourne, W. M. and Patel, S. V. 2010. Automated Assessment of Keratocyte Density in Stromal Images from the ConfoScan 4 Confocal Microscope. *Investigative Ophthalmology & Visual Science* 51(4), pp. 1918-1926.

Meek, K. and Holmes, D. 1983. Interpretation of the electron microscopical appearance of collagen fibrils from corneal stroma. *Int J Biol Macromol* 5, pp. 17-25.

Meek, K. M. and Blamires, T. and Elliott, G. F. and Gyi, T. J. and Nave, C. 1987. The organisation of collagen fibrils in the human corneal stroma: a synchrotron X-ray diffraction study. *Curr Eye Res* 6(7), pp. 841-846.

Meek, K. M. and Boote, C. 2004. The organization of collagen in the corneal stroma. *Exp Eye Res* 78(3), pp. 503-512.

Meek, K. M. and Boote, C. 2009. The use of X-ray scattering techniques to quantify the orientation and distribution of collagen in the corneal stroma. *Prog Retin Eye Res* 28(5), pp. 369-392.

Meek, K. M. and Elliott, G. F. and Hughes, R. A. and Nave, C. 1983. The axial density in collagen fibrils from human corneal stroma. *Current Eye Research* 2(7), pp. 471-478.

Meek, K. M. and Elliott, G. F. and Sayers, Z. and Whitburn, S. B. and Koch, M. H. 1981. Interpretation of the meridional x-ray diffraction pattern from collagen fibrils in corneal stroma. *J Mol Biol* 149(3), pp. 477-488.

Meek, K. M. and Fullwood, N. J. and Cooke, P. H. and Elliott, G. F. and Maurice, D. M. and Quantock, A. J. and Wall, R. S. and Worthington, C. R. 1991. Synchrotron x-ray diffraction studies of the cornea, with implications for stromal hydration. *Biophys J* 60(2), pp. 467-474.

Meek, K. M. and Leonard, D. W. 1993. Ultrastructure of the corneal stroma: a comparative study. *Biophys J* 64(1), pp. 273-280.

Meek, K. M. and Leonard, D. W. and Connon, C. J. and Dennis, S. and Khan, S. 2003. Transparency, swelling and scarring in the corneal stroma. *Eye (Lond)* 17(8), pp. 927-936.

Meek, K. M. and Newton, R. H. 1999. Organization of collagen fibrils in the corneal stroma in relation to mechanical properties and surgical practice. *J Refract Surg* 15(6), pp. 695-699.

Meek, K. M. and Quantock, A. J. 2001. The use of X-ray scattering techniques to determine corneal ultrastructure. *Prog Retin Eye Res* 20(1), pp. 95-137.

Meek, K. M. and Quantock, A. J. and Elliott, G. F. and Ridgway, A. E. and Tullo, A. B. and Bron, A. J. and Thonar, E. J. 1989. Macular corneal dystrophy: the macromolecular structure of the stroma observed using electron microscopy and synchrotron X-ray diffraction. *Exp Eye Res* 49(6), pp. 941-958.

Meek, K. M. and Tuft, S. J. and Huang, Y. and Gill, P. S. and Hayes, S. and Newton, R. H. and Bron, A. J. 2005. Changes in collagen orientation and distribution in keratoconus corneas. *Invest Ophthalmol Vis Sci* 46(6), pp. 1948-1956.

Melles, G. R. and Binder, P. S. 1990. A comparison of wound healing in sutured and unsutured corneal wounds. *Archives of Ophthalmology* 108(10), pp. 1460-1469.

Michael, R. and van Marle, J. and Vrensen, G. and van den Berg, T. 2003. Changes in the refractive index of lens fibre membranes during maturation - impact on lens transparency. *Experimental Eye Research* 77(1), pp. 93-99.

Midura, R. J. and Hascall, V. C. and Maccallum, D. K. and Meyer, R. F. and Thonar, E. and Hassell, J. R. and Smith, C. F. and Klintworth, G. K. 1990. Proteoglycan biosynthesis by human corneas from patients with type 1 and type 2 macular corneal dystrophy. *Journal of Biological Chemistry* 265(26), pp. 15947-15955.

Mie, G. 1908. Articles on the optical characteristics of turbid tubes, especially colloidal metal solutions. *Annalen Der Physik* 25(3), pp. 377-445.

Moller-Pedersen, T. 2004. Keratocyte reflectivity and corneal haze. *Experimental Eye Research* 78(3), pp. 553-560.

Moller-Pedersen, T. and Li, H. F. and Petroll, W. M. and Cavanagh, H. D. and Jester, J. V. 1998. Confocal microscopic characterization of wound repair after photorefractive keratectomy. *Investigative Ophthalmology & Visual Science* 39(3), pp. 487-501.

Morrison, J. C. and Swan, K. C. 1982a. Bowman's layer in penetrating keratoplasties of the human eye. *Archives of Ophthalmology* 100(11), pp. 1835-1838.

Morrison, J. C. and Swan, K. C. 1982b. Full thickness lamellar keratoplasty: a histologic study in human eyes. *Ophthalmology* 89(6), pp. 715-719.

Morrison, J. C. and Swan, K. C. 1983. Descemet's membrane in penetrating keratoplasties of the human eye. *Archives of Ophthalmology* 101(12), pp. 1927-1929.

Muller, L. J. and Pels, L. and Vrensen, G. 1995. Novel aspects of the ultrastructural organization of human corneal keratocytes. *Investigative Ophthalmology & Visual Science* 36(13), pp. 2557-2567.

Musch, D. C. and Niziol, L. M. and Stein, J. D. and Kamyar, R. M. and Sugar, A. 2011. Prevalence of Corneal Dystrophies in the United States: Estimates from Claims Data. *Investigative Ophthalmology & Visual Science* 52(9), pp. 6959-6963.

Musselmann, K. and Hassell, J. R. 2006. Focus on molecules: CHST6 (carbohydrate sulfotransferase 6; corneal N-acetylglucosamine-6-sulfotransferase). *Experimental Eye Research* 83(4), pp. 707-708.

Musselmann, K. and Kane, B. P. and Alexandrou, B. and Hassell, J. R. 2008. IGF-II is present in bovine corneal stroma and activates keratocytes to proliferate in vitro. *Experimental Eye Research* 86(3), pp. 506-511.

Musselmann, K. and Kane, B. P. and Hassell, J. R. 2003. Isolation of a putative keratocyte activating factor from the corneal stroma. *Experimental Eye Research* 77(3), pp. 273-279.

Nakazawa, K. and Hassell, J. R. and Hascall, V. C. and Lohmander, L. S. and Newsome, D. A. and Krachmer, J. 1984. Defective processing of keratan sulfate in macular corneal dystrophy. *Journal of Biological Chemistry* 259(22), pp. 3751-3757.

Napper, D. H. 1967. A Diffraction Theory Approach to Total Scattering by Cubes. *Kolloid-Zeitschrift and Zeitschrift Fur Polymere* 218(1), pp. 41-46.

Neame, P. J. and Kay, C. J. and McQuillan, D. J. and Beales, M. P. and Hassell, J. R. 2000. Independent modulation of collagen fibrillogenesis by decorin and lumican. *Cellular and Molecular Life Sciences* 57(5), pp. 859-863.

Netto, M. V. and Mohan, R. R. and Sinha, S. and Sharma, A. and Dupps, W. and Wilson, S. E. 2006. Stromal haze, myofibroblasts, and surface irregularity after PRK. *Experimental Eye Research* 82(5), pp. 788-797.

Newsome, D. A. and Foidart, J. M. and Hassell, J. R. and Krachmer, J. H. and Rodrigues, M. M. and Katz, S. I. 1981. Detection of specific collagen types in normal and keratoconus corneas. *Investigative Ophthalmology & Visual Science* 20(6), pp. 738-750.

Newsome, D. A. and Gross, J. and Hassell, J. R. 1982. Human corneal stroma contains three distinct collagens. *Investigative Ophthalmology & Visual Science* 22(3), pp. 376-381.

Newton, R. H. and Meek, K. M. 1998a. Circumcorneal annulus of collagen fibrils in the human limbus. *Invest Ophthalmol Vis Sci* 39(7), pp. 1125-1134.

Newton, R. H. and Meek, K. M. 1998b. The integration of the corneal and limbal fibrils in the human eye. *Biophys J* 75(5), pp. 2508-2512.

Nirankari, V. S. and Karesh, J. and Bastion, F. and Lakhanpal, V. and Billings, E. 1983. Recurrence of keratoconus in donor cornea 22 years after successful keratoplasty. *British Journal of Ophthalmology* 67(1), pp. 23-28.

Orgel, J. P. and Wess, T. J. and Miller, A. 2000. The in situ conformation and axial location of the intermolecular cross-linked non-helical telopeptides of type I collagen. *Structure with Folding & Design* 8(2), pp. 137-142.

Paganin, D. and Nugent, K. A. 1998. Noninterferometric phase imaging with partially coherent light. *Physical Review Letters* 80(12), pp. 2586-2589.

Palka, B. P. and Sotozono, C. and Tanioka, H. and Akama, T. O. and Yagi, N. and Boote, C. and Young, R. D. and Meek, K. M. and Kinoshita, S. and Quantock, A. J. 2010. Structural Collagen Alterations in Macular Corneal Dystrophy Occur Mainly in the Posterior Stroma. *Current Eye Research* 35(7), pp. 580-586.

Pappa, A. and Brown, D. and Koutalos, Y. and DeGregori, J. and White, C. and Vasiliou, V. 2005. Human aldehyde dehydrogenase 3A1 inhibits proliferation and promotes survival of human corneal epithelial cells. *Journal of Biological Chemistry* 280(30), pp. 27998-28006.

Parfitt, G. J. and Pinali, C. and Young, R. D. and Quantock, A. J. and Knupp, C. 2010. Three-dimensional reconstruction of collagen-proteoglycan interactions in the mouse corneal stroma by electron tomography. *Journal of Structural Biology* 170(2), pp. 392-397.

Patel, S. and Marshall, J. and Fitzke, F. 1995. Refractive Index of the human corneal epithelium and stroma. *Journal of Refractive Surgery* 11(2), pp. 100-105.

Patel, S. V. and McLaren, J. W. and Hodge, D. O. and Bourne, W. M. 2001. Normal human keratocyte density and corneal thickness measurement by using confocal microscopy in vivo. *Investigative Ophthalmology & Visual Science* 42(2), pp. 333-339.

Patel, S. V. and Tester, R. and Soong, H. K. and Sugar, A. and Farjo, Q. A. 2005. Recurrent ectasia after penetrating keratoplasty for keratoconus. *Investigative Ophthalmology & Visual Science* 46.

Pellegata, N. S. and Dieguez-Lucena, J. L. and Joensuu, T. and Lau, S. and Montgomery, K. T. and Krahe, R. and Kivela, T. and Kucherlapati, R. and Forsius, H. and de la Chapelle, A. 2000. Mutations in KERA, encoding keratocan, cause cornea plana. *Nature Genetics* 25(1), pp. 91-95.

Pettinelli, D. J. and Starr, C. E. and Stark, W. J. 2005. Late traumatic corneal wound dehiscence after penetrating keratoplasty. *Archives of Ophthalmology* 123(6), pp. 853-856.

Piatigorsky, J. 2000. Review: A case for corneal crystallins. *Journal of Ocular Pharmacology and Therapeutics* 16(2), pp. 173-180.

Piatigorsky, J. 2001. Enigma of the abundant water-soluble cytoplasmic proteins of the cornea - The "refracton" hypothesis. *Cornea* 20(8), pp. 853-858.

Pierscionek, B. K. 1995. The refractive index along the optic axis of the bovine lens. *Eye* 9, pp. 776-782.

Pierscionek, B. K. 1997. Refractive index contours in the human lens. *Experimental Eye Research* 64(6), pp. 887-893.

Pijanka, J. K. and Abass, A. and Sorensen, T. and Elsheikh, A. and Boote, C. 2013. A wide-angle X-ray fibre diffraction method for quantifying collagen orientation across large tissue areas: application to the human eyeball coat. *Journal of Applied Crystallography* 46, pp. 1481-1489.

Pijanka, J. K. and Coudrillier, B. and Ziegler, K. and Sorensen, T. and Meek, K. M. and Nguyen, T. D. and Quigley, H. A. and Boote, C. 2012. Quantitative Mapping of Collagen Fiber Orientation in Non-glaucoma and Glaucoma Posterior Human Sclerae. *Investigative Ophthalmology & Visual Science* 53(9), pp. 5258-5270.

Pinsky, P. M. and Datye, D. V. 1991. A microstructurally based finite element model of the incised human cornea. *Journal of Biomechanics* 24(10), pp. 907-922.

Polack, F. M. 1961. Morphology of the cornea 1. Study with silver stains. *American Journal of Ophthalmology* 51(5), pp. 1051-1056.

Popper, M. and Morgado, A. M. and Quadrado, M. J. and Van Best, J. A. 2004. Corneal cell density measurement in vivo by scanning slit confocal microscopy: Method and validation. *Ophthalmic Research* 36(5), pp. 270-276.

Prahl, S. 2012. *Mie Scattering Calculator* [Online]. Oregon Medical Laser Center. Available at: http://omlc.ogi.edu/calc/mie_calc.html

Pramanik, S. and Musch, D. C. and Sutphin, J. E. and Farjo, A. A. 2006. Extended long-term outcomes of penetrating keratoplasty for keratoconus. *Ophthalmology* 113(9), pp. 1633-1638.

Prydal, J. I. and Franc, F. and Dilly, P. N. and Muir, M. G. K. and Corbett, M. C. and Marshall, J. 1998. Keratocyte density and size in conscious humans by digital image analysis of confocal images. *Eye* 12, pp. 337-342.

Quantock, A. 1991. *The ultrastructure of normal and pathologic human corneas.* The Open University.

Quantock, A. J. and Klintworth, G. K. and Schanzlin, D. J. and Lenz, M. E. and Thonar, E. 1997. Proteoglycans contain a 4.6-angstrom repeat in corneas with macular dystrophy .2. Histochemical evidence. *Cornea* 16(3), pp. 322-326.

Quantock, A. J. and Meek, K. M. and Ridgway, A. E. and Bron, A. J. and Thonar, E. J. 1990. Macular corneal dystrophy: reduction in both corneal thickness and collagen interfibrillar spacing. *Curr Eye Res* 9(4), pp. 393-398.

Quantock, A. J. and Meek, K. M. and Thonar, E. J. and Assil, K. K. 1993. Synchrotron X-ray diffraction in atypical macular dystrophy. *Eye (Lond)* 7 (Pt 6), pp. 779-784.

Rabinowitz, Y. S. 1998. Keratoconus. *Survey of Ophthalmology* 42(4), pp. 297-319.

Rada, J. A. and Cornuet, P. K. and Hassell, J. R. 1993. Regulation of corneal collagen fibrillogenesis in-vitro by corneal proteoglycan (lumican and decorin) core proteins. *Experimental Eye Research* 56(6), pp. 635-648.

Radner, W. and Zehetmayer, M. and Aufreiter, R. and Mallinger, R. 1998a. Interlacing and cross-angle distribution of collagen lamellae in the human cornea. *Cornea* 17(5), pp. 537-543.

Radner, W. and Zehetmayer, M. and Skorpik, C. and Mallinger, R. 1998b. Altered organization of collagen in the apex of keratoconus corneas. *Ophthalmic Research* 30(5), pp. 327-332.

Rawe, I. M. and Meek, K. M. and Leonard, D. W. and Takahashi, T. and Cintron, C. 1994. Structure of corneal scar tissue: an X-ray diffraction study. *Biophys J* 67(4), pp. 1743-1748.

.

Roberts, C. 2000. The cornea is not a piece of plastic. *Journal of Refractive Surgery* 16(4), pp. 407-413.

Rodahl, E. and Van Ginderdeuren, R. and Knappskog, P. M. and Bredrup, C. and Boman, H. 2006. A second decorin frame shift mutation in a family with congenital stromal corneal dystrophy. *American Journal of Ophthalmology* 142(3), pp. 520-521.

Sandberg-Lall, M. and Hagg, P. and Wahlstrom, I. and Pihlajaniemi, T. 2000. Type XIII collagen is widely expressed in the adult and developing human eye and accentuated in the ciliary muscle, the optic nerve and the neural retina. *Experimental Eye Research*, pp. 401-410.

Sawaguchi, S. and Fukuchi, T. and Abe, H. and Kaiya, T. and Sugar, J. and Yue, B. Y. J. T. 1998. Three-dimensional scanning electron microscopic study of keratoconus corneas. *Archives of Ophthalmology* 116(1), pp. 62-68.

Sayers, Z. and Koch, M. H. J. and Whitburn, S. B. and Meek, K. M. and Elliott, G. F. and Harmsen, A. 1982. Synchrotron X-ray diffraction study of corneal stroma. *Journal of Molecular Biology* 160(4), pp. 593-607.

Scott, J. E. 1980. Collagen-preteoglycan interaction - localization of preteoglycans in tendon by electron microscopy. *Biochemical Journal* 187(3), pp. 887-891.

Scott, J. E. 1985. Proteoglycan histochemistry - A valuable tool for connective-tissue biochemists. *Collagen and Related Research* 5(6), pp. 541-575.

Scott, J. E. 1991. Chondroitin sulfate and keratan sulfate are almost isosteric. *Biochemical Journal* 275, pp. 267-268.

Scott, J. E. 1992. Morphometry of Cupromeronic blue-stained proteoglycan molecules in animal corneas, versus that of purified proteoglycans stained in-vitro, implies that tertiary structures contribute to corneal ultrastructure. *Journal of Anatomy* 180, pp. 155-164.

Scott, J. E. and Haigh, M. 1985. Proteoglycan type I collagen fibril interactions in bone and non-calcifying connective tissues. *Bioscience Reports* 5(1), pp. 71-81.

Scott, J. E. and Haigh, M. 1988. Keratan sulfate and the ultrastructure of cornea and catilage - a stand-in for chondroitin sulfate in conditions of oxygen lack. *Journal of Anatomy* 158, pp. 95-108.

Scott, J. E. and Orford, C. R. 1981. Dermatan sulfate-rich proteoglycan associates with rat tail tendon collagen at the D-band in the gap region. *Biochemical Journal* 197(1), pp. 213-216.

Sen, D. K. and Mohan, H. and Gupta, D. K. 1969. Bilateral Peripheral Sclero-cornea. *Acta Ophthalmologica* 47(4), pp. 1041-1043.

Silverman, B. and Alexander, R. J. and Henley, W. L. 1981. Tissue and species specificity of BCP-54, the major soluble protein of bovine cornea. *Experimental Eye Research* 33(1), pp. 19-29.

Sivak, J. 1988. *Corneal Optics in aquatic animals: how they see above and below. In The Cornea: Transactions of the World Congress on the Cornea III*. New York: Raven Press Ltd.

Smelser, G. K. and Polack, F. M. and Ozanics, V. 1965. Persistence of Donor Collagen in Corneal Transplants. *Experimental Eye Research* 4(4), pp. 349-354.

Smith, J. W. 1969. The transparency of the corneal stroma. *Vision Research* 9(3), pp. 393-396

Stapleton, W. M. and Chaurasia, S. S. and Medeiros, F. W. and Mohan, R. R. and Sinha, S. and Wilson, S. E. 2008. Topical interleukin-1 receptor antagonist inhibits inflammatory cell infiltration into the cornea. *Experimental Eye Research* 86(5), pp. 753-757.

Stoiber, J. and Muss, W. H. and Ruckhofer, J. and Thaller-Antlanger, H. and Alzner, E. and Grabner, G. 2000. Recurrent keratoconus in a patient with Leber congenital amaurosis. *Cornea* 19(3), pp. 395-398.

Stone, D. L. and Kenyon, K. R. and Green, W. R. and Ryan, S. J. 1976. Congenital central corneal leukoma (Peter's anomaly). *American Journal of Ophthalmology* 81(2), pp. 173-193.

Stramer, B. M. and Zieske, J. D. and Jung, J. C. and Austin, J. S. and Fini, M. E. 2003. Molecular mechanisms controlling the fibrotic repair phenotype in cornea: Implications for surgical outcomes. *Investigative Ophthalmology & Visual Science* 44(10), pp. 4237-4246.

Sultana, A. and Klintworth, G. K. and Thonar, E. J. M. A. and Vemuganti, G. K. and Kannabiran, C. 2009. Immunophenotypes of macular corneal dystrophy in India and correlation with mutations in CHST6. *Molecular Vision* 15(30-32), pp. 319-325.

Sun, X. and Tang, H. and Yuan, G. 2008. Anomalous diffraction approximation method for retrieval of spherical and spheroidal particle size distributions in total light scattering. *Journal of Quantitative Spectroscopy & Radiative Transfer* 109(1), pp. 89-106.

Taflove, A. and Hagness, S. 2005. *Computational Electrodynamics: The Finite Difference Time Domain Method*. 3rd ed. Norwood, MA: Artech House, Inc.

Teague, M. R. 1983. Deterministic phase retrieval - a Green-function solution. *Journal of the Optical Society of America* 73(11), pp. 1434-1441.

Thalasselis, A. and Etchepareborda, J. 2002. Recurrent keratoconus 40 years after keratoplasty. *Ophthalmic and Physiological Optics* 22(4), pp. 330-332.

Thonar, E. J. and Meyer, R. F. and Dennis, R. F. and Lenz, M. E. and Maldonado, B. and Hassell, J. R. and Hewitt, A. T. and Stark, W. J. J. and Stock, E. L. and Kuettner, K. E. and Klintworth, G. K. 1986. Absense of normal keratan sulfate in the blood of patients with macular corneal dystrophy. *American Journal of Ophthalmology* 102(5), pp. 561-569.

Tisdale, A. S. and Spurrmichaud, S. J. and Rodrigues, M. and Hackett, J. and Krachmer, J. and Gipson, I. K. 1988. Development of the anchoring structures of the epithelium in rabbit and human-fetal corneas. *Investigative Ophthalmology & Visual Science* 29(5), pp. 727-736.

Trelstad, R. L. and Coulombre, A. J. 1971. Morphogenesis of collagenous stroma in chick cornea. *Journal of Cell Biology* 50(3), pp. 840-858.

Tuominen, I. S. J. and Tervo, T. M. T. and Teppo, A. M. and Valle, T. U. and Gronhagen-Riska, C. and Vesaluoma, M. H. 2001. Human tear fluid PDGF-BB, TNF-alpha and TGF-beta 1 vs corneal haze and regeneration of corneal epithelium and subbasal nerve plexus after PRK. *Experimental Eye Research* 72(6), pp. 631-641.

Unal, M. and Yucel, I. and Akar, Y. and Akkoyunlu, G. and Gultekin, I. 2007. Recurrence of keratoconus in two corneal grafts after penetrating keratoplasty. *Cornea* 26(3), pp. 362-364.

Vaddavalli, P. K. and Hurmeric, V. and Wang, J. H. and Yoo, S. H. 2012. Corneal Haze Following Disruption of Epithelial Basement Membrane on Ultra-high-resolution OCT Following Femtosecond LASIK. *Journal of Refractive Surgery* 28(1), pp. 72-74.

Van de Hulst, H. 1957. *Light Scattering by Small Particles*. New York: Courier Dover Publications.

van den Berg, T. J. 1996. Depth-dependent forward light scattering by donor lenses. *Investigative Ophthalmology & Visual Science* 37(6), pp. 1157-1166.

van den Berg, T. J. and Spekreijse, H. 1999. Light scattering model for donor lenses as a function of depth. *Vision Research* 39(8), pp. 1437-1445.

Wandell, B. 1995. *Foundations of Vision*. Stanford: Sinauer Associates.

Weiss, J. S. and Moller, H. U. and Lisch, W. and Kinoshita, S. and Aldave, A. J. and Belin, M. W. and Kivelae, T. and Busin, M. and Munier, F. L. and Seitz, B. and Sutphin, J. and Bredrup, C. and Mannis, M. J. and Rapuano, C. J. and Van Rij, G. and Kim, E. K. and Klintworth, G. K. 2008. The IC3D Classification of the Corneal Dystrophies. *Cornea* 27(10), pp. S1-S42.

Wessel, H. and Anderson, S. and Fite, D. and Halvas, E. and Hempel, J. and SundarRaj, N. 1997. Type XII collagen contributes to diversities in human corneal and limbal extracellular matrices. *Investigative Ophthalmology & Visual Science*, pp. 2408-2422.

Wilson, S. E. 2000. Role of apoptosis in wound healing in the cornea. *Cornea* 19(3), pp. S7-S12.

Wilson, S. E. and Hong, J. W. 2000. Bowman's layer structure and function - Critical or dispensable to corneal function? A hypothesis. *Cornea* 19(4), pp. 417-420.

Woodhead-Galloway, J. and Hukins, D. W. L. and Knight, D. P. and Machin, P. A. and Weiss, J. B. 1978. Molecular packing in elastoidin spicules. *Journal of Molecular Biology* 118(4), pp. 567-578.

Worthington, C. R. and Inouye, H. 1985. X-ray diffraction study of the cornea. *International Journal of Biological Macromolecules* 7(1), pp. 2-8.

Yamamoto, Y. and Shinohara, K. 2002. Application of X-ray microscopy in analysis of living hydrated cells. *Anatomical Record* 269(5), pp. 217-223.

Yang, C. J. and Sundarraj, N. and Thonar, E. J. and Klintworth, G. K. 1988. Immunohistochemical evidence of heterogeneity in macular corneal dystrophy. *American Journal of Ophthalmology* 106(1), pp. 65-71.

Yee, K. S. 1966. Numerical solution of initial boundary value problems involving Maxwell's equations in isotropic media. *IEEE Transactions on Antennas and Propagation* AP14(3), pp. 302-307.

Yeniad, B. and Alparslan, N. and Akarcay, K. 2009. Eye Rubbing as an Apparent Cause of Recurrent Keratoconus. *Cornea* 28(4), pp. 477-479.

Young, B. and Zhang, G. and Koch, M. and Birk, D. 2002. The roles of types XII and XIV collagen in fibrillogenesis and matrix assembly in the developing cornea. *Journal of Cellular Biochemistry*, pp. 208-220.

Young, R. D. and Knupp, C. and Pinali, C. and Png, K. M. Y. and Ralphs, J. R. and Bushby, A. J. and Starborg, T. and Kadler, K. E. and Quantock, A. J. 2014. Three-dimensional aspects of matrix assembly by cells in the developing cornea. *Proceedings of the National Academy of Sciences* 111(2), pp. 687-692.

Zhou, L. and Beuerman, R. W. and Huang, L. and Barathi, A. and Foo, Y. H. and Li, S. F. Y. and Chew, F. T. and Tan, D. 2007. Proteomic analysis of rabbit tear fluid: Defensin levels after an experimental corneal wound are correlated to wound closure. *Proteomics* 7(17), pp. 3194-3206.